Report SDSMT/IAS/R-98/01 September 1998

REPORT ON T-28 ELECTRIC FIELD MEASUREMENTS AND THEIR CALIBRATION

By: Rand E. Feind, Qixu Mo, and Andrew G. Detwiler

Prepared for:

Division of Atmospheric Sciences
National Science Foundation

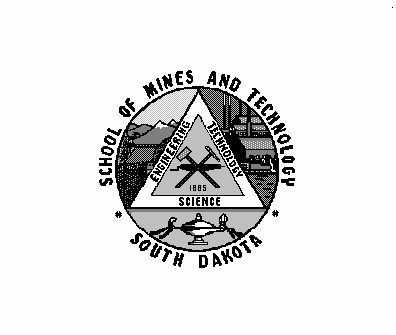

Institute of Atmospheric Sciences
South Dakota School of Mines and Technology
501 E. St. Joseph Street
Rapid City, South Dakota 57701-3995

TABLE OF CONTENTS

List of Figures **Pg. No.**

List of Tables

1. INTRODUCTION

1.1 Purpose

The purpose of this report is to provide documentation for the methods used to derive electric field measurements from electric field meters mounted on the South Dakota School of Mines and Technology (SDSMT) armored T-28 aircraft. The report describes the circumstances attending to 1990 and 1997 intercomparison flights involving the T-28 along with the New Mexico Institute of Mining and Technology (NMIMT) Special Purpose Test Vehicle for Airborne Research (SPTVAR). The SPTVAR carries a well-calibrated system of meters from which reliable electric field estimates can be derived. We document performance of the T-28 electric field meter system using data obtained during these intercomparison flights. We look at the long-term stability and reliability of measurements obtained with a 4-meter system carried on the T-28 from 1989 - 1997 (Sections 4.2 and 4.3). We use data obtained during the 1997 intercomparisons to derive a new response matrix for a 5-meter system on the T-28, including the 4 meters flown since 1989 and a 5^{th} meter installed in 1993. Finally, we demonstrate methods used to identify artifacts in data from this system (Section 4.4).

1.2 Historical Background

The SDSMT armored T-28 has been used since the mid-1980's to measure ambient electrostatic fields during thunderstorm penetrations. The earliest work began in 1986 with two rotating-shutter electric field meters (also known as field mills), borrowed from the National Aeronautics and Space Administration (NASA) Marshall Space Flight Center. These were mounted, one facing upward from back of the canopy, the other downward from the baggage bay door on the bottom of the fuselage, in a configuration that was suitable, with certain simplifying assumptions, for determining the vertical component of the ambient electric field as well as charge on the aircraft. However, several procedures required to use the meter readings to calculate accurately the desired field strength were not accomplished. Attempts to charge the aircraft artificially in clear air in the absence of an electric field were unsuccessful. In addition, there was no opportunity to calibrate the response of the meters to a known ambient field in the absence of aircraft charge. (See Winn, 1993.) This made it impossible to construct accurately a quantity based on a combination of the two meter readings that is independent of aircraft charge.

The 1986 data were examined, and estimates of relative variations in the vertical component of ambient fields were performed. These estimates were based on observations of the relative response of the field meters to ambient fields, compared to their response to aircraft charging, due to hydrometeors encountered during particular thunderstorm penetrations. On some of these penetrations, it was clear from the response pattern of the two meters that aircraft charging dominated. The meters yielded readings of the same sign in constant proportion to each other. Data from these penetrations yielded qualitative estimates of the relative response of one meter to the other, responding to charge on the

aircraft, with the top meter reading ~2x the bottom meter for a given charge on the aircraft. On other penetrations, it was clear that ambient electric field dominated. On these penetrations, the top and bottom meters yielded readings of opposite sign, but with the absolute magnitudes in constant proportion to each other. During these penetrations the magnitude of the field at the top meter also was ~2x that at the bottom.

With the assumption that the meters were responding only to the vertical component of the ambient field and to charge on the aircraft, it was possible to qualitatively estimate the relative magnitude of these two components of the total electric field at the surface of the aircraft even during penetrations when the aircraft was charged and there was an ambient electric field. However, without a set of measurements in a field of known strength, or in the presence of a known value of charge on the aircraft, these relative field components could not be converted to quantitative estimates of the ambient field or of charge on the aircraft.

During fieldwork in 1989, the NASA field meters used earlier were replaced with two rotating shutter meters from the NMIMT. Their operating principles are similar to the NASA meters used earlier. The mounting positions were the same as in 1986. Two additional meters of the same type, borrowed from the National Center for Atmospheric Research (NCAR), were mounted, one in each wing tip, facing outward. See Figure 1. The additional two meters made it possible to compute, in principle, all three components of the ambient field and the component due to charge on the aircraft. Also in 1989, it became possible to charge the aircraft artificially, in clear air in the absence of significant electric fields.

Results obtained during 10 weeks of field operations verified quantitatively the relative responses of the two fuselage-mounted mills to aircraft charging and to ambient fields, as were determined earlier based on the 1986 observations. Relative responses of the wing tip mills to both ambient field and to charge on the aircraft were determined as well. Relative response of the different meters to the same ambient field was determined from rapid roll maneuvers, while relative response to charge was determined during artificial charging experiments. However, no absolute calibration was possible, as there was no independent estimate of the true electric field or charge magnitude during any of these maneuvers or self-charging tests.

In 1990, the T-28 was deployed to Albuquerque, New Mexico, in order to carry out formation flights with the SPTVAR. This single-engine monoplane had a well-calibrated system for measuring ambient electric fields. Results from these flights yielded an absolute calibration for calculations of ambient field components from the T-28 4-meter system. (Giori and Nanevicz, 1992; Giori and Detwiler, 1993). These results have been used to reduce the electric field data from many field projects in which the T-28 has participated in since 1986.

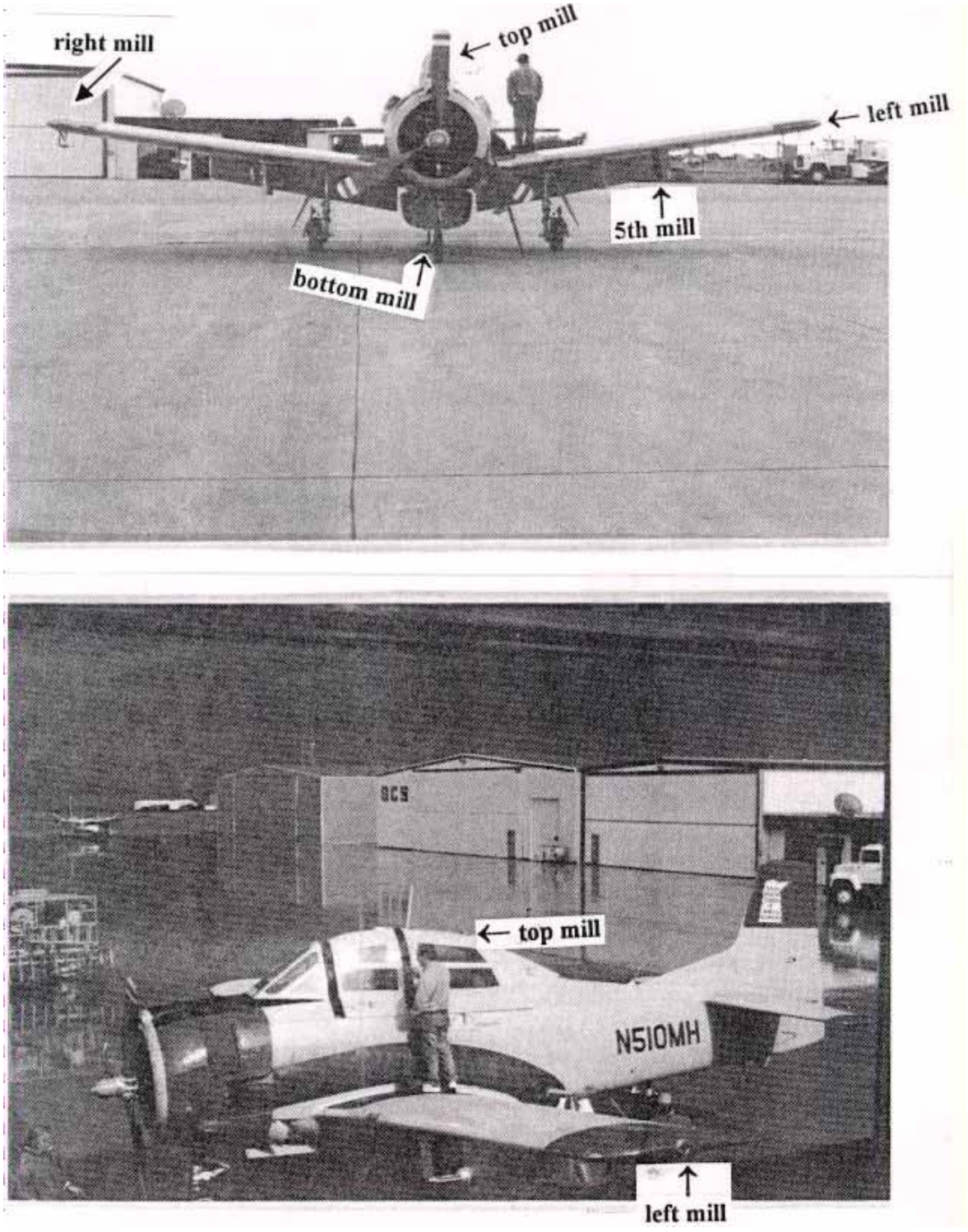

Fig. 1. Picture of T-28. Locations of electric field meters are indicated with arrows.

The relationship between individual meter readings, and the ambient field and net charge on the aircraft that produce them, can be summarized in a matrix of enhancement factors. The enhancement factor used with the T-28 system is based on the matrix derived by Giori and Nanevicz using the 1990 intercomparison data.

$$\begin{pmatrix} E_t \\ E_b \\ E_l \\ E_r \end{pmatrix} = \begin{pmatrix} 0 & 0 & 5.3 & 4.2 \\ 0 & 0 & -2.8 & 2.0 \\ 10 & 22.4 & -1 & 10.8 \\ 10 & -22.4 & -1 & 10.8 \end{pmatrix} \begin{pmatrix} E_x \\ E_y \\ E_z \\ E_Q \end{pmatrix} \qquad (1)$$

The orthogonal coordinate system used here is defined by E_z positive upwards, E_y positive to the left of the aircraft heading, and E_x positive in the direction of the aircraft heading. The matrix can be interpreted in the following way, using the top row as an example. The reading of the top meter, E_t, is equal to 5.3 times E_z plus 4.2 times the charge on the aircraft, Q, where Q is scaled in magnitude so that one unit of charge produces the same reading as an ambient field of 0.5 kV m^{-1}. The remaining rows can be interpreted similarly, with E_b, E_l, and E_r, representing readings from the bottom, left and right meters, respectively. Factors have been adjusted slightly compared to Giori and Nanevicz (1992) based on the analysis of roll and self-charging maneuvers subsequent to 1990.

The procedure used in deriving this matrix was to force the T-28 and SPTVAR systems to agree on the magnitude of E_z. Then enhancement factors for the wing tip meters were adjusted by comparing the relative responses of the vertically-oriented fuselage meters to the horizontally-oriented wing tip meters during roll maneuvers during which first one pair then the other pair of the field meters was oriented in the direction of the ambient electric field.

A direct solution for $\{E_x, E_y, E_z, Q\}$ in terms of $\{E_t, E_b, E_l, E_r\}$ can be obtained by inverting the matrix in (1). However, in the electrically noisy environments in which the T-28 normally operates, it is sometimes difficult to track noise in the reading of one meter backwards through the matrix and discerns how it influences the retrieved ambient field. Therefore a somewhat simpler scheme has been used to estimate ambient fields using measurements from the T-28 meter system. It takes advantage of the near-symmetry in the installation of the two fuselage meters, and two wing tip meters, as evidenced in the matrix in (1). In addition, E_x is not routinely estimated, as it is strongly influenced by aircraft charging in most storm penetrations.

$$E_y = [E_l - E_r]/44.8 \qquad (2)$$

$$E_z = [E_t - 2.1\, E_b]/11.2$$

$$E_{Qy} = [E_l + E_r]/21.6$$

$$E_{Qz} = [E_t + 2E_b]/8$$

When ambient fields are small, E_{Qy} and E_{Qz} should be numerically equal, but E_{Qy} and E_{Qz} are not equal when there is ambient field, particularly when the ambient field is strong, which will be explained in later sections. Equation (2) is almost equivalent to Equation (1). Further discussion and physical interpretation of these relationships is presented below.

In 1993, a fifth field meter was added to the T-28, mounted facing downward in the outboard pylon of the hail spectrometer under the left wing. See Figure 1. The response of this meter to the three components of the ambient field and to charge on the aircraft is discussed in section 4.4.

In 1997, the T-28 again deployed to Albuquerque for a new set of intercomparison flights with the SPTVAR. At this time, scientists working with SPTVAR had developed an improved system for measuring electric fields (Mo and Winn, 1998), yet the aircraft also still carried the same system with which it had been equipped in 1990. Thus it was possible to test the T-28 and old SPTVAR systems for consistent response over the 7-year interval between intercomparisons, as well as to compare these systems to the new SPTVAR system. It was also an opportunity to verify the response of the meter in the T-28 hail spectrometer pod to the independently-determined electric fields from SPTVAR and to verify a response matrix for the 5-meter system.

2. 1990 INTERCOMPARISONS

T-28 crew for this one-week exercise was:

Dan Custis - pilot
Jon Leigh - mechanic
Gary Johnson - engineer
Ken Hartman - programmer/data analyst
Andy Detwiler - facility scientist

Ground crew members arrived in Albuquerque on Sunday, 22 July. The T-28 also arrived on Sunday and was hangared at Cutter Flying Service, located at Albuquerque International Airport (ABQ). The aircraft carried its normal complement of instrumentation, described in Appendix A. Data items recorded or computed are listed in Appendix B.

On Monday, 23 July, T-28 crewmembers traveled to Socorro to get acquainted with the NMIMT operations from Socorro Airport and discuss flight coordination procedures. NMIMT staff involved in SPTVAR operations were J.J. “Dan” Jones, William Winn, and Steve Hunyady, all affiliated with the Langmuir Laboratory at NMIMT. The SPTVAR was flown on different days by one of two pilots, J.W. “Bill” Bullock, of AIRO, Inc., in Colorado Springs, and Peter Fleischacker.

Plans were made to rendezvous to the north of the Baldy peaks at the intersection of Rt. 60 and Water Canyon Rd., a landmark easily visible from the air under VFR conditions, and to fly in formation under small thunderstorms in the vicinity of Langmuir Laboratory on Baldy Peak. A map of the region around Langmuir Laboratory, showing the locations of the laboratory and the Baldy Peak rendezvous point, is shown in Figure 2. The mismatch in performance between the two aircraft required the T-28 to operate with flaps extended in order to fly slowly enough to do formation flying with the SPTVAR. On the other hand, the SPTVAR was trimmed for maximum speed. The T-28 would fly slightly behind (~50 ft, according to later visual estimates by Custis during the actual flights) and to the right of the SPTVAR.

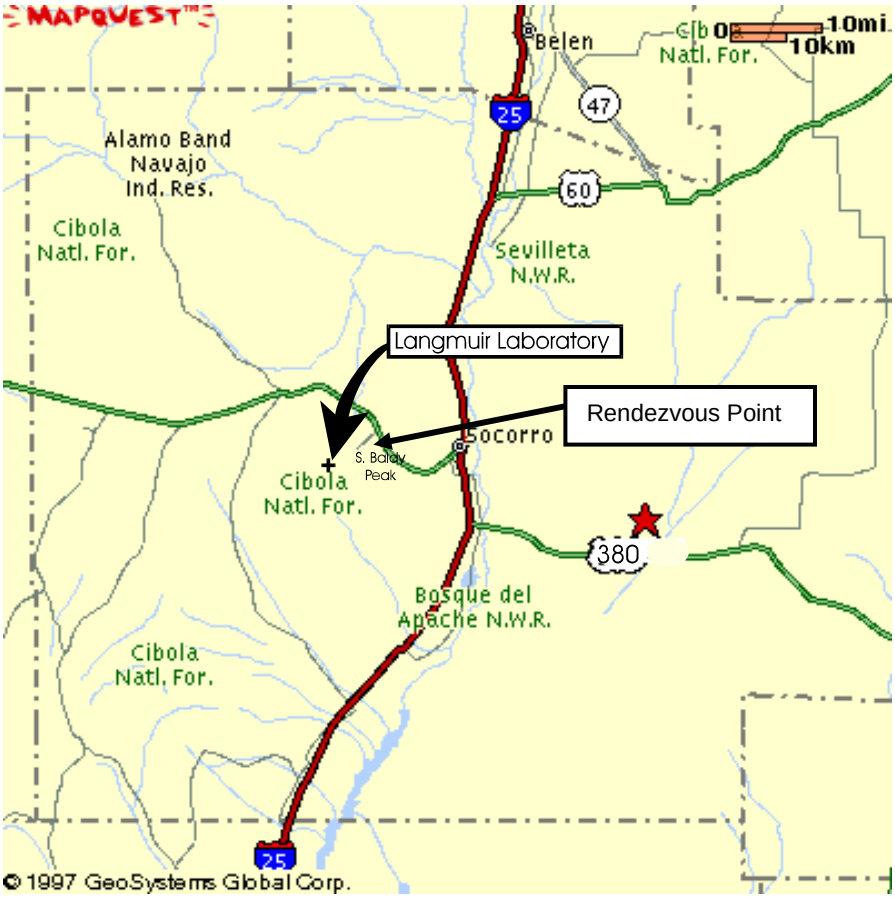

Figure 2. Map showing the region around Langmuir Laboratory

On the return flight from Socorro to Albuquerque on this day, the T-28 flew through episodes of light rain under an extended thunderstorm anvil formation. The data were recorded as Flight 528. The only apparent instrumentation problems were with the VOR unit.

The rest of the week saw two successful intercomparison flights and a storm electricity research flight on three successive days, Tuesday through Thursday, 24-27 July. On each day small thunderstorms formed within range for telemetry from the SPTVAR to

its ground data system located at Socorro Airport. Summaries of flight operations and data obtained are given below for each flight.

[Note: The T-28 data system operated on a clock set to MDT. The SPTVAR telemetry computer operated on MST, and operations were directed from the SPTVAR telemetry trailer where the clock displayed MST. Event times listed in this report have been translated to MDT unless otherwise noted.]

✈Research Flights

2.1 Tuesday, 24 July - T-28 Flight 529

Small thunderstorms began to develop in the Socorro area between 12:30 and 13:30 MDT. Clouds appeared to be developing from Mt. Wittington and moving northeastward across the Langmuir Lab site. Rainshafts and cloud-to-ground lightning were visible from the airport. The convection was strong enough to produce development of the anvil upshear as well as downshear, from some clouds.

The T-28 take-off was at 14:40 MDT. SPTVAR and T-28 linked up near the rendezvous point at 15:14 MDT. They began coordinated flight legs along the edges of the bases of thunderstorms near Langmuir Laboratory. Cloud bases were around 3.8 km MSL. Storms continued in the area for the duration of the flight. The times and characteristics of the best of the coordinated flight legs with measurable electric fields are listed in Table 1. Estimates of maximums and minimums in electric field components are based on SPTVAR data.

TABLE 1

Intercomparison Legs on 24 July 1990

Begin Time	End Time	Extreme E_z (kV/m)	Extreme E_y (kV/m)	Rain?
1530	1537	43/-30	16/-4	begin & end
1539	1547	36/-22	7/-6	
1549	1555	26/-8	Missing	some
1556	1600	35/-1	3/-11	

A self-charging test was performed by the T-28 beginning just after 1603 as the two aircraft continued to fly in formation. The T-28 data system clock was observed at this time to be 4 sec behind SPTVAR's. The aircraft separated just before 1615 and the T-28 returned to ABQ, landing at 1630.

2.2 Wednesday, 25 July – T-28 Flight 530

An early morning sounding from Socorro showed light winds in lower troposphere. A dry layer at 6.1 km slowed cloud development.

Eventually some small thunderstorms developed near Langmuir Lab around mid-afternoon. Light showers reached ground. Several shafts were in sight at any one time. The clouds did not seem to be anchored to the mountains and drifted generally S or SE. Tops extended up to 9.1 km. Lightning was infrequent; only a few cloud-to-ground flashes were visible.

The T-28 departed ABQ at 1533. Aircraft linked up at 1610. Cloud bases were around 3.7 km. The times and characteristics of the best of the coordinated passes with measurable electric fields are listed in Table 2. Peak electric field components are again based on SPTVAR measurements.

TABLE 2

Intercomparison Legs on 25 July 1990

Begin Time	End Time	Extreme E_z (kV/m)	Extreme E_y (kV/m)	Rain?
1610	1616	23/0	3/-7	Light
1616	1620	24/0	5/-3	Yes
1621	1626	24/0	8/0	Yes
1626	1631	17/0	6/0	
1631	1637	23/0	3/-6	Light
1637	1642	11/0	2.5/-1	

The aircraft separated at 1643. The T-28 did a self-charging test at 1646 on the way back to ABQ, and landed near 1700. A time check showed that the T-28 data system clock was still 4 sec behind the SPTVAR data system clock.

2.3 Thursday, 26 July - T-28 Flight 531

Clouds over Langmuir Lab were disorganized and anemic-looking after lunch. Bigger ones were observed to the southwest. At about 15:00 MDT there were some showers north of LL that were intensifying and moving southeastward over it.

On this day the aircraft made coordinated penetrations of the same storm at different altitudes. The T-28 departed ABQ at 1602. Beginning at 1621, it made penetrations near cloud base (4 km) while the SPTVAR made penetrations at altitudes between 6.0 and 7.5 km. Later in the flight, the T-28 climbed to 4.5 km for penetrations

just above cloud base, while the SPTVAR reached 8.2 km as the storm matured. Storm tops were estimated to be greater than 9.1 km. At 1715 the T-28 broke away from the mission and returned to ABQ, doing a self-charge test on the way.

2.4 Summary of 1990 Flights

A summary of flight activity associated with this deployment is presented in Table 3.

TABLE 3
T-28 Flights - July 1990

Date	Flight No.	Duration (h)	Purpose
12 July	524	2.2	Local test
22 July	525	1.9	Ferry to Pueblo, CO
22 July	526	1.6	Ferry to ABQ
23 July	527	0.7	Ferry to Socorro
23 July	528	1.4	Return to ABQ, local check
24 July	529	2.3	Intercomparison
25 July	530	1.8	Intercomparison
26 July	531	2.4	Intercomparison
28 July	532	1.8	Ferry to Pueblo
28 July	533	1.8	Ferry to RAP
	Total	17.9	

3. 1997 INTERCOMPARISONS

Similar procedures were followed again in a deployment to ABQ during August, 1997. The T-28 crew for this deployment included:

Tom Root - pilot
Charles Summers - pilot/mechanic
Gary Johnson - engineer
Rand Feind - programmer/data analyst
Andy Detwiler - facility scientist

The T-28 carried a reduced complement of instrumentation, with no PMS FSSP, no PMS OAP-2DC, and a J-W cloud liquid water probe with inoperative heaters. In addition, GPS altitude was not recorded. A complete list of instrumentation and data recorded is contained in Appendices A and B.

Crewmembers traveled to Albuquerque over the first weekend in August, arriving on Monday, 4 August. The aircraft was ferried to ABQ from Rapid City (RAP) on Monday, 4 August, and hangared at Cutter Flying Services.

Telemetry and communications equipment was installed at the NMIMT operations trailer at Socorro Airport on Tuesday, 5 August. The T-28 crew met with NMIMT staff to discuss intercomparison flight procedures. Pilots for the SPTVAR were Arnold Ebneter and Peter Fleishacker. Directing SPTVAR operations during the intercomparisons were William Winn and Qixu Mo.

One novel procedure tried with the T-28 during this deployment was to boot the data system only when the aircraft had come within range of the T-28 telemetry receiving station at Socorro Airport. This was done in order to avoid accumulating a large backlog of data in the data spooler on the aircraft that could not be telemetered until the aircraft was within line-of-sight range of the receiving station. Given the relatively low rate of data transmission, this backlog would not be cleared before the intercomparison work began, and current data could not be received during this most important phase of the flight. By switching on the data system after takeoff, when in range of the receiving station, no backlog developed and current data were available immediately at the ground for use in coordinating flight operations.

Most SPTVAR data are not recorded on-board, but are telemetered to ground for recording. Thus all operations had to be conducted within telemetry range of the airport for the SPTVAR system. The time convention in SPTVAR data was UT for the 1997 intercomparisons. Times in this report are all converted to MDT.

On Wednesday, 6 August, a joint flight was conducted during the late morning during which no thunderstorms were present until late in the flight. The pilots were able to work out procedures for performing their formation flights. Root landed the T-28 at Socorro for re-fueling before returning to ABQ. T-28 data were recorded as Flight 693, and all instruments appeared to be working well, except that the reverse-flow temperature sensor was reading ~2°C high compared to the T-28 Rosemount temperature sensor and the two SPTVAR temperature sensors.

The first opportunity to fly an intercomparison around thunderstorms came 3 days later.

✈Research Flights

3.1 Saturday, 9 August – T-28 Flight 694

Thunderstorms began developing in the vicinity of Langmuir Laboratory in the early afternoon. The aircraft were launched near 1445, and rendezvoused near Langmuir Laboratory at 1523 at the north side of a rain shower. Summers was the T-28 pilot, while Fleischacker flew the SPTVAR. The two aircraft flew alongside of the bases of storms in the region, and in some cases into some light precipitation falling from their bases. Average altitude was 3.7 km MSL with temperatures ranging from 7 to 8°C. Straight-line intercomparison legs and their characteristics are listed in Table 4. Extreme values of electric field components are based on T-28 observations.

TABLE 4

Intercomparison Legs on 9 August 1997

Begin (MDT)	End (MDT)	Extreme E_z (kV/m)	Extreme E_y (kV/m)	Rain?
152600	153000	32/-7	11/-2	Yes
153000	153340	1/-7	2/0	No
153400	153630	2/0	7/0	No
153700	153900	0/-23	8/-3	No
153930	154100	0/-10	0/-4	No
154130	154300	0/-2	0/-2	No
154320	154600	0/-1	1/-1	No
154700	154830	0/-1	0/0	No
154900	155400	1/-6	6/0	No

The aircraft broke formation at 1555 and the T-28 returned to ABQ, landing at ~1615.

Data quality was generally good. A T-28 self-charging test attempted at 1523 did not produce any signal in the electric field meters.

3.2 Sunday, 10 August – T-28 Flight 695

Suitable storms developed in the vicinity of Langmuir Laboratory again the next day. The aircraft were launched just after 1400, and linked up north of Langmuir Laboratory at 1440. Many intercomparison legs were conducted in the vicinity of these storms. The aircraft penetrated the fringes of precipitation shafts fairly often on this flight. Altitude ranged from 2.7 to 3.2 km MSL, with temperatures ranging from 14 to 10°C. A summary of intercomparison legs is contained in Table 5.

TABLE 5

Intercomparison Legs on 10 August 1997

Begin (MDT)	End (MDT)	Extreme E_z (kV/m)	Extreme E_y (kV/m)	Rain?
144600	145000	25/0	1/-11	Yes
145030	145500	30/-10	14/-15	Yes
145900	150500	20/-15	21/-6	Yes
150600	150930	18/-2	6/-4	Yes
151020	151400	1/-1	0/-1	No
151800	152050	11/-6	6/-3	Yes
152130	152520	9/-17	7/-6	Yes

A view of the sky to the north of Socorro Airport in Figure 3 shows the clouds around which the aircraft operated during their intercomparison legs on 10 August. After 1526, the aircraft separated and the T-28 returned to ABQ. Root attempted some dog-leg maneuvers between 1527 and 1528 while still under an overhanging anvil as he headed toward ABQ, hoping to obtain electric field meter readings that could be used for a self-calibration, as described in Winn (1993). This type of maneuver basically involves orienting the aircraft in as many different directions as possible and as quickly as possible while the ambient field is nearly constant over the path of the aircraft during the maneuvers, as will be discussed in more detail below. An examination of the data obtained on this flight during these maneuvers suggests that the field was not constant for such distances during these maneuvers.

All T-28 data appeared to be of good quality. A self-charging test conducted between 143040 and 143120 did produce measurable readings on the field meters.

The next day again produced thunderstorms in the vicinity of Langmuir Laboratory. As these storms were relatively well-separated and their anvils relatively extensive, it was decided to fly the T-28 solo and to concentrate on performing self-calibration maneuvers.

Fig. 3. View of sky over Socorro Airport during operations on 10 August 1997.

3.3 Monday, 11 August – T-28 Flight 696

The T-28 launched from ABQ ~1500 with Root in command. Several well-developed thunderstorms were present in the vicinity of Socorro Airport when the T-28 arrived. A view to the northeast from the Socorro Airport taxiway is shown in Figure 4. An anvil from a storm to the southwest of the airport is shown stretching northeastward over the airport. The T-28 approached the vicinity of Socorro Airport and began to conduct flight legs out and back from storms, under the storm anvils. Average altitude was 5.2 km, which kept the aircraft 300 m or so below the bases of the anvils. A summary of the dog-leg maneuvers conducted during this flight is shown in Table 6.

Fig. 4. View of sky over Socorro Airport during operations on 11 August 1997

TABLE 6

Self-Calibration Legs on 11 August 1997

Begin (MDT)	End (MDT)	Location
152600	153000	Under storm to N
153630	153830	going N away from storm to S
153930	154130	going S toward storm to S
154230	154330	going N away from storm to S
154430	154830	going S toward storm to S
155200	155500	going N away from storm to S
155840	160100	roll maneuvers

Fields were generally weak, ranging up to a few kV m^{-1}. Preliminary examination of the data suggested that fields were not constant over extensive portions of the flight track. Further details are developed in the analysis that follows later in this report.

The most important aspect of the data obtained during this flight, from the point of view of self-calibration, is that the heading indicator was not turned on until after the dog-leg maneuvering was completed. This necessitates using changes in the GPS ground track

angle to indicate changes in the aircraft heading during these maneuvers when applying the Winn (1993) self-calibration procedures. This is discussed in more detail below.

3.4 Wednesday, 13 August – T-28 Flight 697

There was no significant thunderstorm activity in the vicinity of Langmuir Laboratory on 12 August, but on 13 August interesting storms developed and a coordinated mission involving the SPTVAR and T-28 was undertaken.

The T-28 was piloted by Root, and SPTVAR was piloted by Ebneter. The T-28 departed ABQ about 1345, and rendezvoused with SPTVAR at about 1415. On this day the two aircraft coordinated in simultaneous penetrations at different levels in a storm that developed just north of Langmuir Laboratory. T-28 penetrations were at the 5 km MSL where the temperature was roughly -2°C. SPTVAR penetrations were at the 7 km MSL level. A summary of T-28 penetrations, as indicated by the pilot-activated in-cloud indications in the data, is presented in Table 7. (The 1427 penetration was not indicated by the pilot, but was inferred from a review of the data.)

TABLE 7

T-28 Cloud Penetrations on 13 August 1997

Begin (MDT)	End	Extreme E_z (kV/m)	Extreme cloud water (g/m^3)	Extreme updraft (m/s)	Precip?
141657	141807	0	0.6	3/-9	No
142231	142312	2/0	1.1	14/-3	No
142700	143200	20/-40	0.3	5/-2	Yes
143515	143558	26/-5	0.1	5/-3	Yes
144111	144328	26/-57	0.7	8/-6	Yes

Dog-leg maneuvers were attempted after 1445 when the T-28 broke off from the study, performed a low pass over the Socorro Airport, and headed for ABQ. Fields were very weak during these maneuvers. The aircraft landed at 1515.

Data from this flight have not been examined carefully, but a preliminary examination shows no obvious problems. The T-28 data system clock was 2 sec ahead of the SPTVAR data system clock. (The SPTVAR clock was slaved to time broadcasts from the WWV shortwave radio service.) T-28 data have been supplied to NMIMT where this case is part of an ongoing study of thunderstorm electrification.

Aircraft and crew departed for Rapid City on Thursday, 14 August, with Summers the pilot on the ferry home.

3.5 Summary of 1997 Flights

A summary of all flight activity connected with this deployment, including pre-deployment test flights, is presented in Table 8.

TABLE 8

T-28 Flights during July, 1997

Date	Flight No.	Time (hr)	Purpose
20 June	688	1.1	local test
8 July	689	1.2	local test
31 July	690	1.2	local test
4 August	691	3.7	ferry RAP-FNL-ABQ
6 August	692	2.3	procedures test
6 August	693	0.6	ferry ONM-ABQ
9 August	694	1.7	research
10 August	695	1.8	research
11 August	696	1.6	research
13 August	697	1.8	research
14 August	698	3.7	ferry ABQ-COS-RAP
	Total	20.7	

4. DATA ANALYSIS

4.1 Self-Charge Test History

One important aspect of inferring the ambient electric field from electric field meters on an aircraft is to understand the response of the system of meters to charge on the aircraft. This can be accomplished by installing a high-voltage power supply on the aircraft and attaching it to a discharge wick. When the power supply is turned on, it produces a discharge that steadily discharges the aircraft. Eventually an equilibrium is reached where the rate of discharge is balanced by discharges of the opposite sign through the engine exhaust and the attachment of ions of the opposite sign to various surfaces of the aircraft. The steady-state net charge on the aircraft in this situation typically amounts to 10's of μC in the case of small, propeller driven aircraft (Jones, 1990).

If there is no ambient field present, and the discharged ions do not themselves influence the readings of any of the meters, then the response of the meters in this situation is purely due to charge on the aircraft. This allows the meter readings to be combined into differences that are independent of charge on the aircraft and dependent only on ambient fields. This is a critical step toward inferring ambient fields from systems of airborne field meters. For further details, see, e.g., Winn (1993), Mo (1997), and Mo and Winn (1998).

Self-charging tests were conducted during both 1990 and 1997, as well as during many flights during other field operations from 1989 through 1997. As these were conducted at the pilot's discretion, and the pilot had no knowledge of the ambient field at the time of the test, some of the tests were compromised due to large ambient fields. Some tests failed due to mechanical or electrical problems in the power supply-discharger system, and some failed for unknown reasons.

A summary of the results from tests that were successful is shown in Table 9. The means of the relative responses of the meters represent our best estimates of the relative response of these meters to charge on the aircraft. The standard deviations represent an estimate of the noise in the measurement. For all meters except the right wing meter the standard deviations of the ratio to the bottom meter is less than 10% of the mean. For unknown reasons, the variation is greater for the right meter than its symmetric partner on the left wing and the other 2 meters. The meter system configuration was stable during this period, save for the addition of the 5th meter in 1993, and there was no discernible trend with time in the relative responses of one meter to any other.

Table 9. T-28 Self-Charging Tests, 1989-1997

Flight	Year	top/bottom	left/bottom	right/bottom	5th/bottom
515	1989	2.0	5.5	5.8	
516	1989	1.8	5.4	5.5	
		1.9	5.7	5.8	
517	1989	2.0	5.0	5.5	
		2.0	5.8	5.9	
519	1989	2.0	5.5	6.0	
520	1989	2.0	5.3	5.6	
		2.0	5.4	5.8	
523	1990	2.0	5.0	5.3	
		2.0	5.3	5.5	
		2.0	5.6	5.6	
		2.0	5.5	5.5	
529	1990	2.0	4.7	4.0	
530	1990	2.0	4.3	3.9	
544	1991	2.1	5.6	5.8	
		2.1	5.9	6.0	
547	1991	2.3	5.8	6.0	
		2.0	6.0	M	

(Table 9 continued)

Flight	Year	top/bottom	left/bottom	right/bottom	5th/bottom
548	1991	2.1	6.0	5.7	
		2.1	5.9	6.1	
556	1991	2.2	5.9	5.9	
557	1991	1.2	5.4	4.0	
558	1991	1.6	7.5	7.5	
559	1991	2.1	6.3	6.6	
		2.3	6.0	5.9	
560	1991	2.4	6.1	5.3	
561	1991	2.3	5.1	4.7	
		2.7	6.5	6.2	
562	1991	2.0	5.2	6.0	
		2.1	6.1	5.6	
572	1991	2.2	6.2	5.7	
576	1991	2.0	5.7	5.7	
590	1992	2.1	6.1	5.8	
610	1993	1.6	5.1	5.1	2.9
612	1993	2.2	6.1	6.0	2.9
		2.2	6.3	6.1	3.2
613	1993	2.1	6.5	5.8	3.1
		2.2	6.6	6.5	3.2
614	1993	2.0	5.9	5.8	3.0
		2.8	7.1	7.6	3.2
620	1994	2.3	5.9	5.8	3.1
621	1994	2.5	5.7	6.6	3.0
622	1994	2.2	5.8	5.8	3.0
		2.2	6.0	5.8	3.3
623	1994	2.2	6.0	5.9	3.0
		2.2	5.8	5.7	2.9
624	1994	2.2	6.1	5.9	3.1
		2.2	5.9	5.8	3.2
		2.2	6.0	6.0	3.1
658	1995	2.2	5.9	5.8	3.1
		2.3	6.1	6.0	3.2
665	1995	2.2	6.0	5.7	3.0
		2.3	5.8	6.1	3.1

(Table 9 continued)

Flight	Year	top/bottom	left/bottom	right/bottom	5th/bottom
667	1995	2.3	6.1	5.9	3.1
		2.3	5.9	5.9	3.1
		2.2	5.9	5.7	3.1
669	1995	2.3	6.1	5.8	3.1
		2.3	6.1	5.8	3.1
		2.3	5.9	5.9	3.1
695	1997	2.0	5.9	5.0	3.0
696	1997	2.2	5.8	5.8	3.1
		2.2	6.0	5.8	3.1
697	1997	2.3	5.9	5.9	3.2
		2.2	5.9	5.8	3.1
	Mean	2.13	5.83	5.67	3.09
	St. Dev.	0.22	0.48	0.92	0.10

4.2 Intercomparison Results from 1990 and 1997

During July of 1990 and August of 1997, formation flights were conducted between the SDSMT T-28 and the NMIMT SPTVAR. In this section, straightforward intercomparisons are presented between the electric field measurements obtained from the two aircraft. For 1990, the electric field estimates of the *Y* (horizontal along the wings) and *Z* (vertical and perpendicular to *Y*) components are intercompared between the T-28 4-meter system and the SPTVAR fuselage meter system. For 1997, the same intercomparison is presented not only for the *Y* and *Z* components, but also the *X* component (horizontal along the fuselage and perpendicular to *Y* and *Z*. These intercomparisons are presented without any data filtering or massaging and provide an overall indication of the long-term stability and reliability of measurements obtained from the two aircraft.

In 1997, the NMIMT SPTVAR also had a new and improved pod meter system (two pods, one on each wing, each with four meters). Therefore, an intercomparison between the new SPTVAR pod meter system and the T-28 4-meter system is also presented.

The results from this section indicate that the field meter measurements obtained from the T-28 system have been consistent and reliable from 1990 to 1997; however, they suggest that some improvements in the enhancement matrix can be made. This was another motivation for conducting the formation flights of 1997; that is, using the electric field measurements from the new SPTVAR pod meter system as a standard, derive adjustments

to or an improved enhancement matrix for a T-28 5-meter system. Through some careful data selection and analysis, and a rigorous methodology, a new enhancement matrix is developed in Section 4.4.

4.2.1 1990

The data recorded from the two meter systems (T-28 and SPTVAR), for the period in which the aircraft were flying in formation, is parsed into four passes (Passes 1-4) for 24 July 1990 and six passes (Passes 1-6) for 25 July 1990. In the comparisons to follow, electric fields were deduced from the electric field meter system on the T-28 using the two fuselage and two wing tip meters. The vertical and transverse field components relative to the aircraft, E_z and E_y, were estimated using (2), which is based on (1). These equations themselves were derived using the T-28/SPTVAR intercomparisons performed in 1990. Thus the 1990 comparison presented here is an illustration of how well two independent airborne systems, one tuned to the other, can measure the same field components. Electric fields were deduced from a 5-meter system on the fuselage of SPTVAR during the 1990 intercomparisons. The SPTVAR electric field components in 1990 were computed using equations (10) in Winn (1993). The 1990 intercomparisons do not include comparison of E_x components, the component in the direction of aircraft motion. Confidence was lacking in the accuracy of E_x as determined both from SPTVAR and from the T-28.

The detailed results from each pass, for all ten passes, are discussed in Appendix C. The discussion is based on plots of field meter measurements that also appear in Appendix C. The types of plots are:

(1) The time sequence, for each of the two systems (T-28 and SPTVAR), for each of two field components (Y and Z).

(2) A scatter plot, with regression statistics, for each pass, for each field component (Y and Z), of the SPTVAR system vs. the T-28 system.

The regression results are summarized in Table 10. For each pass, the explained variance r^2, slope, Y-intercept, and standard deviation about the regression line, are shown for each pass and each of two field components.

Z Component

In all ten passes, the correlations are very good with r^2 values ranging from 0.98 to 1.00. The slopes of the regression lines range from 0.92 to 1.06. The mean value is 0.98 and standard deviation is 0.04.

Y Component

In one of the 10 passes (Pass 3, 24 Jul 90), the SPTVAR system experienced a dropout of about two minutes and forty-five seconds duration (~15:51:00 to ~15:52:50).

Although the two systems indicate similar trends in the field before and after this interval, this dropout corrupts the regression statistics within this interval.

In the other nine passes, the correlations are good with r^2 values ranging from 0.79 to 0.98. The slopes of the linear regressions range from 0.67 to 1.09. The mean value is 0.85 and standard deviation is 0.12.

The T-28 E_y readings are, on average, only 85% of the corresponding SPTVAR reading because the meter enhancement factors used to compute the T-28 E_y were not tuned to the SPTVAR E_y, but selected to make the T-28 E_y readings consistent with the T-28 E_z readings during rolls when both the vertical meter pair and the horizontal meter pair were alternately aligned to the same ambient electric field component. The T-28 meter enhancement factors for E_z were selected so that, on average, the SPTVAR and T-28 E_z estimates were equal.

The T-28 wing tip meters, the ones from which E_y estimates are derived, are away from the fuselage while the SPTVAR meters were all on the fuselage in 1990. Effects of corona on the fuselage meters (see Section 4.4) may have contributed to the greater disparity and noise in the E_y comparisons between the two systems compared to the E_z comparisons (see below).

4.2.2 1997

The 1997 intercomparisons were conducted in a manner similar to the 1990 intercomparisons. The significant difference between the two campaigns is that in 1997 the SPTVAR carried two independent electric field meter systems—including the old 5-meter fuselage system which was also involved in the 1990 intercomparisons and a newer system consisting of twin 4-meter pods, one mounted under each wing. (See Mo and Winn, 1998.) In 1997 the electric field components estimates based on the SPTVAR fuselage meter system were computed using the matrix of equations (19) in Winn (1993). There are some differences in the results obtained using equations (10), as was done in 1990, compared to equations (19) as was done in 1997. The matrix method explicitly couples estimates of one component to the other two, whereas the differences represented by equations (10) do not explicitly couple the response of the meters to all 3 components. Typically, though, results obtained with the two methods are very similar.

The under-wing pod electric field meter system was used on the SPTVAR only in 1997. The appropriate enhancement factor matrix for this system was deduced using as a standard the electric fields computed from the older fuselage meter system computed with equations (19) from Winn (1993). This computation was done using measurements obtained when the aircraft was not producing corona. See Mo and Winn (1998) for details. The work of Mo and Winn (1998) shows that the pod meters are less affected than the

Table 10 Intercomparison Statistics - 1990

			Time		Duration		Regression			Max (kV/m)				
Flt	Pass	Ax	ST	ET	Sec	r^2	Slp	Y-Int	SD	SPT (-)	SPT (+)	T-28 (-)	T-28 (+)	Comments
1	1	Y	15.50	15.62	420	0.84	0.88	0.37	1.27	-3.79	12.86	-2.81	9.25	
1	2	Y	15.65	15.78	480	0.89	0.82	0.04	0.75	-6.41	6.73	-6.18	5.79	
1	3	Y	15.82	15.92	360	0.23	0.14	0.73	1.68	-1.99	14.91	-1.58	7.33	Long dropout in SPTVAR
1	4	Y	15.93	16.00	239	0.79	1.09	0.22	1.63	-10.87	2.43	-11.10	1.33	
1	1	Z	15.50	15.62	420	0.99	0.97	0.32	1.30	-29.79	46.64	-27.63	43.46	
1	2	Z	15.65	15.78	480	0.99	0.99	0.01	1.03	-21.59	35.59	-20.92	33.10	
1	3	Z	15.82	15.92	360	0.99	0.97	0.11	0.91	-7.69	36.71	-7.58	25.21	
1	4	Z	16.00	15.93	239	0.99	1.01	0.36	1.05	-1.80	35.52	-1.67	34.71	
2	1	Y	16.17	16.27	360	0.94	0.87	-0.05	0.41	-6.93	2.84	-6.27	2.68	
2	2	Y	16.27	16.33	240	0.92	0.69	0.21	0.37	-3.42	4.90	-1.86	4.08	
2	3	Y	16.35	16.43	299	0.97	0.92	-0.10	0.41	-0.09	8.33	-0.02	7.43	
2	4	Y	16.43	16.52	300	0.96	0.81	-0.04	0.27	-0.05	5.91	0.00	4.42	
2	5	Y	16.52	16.62	360	0.98	0.67	0.03	0.20	-5.94	3.39	-3.81	2.15	
2	6	Y	16.62	16.70	300	0.92	0.63	0.04	0/14	-1.10	2.70	-0.43	1.73	
2	1	Z	16.17	16.27	360	0.98	1.06	0.07	1.12	0.06	23.56	-0.18	25.78	
2	2	Z	16.27	16.33	240	0.99	1.03	0.18	0.99	0.35	24.34	0.56	24.53	
2	3	Z	16.35	16.43	299	1.00	0.98	0.23	0.50	-0.07	24.52	-0.02	23.88	
2	4	Z	16.43	16.52	300	1.00	0.94	0.24	0.37	-0.19	17.25	0.03	15.88	
2	5	Z	16.52	16.62	360	1.00	0.96	0.17	0.45	-0.24	23.04	-0.01	21.89	
2	6	Z	16.62	16.70	300	1.00	0.92	0.22	0.22	-0.40	11.03	-0.34	9.96	

fuselage meters by corona emissions from the aircraft in the presence of significant electric fields, and that in general the pod electric field meter system should yield better estimates of ambient field when the field magnitude is greater than 10-20 kV m^{-1} and corona is likely.

A second difference is that in the 1997 intercomparisons attention was paid to all 3 components of the electric field vector, E_z, E_y, and E_x. Analysis of the 1990 intercomparisons led Giori and Nanevicz (1992) to the conclusion that the sum of the readings from the T-28 wing tip meters was proportional both to charge on the aircraft, E_q, and to the component of the field along the direction of motion, E_x. More recent work by Mo (1997) suggests that in clear air and in light precipitation, net charge on an aircraft can build up only to some tens of microcoulombs, and that the sum of the wing tip meter readings on the SPTVAR or T-28 is in these situations determined mainly by E_x, rather than E_q. In the discussion to follow, the T-28 E_{qy}, based on a scaled sum of the wing tip meter readings, is compared to the SPTVAR E_{xo} (based on readings from the old meter system) and E_{xn} (based on readings from the new meter system). It will be seen that the T-28 wing tip scaled sum is indeed more influenced by E_x than by charge on the aircraft.

A third difference was that in 1997 the pilots were directed to try to penetrate precipitation shafts more than was attempted during the 1990 intercomparisons. The purpose was to look at intercomparisons in noisier measurement environments, as most measurements of scientific interest during thunderstorm field programs will be obtained in an environment containing precipitation. However, only regions of light precipitation could be penetrated, as formation flight requires good visibility.

In the intercomparisons to follow, the same enhancement factors and procedures used for the 1990 intercomparison (i.e. equation [2]) was used again for computing electric field components from the T-28 system.

To facilitate data manipulation and analysis, the data recorded for all three meter systems (the one on the T-28 and the two on the SPTVAR), for the period in which the aircraft were flying in formation, is parsed into seven intercomparison legs (Passes 1-7) for both 9 Aug 1997 (Flight 694) and 10 Aug 1997 (Flight 695). The results obtained from each pass, of the fourteen passes, are discussed in some detail in Appendix D. The discussion is based on plots of field meter measurements that also appear in Appendix D. The types of plots that appear in Appendix D are:

1) The time sequence, for each of the three systems (T-28, old and new SPTVAR), for each of the three field components (X, Y, and Z).

2) A scatter plot, with regressions, for each component of the field, for the new SPTVAR system vs.: a) the T-28 system, and b) the old SPTVAR system.

3) The electric field, as measured by the T-28 system, superimposed on the trajectory of the aircraft, in both the horizontal and vertical planes.

4) The attitude measurements (pitch, roll, and heading), for each pass, for the T-28.

A general idea of the pattern of all of the intercomparison flights can be illustrated with examples from Flight 694 on 9 August 1997 and Flight 695 on 10 August 1997. The T-28 trajectory for Flight 694 is shown in Figures 5a-d and 6a-g. The trajectory for Flight 695 is shown in Figures 7a-d and 8a-g. Figures 5a-d and 7a-g depict the trajectory in 2D perspective while figures 6a-d and 8a-g are in 3D perspective. In Figures 5a-d and 7a-d, the viewing aspect for each figure is as follows:

	View From	Orientation of Plane of Projection
5a, 7a	above	horizontal
5b, 7b	below	horizontal
5c, 7c	south	vertical
5d, 7d	east	vertical

Each line type corresponds to a specific pass (or intercomparison leg) as indicated by the legend. In Figures 6a-g and 8a-g, each figure corresponds to a single pass as follows:

	Pass Number
6a, 8a	1
6b, 8b	2
6c, 8c	3
6d, 8d	4
6e, 8e	5
6f, 8f	6
6g, 8g	7

The lines used to plot each figure in Figures 6a-g and 8a-g correspond to the lines used for each pass in Figures 5a-d and 7a-d.

The discussion and results found in Appendix D are summarized below.

New SPTVAR vs. T-28 System

The regression results are summarized in Table 11. The variance explained by a linear relationship, r^2, along with slope, Y-intercept, and standard deviation about the regression is shown for each pass and field component.

X Component

In nine of the 14 passes, the statistics indicate fair to poor correlation between the three systems. In four of those nine passes (694-2, 6, 7 and 695-5), the fields are very small (<1.3 kV/m) and the signal is very noisy. In three of the passes (695-1, 4, 7), the measurements appear to correlate well but transients in the new SPTVAR data significantly affect the statistics. The T-28 measurements on many passes appear to trail those of the new SPTVAR by about 5 seconds. The T-28 was physically behind the SPTVAR all of the time. This distance varied and was not recorded. Differences between the T-28 data system clock (which was not slaved to the WWV time standard) and the SPTVAR data system clock (which was) should have been the same for all passes on a flight and cannot account for the time discrepancy that appears for some legs and not others on the same flight.

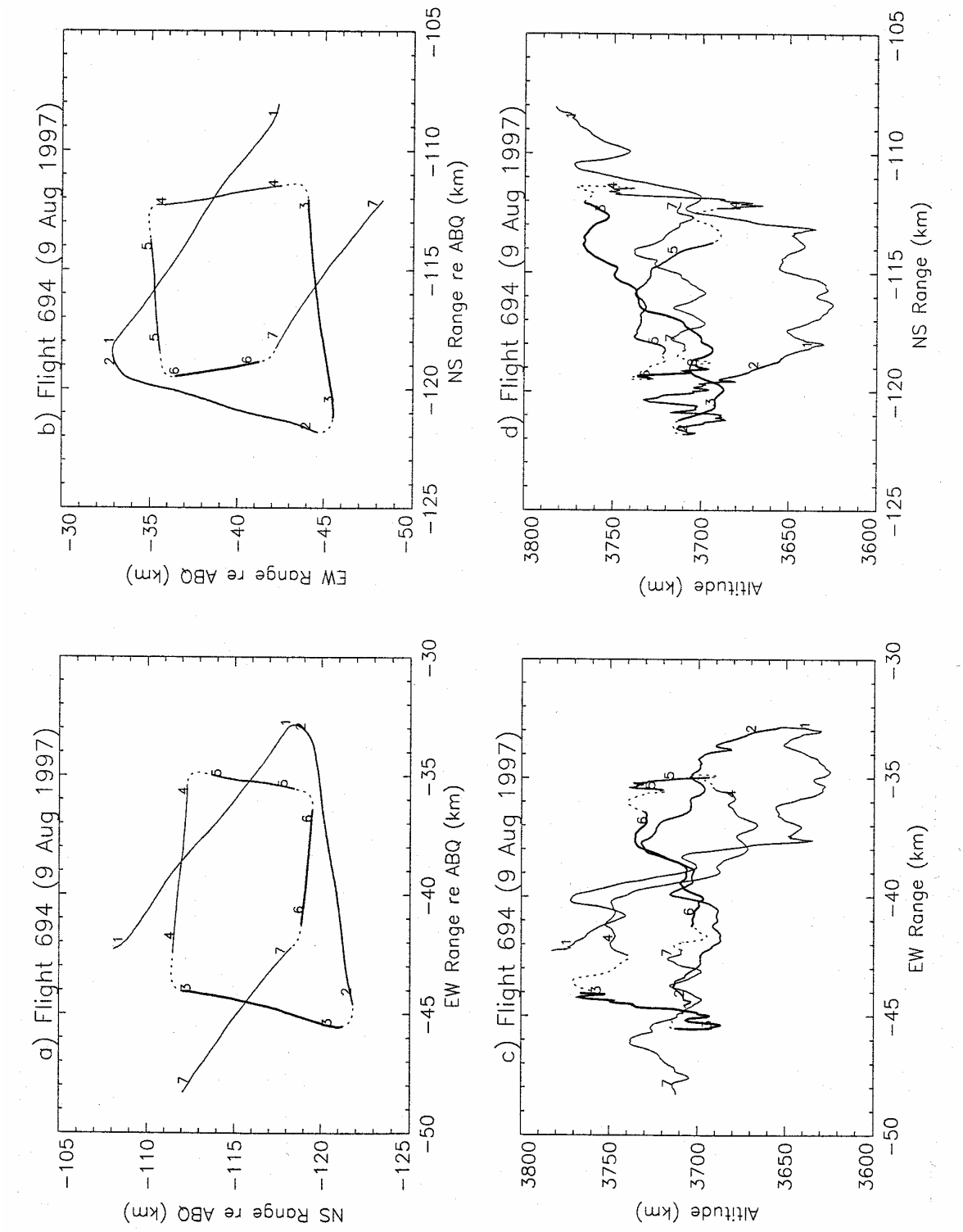

Fig. 5. T-28 flight tracks during Flight 694, 9 August 1997.

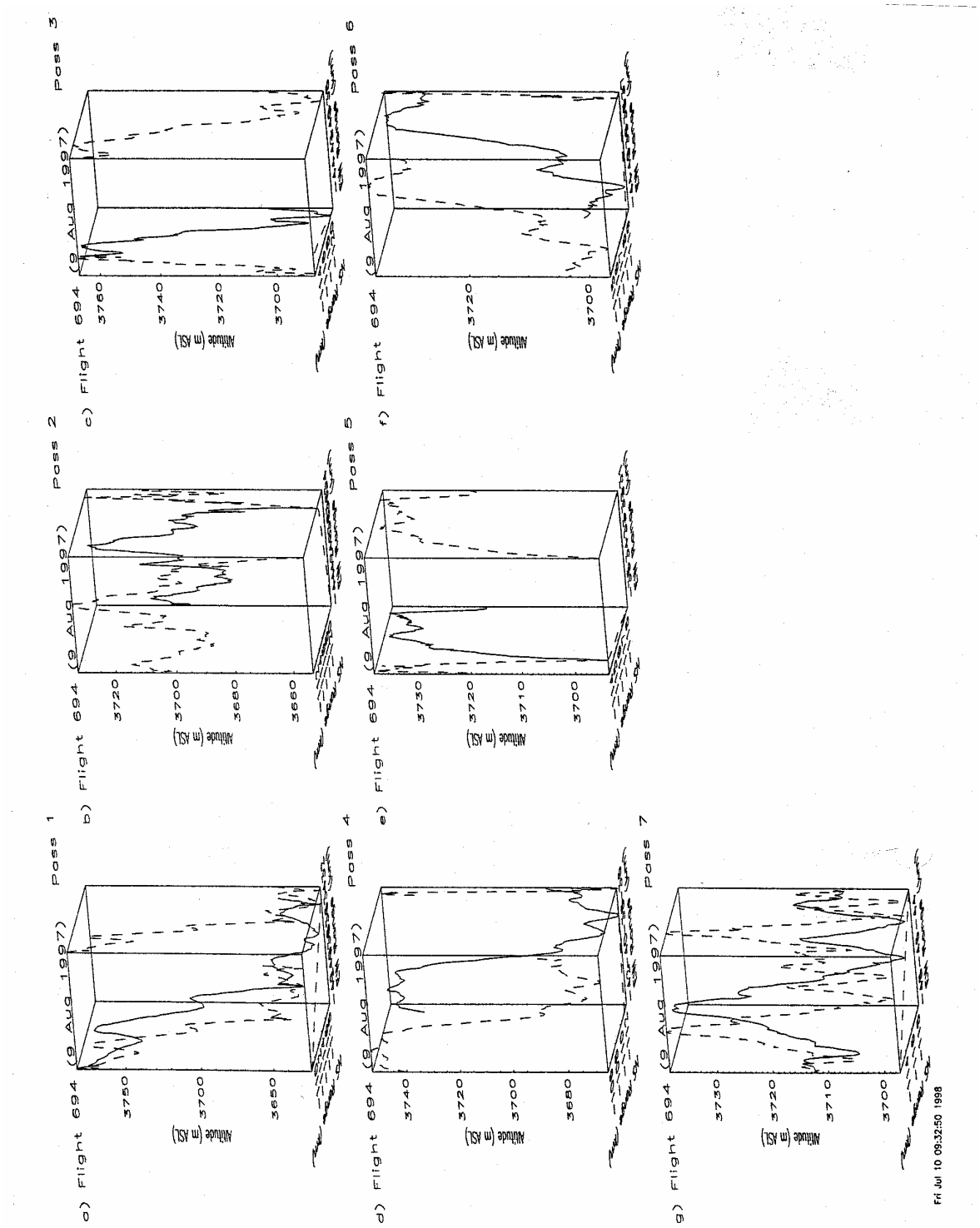

Fig. 6. Three-dimensional perspective of individual intercomparison legs on Flight 694, 9 August 1997.

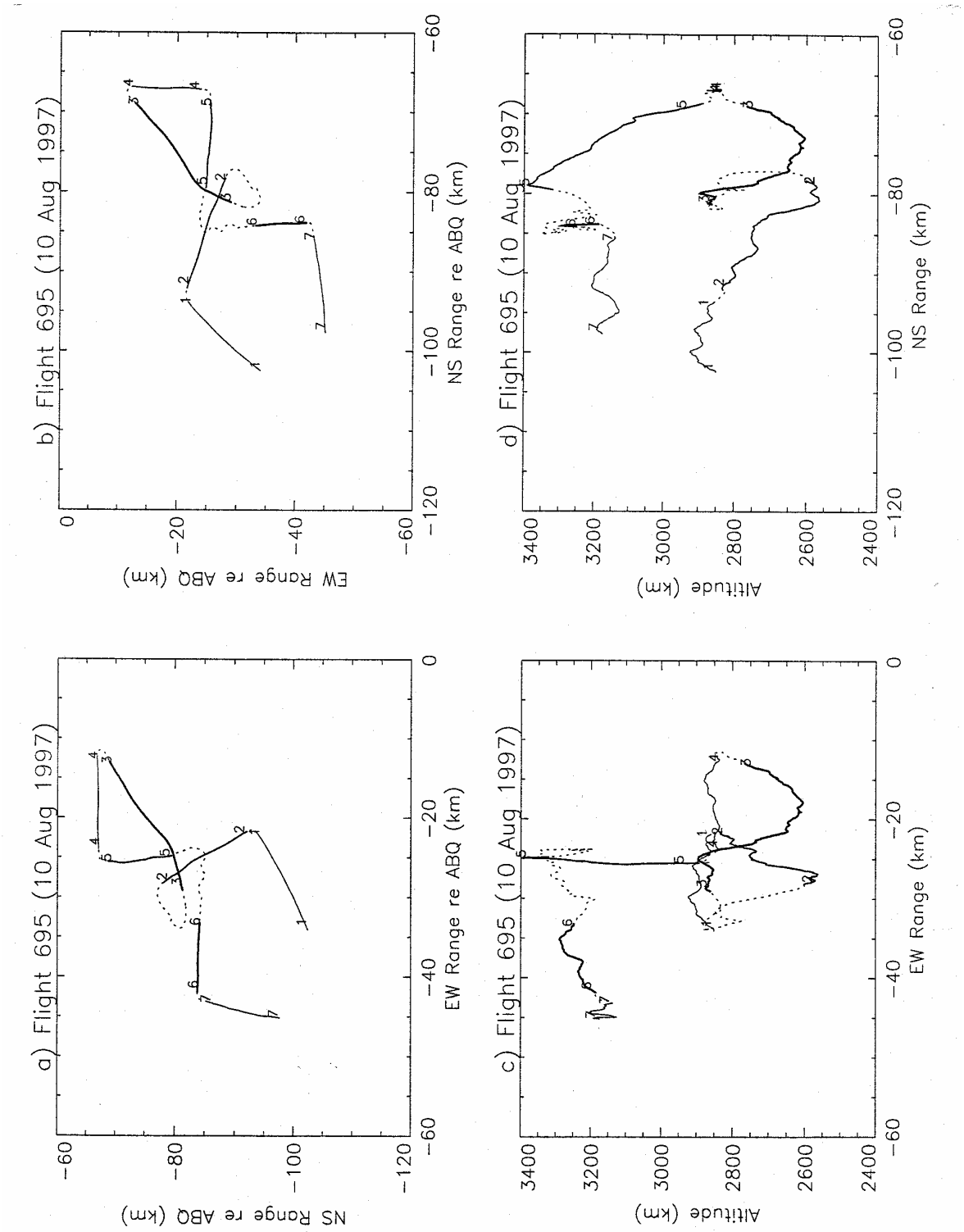

Fig. 7. T-28 flight tracks during Flight 695, 10 August 1997

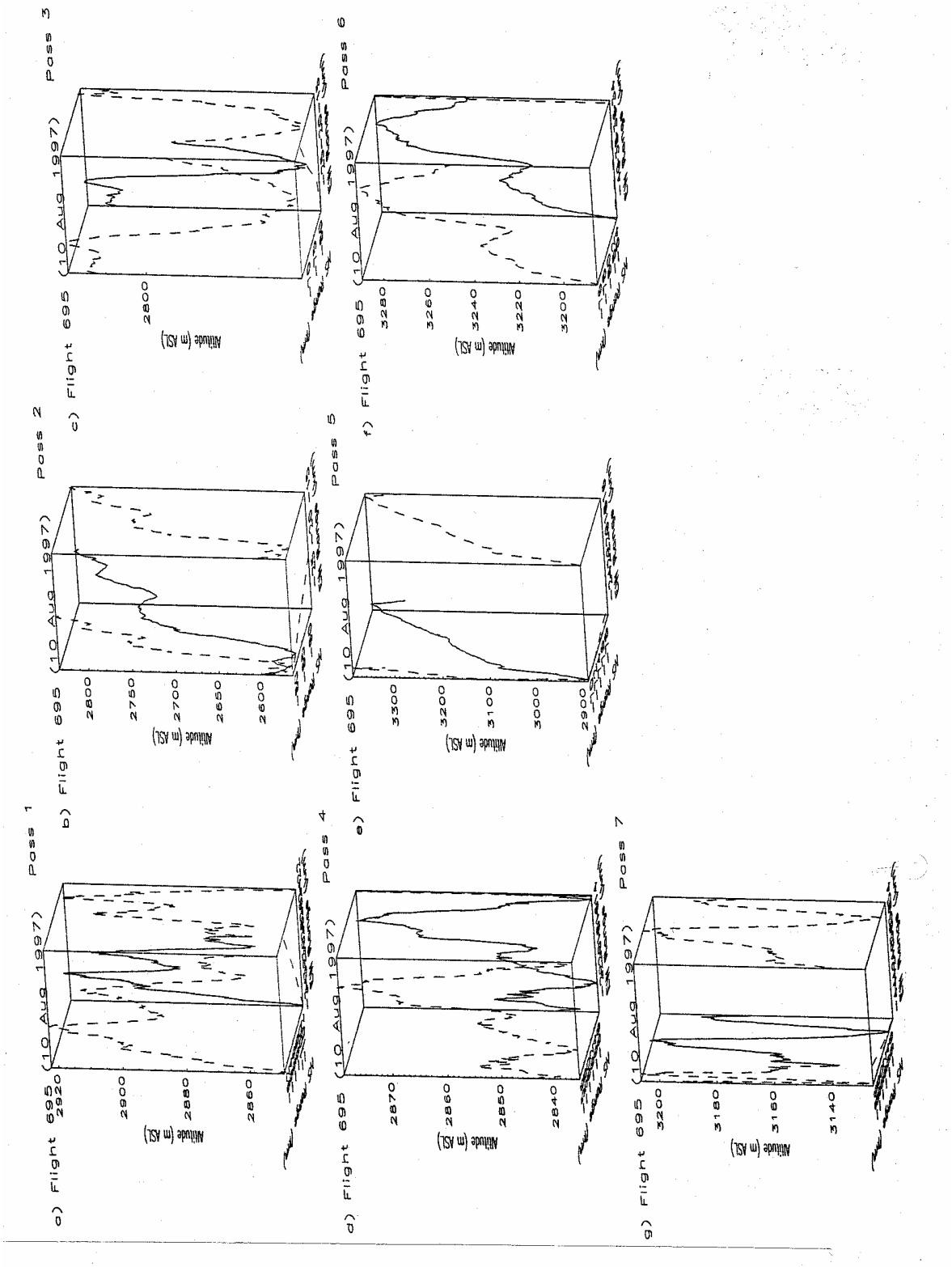

Fig. 8. Three-dimensional perspective of individual intercomparison segments on Flight 695, 10 August 1997.

For five passes (694-1, 5 and 695-2, 3, 6), the T-28 correlations with SPTVAR are fair to good and the E_x components are of significant magnitude. In these passes, the r^2 values are 0.80, 0.90, 0.95, 0.73, and 0.91. The corresponding slopes in the best linear fits are 0.64, 0.47, 0.64, 0.54, and 0.59. The mean value is 0.58 and standard deviation is 0.07. Slope values less than one indicate that E_{qy} from the T-28 is underestimating SPTVAR E_{xn}. These results indicate the T-28 E_{qy} enhancement factors should be decreased by approximately 70% in order to increase the T-28 E_{qy} so it represents the SPTVAR E_{xn}.

Y Component

In three of the fourteen passes (694-1, 4, 5), poor correlation is indicated between the T-28 and new SPTVAR systems. Also, there is poor agreement between the old and new SPTVAR systems. In one case (694-1), the T-28 and new SPTVAR measurements correlate well except for a large excursion in E_{yn} that is not reflected in either E_y or E_{yo}. In the other two cases (694-4, 5), there is little correlation among all three systems.

In the remaining eleven passes, the correlation between T-28 and the new SPTVAR system are fair to good with r^2 values ranging from 0.75 to 1.0. The slope ranged from 0.47 to 0.92. The mean slope is 0.7 with a standard deviation of 0.16. These results indicate the T-28 E_y is biased too low and the wingtip E_y enhancement factors should be decreased by approximately 40 percent to bring the T-28 E_y into agreement with the SPTVAR E_{yn}. For comparison, note that the slope of the relationship E_{yo}/E_{yn} averages 0.85.

Z Component

In six of the fourteen passes (694-2, 4, 5, 6 and 695-5, 7), poor correlation between T-28 and SPTVAR are obtained. In one of these passes (694-4), fields are strong yet there is little correlation among all three systems. In the following pass (694-5), the poor correlation among all three systems persists in the first half, but improves significantly over the last half. In another pass (694-6), the correlation between E_{zn} and E_z appears to be good except for a large transient in E_{zn}. In two of the remaining passes (694-2 and 695-5), poor correlation statistics are the result of small and noisy signals. In one case, (694-2), the poor correlation is due to radio transmission transients in the T-28 data. Finally, in the remaining pass (695-7), the T-28 data appear to lag the new SPTVAR data by a few seconds.

Table 11 Intercomparison Statistics – 1997

			Time		Duration	Regression Statistics r^2		Slope		Y-Inter		SD		
Flt	Pass	Ax	ST	ET	Sec	T-28	SPT	T-28	SPT	T-28	SPT	T-28	SPT	Comments
(1)			(2)	(3)		(4)	(5)	(6)	(7)	(8)	(9)	(10)	(11)	(12)
694	1	X	15.43	15.50	238	0.80	0.91	0.64	0.79	0.50	-0.30	1.81	1.35	G
694	2	X	15.50	15.56	218	0.00	0.86	-0.02	0.96	-0.06	0.01	0.26	0.22	P-small field values
694	3	X	15.57	15.61	148	0.67	0.99	0.37	1.07	0.20	-0.06	0.54	0.25	F-T-28 leads in time
694	4	X	15.62	15.65	118	0.05	0.11	0.19	0.28	-2.45	-1.10	4.89	4.62	P-T-28 leads in time
694	5	X	15.66	15.68	88	0.90	0.87	0.47	0.75	-0.53	0.69	0.32	0.59	F
694	6	X	15.69	15.72	88	0.07	0.55	-0.11	0.65	-0.11	0.36	0.15	0.22	P-small field values
694	7	X	15.72	15.77	158	0.00	0.24	-0.01	0.41	-0.14	0.14	0.06	0.18	P-small field values
694	1	Y	15.43	15.50	238	0.33	0.00	-0.25	-0.01	1.72	0.70	2.10	1.44	P-large E_{yn} transient
694	2	Y	15.50	15.56	218	0.99	0.97	0.86	0.94	-0.09	-0.49	0.10	0.16	VG
694	3	Y	15.57	15.61	148	1.00	0.99	0.90	0.94	-0.25	-0.54	0.11	0.18	VG
694	4	Y	15.62	15.65	118	0.01	0.06	-0.02	-0.07	3.13	4.08	2.22	2.20	P-none compare well
694	5	Y	15.66	15.68	88	0.38	0.36	0.35	0.13	-1.60	-0.89	0.66	0.26	P-none compare well
694	6	Y	15.69	15.72	88	0.98	0.96	0.92	1.04	-0.39	-0.68	0.09	0.16	VG
694	7	Y	15.72	15.77	158	0.87	0.85	0.58	0.87	-0.14	-0.61	0.10	0.16	G
694	1	Z	15.43	15.50	238	0.84	0.98	0.70	0.84	0.59	0.47	2.65	1.04	F
694	2	Z	15.50	15.56	218	0.11	0.76	0.66	0.72	0.06	0.33	0.67	0.15	P-radio interference, small fields
694	3	Z	15.57	15.61	148	0.91	0.97	0.74	0.98	0.16	0.46	0.28	0.19	G
694	4	Z	15.62	15.65	118	0.30	0.07	-0.28	0.11	-8.08	-4.26	4.38	4.19	P-none compare well
694	5	Z	15.66	15.68	88	0.36	0.58	-0.43	0.52	-7.00	-1.77	2.37	1.90	P
694	6	Z	15.69	15.72	88	0.07	0.06	0.07	0.09	-0.95	-0.94	0.20	0.27	P-good exc for E_{zn} transients
694	7	Z	15.72	15.77	158	0.94	0.92	0.89	0.95	0.18	0.29	0.11	0.13	G

Table 11 Intercomparison Statistics – 1997 continued

						Regression Statistics								
			Time		Duration	r^2		Slope		Y-Inter		SD		
Flt	Pass	Ax	ST	ET	Sec	T-28	SPT	T-28	SPT	T-28	SPT	T-28	SPT	Comments
(1)			(2)	(3)		(4)	(5)	(6)	(7)	(8)	(9)	(10)	(11)	(12)
695	1	X	14.77	14.83	238	0.64	0.54	0.42	0.47	1.99	0.54	2.05	2.78	F-E_{xn} transients
695	2	X	14.84	14.92	268	0.95	0.68	0.64	0.43	1.26	-0.06	1.38	2.70	G
695	3	X	14.98	15.08	357	0.73	0.77	0.54	0.73	1.37	0.60	1.79	2.17	G
695	4	X	15.10	15.16	207	0.22	0.28	0.17	0.23	0.38	-1.76	2.46	2.90	F-E_{xn} transients
695	5	X	15.17	15.23	217	0.01	0.35	-0.03	0.44	-0.08	-0.15	0.07	0.15	P-small values
695	6	X	15.30	15.35	167	0.91	0.96	0.59	0.70	0.54	0.23	0.96	0.76	G
695	7	X	15.36	15.42	228	0.13	0.24	0.12	0.15	0.12	0.60	4.53	3.92	F-E_{xn} transients
695	1	Y	14.77	14.83	238	0.87	0.97	0.61	0.75	0.18	-0.75	1.02	0.60	F
695	2	Y	14.84	14.92	268	0.92	0.96	0.71	0.74	0.78	-0.07	2.29	1.54	F
695	3	Y	14.98	15.08	357	0.91	0.99	0.82	0.78	1.35	-0.51	1.80	0.62	G
695	4	Y	15.10	15.16	207	0.87	0.85	0.57	0.83	1.14	-0.22	1.00	1.61	G
695	5	Y	15.17	15.23	217	0.94	0.90	0.77	0.96	0.02	-0.44	0.07	0.11	G
695	6	Y	15.30	15.35	167	0.75	0.98	0.52	0.79	0.81	-0.33	0.94	0.34	F
695	7	Y	15.36	15.42	228	0.84	0.94	0.47	0.71	-0.40	-1.37	1.32	1.18	F
695	1	Z	14.77	14.83	238	0.90	0.92	0.91	1.02	0.54	0.22	2.14	2.13	VG
695	2	Z	14.84	14.92	268	0.96	0.97	0.86	0.95	0.00	0.37	2.22	1.91	G
695	3	Z	14.98	15.08	357	0.97	0.87	0.95	1.06	-0.31	-0.43	1.43	3.21	VG
695	4	Z	15.10	15.16	207	0.93	0.94	0.91	1.01	0.57	1.01	1.82	1.78	G
695	5	Z	15.17	15.23	217	0.49	0.76	1.03	0.81	0.14	0.28	0.25	0.11	F-small field values, noisy
695	6	Z	15.30	15.35	167	0.97	0.99	0.89	0.93	0.03	-0.02	0.75	0.49	G
695	7	Z	15.36	15.42	228	0.44	0.60	0.42	0.58	1.44	1.53	3.65	3.64	P - T-28 lags

(1) = 694 9 Aug 1998
= 695 10 Aug 1998
(2) = Start time of pass in hr min sec
(3) = End time of pass in hr min sec
(4), (6), (8), (10) = new SPTVAR vs. T-28
(5), (7), (9), (11) = new SPTVAR vs. old SPTVAR
(12) VG-very good, G-good, F-fair, P-poor

In the remaining eight passes (694-1, 3, 7 and 695-1, 2, 3, 4, 6), the correlation between the T-28 and new SPTVAR systems is fair to good with r^2 values ranging from 0.84 to 0.97. The slope values range from 0.70 to 0.86 with a mean value of 0.86 and standard deviation of 0.09. These results indicate that the T-28 E_z is biased low compared to E_{zn} estimated from the new SPTVAR system. It is interesting to note that SPTVAR E_{zo} is biased only slightly low relative to SPTVAR E_{zn}, with a mean ratio for these same passes of 0.97. A decrease in the fuselage meter E_z enhancement factors by 16% would give good agreement between the two systems.

In Section 4.4 the best portions of these 1997 intercomparisons will be used to derive a response matrix for the T-28 meter system involving all 5 meters. A link between poor agreement between T-28 and SPTVAR along some flight segments will be shown to be ions released by corona from the propeller and released during combustion that influence the readings of the T-28 fuselage meters.

4.3 Self Calibration of the T-28 Field Mills – Dogleg Maneuvers

One of the 5 flights conducted in New Mexico, during August, 1997, (Flight 696 - 11 Aug 97), was flown specifically to obtain data from the T-28 field mills while the plane was conducting significant roll (dogleg) maneuvers in the presence of electric fields. The dogleg maneuver is executed by rolling the aircraft to a large angle (>20 degrees) in one direction (e.g., right wing up and left wing down), followed immediately by a roll to a large angle in the other direction (e.g., right wing down and left wing up). The whole maneuver should be completed in a relatively short period of time (<20 seconds). During the sequence of roll maneuvers the aircraft experiences large changes in roll, heading and pitch (See Figure 9). In this way the aircraft coordinate system is rotated through significant angles along all three axes and the field meters are exposed to (hopefully) the same electric field from a variety of orientations. Other flights include periods in which the plane conducted similar maneuvers; however, this flight by far had more dogleg maneuvers than any other flight.

The results from two analyses based on observations obtained on this flight are described here.

4.3.1 Method 1 – Regression of Roll vs. Arctan(z,y)

While the aircraft is rolling back and forth, if the electric field vector is nearly constant and the heading does not change significantly, the angle formed by the vertical and horizontal components of the ambient electric field, as measured by the T-28 system, should vary directly with the roll angle of the aircraft. An example is shown in Figure 10 for one 50-point data segment in which the T-28 is performing a roll maneuver. As a test of this, a regression analysis is applied to the 20 Hz electric field data set for Flight 696. A sliding window, 50 points wide (2.5 seconds duration), is applied to the data over the entire flight. The arctan(E_z, E_y) is regressed against the aircraft roll angle for each 50 point time window

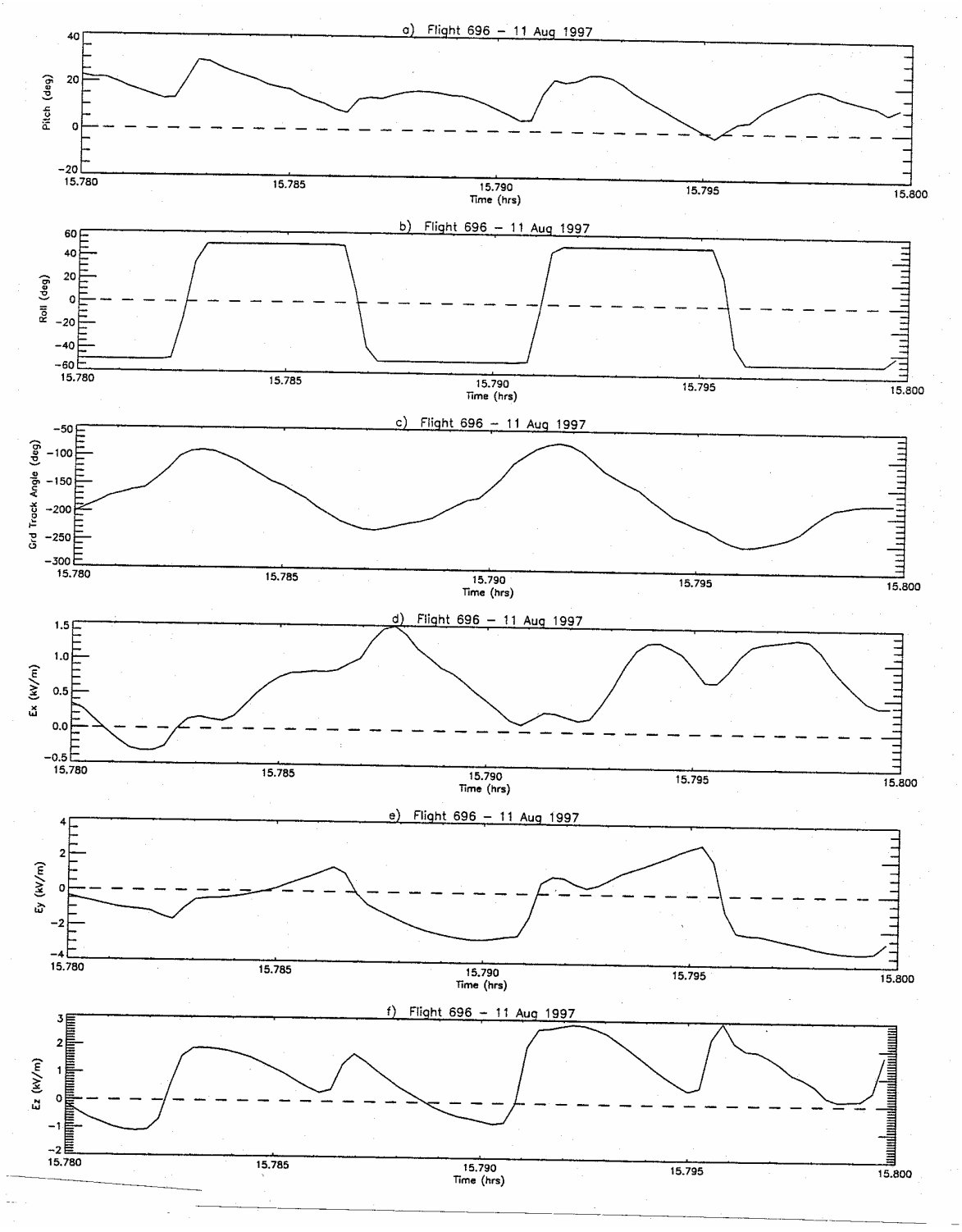

Fig. 9. (a) Pitch, (b) roll, (c) ground track angle, (d) T-28 E_x, (e) T-28 E_y, and (f) T-28 E_z during dog-leg maneuvers on Flight 696, 11 August 1997, during time period 1578 to 1580 hrs MDT. The roll signal saturates at 50°.

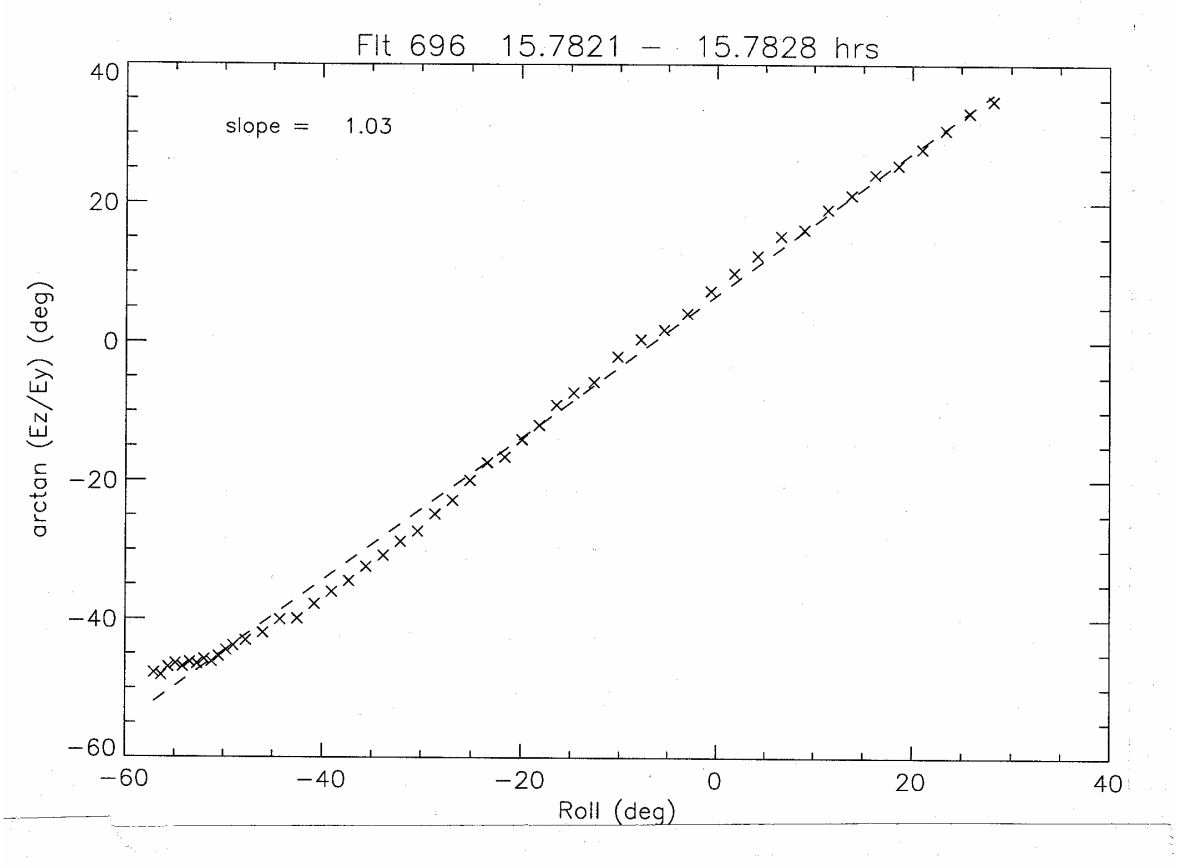

Fig. 10. Example showing a linear relationship between arctan(E_z/E_y) and aircraft roll angle during a rapid roll maneuver.

and the slope, standard deviation of the error about the regression, and the square of the correlation coefficient is calculated.

A sequence of three criteria is tested to determine time points/intervals in which the data indicate the relative calibration between the vertical and horizontal components is good. The three criteria are as follows:

1) The absolute value of the slope is between 0.8 and 1.2.
2) The standard deviation of the error about the regression is less than 10 kV/m.
3) The square of the correlation coefficient is greater than 0.8

Time points/intervals that pass these three criteria indicate that:

1) For one degree of aircraft roll, the angle between the electric field vector and aircraft-relative vertical changes by one degree.
2) The dispersion of the points about the regression line is low.
3) Most of the variation in arctan(E_z,E_y) can be explained or predicted by the aircraft roll angle.

The results from this analysis are shown in Figure 11 in which time vs. roll angle is plotted. Those points, corresponding to the beginning of the 50-point interval of the

sliding window, that met the aforementioned criteria, are plotted with bold lines. In general, the criterion is only met when the rate of roll is high. The numerous time intervals over which the criterion is met indicate that the relative calibration between the computed vertical and horizontal components of the electric field is 1:1. In Figure 12, a histogram of the roll rate only for those points that met the three criterion, is superimposed over the histogram of the roll rate for the entire flight. As expected, the highest frequency of occurrence of roll rate over the entire flight is over the lower values; however, the frequency of occurrence of roll rates for points that met the three criterion, expressed as a fraction of the total number of roll rate values over the entire flight in that histogram interval, is distributed toward the higher roll rate values.

4.3.2 Method 2 – The Winn Method (Winn, 1993)

This method is more rigorous than the above technique in that a complete enhancement matrix is derived which, when applied to the field mill measurements, provides all three components of the ambient electric field in a relative sense. Absolute calibration must be accomplished through comparison with an externally calibrated source; however, the relative enhancement matrix provides estimates of the electric field components that give the correct direction of the electric field vector. In contrast to the roll analysis, which verifies the relative response of the meters only to the measured *y* and z components, the Winn method compares the relative response of the different meters to all 3 components. The problem with the Winn method is in finding data sequences, from dogleg maneuvers, when the ambient electric field is sufficiently constant for the technique to work.

In the Winn method (Winn 1993), combinations of meter readings which are independent of charge are formed, based on high voltage, self-charging tests performed, in flight, when no ambient electric field is present (see section on self-charging tests). Preferably, each charge-independent quantity corresponds nearly uniquely to one of the components of the electric field as defined in the aircraft-relative Cartesian coordinate system (*X, Y,* or *Z*). When the aircraft performs a dog-leg maneuver, while in a constant electric field, the ambient electric field vector transitions through each of the measured, charge-independent quantities as the aircraft is exercised through all three degrees of rotational freedom.

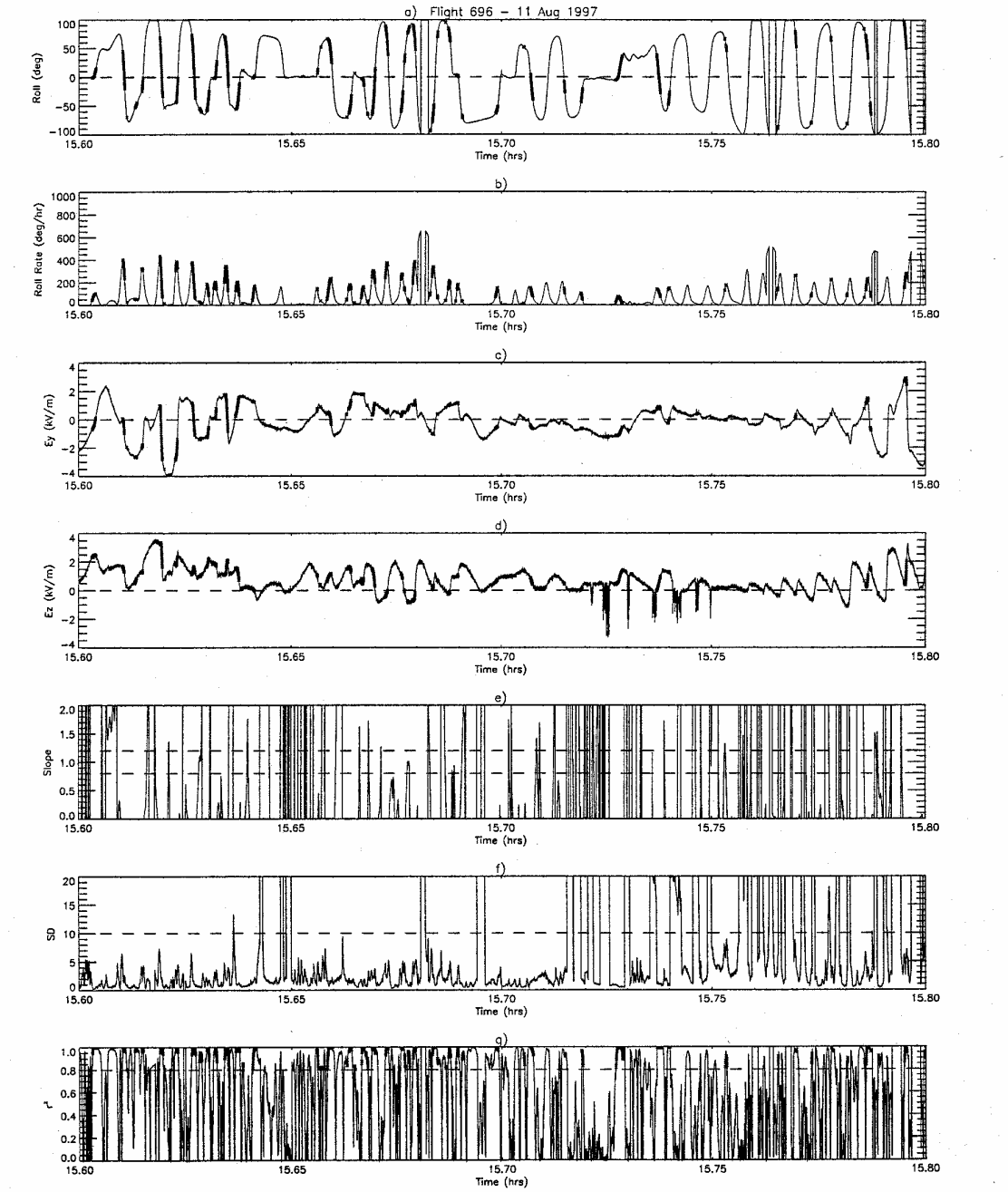

Fig. 11. (a) Roll angle, (b) roll rate, (c) E_y, (d) E_z, (e) slope of regression line, (f) standard deviation of regression, and (g) r^2 vs. time during Flight 696, 11 August 1997. Bold lines indicate flight segments where ambient electric field was relatively constant and variation in E_z and E_y was caused mostly by changing of aircraft orientation. In (a) roll has been extrapolated outside the range of recorded data when the recorded signal is saturated (at +/- 50 degrees). The dashed lines in (e) indicate the range of slope values valid for the test. The dashed line in (f) indicates the maximum acceptable value of standard deviation for the test. The dashed line in (g) indicates the minimum acceptable value of r^2 for the test.

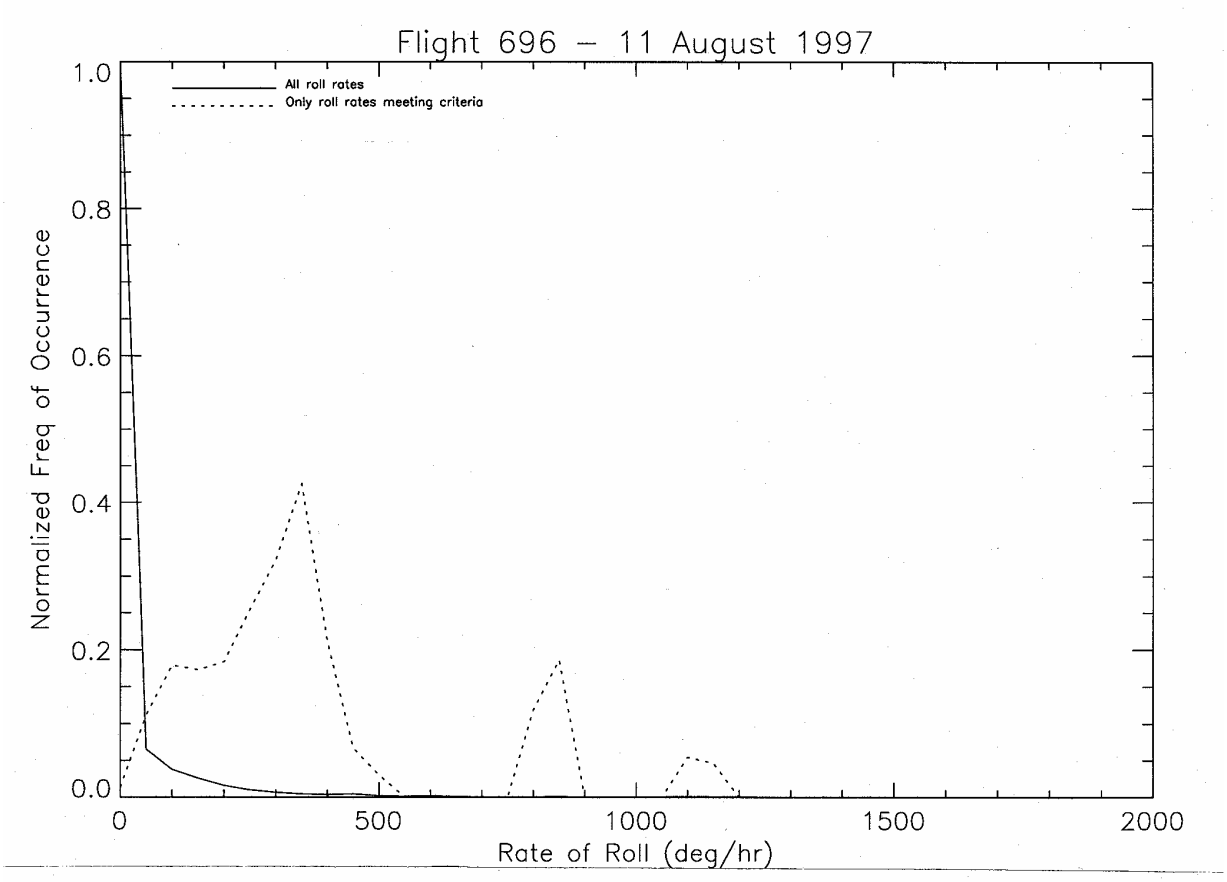

Fig. 12. Frequency of occurrence of roll rate during which the ambient electric field was relatively constant (dotted line). The solid line indicates the frequency of occurrence of roll rate for all times in Flight 696.

The goal of the method is to determine a set of coefficients (enhancement matrix) that describes the contribution of each component of the ambient electric field (in the aircraft coordinate system) to the charge-independent quantities. For example, if f_x is a charge-independent quantity (derived from a linear combination of field mill measurements) at a given time point, the following relationship can be constructed:

$f_x = B_0 \bullet E_x + B_1 \bullet E_y + B_2 \bullet E_z$

where

E_x, E_y, and E_z are the components of the ambient electric field in the aircraft coordinate system, for a given time point

B_0, B_1, and B_2 are the coefficients (enhancement matrix/vector) that describe the contribution, for any time point, of each component of the electric field to f_x.

Any number of these relationships for charge-independent quantities can be constructed. Experience indicates that 1-4 equations, or sets of *B* values, provide the best results. Once this enhancement matrix is known, it is then inverted and applied to the measured charge-independent quantities (*f* values) to derive the three components of the electric field (E_x, E_y, and E_z).

The *B* values for each relationship are determined from the measured time sequence of the charge-independent quantity, obtained during the dog-leg maneuver, by forming a set of over-determined linear equations. For example,

$$f_x(t) = B_0 \bullet E_x(t) + B_1 \bullet E_y(t) + B_2 \bullet E_z(t) \quad (3)$$
for $t = 1,2, \ldots ,n$

In an electric field constant relative to the earth, the variation in E_x, E_y, and E_z, as a function of time, is caused only by the rotation of the aircraft about its three axes. The change in the charge-independent quantity is caused by the aircraft rotation as each field mill is exposed to the same ambient electric field from a variety of orientations. The *B* coefficients cannot be determined without knowing E_x, E_y, and E_z; however, since the goal is to obtain a relative calibration (as opposed to an absolute one), the magnitude of the electric field can be assumed to be one. Then only the direction of the field is unknown. By defining the direction of the constant ambient electric field in two angles relative to the aircraft, a set of *B* values can be determined for each combination of the two angles over a regularly-spaced grid. The first angle (θ) is defined as the angular distance between vertical (with up being positive) and the electric field vector, in the plane defined by the vertical and electric field vectors. The second angle (ϕ) is defined as angular distance between grid north (the reference for aircraft heading) and the projection of the electric field vector on the horizontal (x-y) plane. Each set of *B* values (corresponding to each grid point in the 2-D θ - ϕ space of possible electric field vector orientations) is used to compute a residual by summing, over the time interval of the dog leg, the differences between the charge-independent quantity ($f_x(t)$) and the products of the *B* values and the assumed E_x, E_y, and E_z. (Note: E_x, E_y, and E_z are computed from the assumed values of θ and ϕ at each grid point and the assumption of magnitude one. The E_x, E_y, and E_z values are defined in an aircraft coordinate system. Measurements of pitch, roll, and heading are used to transform the electric field vector, which is defined in an Earth-based system, to an aircraft-based coordinate system. For example,

$$R = \sum_{t=1}^{n} \left\{ f_x(t) - \left[B_o(\theta,\phi).\, E_x(t,\theta,\phi) + B_1(\theta,\phi).\, E_y(t,\theta,\phi) + B_2(\theta,\phi).\, E_z(t,\theta,\phi) \right] \right\} \quad (4)$$

A surface of residuals, over the θ - ϕ space, then is constructed and the minimum in that surface indicates the correct direction of the constant electric field vector. The set of *B* values corresponding to the pair of angles at the surface minimum is the desired enhancement matrix for the charge-independent quantity.

Unfortunately, examination of the vector sum of the three measured components determined using (1), during dogleg maneuvers, from the T-28, suggests that the electric

field was not sufficiently constant for the technique to work. The Winn technique has been applied to several of the most promising maneuver periods but a solution converging to a plausible B-matrix was not found. However, future flights will be conducted with dogleg maneuvers as we continue to look for an appropriate data sequence.

4.4 Revised Estimate of the T-28 Field Meter System Response Matrix Using Data From 1997 T-28-SPTVAR Formation Flights

Although the T-28's 1997 dogleg maneuvers were not suitable for self-calibration, we can use data from its 1997 formation flights with SPTVAR to make an improved estimate of the T-28's response matrix:

$$\begin{bmatrix} E_t \\ E_b \\ E_l \\ E_r \\ E_f \end{bmatrix} = \begin{pmatrix} A_{tx} A_{ty} A_{tz} A_{tq} \\ A_{bx} A_{by} A_{bz} A_{bq} \\ A_{lx} A_{ly} A_{lz} A_{lq} \\ A_{rx} A_{ry} A_{rz} A_{rq} \\ A_{fx} A_{fy} A_{fz} A_{fq} \end{pmatrix} * \begin{pmatrix} E_x \\ E_y \\ E_z \\ Q \end{pmatrix} .... \qquad (5)$$

where E_i ($i = t, b, l, r, f$) are the local electric field at the position of the i^{th} field meter, and t represents the top, b the bottom, l the left, r the right, and f the hail spectrometer pod, or fifth, field meter. E_x, E_y and E_z are the ambient electric field components in the airplane coordinate system. Q is the net charge carried by the airplane. The coefficients A_{ix}, A_{iy} , A_{iz} and A_{iq} represent the individual meter E_i responses to the x, y, z ambient electric field components and airplane charge. This represents an improvement over (1) in the sense that it includes all 5 meters and is based on SPTVAR measurements from an improved system of meters.

The E_i are obtained from the output voltages of the field meters through a bench calibration. A_{ix}, A_{iy} and A_{iz} are dimensionless. A_{iq} can have a dimension of kV/(m coulomb); however, in equation (5), multiplying all the A_{iq} by a constant and then inverting the A matrix has no effect on the derived E_x, E_y, and E_z. Thus, at present, we will assume A_{bq} =1 kV/(m μC) and use ratios of A_{iq}/A_{bq} as the A_{iq} in equation (5). The ratios are known from past artificial charging tests of the airplane. See Table 9 in Section 4.1. They are A_{tq} = 2.1, A_{bq} = 1, A_{lq} = 5.7, A_{rq} = 5.7, A_{fq} = 3.1. With the assumption for A_{bq}, and based on typically observed field meter readings, Q is in the range of about 1 to 10 μC. An exact calibration of Q can be done later using Jones' method (Jones, 1990) when appropriate data are available.

Our current task is to find the other A_{ij} ($j = x, y, z$) coefficients. They can be found using data from the T-28-SPTVAR formation flights in 1997. That is possible as, during the formation flights, the T-28 was mostly flying in clear air near the base of some strongly-electrified thunderclouds. When the T-28 is flying in clear air near electrified storms, we can assume that the effect of airplane charge on the field meter is small compared to the large signal produced from the ambient field. This assumption is based on

the following facts and reasoning. In artificial charging tests of the T-28, when the high voltage (HV) power supply's charging current is in equilibrium with the discharging current through engine exhaust and corona emission (if there are any) from the sharp points of the airplane, the T-28 acquires a maximum charge. This charge produces some equilibrium "measurable" signals on the five electric field meters. In clear sky, if the aircraft is emitting corona ions from points on some parts of the airplane because of the strong polarization of the airframe by the ambient electric field, the airplane cannot be charged without limit because the airplane also is emitting corona ions of an opposite sign from other points, after a maximum charge (equilibrium charge) is reached. That maximum charge should be comparable to the maximum value during an artificial charging test. Jones (1990) found that discharge through engine exhaust and corona emission can eliminate the airplane charge for periods of seconds to tens of seconds. This is also confirmed in the case of the T-28 by artificial charging tests. In Appendix E is an example of a flight segment during which the airplane charge remains almost negligible during the entire time interval when the airplane was penetrating a thunderstorm and the significant ambient field caused strong corona emission from the T-28.

If one neglects effects of Q, equation (5) becomes:

$$\begin{bmatrix} E_t \\ E_b \\ E_l \\ E_r \\ E_f \end{bmatrix} = \begin{pmatrix} A_{tx} A_{ty} A_{tz} \\ A_{bx} A_{by} A_{bz} \\ A_{lx} A_{ly} A_{lz} \\ A_{rx} A_{ry} A_{rz} \\ A_{fx} A_{fy} A_{fz} \end{pmatrix} * \begin{pmatrix} E_x \\ E_y \\ E_z \end{pmatrix} \tag{6}$$

Quantities E_i ($i = t, b, l, r, f$) are known from the T-28's measurements and (E_x E_y E_z) are the ambient electric field components in the airplane coordinate system. Using the SPTVAR (E_x E_y E_z) as the T-28 (E_x E_y E_z) during formation flying, all coefficients A_{ij} in equation (6) can be found by a least-squares fit.

4.4.1 Data Used

When using one airplane's measurements to calibrate the other airplane, the two airplanes should be close to the same position at the same time. Small shifts were made in the timing of the T-28 data relative to the SPTVAR data in order to line up the larger peaks. Also, it is necessary to ensure the coordinate systems of the two airplanes are in the same orientation. Figures 13a through 13e show heading, roll and pitch angles of the two airplanes, and the ambient E-field components measured by each airplane during five different formation flight segments (other data during these time intervals are shown in Appendix D). Quantity $E_{qy} = 0.031(E_l+E_r)$, from the T-28, is a rough approximation of E_x field component. E_y and E_z from the T-28 are calculated as $0.0223\ (E_l-E_r)$ and $0.0893(E_t-2E_b)$, respectively. These relationships follow from (2), except for the relationship for E_{qy}, which was modified according to the results presented in Section 4.2.2 to better represent

E_x. Electric field components (E_x E_y E_z) from the SPTVAR are calculated based on the pod meters in the SPTVAR's coordinate system with E_y in the direction along the pod-to-pod (or wing-tip-to-wing-tip) line [using equation (21), page 54, Mo, 1997].

By examining the heading, roll, and pitch in Figures 13a-e, it can be seen that, during these formation flight comparison legs, the orientation of each plane is approximately the same at the same time. The T-28 pitch is a few degrees larger because it has to fly close to a stall configuration to be slow enough to stay in formation with the SPTVAR. The differences in the attitude angles are sufficiently small to perform the calibration procedure. Also note that the local minima and maxima in the *E*-field components are coincident. The minor discrepancies in timing discussed in Section 4.2.2 are relatively insignificant. This justifies the use of (E_x E_y E_z) measured by SPTVAR to calibrate the T-28 field meter system.

It also can be seen that the electric field measured by both airplanes agrees fairly well with the exception that sometimes E_z from the T-28 is smaller than E_z from the SPTVAR. Additional details are given in Appendix D. The discrepancies appear to be due to corona ions affecting the T-28's fuselage meters. For example, Mo *et al.* (1998) demonstrate that E_z calculated using the fuselage meters on SPTVAR is often smaller than the correct E_z because the fuselage meters are often affected by the corona ions. Like the SPTVAR, the T-28 also is driven by a single propeller, and probably emits charge from locations analogous to those emitted on the SPTVAR. Therefore, it is reasonable to suspect that the T-28 fuselage field meters may experience the effects of charge in the same way that the SPTVAR does.

To find the coefficients of equation (6), we will not use those intervals of the data when corona ions are suspected of affecting the T-28's fuselage meters. It will be demonstrated below how the coefficients are determined.

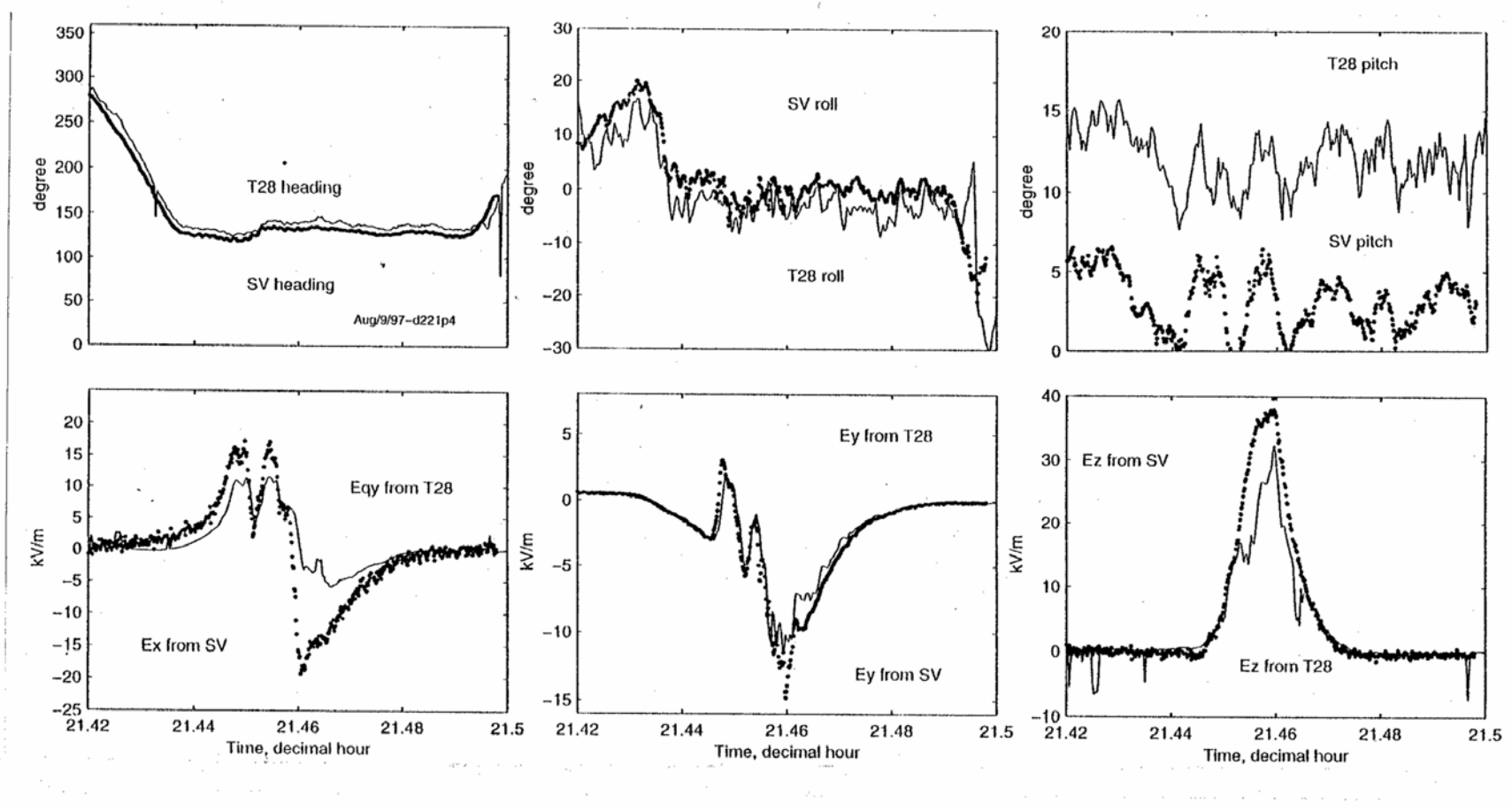

Fig.13a. Inter-comparison data of T-28 (solid) and SPTVAR (dotted) from 21:25:12 to 21:30 UTC (15:25:12 to 15:30 MDT) on Aug. 9, 1997. Top row shows the heading, roll and pitch of the two airplanes. Bottom row shows the E-field components. (E_x E_y E_z) from SPTVAR are calculated from the pod meters in a coordinate system with E_y along the line linking the two pods. E_{qy} from the T-28 is an approximation of E_x component with $E_{qy}=0.0310\ (E_l+E_r)$; E_y from T-28 is $0.02230\ (E_l-E_r)$, and E_z from the T-28 is $0.0893\ (E_t-2E_b)$. The T-28 has a larger pitch angle because it has to fly slower than normal to keep pace with the SPTVAR.

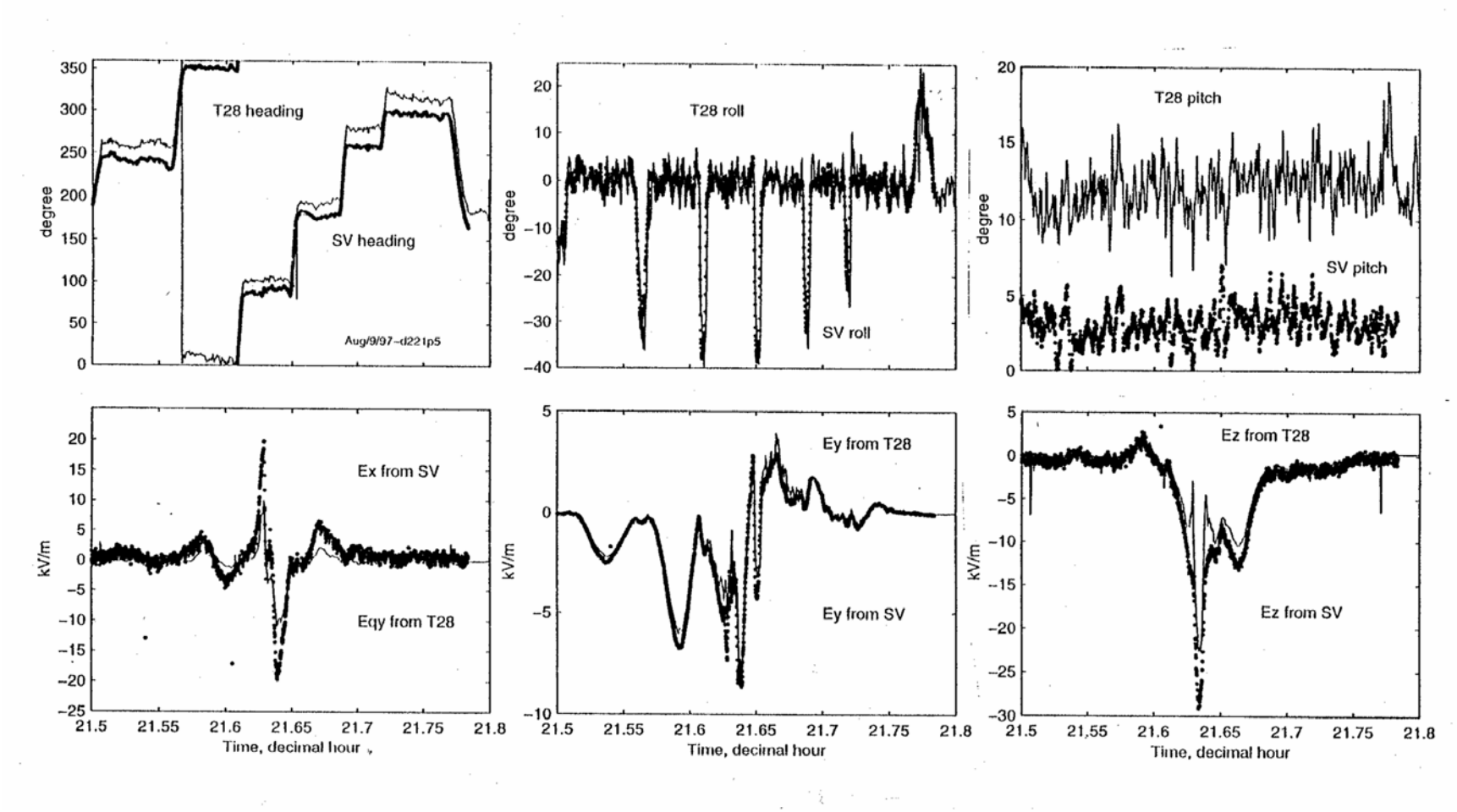

Fig.13b. Same as in Fig.13a, but time is from 21:30 to 21:48 UTC (15:30 to 15:48 MDT) on Aug.9, 1997, immediately following the time interval of Fig.13a.

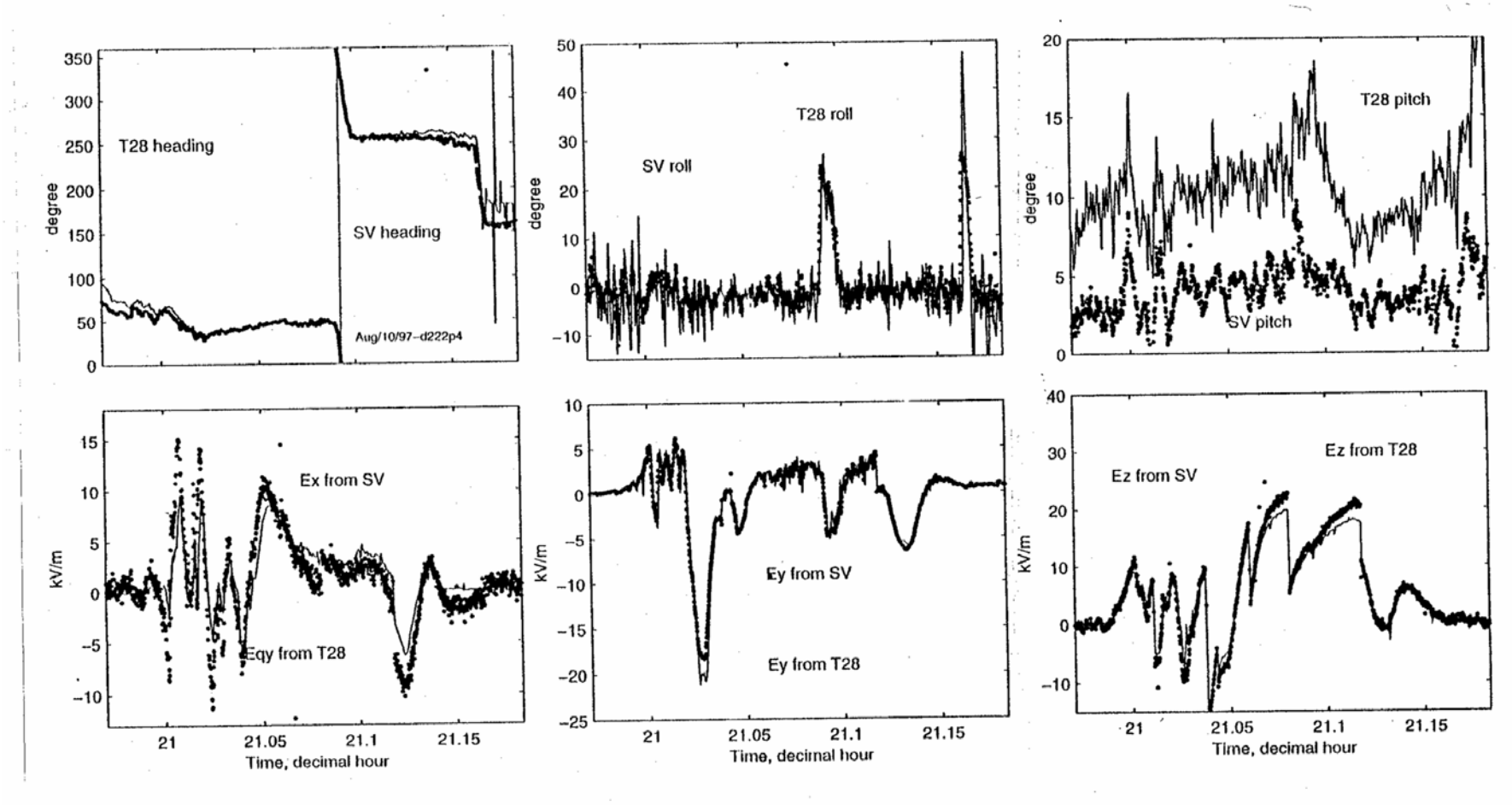

Fig.13c. Same as in Fig.13a, but time is from 20:57 to 21:11 UTC (14:57 to 15:11 MDT) on Aug.10, 1997.

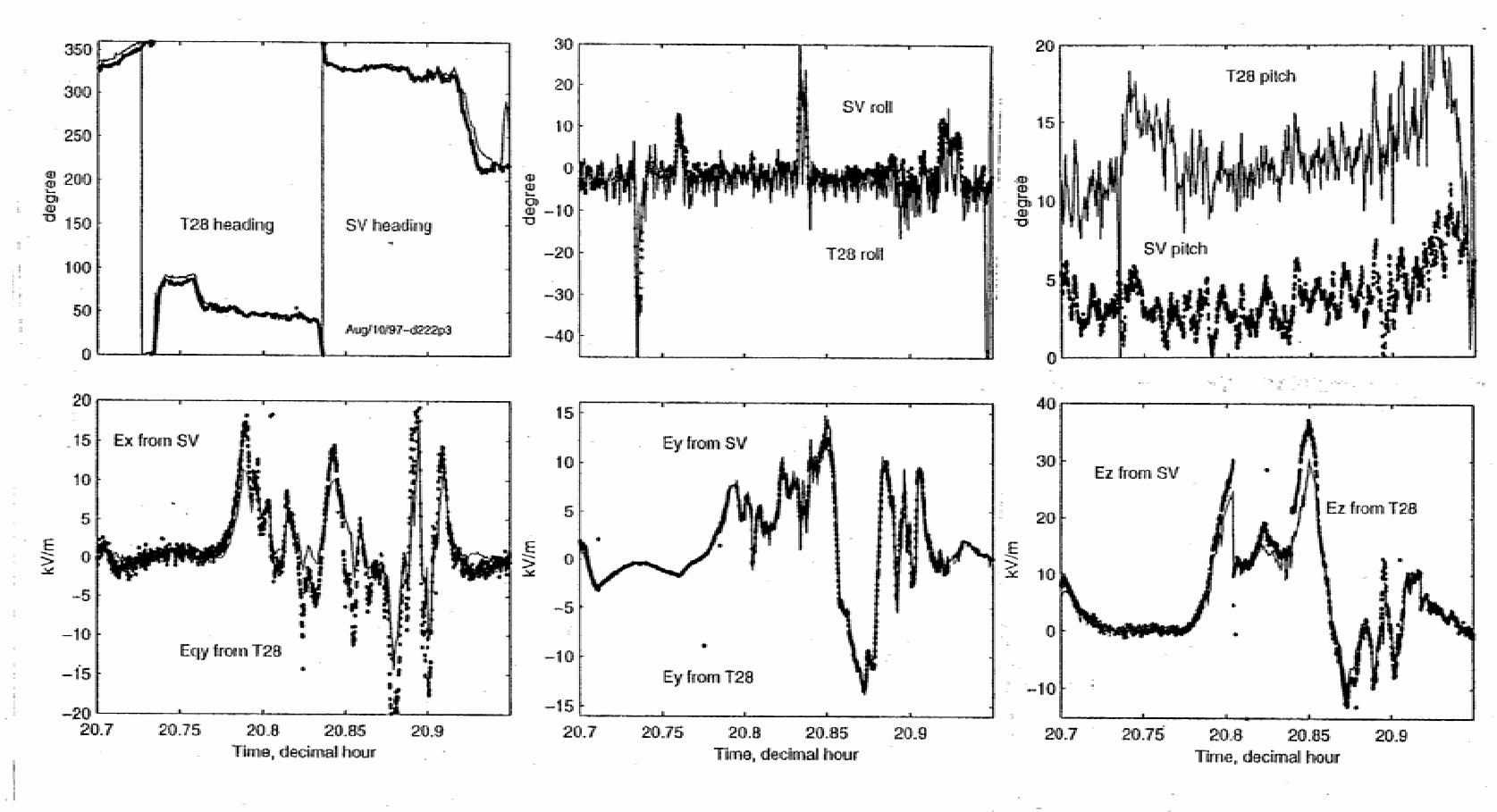

Fig.13d. Same as in Fig.13a, but time is from 20:42 to 20:57 UTC (14:42 to 14:57 MDT) on Aug. 10, 1997, continuation of Fig.13c.

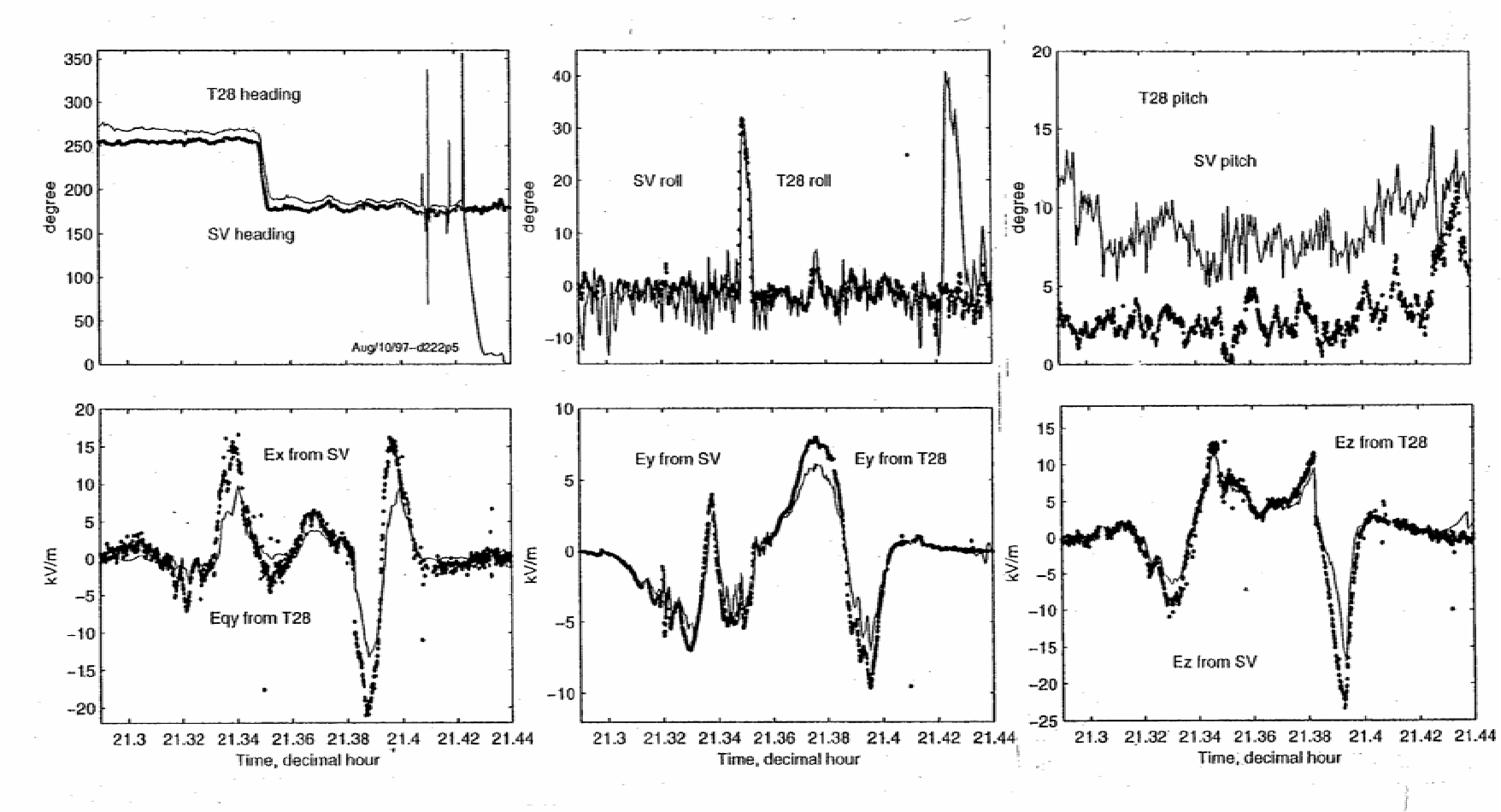

Fig.13e. Same as in Fig.13a, but time is from 21:17 to 21:26 UTC (15:17 to 15:26 MDT) on Aug.10, 1997, continuation of Fig.13d.

4.4.2 T-28's response A matrix.

Figure 14a shows the least squares fit result of the T-28 E_t to the ambient electric field (E_x E_y E_z) calculated from the SPTVAR pod meters in the airplane's coordinate system. Data are concatenated from most parts of the formation flight segments shown in Figures 13a through 13e, excluding parts when E_t is suspected of being affected by corona ions. (See 4.4.3.) E_t is a unique function of the ambient field (E_x E_y E_z) and airplane charge Q [Winn, 1993]. That is, $E_t = A_{tx}E_x + A_{ty}E_y + A_{tz}E_z + A_{tq}\,Q$. Because ($E_x$ E_y E_z Q) are independent of each other, for a large ensemble of data, if a linear function ($aE_x + bE_y + cE_z$) fits E_t in the least squares sense when Q is zero or negligible, we have $A_{tx} = \sim a$, $A_{ty} = \sim b$, $A_{tz} = \sim c$. Thus, for E_t from Figure 14a, we have $A_{tx} = 1.025$, $A_{ty} = -0.796$, $A_{tz} = 5.370$. As expected, the upward facing top meter responds most strongly to the z-component of the electric field.

Similarly, the least squares fit results for the other E_i's ($i = b, l, r, f$) are shown in Figures 14b to 14e. By taking the coefficients in Figures 14a to 14e as our best estimates of the A_{ix}, A_{iy} and A_{iz} coefficients, we have:

$$\begin{bmatrix} E_t \\ E_b \\ E_l \\ E_r \\ E_f \end{bmatrix} = \begin{pmatrix} 1.025 & -0.796 & 5.370 \\ 0.3627 & 0.1036 & -2.034 \\ 8.134 & +20.390 & 2.836 \\ 8.858 & -22.11 & 2.308 \\ 5.12 & 6.994 & -4.083 \end{pmatrix} * \begin{pmatrix} E_x \\ E_y \\ E_z \end{pmatrix} .... \qquad (7)$$

when the contribution from airplane charge Q is zero or negligible as compared to the contributions from the ambient field. The first 4 rows of this matrix (7) compare well with matrix (1), with some minor differences.

Incorporating into the above matrix equation the relative magnitude of all A_{iq} coefficients obtained from airplane artificial charging test in the past (the means listed at the bottom of Table 9), we have a full enhancement matrix equation for the T-28:

$$\begin{bmatrix} E_t \\ E_b \\ E_l \\ E_r \\ E_f \end{bmatrix} = \begin{pmatrix} 1.025 & -0.796 & 5.370 & 2.1 \\ 0.3627 & 0.1036 & -2.034 & 1.0 \\ 8.134 & +20.390 & 2.836 & 5.7 \\ 8.858 & -22.11 & 2.308 & 5.7 \\ 5.12 & 6.994 & -4.083 & 3.1 \end{pmatrix} * \begin{pmatrix} E_x \\ E_y \\ E_z \\ Q \end{pmatrix} .... \qquad (8)$$

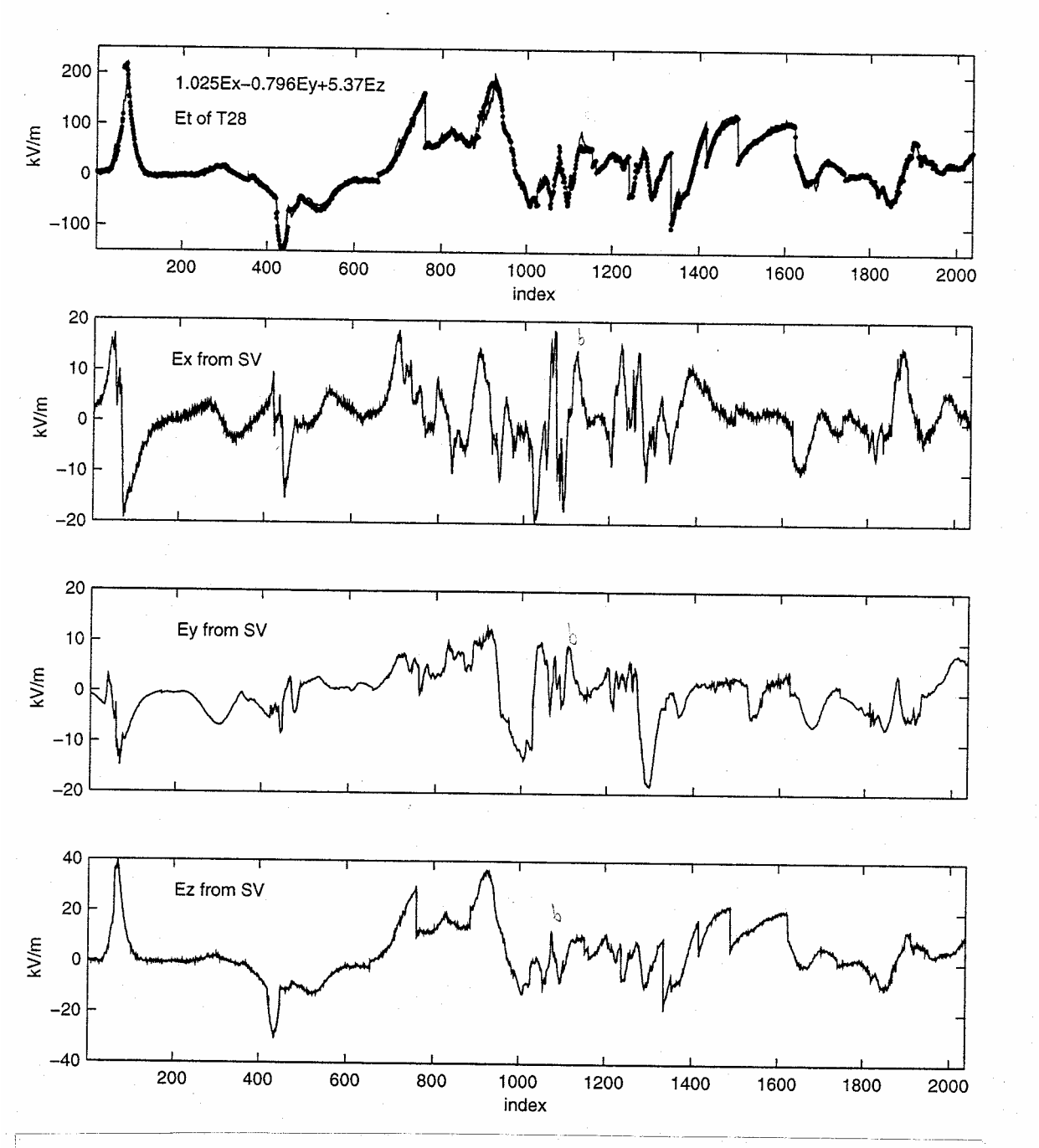

Fig.14a. Finding the A_{ti} (i=x,y,z) coefficients for the T-28 top fuselage meter. The top panel shows that the linear function ($1.025E_x$-$0.796E_y$ +$5.370E_z$) fits the measured E_t. (E_x E_y E_z), which also are shown in other frames, are deduced from the SPTVAR using pod meters. Data are concatenated from the formation flight data shown in Fig.13a through Fig.13e, excluding parts of the data when E_t are suspected to be affected by corona ions. Sampling rate is 1 Hz. (SV indicates SPTVAR.)

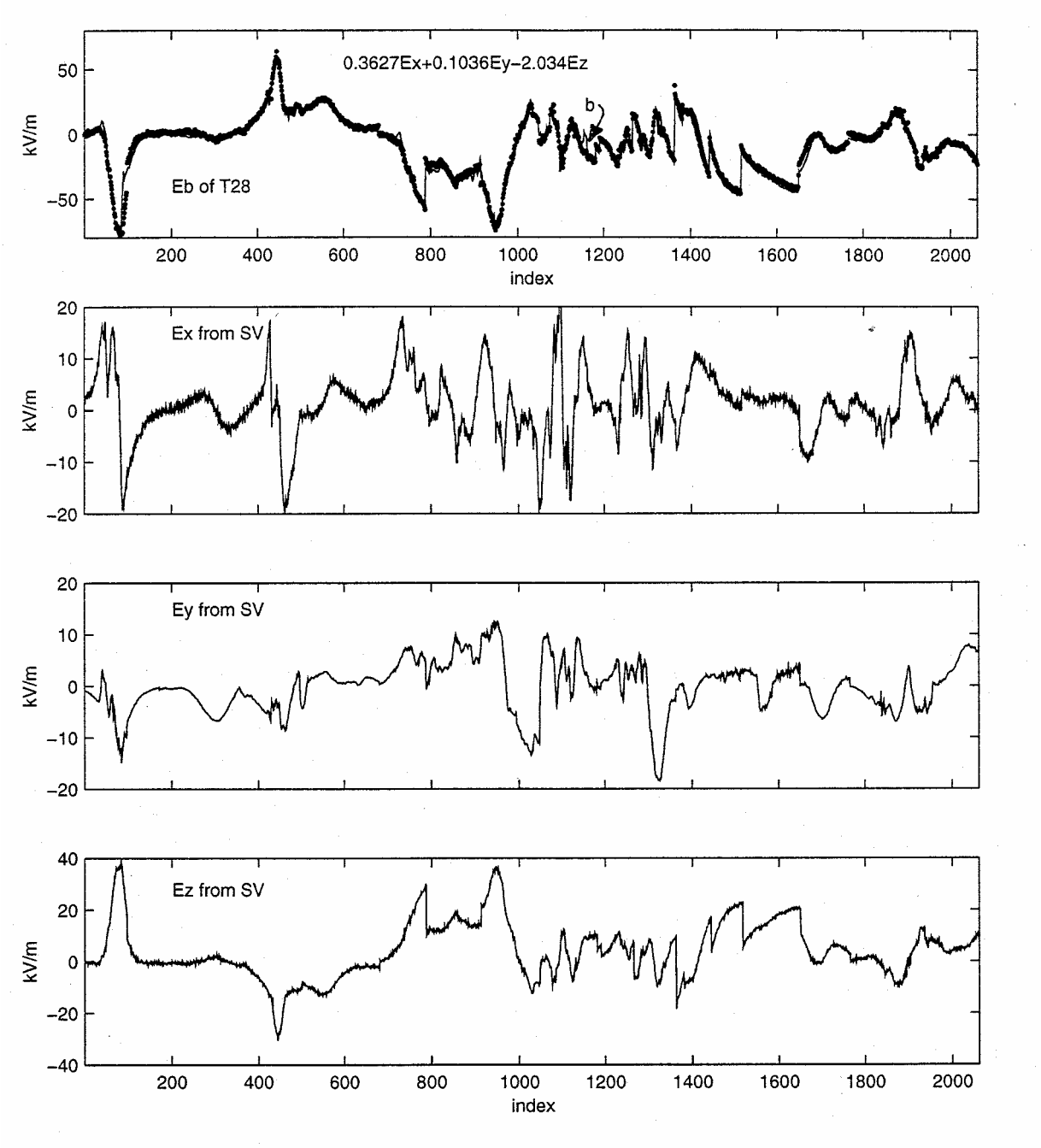

Fig.14b. Same as Fig.14a, but for bottom fuselage meter E_b. Note that it uses more data points than Fig.14a.

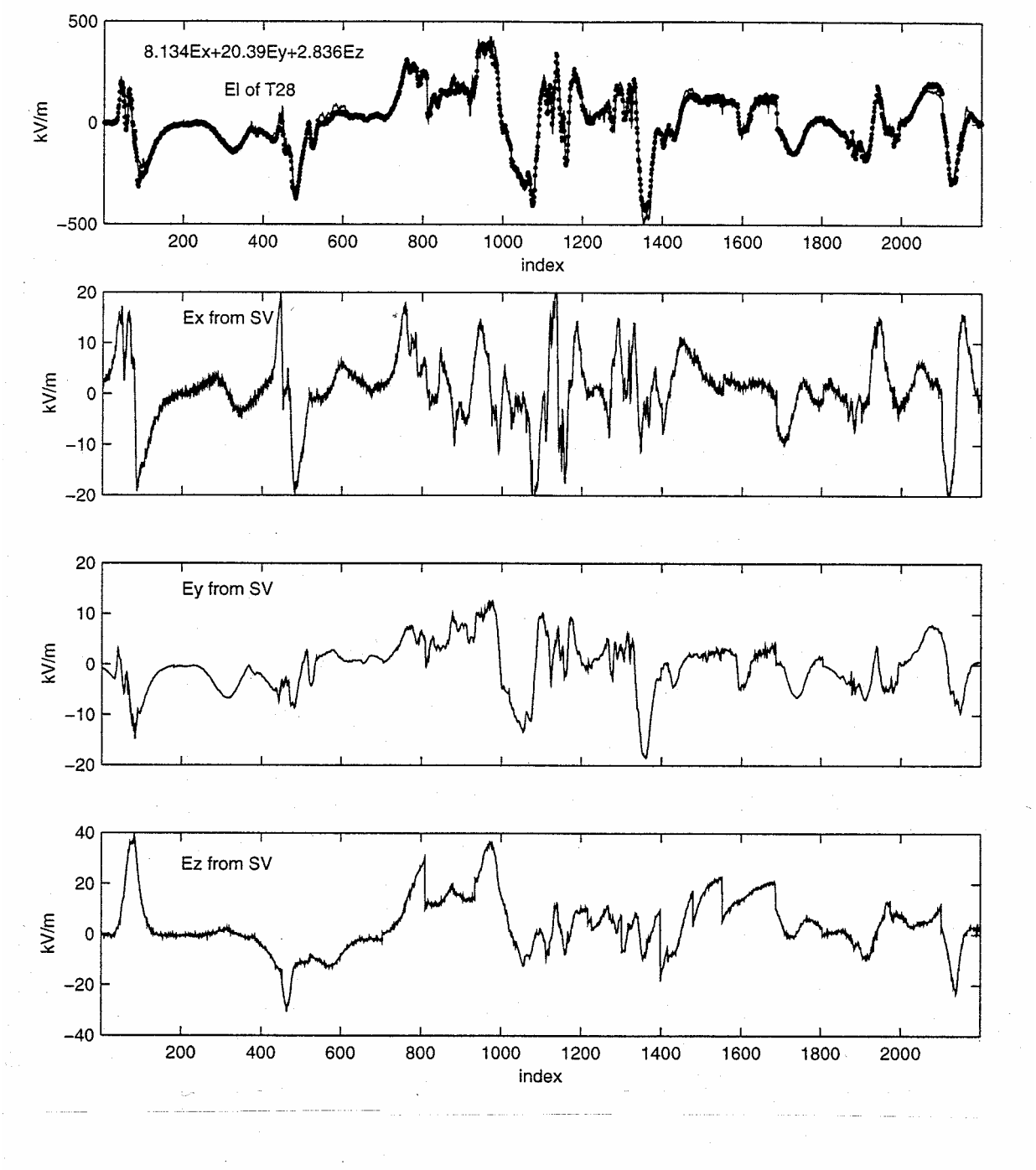

Fig.14c. Same as Fig.14a, but for left wing-tip meter E_l. Note that it uses more data points than Fig.14a or Fig.14b.

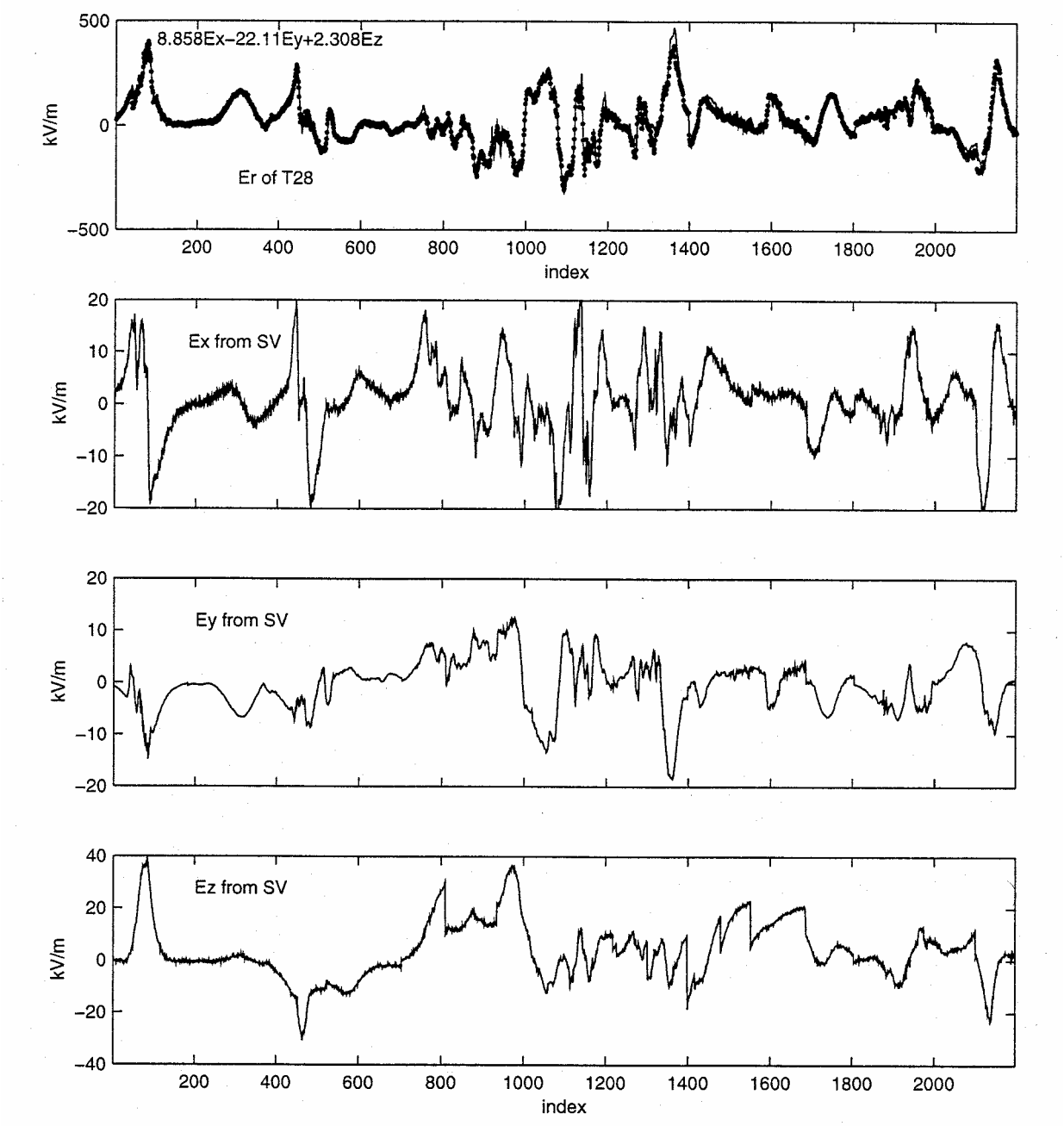

Fig.14d. Same as Fig.14a, but for right wing-tip meter E_r. Note that it uses more data points than Fig.14a or Fig.14b.

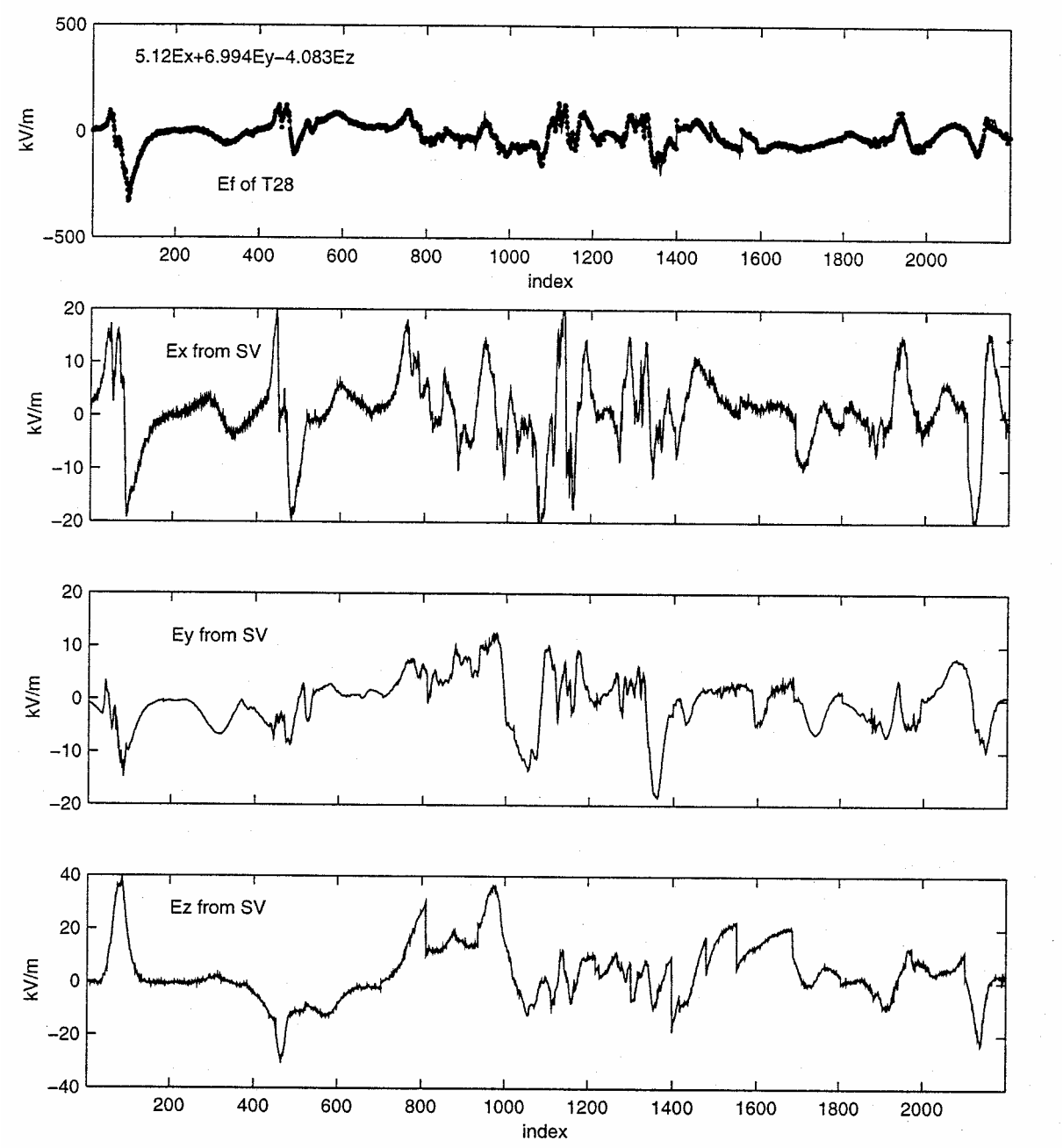

Fig.14e. Same as Fig.14a, but for the fifth meter E_f. Note that it uses more data points than Fig.14a or Fig.14b.

Qualitatively, the coefficients of the matrix equation (8) appear to be reasonable, and quantitatively they are in close agreement with (1), derived from the 1990 measurements. The following observations are offered.

(1) For the first column, the observations that all A_{ix} are positive suggests that all meters are forward of the E_x polarization neutral points on the airplane. The neutral points are defined as the points at which the induced surface density is zero when the airplane is in a uniform ambient E_x field along the fuselage. If E_x is positive, the polarized charge density is positive forward of these points and the induced polarization charge is negative aft of these points. Since the top meter and bottom meter are closer to the neutral points than the meters on the wings, their coefficients A_{tx} and A_{bx} are smaller. Since the top meter is mounted on a high protruding canopy surface, while the bottom meter is on a flat bottom surface, it is understandable that in a uniform E_x field, the top meter will sense a stronger local field than the bottom meter, due to more polarization surface charge at the top meter location. Therefore A_{tx} is larger than A_{bx}. Similarly, because the wing tip meters are also located on places of small curvature and more forward of the neutral points, the E_x-polarization surface charge density is much larger for these meters. Thus the wingtip meters have very large A_{lx} and A_{rx} coefficients.

(2) For the second column, meters on the wings have the largest A_{iy} coefficients because, in general, the farther away from the fuselage, the larger the E_y-polarization surface charge density and the larger the outward-directed field. As for A_{ty} and A_{by}, it is reasonable that A_{ty} has some dependence on E_y because it is difficult to place a field meter exactly symmetrically on the airplane on the small curvature surface of the canopy, where there is a high gradient of E_y polarization charge density. However, at the location of the bottom meter, a relatively flat surface, the gradient of charge density is much smaller. The symmetry requirement for installation is probably less stringent with the result that A_{by} is much less than A_{ty}. Certainly, there also is a possibility that A_{ty} and A_{by} are in part derived from "statistical noise " in the data used, particularly for A_{by}.

(3) For the third column, it is reasonable for A_{tz} to be larger than A_{bz} since the top meter is protruding into the upper *Z*-space, having a much larger exposure angle than the bottom meter's exposure angle to the lower *Z*-space. It is also reasonable for A_{rz} and A_{lz} to be positive because of the wing-tips' slight upward dihedral-angle in flight. Thus, the field meters actually are facing upward slightly in flight. In a positive uniform E_z field there will be more field lines going out from the upper part of the electrodes than the field lines terminating on the lower part of the electrode, resulting in positive A_{lz} and A_{rz} coefficients. Note also that the E_z-polarization charge density on the wingtip should be large and may have a high gradient from positive at the top edge to negative at the bottom edge. It is very difficult to install the field meter in precisely an orientation such that the total induced charge on the electrode is zero in a uniform E_z field. A slightly upward-facing electrode surface will ensure A_{rz} and A_{lz} are positive.

Matrix A can help us to understand and examine the measurement data, gaining insight into the data and the deduced electric fields. For example, when E_z is dominant, (E_x and E_y = 0), coefficients A_{tz} and A_{bz} tell us that signal E_t will be about 2 times E_b and they are of opposite

sign. When E_x is dominant ($E_y = E_z = 0$ for example), E_t will be about 2 times E_b and they are of the same sign.

This example helps us understand why E_{qy}, computed using the sums of the wingtip meter readings and the methods described earlier in the report, is roughly proportional to E_x as measured by the SPTVAR. For E_l and E_r, since A_{rx} and A_{lx} are large, only when E_y is dominant will E_r and E_l be approximately equal and opposite. Otherwise E_l and E_r will be quite different in their variations with time, and their sum, after scaling by a constant factor, will have a strong correlation with the E_x field component. This can be seen in the lower left plot of Figures 13a to 13e.

Since A_{fx}, A_{fy} and A_{fz} are all large and comparable, E_f will respond strongly to E_x when E_x is dominant, to E_y when E_y is dominant and to E_z when E_z is dominant. Figure 15 shows an example where E_l, E_r and E_f are quite different from each other; however, since all of their coefficients A_{ij} are known, we can approximate all three *E*-field components using these three meters alone, since, in this case, the contribution from *Q* appears to be negligible. The components computed in this way agree with the *E*-field components deduced from the pod meters of the SPTVAR. As complex as E_l, E_r, and E_f are, the deduced E_x and E_z field components from them are simple and reasonable. In Figure 15, we also can see how E_f changes as the E_x, E_y and E_z fields change with time. Finally, this figure shows that E_z estimated from the T-28 meters not on the fuselage agrees well with E_z estimated from the SPTVAR pod meter system.

4.4.3 Reliability of newly obtained T-28 calibration Matrix A

Matrix equation (8) is obtained by using the SPTVAR's (E_x E_y E_z) as reference under the assumption that, for the inter-comparison flights, the charge *Q* on T-28 is zero or close to zero. In this section, we use this A matrix to calculate *Q* to show that *Q* was indeed relatively small, and to derive a redundancy equation with which to show that matrix A is reliable.

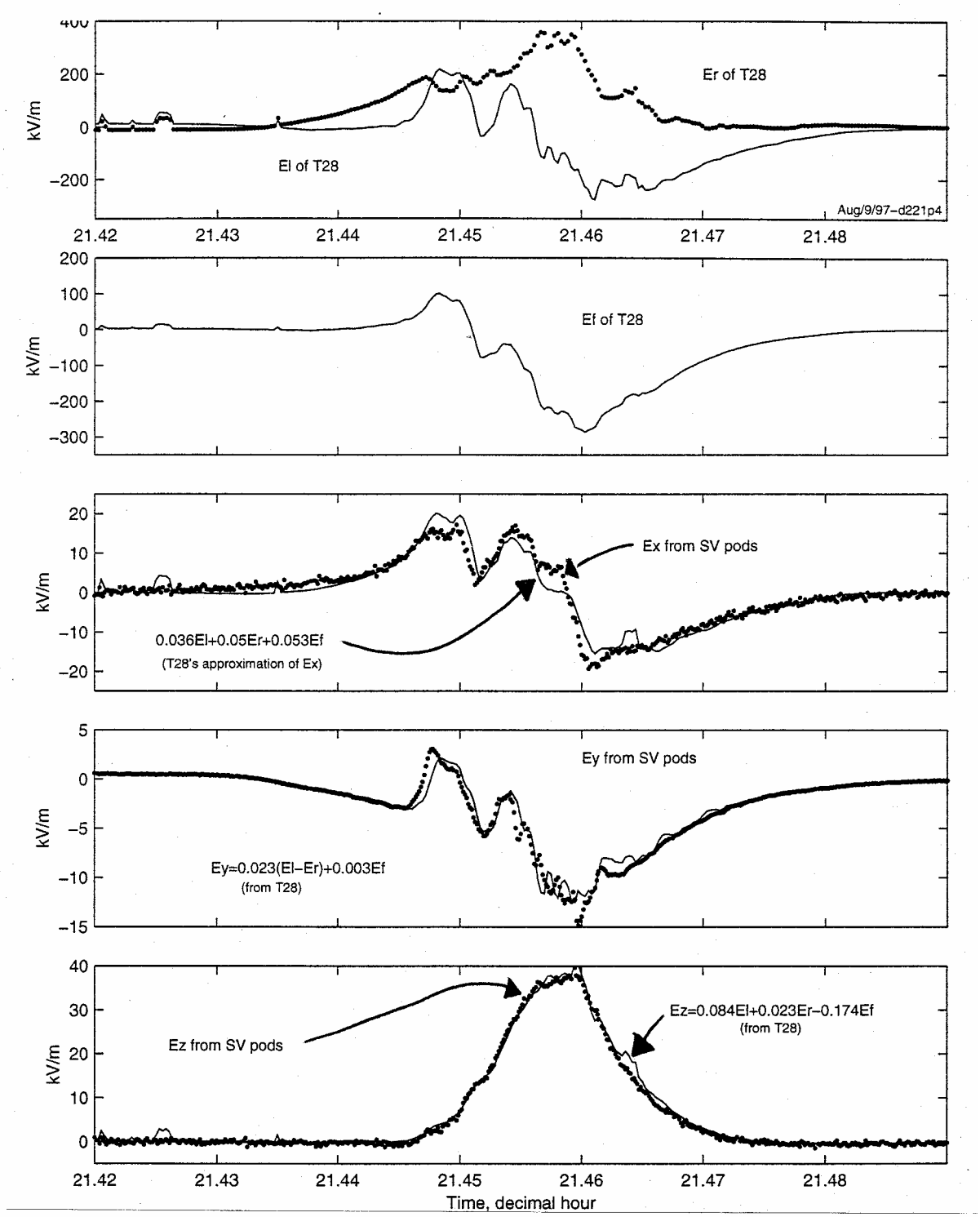

Fig. 15. Three signals from the T-28 field meters on the wings and the approximation of (E_x, E_y, E_z) from the three signals alone. The approximation (E_{x3} E_{y3} E_{z3}) agrees with the (E_x E_y E_z) deduced from the SPTVAR pod meters. Data is collected from 21:25 to 21:30 UTC on Aug. 9, 1997. The two airplanes were in formation. Also see Fig. 13a.

Self-consistency of Matrix equation (8) and Redundancy

To check the reliability of matrix equation (8) or its self-consistency, we first derive a redundancy equation. There are five meters on the T-28, but only four meters are needed to find (E_x E_y E_z Q) if they are properly located. The extra fifth meter is redundant; that is, it should be possible for its measurement to be computed using a linear function of the measurements from the other four meters [Winn 1993]. Using the first four equations of (8) and inverting the equation set, one has:

$$\begin{bmatrix} E_x \\ E_y \\ E_z \\ Q \end{bmatrix} = \begin{pmatrix} -0.239 & -0.441 & 0.0827 & 0.0828 \\ -0.004 & -0.007 & 0.025 & -0.022 \\ 0.110 & -0.207 & 0.000 & -0.005 \\ 0.311 & 0.741 & -0.032 & -0.0371 \end{pmatrix} * \begin{pmatrix} E_t \\ E_b \\ E_l \\ E_r \end{pmatrix} .... \qquad (9)$$

Substituting E_x, E_y, E_z and Q from the above equation into the equation for E_f in (8), we have:

$$E_f = -0.7646E_t + 0.8794E_b + 0.4973E_l + 0.1740E_r \text{ .....} \qquad (10)$$

Equation (10) is the redundancy equation. If all of the coefficients in (8) are correct, that is $E_i = A_{ix}E_x + A_{iy}E_y + A_{iz}E_z + A_{iq}Q$, and there are no corona ions affecting any of the field meters' measurements, then the left side of (10) should be identical to the right side. However, when corona ions are affecting some of the field meters' measurements, the left side of (10) may not be equal to its right side. Thus we can use equation (10) to check if the matrix equation (8) is reliable and to check if corona ions are affecting the measurements.

There are some subtleties in using equation (10). For example, if all signals are correct except E_r, then when using (10), as it is, it will sometimes be difficult to detect a small error in the signal E_r since the error contained in E_r in equation (10) is diminished by the multiplication of the smallest coefficient 0.174.

For convenience, we can transpose E_f and E_t in (10) to get:

$$E_t = 1.15E_b + 0.65E_l + 0.23E_r - 1.31\,E_f \text{ .....} \qquad (11)$$

We do this because the top fuselage meter is a meter that is most sensitive to the field component E_z and the variation of E_z along a storm penetration track usually is simple, smooth and easy to understand. Hence, the signal E_t should be simple and smooth. We do this also because E_t is often suspected to be affected by corona ions.

The top frames of Figures 16a through 16e show the redundancy check for data from all formation flight segments in 1997. For most of the times, E_t equals the right side of equation (11). Thus there is reason to believe that matrix equation (8) is reliable.

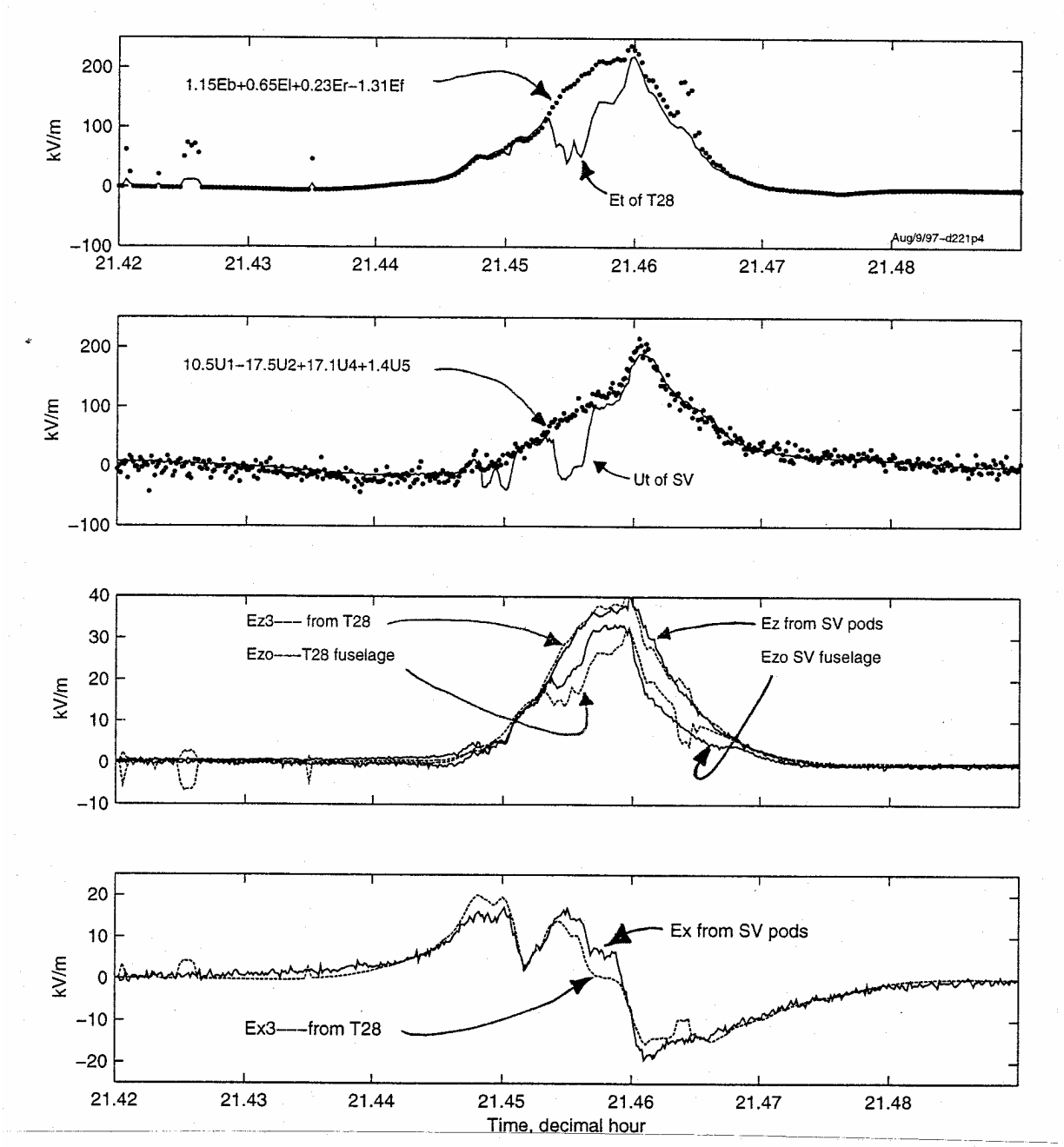

Fig.16a. Redundancy of T-28 and SPTVAR electric field measurements during formation flight. When E_x and E_z are strong, both airplanes' top fuselage meters are affected by corona ions, resulting in measured signals E_t or U_t not being equal to their equivalent linear combination formed by the other meters on each aircraft. Because of corona ions, the E_z field components deduced from the fuselage meters, E_{zo}, differ greatly from the simple and smooth E_z (SPTVAR) and E_{z3} (T-28) deduced from the pod meters and from the meters on the T-28 wings. Time is from 21:25 to 21:30 UT (15:25 to 15:30 MDT) on Aug. 9, 1997, as in Fig. 13a.

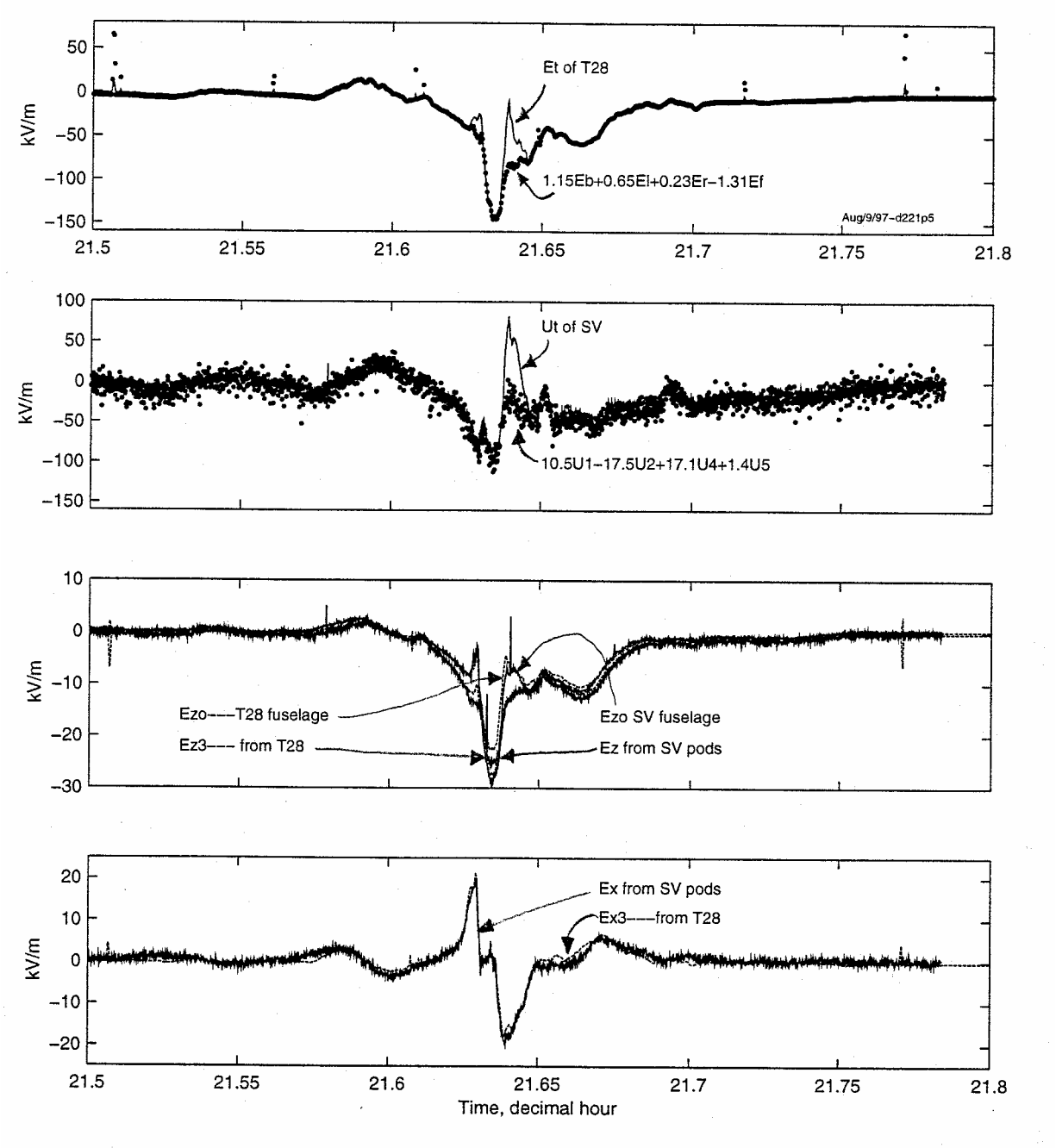

Fig.16b. Same as Fig.16a, but time is from 21:30 to 21:48 UT (15:30 to 15:48 MDT) on Aug. 9, 1997.

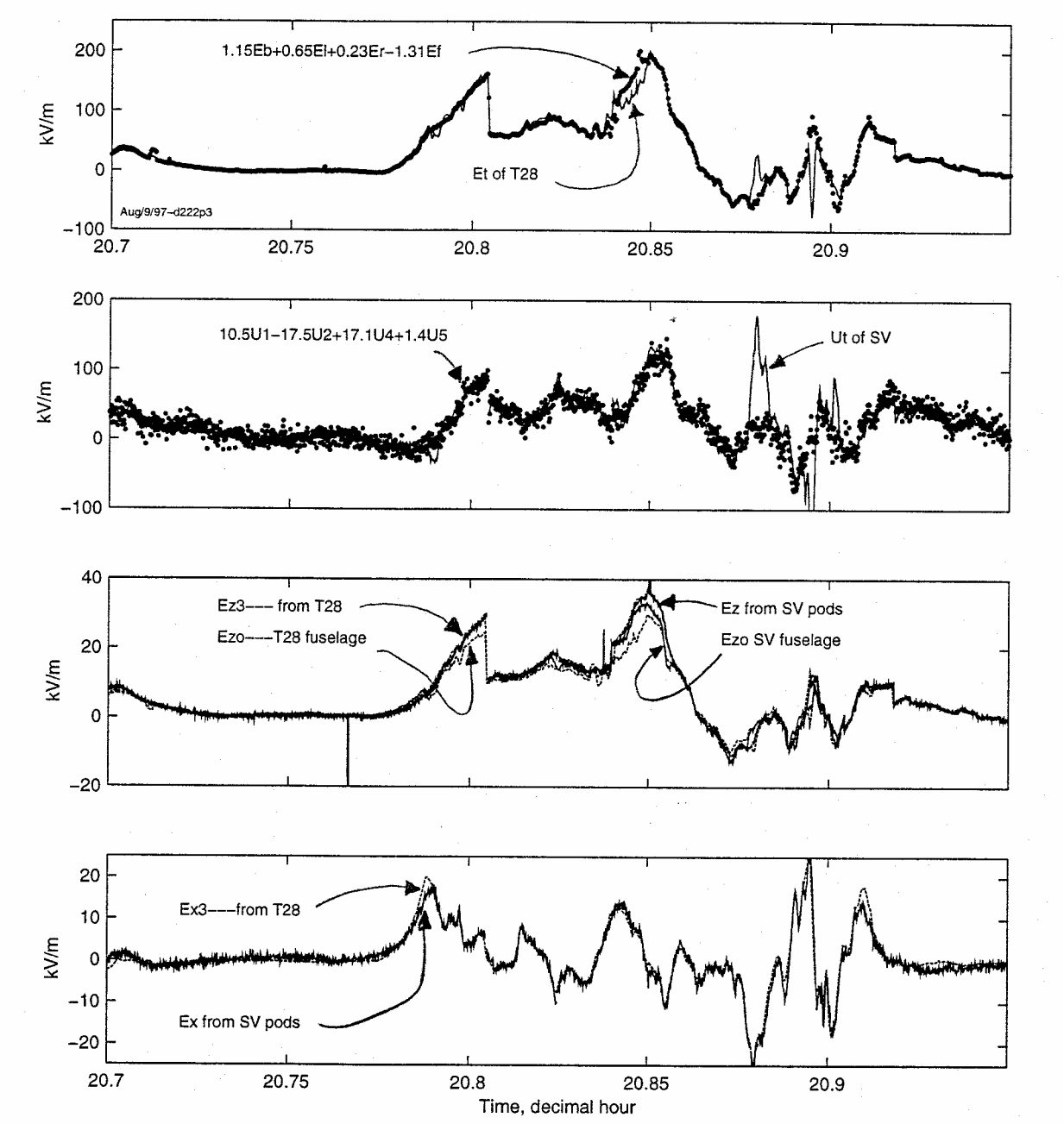

Fig.16c. Same as Fig.16a, but time is from 20:42 to 20:57 UT (14:42 to 14:57 MDT) on Aug. 10, 1997.

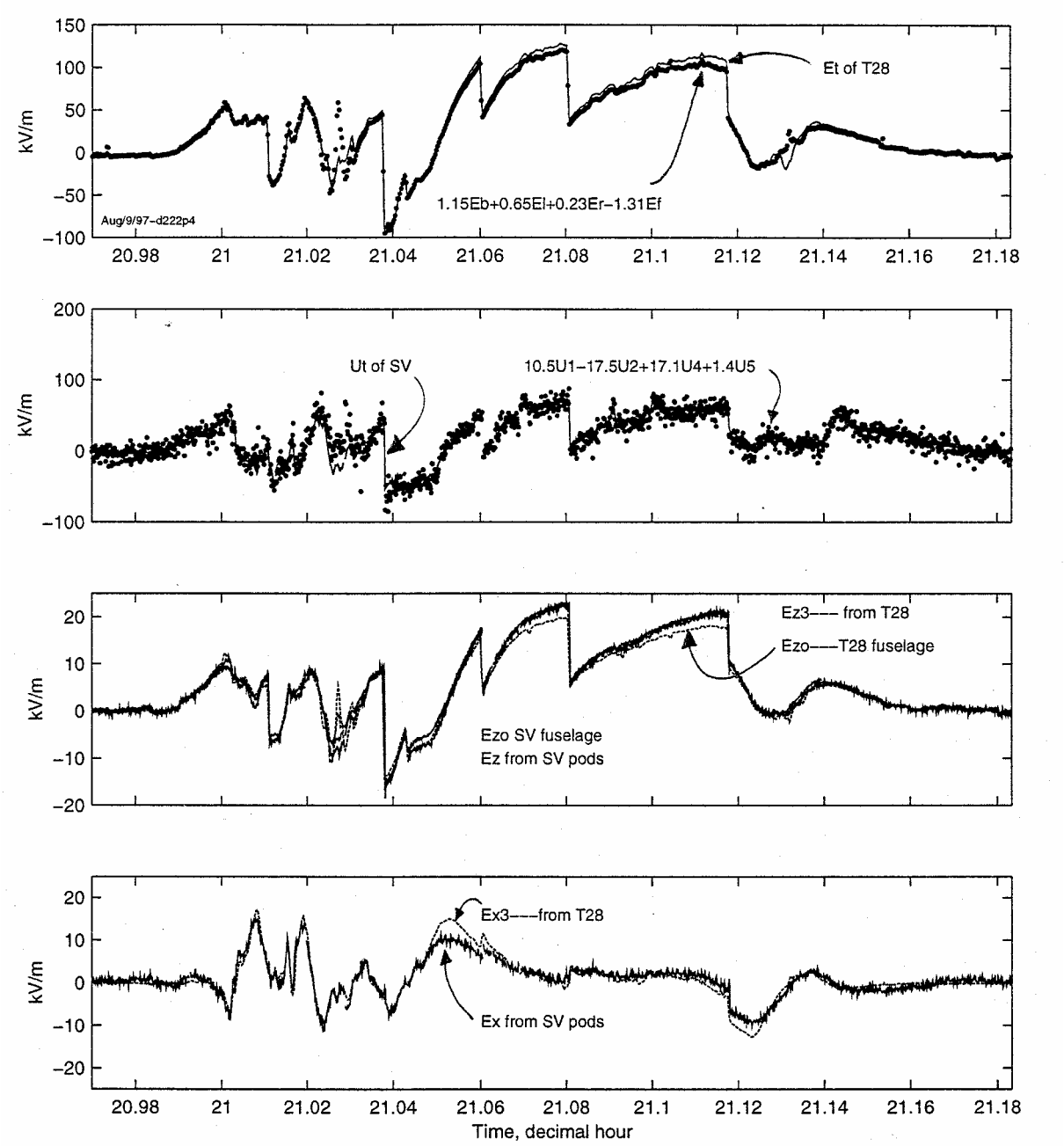

Fig.16d. Same as Fig.16a, but time is from 20:57 to 21:11 UT (14:57 to 15:11 MDT) on Aug. 10, 1997.

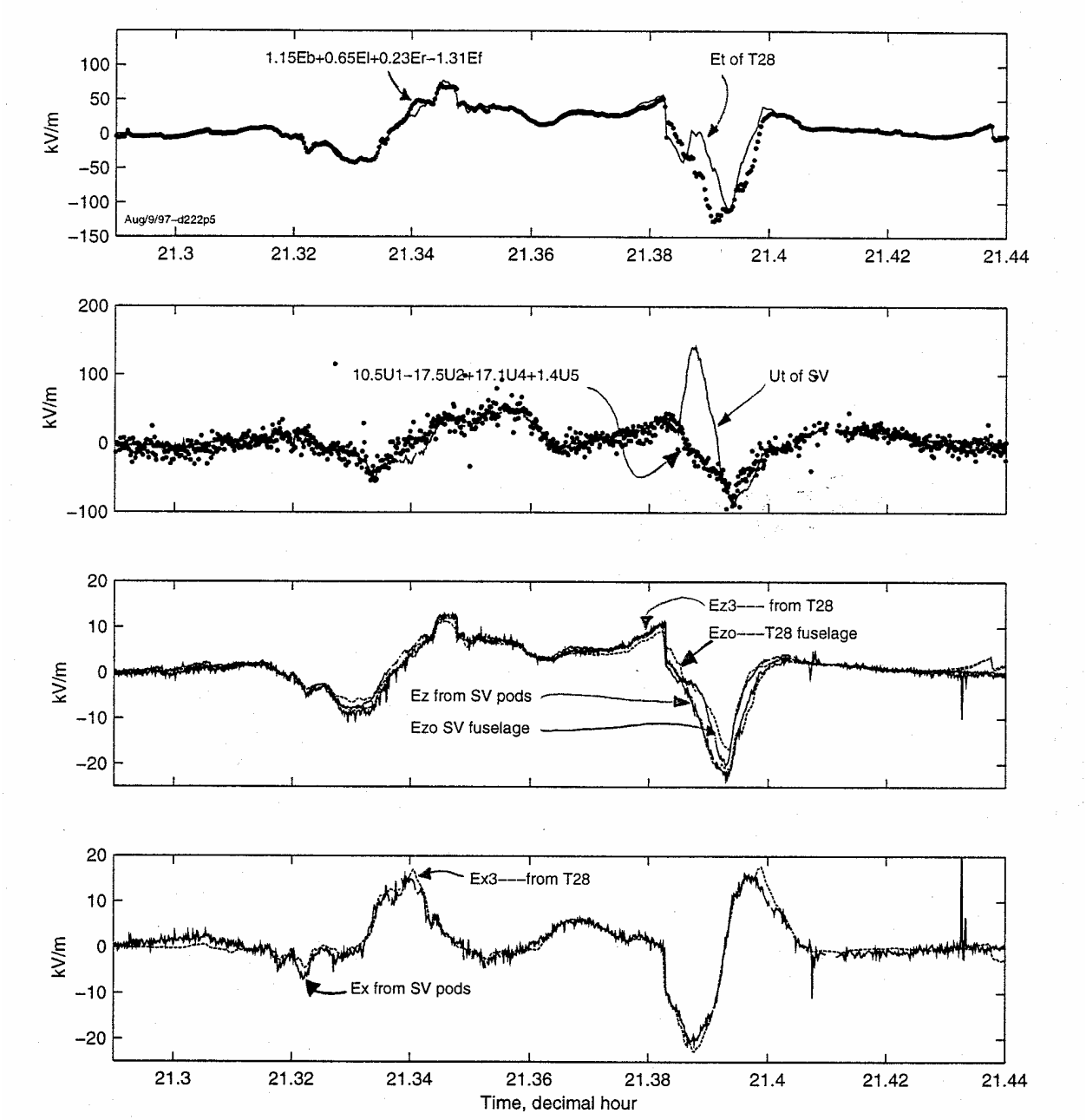

Fig.16e. Same as Fig.16a, but time is from 21:17 to 21:26 UT (15:17 to 15:26 MDT) on Aug. 10, 1997.

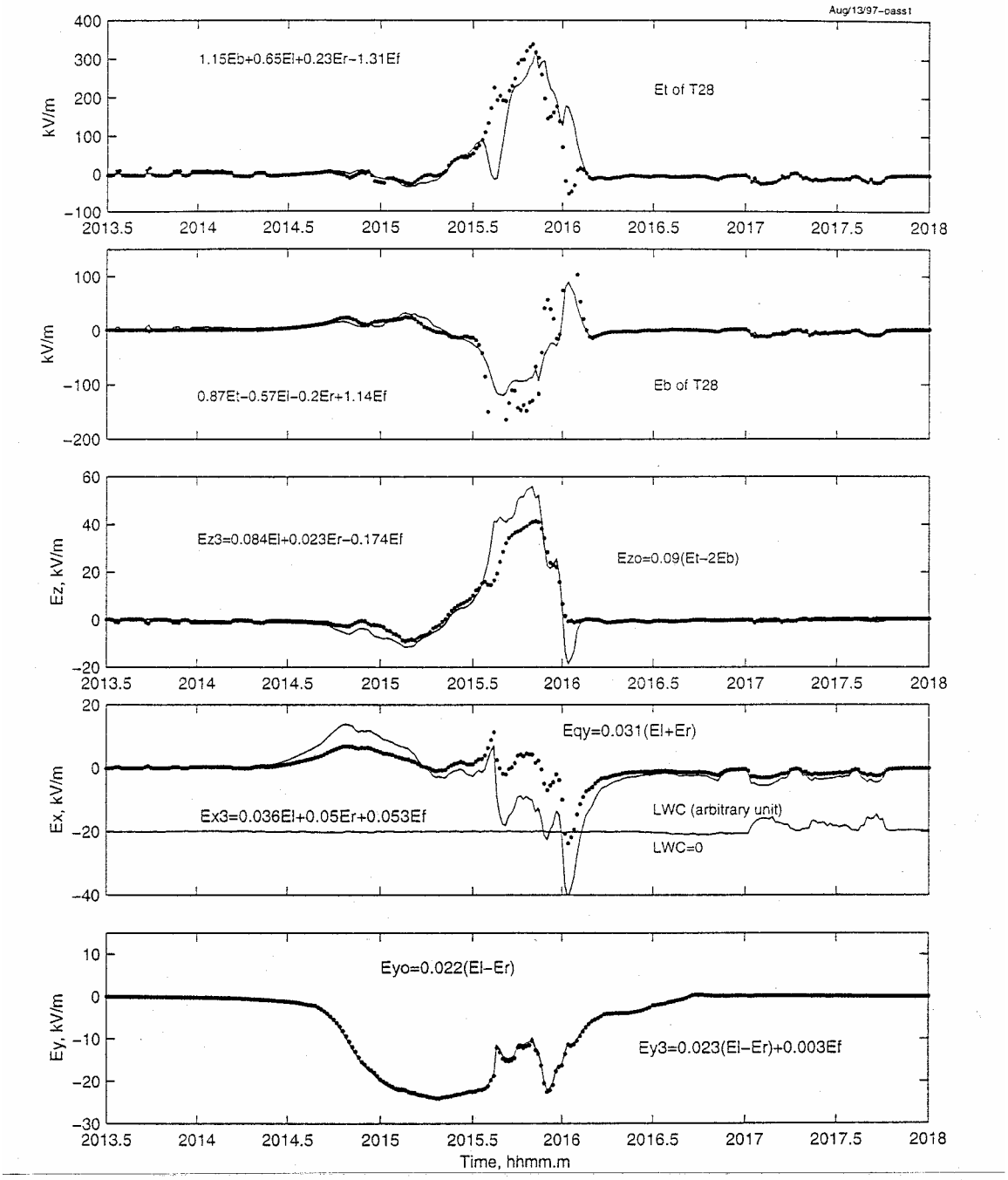

Fig.16f. Redundancy of T-28 Electric field measurements when penetrating a thunderstorm. When E_x and E_z are larger than about 15kV/m, corona ions are emitted, resulting in the measured signals E_t and E_b no longer being equal to their equivalent linear combination formed by other four meters. Because of corona ions, the E_z field component deduced from the fuselage meters differs greatly from the more reasonable and smooth E_z field deduced from the field meters on the T-28 wings. Time is from 20:13:30 to 20:18 UT (14:13:30 to 14:18:00 MDT), the first penetration of a New Mexico thunderstorm on Aug. 13, 1997.

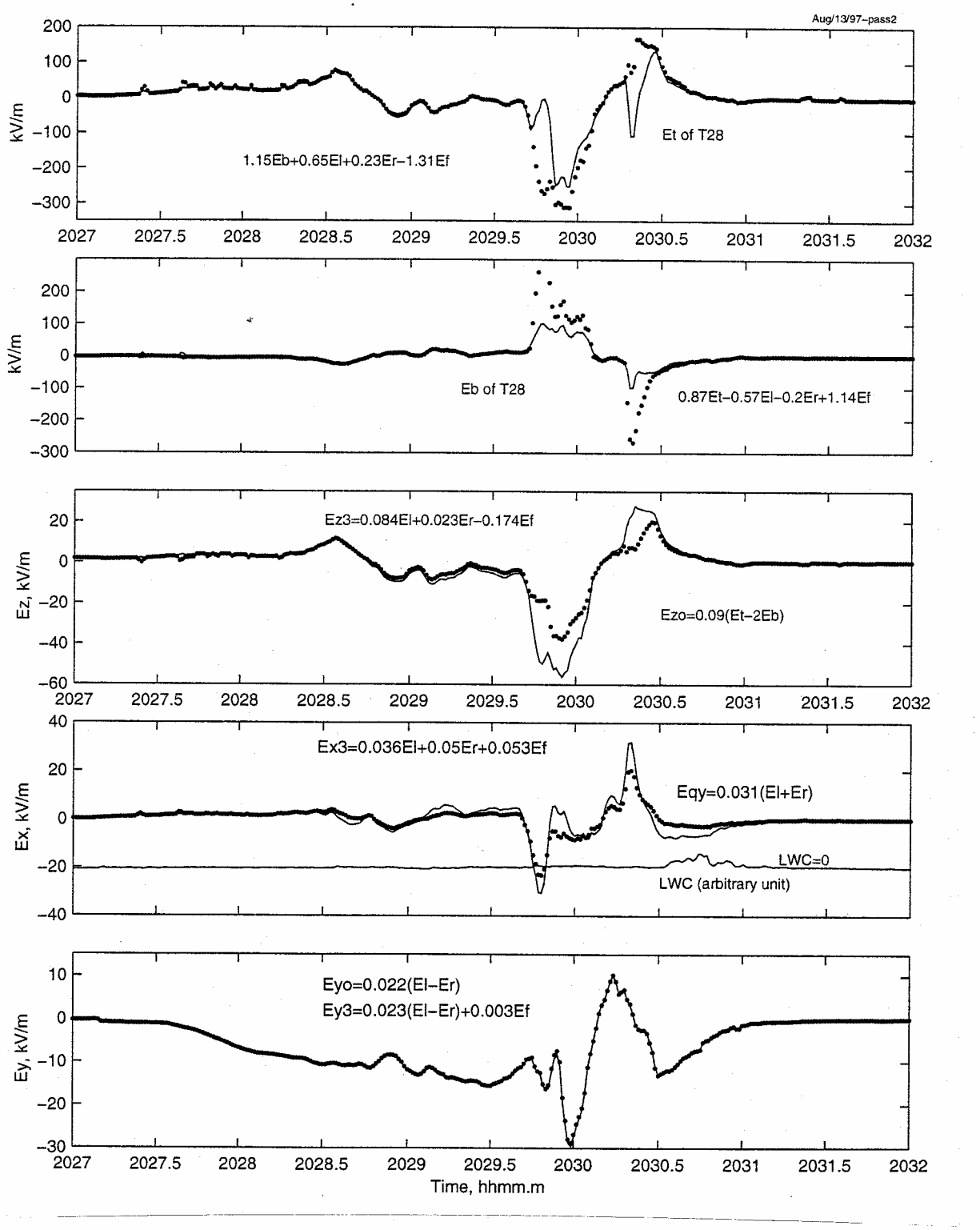

Fig. 16g. Same as Fig. 16f, but time is 20:27 to 20:32 UT (14:27 to 14:32 MDT) on Aug. 13, 1997, the second penetration of the same storm on same day.

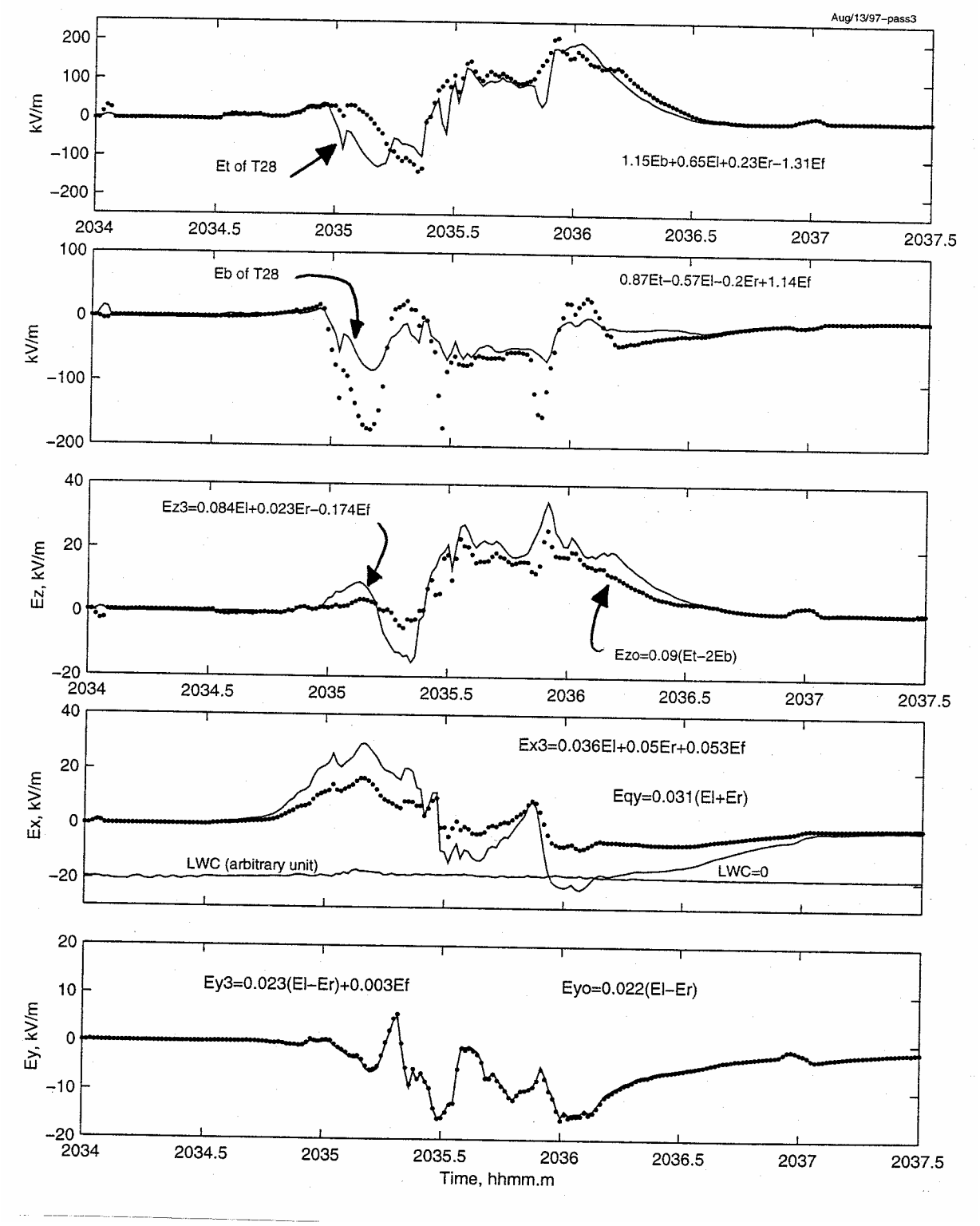

Fig. 16h. Same as Fig. 16f, but time is 20:34 to 20:37:30 UT (16:34 to 16:37:30 MDT) on Aug. 13, 1997, the third penetration of the same storm.

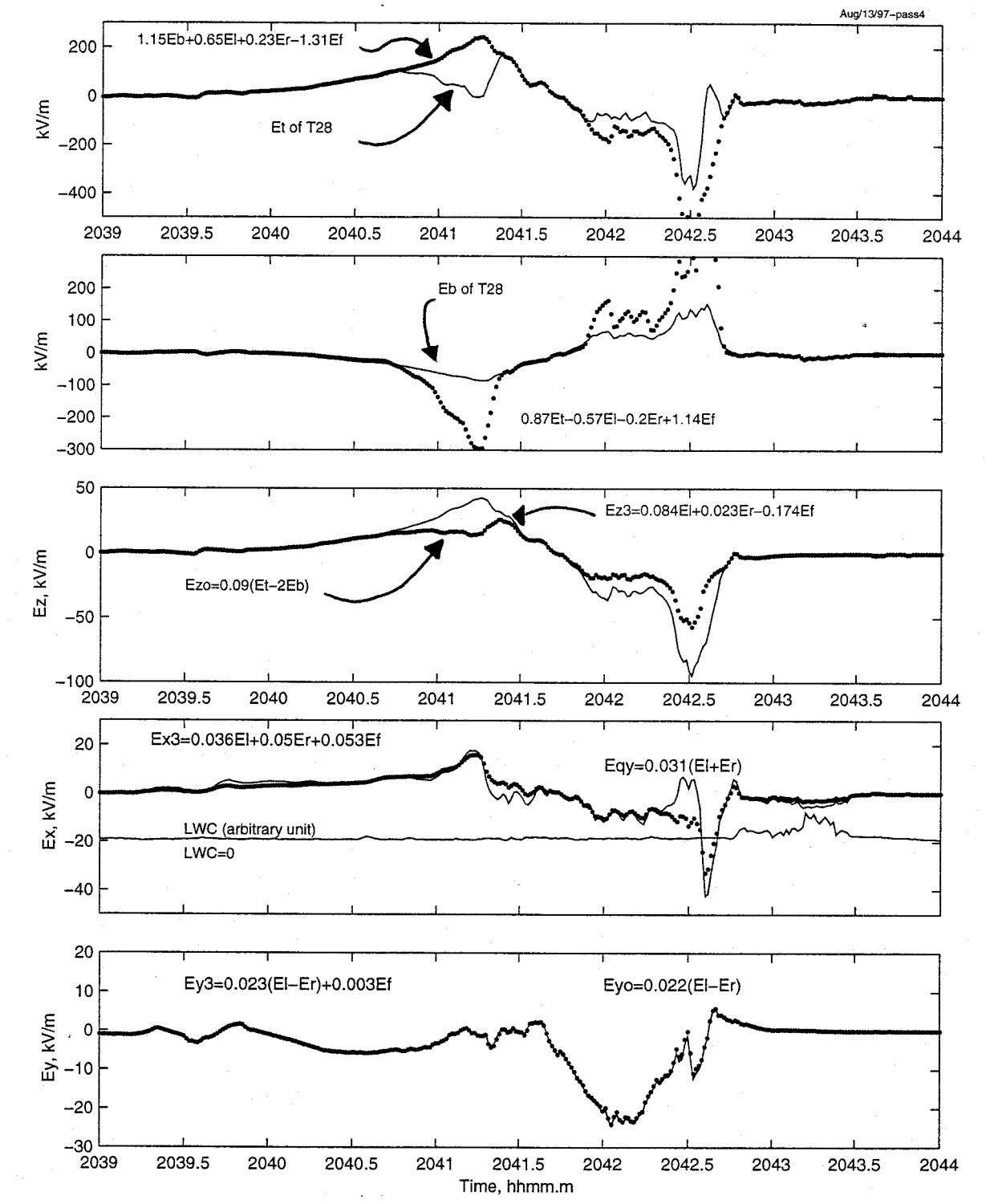

Fig. 16i. Same as Fig. 16f, but time is 20:39 to 20:44 UT (16:30 to 16:44 MDT) on Aug. 13, 1997, fourth penetration of the same storm.

Sometimes, E_t suddenly changes its trend, after which equation (11) no longer holds true for a certain time interval, and then equation (11) holds true again. These episodes are good indicators that E_t or some other field meter's signals are being affected by corona ions. The problem is the corona ions rather than problems with the A matrix (equation [8]) since the lack of agreement is episodic and corresponds to situations in which the ambient field has large magnitude.

Another good reason to believe that these episodes are effects of corona ions is their concurrence is simultaneous with the lack of agreement in the redundancy check on SPTVAR's signals. The redundancy of SPTVAR data is shown in the second frames of the Figures 16a to 16e. In these figures, the SPTVAR top fuselage meter's signal U_t is not equal to its equivalent linear combination based on the four meters on the pods. Since the pod meters are not affected by the corona ions [Mo *et al.* 1998], the disagreement must be because U_t is affected by the corona ions. The simultaneous occurrence of the lack of agreement in the redundancy check for both aircraft during the same flight segments suggests that both the SPTVAR's and the T-28's fuselage meters are affected by corona ions. A detailed analysis of the corona ions emission and their effects is presented in 4.4.3.

The third and fourth frames of Figure 16a compare E_x and E_z field deduced from the T-28 with those from SPTVAR. E_{x3} and E_{z3} from the T-28 are deduced using only the 3 wing meters (E_r E_l E_f) to minimize or avoid the effects of corona ions. It is reasonable to use only E_l, E_r and E_f to find (E_x E_y E_z) because airplane charge is usually small and only 3 meter readings are needed to determine the 3 components of the vector electric field in the absence of aircraft charge. For the T-28 system, the 3 meters that are not on the fuselage are less prone to effects of corona emission which causes most problems. Because the aircraft were flying mostly in clear sky close to thunderstorms, there was negligible aircraft charging due to impacts with precipitation particles.

If there is a strong ambient field in clear sky so that the airplane is polarized to emit corona ions at one extreme of the airframe, then there must be equal and opposite numbers of corona ions emitted from the other extreme of the airplane once the airplane acquires a maximum equilibrium charge value. For the T-28, that maximum value may be rather small, as suggested in an example shown in Figure E1d in Appendix E.

A second reason to use only 3 meters from the T-28 system is that $A_{lx}/A_{lq} = 1.43$, $A_{rx}/A_{rq} = 1.55$, $A_{fx}/A_{fq} = 1.65$. Because these ratios are almost equal to each other, E_x and Q can almost be eliminated from the last three equations of (8), leaving two equations with two unknowns, E_y and E_z to be solved with good approximation.

The procedure to solve for (E_{x3} E_{y3} E_{z3}) and the result is given below. Assume Q is zero and inverting the equation set formed by using the last three equations of (7), we have:

$$E_{x3} = 0.0357\, E_l + 0.0496\, E_r + 0.0528\, E_f$$
$$E_{y3} = 0.231\, E_l - 0.0230\, E_r + 0.0031\, E_f \qquad (12)$$
$$E_{z3} = 0.0843\, E_l + 0.0229\, E_r - 0.1735\, E_f$$

Substituting E_r, E_l, E_f in terms of (E_x E_y E_x Q), using the coefficients from equation (8), equation (12) reduces to

$$\begin{aligned} E_{x3} &= E_x + 0.6498\, Q \\ E_{y3} &= E_y + 0.0102\, Q \\ E_{z3} &= E_z + 0.0730\, Q \end{aligned} \qquad (13)$$

Equation (13) indicates that when Q is small, the difference between E_{y3} and the true E_y, and E_{z3} and true E_z, are negligible. Only E_{x3} may be significantly different from E_x. From the T-28's artificial charging test at time 203040 UTC on August 10, 1997, just 10 minutes before the beginning of the formation flight shown in Figure 13c, the maximum airplane charge Q_{max} was less than the equivalent of 2.5 micro-coulombs (1 micro-coulomb contributes a 1 kV/m local E-field to E_b with the assumption that A_{bq} =1 kV/(m micro-coulomb)) at the equilibrium state when the corona current from the HV power supply equals discharging current from the engine's exhaust and corona emission. Therefore, if Q in equation (13) is small compared to E_x, E_{x3} is a good approximation of E_x.

The fact that E_{x3} and E_{z3} in Figure 16a agree with E_{x_sv} and E_{z_sv} from the SPTVAR is another indication that the A matrix is probably correct and Q indeed was small during these flight segments. The third frame in Figure 16a also shows the E_z-field components deduced from the fuselage meters of the two airplanes. The E_z deduced from fuselage meters are considerably smaller than E_z from the wing-mounted instruments when the magnitude of ambient field components E_x and E_z are greater than about 10 to 15kV/m. In this example, the fuselage meters of both airplanes are affected by corona ions for a period of about 1 minute around time 21.46 hours UT.

Similar results can be found in Figures 16b through 16i. Figures 16b through 16e are from the other formation flights discussed earlier, while Figure 16f through 16i are from four penetrations by the T-28 through a thunderstorm at an altitude of about 16,000 feet (0^oC level) on August 13, 1997. Data in Figures 16f through 16i are completely independent of those data used to derive the A-matrix equation (8). In Figures 16f through 16i, the T-28 measured significant cloud liquid water content (LWC) at the sides of the cloud, and measured much stronger electric fields within the storm than was measured during the intercomparison legs flown around storms. The magnitude of E_x ranged up to about 40kV/m and that of E_z up to 100kV/m.

At the same time, the SPTVAR was flying directly overhead at an altitude of about 26,000 feet (-27^oC level) through the same storm that the T-28 penetrated. SPTVAR also measured about the same magnitude of electric field, with E_x up to 100 kV/m after the T-28 left the cloud to go back to Albuquerque airport. (SPTVAR's observations are not shown in Figure 16f through 16i.).

Figure 17 shows in more detail the effects of corona ion emission. Many other cases are similar. The same data in different format appear in Figures 13a, 15, and 16a. As the bottom frame of Figure 15 shows, E_{z3} from the T-28's (E_r E_l E_f) meters agrees with E_z from the SPTVAR pod meter system, an indication that (E_r E_l E_f) are not affected by corona ions. But the E_{zo} calculated using the T-28 fuselage meters, E_t and E_b, in the top frame of Figure 17, differs considerably from E_z of SPTVAR for the time period labeled *b* to *d* (in the middle panel).

As was discussed in Figure 16a, one reason for these discrepancies is that E_t is being affected by corona ions for the time period from *b* to *c*. (The redundancy check is shown again in the second frame of Figure 17.) Also shown in the second frame of Figure 17 are E_b and its equivalent linear combination ($0.87E_t$ $-0.57E_l$ $-0.2E_r$ $+1.14E_f$). For the time period from *c* to *d,* the discrepancy between E_b and its equivalent linear combination suggest that E_b is being affected by corona ions. Thus first E_t is affected by the corona ions and then E_b is affected by the corona ions, making $E_{zo}=0.09(E_t-2E_b)$ incorrect during the time period from b to d shown in the top frame of Figure 17.

Note in Figure 17 that the smoothed E_t is about 5 times E_z and the smoothed E_b is about 2 times E_z but with an opposite sign, which agrees well with the calibration matrix (8). Note also that the excursions labeled x are due to radio communication interference.

A close look at Figure 16a and the second frame of Figure 17 also reveals that E_t is affected by corona ions at the time labeled a in the same way that the SPTVAR's top fuselage meter U_t is affected by corona ions. SPTVAR's data are shown in the second frame of Figure 16a.

The corona emission mechanism appears to work like this: At point *a*, the E_x field component (shown in the bottom frame) reaches a threshold for emission of positive corona ions at the front and top of the nose and propeller tip since they have the strongest polarized positive charge. The positive corona ions are emitted and swept past the top meter causing E_t to sense an additional negative local field, therefore E_t shows a little dip at *a*. After *a,* since E_x becomes lower, little or no corona ions are emitted. Then E_t of the T-28 agrees well with the equivalent linear combination formed by the other four meters on the T-28 again.

At *b*, when E_x becomes larger again and E_z also becomes greater, more positive polarization charge is produced at the top parts of the nose, canopy and propeller, so that more corona ions are emitted, affecting E_t severely from time *b* to *c*. However, at the location of the bottom meter, because the total effects of positive E_z and E_x partially cancel, the bottom front part of the airplane is not polarized with sufficient positive charge to cause corona ions to be emitted and affect E_b. Thus E_b keeps varying as smoothly as the E_z field from time *b* to *c.* After *c*, E_x changes to negative and E_z is still positive, which causes the bottom front parts of the airplane to acquire a much larger negative polarization charge. Corona ions are emitted there, swept past the E_b meter only, making the bottom meter measure an additional local electric field as compared to the correct value. Therefore, after *c*, E_b of the T-28 differs from its equivalent linear combination formed by the other four meters on the T-28.

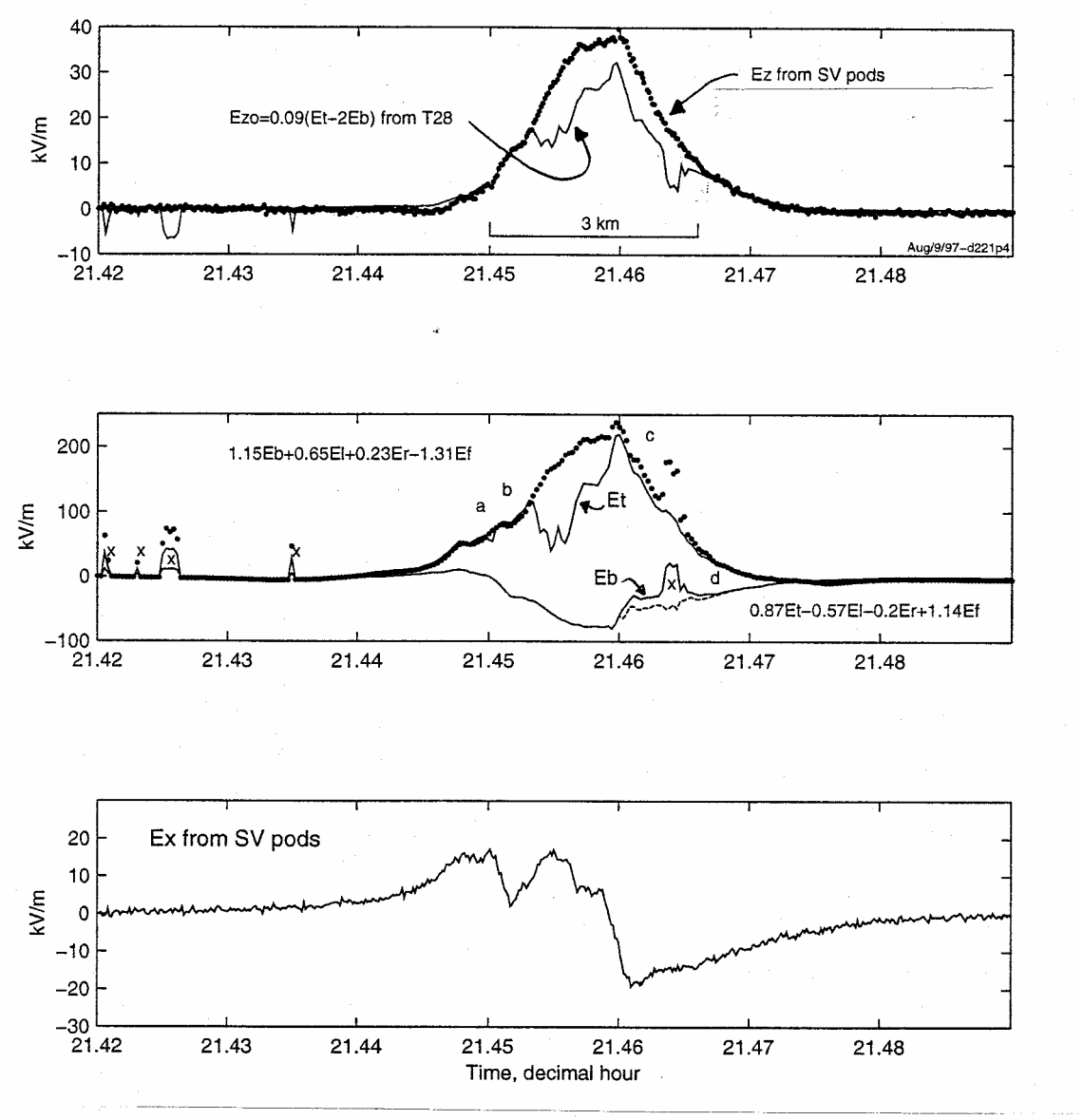

Fig. 17. Details of the effect of corona ions on the fuselage meters. When E_x and E_z are strong, corona ions cause E_z from the fuselage meters to become smaller and incorrect (top). The source of corona ions emitted from the fuselage seems to the polarization surface charge on the airplane caused by the ambient E_x and E_z field components. When E_x is greater than about 18kV/m and E_z is positive, the top fuselage meter is affected by positive corona ions. When E_x is negative, the corona ions change sign and affects the bottom meter since E_z is still positive (middle frame). Note that the transients labeled by x are due to radio communication interference. Data are from 21:25 to 21:30 UT (15:25 to 16:30 MDT) on Aug. 9, 1997.

From this example, and other similar cases, it seems that the threshold for corona ions emission from the front parts of the T-28 is around E_x = 15 to 18 KV/m. If E_z is stronger, the E_x threshold is smaller. Similarly there is a comparable threshold for corona emission due to E_z. If E_x is smaller, the E_z threshold is larger.

Using the above corona emission explanation and the individual field meter coefficients of the A matrix in equation (8), an interesting phenomenon which has been puzzling us for many years is explained. As the aircraft charges up, the sign of E_{qz} and E_{qy} is similar until the ambient field exceeds some value ranging from 5 to 10 kV/m. Then the sign of E_{qz} reverses compared to the sign of E_{qy} but the magnitudes remain similar. This pattern persists until the ambient field decreases below the same threshold. The phenomenon is further described and explained in Appendix E. Our successful explanation of the phenomenon is another indication that the matrix A is reliable.

Airplane Charge and its Contribution

Equation (8) is obtained using parts of the data from Figures 13a to 13e under the assumption that the airplane charge is negligible. With equation (8), we can calculate the airplane charge Q and see how small it is.

There are several ways to calculate the airplane charge Q. In the following, only four ways are given:

$$Q = 1.0967E_b + 0.1712E_l + 0.0339E_r - 0.4083E_f \quad (14)$$

$$Ql = (E_l - 8.134E_x - 20.39E_y - 2.836E_z)/5.7 \quad (15)$$

$$Qr = (E_r - 8.858E_x + 22.11E_y - 2.306*E_z)/5.7 \quad (16)$$

$$Qf = (E_f - 5.12E_x - 6.994E_y + 4.083*E_z)/3.1 \quad (17)$$

Charge Q given by equation (14) is obtained by inverting the last four equations of (8). Charge Q given by equations (15), (16) and (17) is calculated using only one of the T-28's field meter signals and the (E_x E_y E_z) field deduced from the SPTVAR pod field meters during the formation flights. The coefficients in the above equations are taken from equation (8), remembering that A_{bq} is assumed to have a magnitude of unity.

For the same time intervals of all formation flight segments shown in Figure 14c through 14e, the airplane charge Q calculated according to Equations (14) through (17) is shown in Figure 18. Charge Q calculated without using the top meter is in the top plot. Charges Q_l, Q_r and Q_f , computed using the meter indicated by the subscript and the SPTVAR-determined electric field, are in the second, third and fourth plots. Note that the unit of airplane charge is not necessarily correct. There may be a factor of 1 to 10 difference from the correct airplane charge; however, in terms of its contribution, it is correct to say that one unit (one micro-coulomb) of Q is equivalent to 1 kV/m local field intensity at the bottom field meter because (A_{bq}*Q) has unit kV/m after we arbitrarily chose A_{bq} = 1kV/(m micro-coulomb).

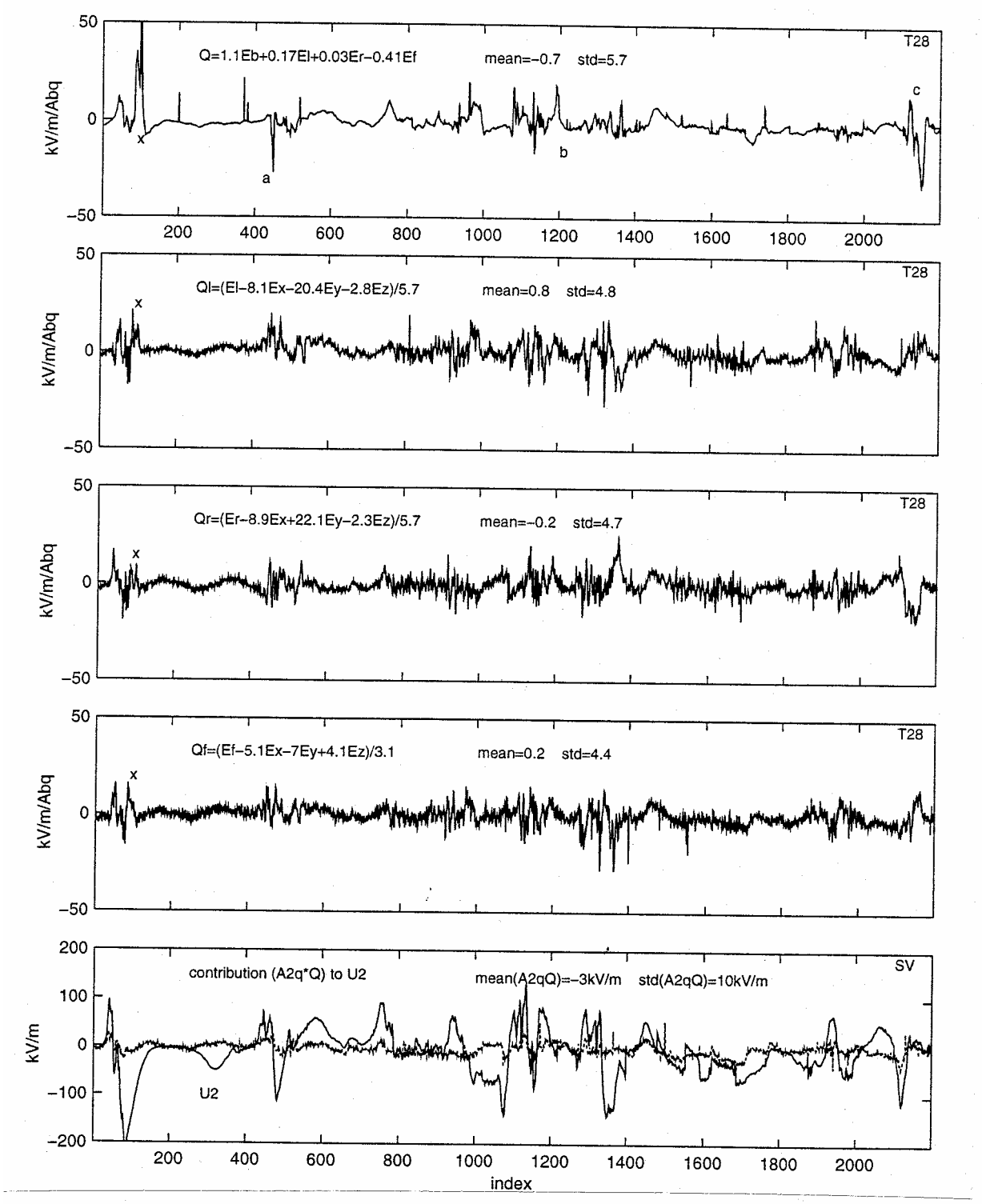

Fig. 18. T-28 airplane charge calculated in four different ways (top four plots) and the contribution of airplane charge on SPTVAR to the SPTVAR signal U_2 (bottom plot). Data are from most of the formation flight intervals in Fig.13a through Fig.13e, The time corresponds to those selected in Fig.14c. Note that at times labeled a, b, and c, the fuselage bottom meter E_b was affected by corona ions, and at the time labeled x, all field meters were affected by the radio communication interference.

Comparing Q, Q_l, Q_r and Q_f in Figure 18, we see that they look similar. Their statistical mean values are close to zero and the standard deviations are also small (in terms of its effect in units of kV/m). Note that larger values of Q near places labeled x are artifacts due to interference from radio transmissions. The larger values of Q at places labeled *a*, *b* and *c* in the top plot appear to be caused by the effect of corona ions on the signal E_b of the bottom fuselage meter since in these places the ambient fields are large, near or even exceeding the corona emission threshold.

In Figure 14b and Figure 14c, we have not excluded all data points that are affected by the corona ions. Figure 14b shows that for some very short intervals E_b does not fit with the linear function ($0.3627E_x + 0.1036E_y - 2.034E_z$). As a reference, the bottom panel of Figure 18 shows the SPTVAR charge's contribution ($A_{2q}*Q$) to the signal U_2 at the same time. Signal U_2 is the signal from SPTVAR's pod field meter number 2, and A_{2q} (= 0.79) is the response coefficient of signal U_2 to the SPTVAR airplane charge Q. Dividing the dashed curve ($A_{2q}*Q$) by 0.79 in the bottom frame gives the charge acquired by the SPTVAR. We can see that the SPTVAR's Q is similar to the airplane charge acquired by the T-28. The comparison between ($A_{2q}*Q$) and U_2 suggests that the effect of SPTVAR charge is almost negligible compared to the total magnitude of U_2 which is quite large most of the time.

Figure 19 shows the T-28's charge contribution ($A_{iq}*Q$) to each field meter's signal E_i for the time intervals of Figure 18. We see that ($A_{iq}*Q$) is indeed much smaller than E_i. In fact, one may treat the contribution ($A_{iq}*Q$) as a "random noise" with small mean value super-imposed on the measured signal E_i. That is why it is possible for us to assume that Q is small and use the least squares fit method to derive a reliable matrix A.

4.4.4 Additional Considerations

In deriving matrix A, we have assumed that the two airplanes' coordinate systems are the same, but in fact, the two systems had some slight difference because the T-28 always had a higher pitch angle. There are some differences in the heading and roll angle of the two airplanes from time to time, but the differences are not very significant and we hope that their effects have been averaged out with the least squares fit methods. In future calibration using inter-comparison formation flight data, it may be worthwhile to transform the *E*-field measured by the other airplane (SPTVAR) to the earth's coordinate first, and then convert that field into the T-28 airplane coordinate. Also, when deriving the A matrix, the time lag between the two airplanes' time system was only roughly corrected so that the peak-valley *E*-field positions measured by the two airplanes match at about the same position. More careful adjustments could be made.

Another problem is that we have assumed in much of our analysis that the airplane charge is zero, but in fact, it sometimes is not. We hope the effects of charge may also have been averaged out because $A_{iq}*Q$ is close to some random "noise" and is relatively much smaller than the signals E_i. As Figure 14b shows, we haven't eliminated all of the data that may be affected by corona ions, further refinement in selecting the data to deduce the A matrix again may be worthy.

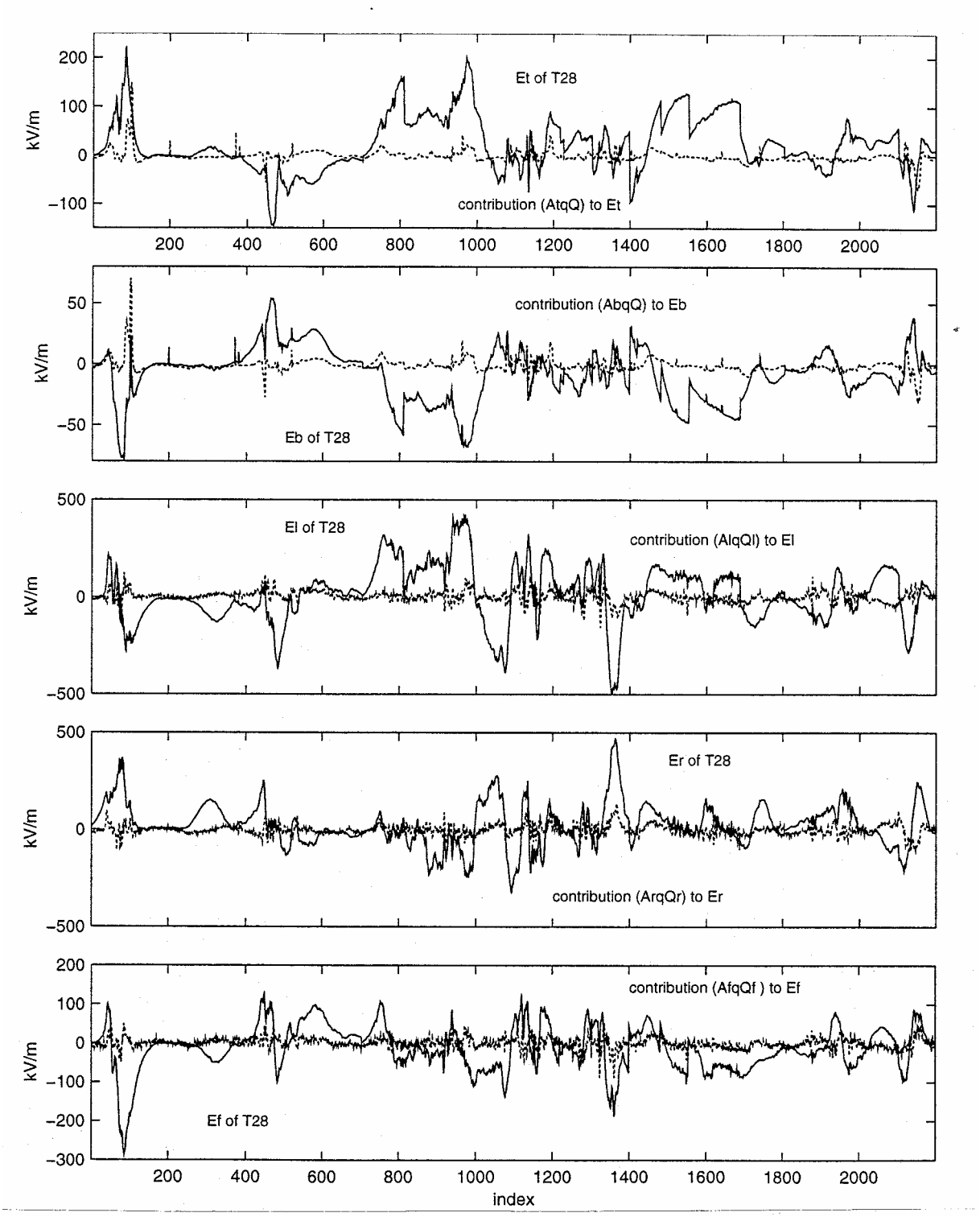

Fig. 19. Comparison of the contribution of T-28 airplane charge with the signal measured at each field meter. Time is the same as those in Fig. 18.

In the future, it also is possible to use the intercomparison data to first derive a B calibration matrix based on combinations of meter readings that are independent of charge [Winn, 1993]; then use the B matrix to derive (E_x E_y E_z) for all of the T-28 data (including intercomparison formation flight data and T-28 solo flight data) to deduce an A matrix. By that method, we have a much larger supply of data to do the same least-square fit calculation as shown in Figures 14a through 14e.

5. DISCUSSION

The response matrices (1) and (8), derived based on the 1990 and 1997 data for the 4 original meter positions, are quite similar. The 1997 matrix (8), based on the 1997 intercomparisons alone, has smaller *y*-enhancement factors compared to the 1990 matrix, Equation (1). The 1990 matrix was based on a combination of the 1990 intercomparisons and the solo roll-maneuvers used to compare responses of the fuselage meters to those of the wing tip meters when directed along the same electric field vector, and incorporates additional information from maneuvers and charge tests accomplished between 1989 and 1993. In 1997, the intercomparison involved the SPTVAR wing-mounted pod field meters, whereas in 1990 the intercomparison involved the SPTVAR fuselage meters.

The statistical summaries in Tables 10 and 11, as well as the extensive analysis in Section 4.4., suggest that when the data are not influenced by artifacts, such as interference from radio communications, misalignment of aircraft or of data system clocks, etc., agreement is good.

The E_z components agree well in the 1990 intercomparison, since the T-28 enhancement factor matrix (1) was derived based on this intercomparison and by forcing agreement in E_z. The fact that the 1997 intercomparison shows the SPTVAR E_z to be consistently larger than the T-28 E_z by about 15% is consistent with the hypothesis that the SPTVAR fuselage meter-based E_z, the basis by which (1) was normalized, is also biased low, on average, relative to the pod meter-based E_z, due to interference from corona ions sweeping along the fuselage in regions of higher ambient field.

The consistent magnitude of the underestimate in E_y by the T-28 compared to the SPTVAR systems, in both 1990 and 1997, was a result of forcing self-consistency on the T-28 matrix (1) in order to make the best possible estimate of the electric field vector projected on the plane perpendicular to the T-28 heading. The T-28 E_y was tied to its E_z. The results of the self-calibration maneuvers in 1997, described above, confirm this relationship based on analyses of earlier roll maneuvers used to establish (1). The wingtip *y*-enhancement factors are quite similar between (1) and (8). Since the T-28 E_z derived using (2) was underestimated compared to the pod system E_z by about 15%, then T-28 E_y is underestimated by about the same percentage compared to SPTVAR pod system, as shown in Section 4.2.2.

It also is interesting to note in Appendix D that agreement between the SPTVAR pod meter system and its fuselage meter system is about as noisy as agreement between the pod system and the T-28 system.

Physical interpretations of the enhancement factor matrices (1) and (8) have been constructed that are plausible. There are higher factors on surfaces with higher curvature. The strongest responses are to ambient field components along the axes of the matched pairs of meters on the fuselage and wing tips. The A_{ix} are all positive because all 5 meters are positioned ahead of the polarization neutral point.

The total net charge that can be acquired is small in light precipitation. Analyses of the 1997 intercomparison data suggest that the effects of charge on individual meter readings can be ignored in this data with little additional error in the retrieved electric field components.

Care is needed in using the full matrix solution when corona emission is a possibility. The relative impact of corona emission on retrieved field components can be estimated by using combinations of 4 meters to estimate the reading of the 5^{th}. If a reliable estimate can be made, then it is probable that corona emission is not significantly affecting any of the meters. When corona emission is indicated, it is best to avoid use of the fuselage meters in estimating ambient field components as these meters are most strongly affected by emission. Reliable estimates of E_x, E_y and E_z can be made using just the wing tip and hail pod meters, even when the aircraft is charged enough to cause interference in the readings of the fuselage meters due to corona emission, as long as this charge is not too great.

What kind of accuracy can one infer for the T-28 electric field measurements, based on these results? If there is no definite sign of interference by corona ions, the repeatability of self-charge tests suggests better than 20% relative accuracy (10% noise in each of a pair of meters used to determine a component) in estimating the magnitude of the electric field due to charge on the aircraft. It is reasonable to assume estimates of ambient field components can be achieved with similar accuracy.

Careful intercomparisons, like those accomplished in 1990 and 1997 using the SPTVAR and T-28, suggest that one aircraft system can be calibrated relative to another to give repeatable measurements with relative accuracy to within a factor of about 10% to 20%. Even when there are corona ions, factor-of-two accuracy is still reasonable. Unless the situation is terribly unusual, sign of the deduced field components should not be in error.

Calibration of the sort described here involves, in essence, tying one system to another system that is regarded as a standard. Based on these SPTVAR/T-28 intercomparisons, systems like those used here can be calibrated with roughly 10% accuracy.

Combining the errors inherent within a system with those involved in comparing between systems, we make a worst-case estimate of the accuracy with which we estimate the magnitude of ambient field components using our T-28 system to be about 33%. This includes 3 factors of 10%, one each for internal accuracy, accuracy of the T-28 relative to the SPTVAR, and the absolute accuracy of the SPTVAR system. If the aircraft is highly charged and corona emission is a significant problem, then accuracy will be worse than this.

6. CONCLUSIONS

The T-28 electric field meter system has performed consistently since the installation of 4 meters in their present configuration in 1989. The meters in the current system, with meters in the 5 positions, have given consistent responses relative to each other from one year to the next.

Techniques are described which can be used to analyze for the effects of corona emission on the retrieved electric field. The process involves using combinations of meters to predict the reading of the remaining meter. When these predictions agree with the reading of the remaining meter, then the system is not being significantly affected by corona emission. The aircraft can carry a measurable charge and still it may be that corona emission is not significantly influencing the estimates of the ambient field components. Even with significant emissions which influence some meters, it may be possible to find a combination of meters little-affected by corona with which to estimate the desired field component.

Overall accuracy of the retrieved electric field components is better than 33% when corona emission is not significantly affecting the meter readings. When corona emission is affecting the measurements, accuracy will be reduced unless one can find a combination of meters, not affected by corona emission, with which to estimate the desired component. We have yet to find a situation where significant fields exist and it is possible that the sign of the estimate of ambient field components is incorrect.

Net aircraft charge most strongly influences the estimate of E_x, as the effects of charge on the meter readings are similar to the effects of polarization of the aircraft by E_x.

7. ACKNOWLEDGEMENTS

It is a pleasure to acknowledge the invaluable assistance of Hugh Christian, William Cooper, Kathy Giori, Steve Hunyady, the late Dr. J. J. “Dan” Jones, Saskia Willemse, and William Winn, without whom this work would not have been possible. Likewise, the dedicated participation of members of the T-28 team in this effort, in engineering, software support, and superb flying, has been crucial in the accomplishments described herein. Support for this effort has been from the National Science Foundation and the State of South Dakota through a series of cooperative agreements under which the armored T-28 has been maintained and used as a national facility for research in convective storm environments. The first of these agreements began in 1987 and the most recent is ATM-9618569.

8. REFERENCES

Giori, K. L. and J. E. Nanevicz, 1992: Comparison of the electrical charging and discharging environments of multiple aircraft-borne electric field measurement systems. *Addendum, Preprints 15th International Aerospace and Ground Conference on Lightning and Static Electricity*, 6-8 October, 1992, Atlantic City. 27-1 - 27-10.

Giori, K. L. and A. G. Detwiler, 1993: Cloud electrification information derived from T-28 aircraft electric-field measurement. Presented at the American Meteorological Society Conference on Atmospheric Electricity, 6-7 October, 1993, St. Louis.

Jones, J. J., 1990, Electric charge acquired by airplanes penetrating Thunderstorms, *J. Geophys. Res.,* **95**, pp16589-16600.

Mo, Q., 1997, "Electric field measurements with an airplane: A solution to problems caused by emitted charge", Ph. D. thesis, New Mexico Institute of Mining and Technology.

Mo, Q., A.E. Ebneter, P. Fleischhacker, and W.P. Winn, 1998, "Electric field measurements with an airplane: A solution to problems caused by emitted Charge", *J. Geophys. Res.,* **103**, 17,163-17,173.

Winn, W. P., 1993: Aircraft measurements of electric field: Self-calibration. *J. Geophys. Res.,* **98**, 7351-7365.

APPENDIX A Basic T-28 Instrumentation

Basic T-28 Instrumentation					
Variable	Instrument	Range	Accuracy	Resolution (as recorded)	Notes
Static Pressure	Rosemount 1301-A-4B	0-15 psi (0-103 kPa)	±0.015 psi (±0.1kPa)	0.0002 psi (0.002 kPa)	
	Rosemount 1301-A-4B	5-15 psi (35-103 kPa)	±0.015 psi (±0.1kPa)	0.0002 psi (0.002 kPa)	
Total Temperature	Rosemount 102AU2AP	-30 - +30°C	±0.5°C	0.001°C	• Platinum wire • –2 s time constant
	NCAR Reverse Flow	-30 - +30°C	±0.5°C	0.001°C	• Platinum RTD element • Several seconds time constant
Cloud Water and Cloud Droplets	Johnson-Williams Liquid Water Meter	0 - 4 g/m^3	±20%	0.0001 g/m^3	• Johnson-Williams cloud water meter had non-functioning de-ice heat in 1997.
	Particle Measuring Systems, Inc. Forward Scattering Spectrometer Probe	Size -1 < 57 µm Concentration 0 - -2000 droplets/ cm^3	±1 size channel in size and ±1% in concentration at ~50/cm^3	1 size channel	• 15 discrete size channels spread over an adjustable range • Sampling rate 300 cm^3/km • Accuracy of computed liquid water concentration ~±50%. Depends on processing. • FSSP was not deployed in 1997.
Precipitation Particle Sizes And Concentrations	Particle Measuring Systems, Inc. 2D Cloud Probe	Size 25 - 800 µm	±25 µm	25 µm	• Computed ice and water mass concentration can vary ±50% with processing technique • Sampling rate: 0.05 m^3/km; DAS can accept ~250 particles/s (2500/km) • PMS-2D-C not deployed in 1997.
	Hail Spectrometer	Size 4.5 mm - 4.5 cm Concentration 0 - 100/m^3	±1 size class	1 size class	• 14 size classes • Sampling rate 100 m^3/km • Alternates with particle camera

Appendix A, continued

Variable	Instrument	Range	Accuracy	Resolution (as recorded)	Notes
Aircraft Motion	Humphrey SA09-D0101-1 Vertically Stabilized Accelerometer	± 2 g's pitch -50° to +50° roll -50° to +50°	0.004 g 0.2° 0.2°	0.00006 g 0.002° 0.002°	
	Rosemount 1301-D-1B Dynamic Pressure	-3 to +3 psi (-20 to +20 kPa)	±0.1%	0.0001 psi (0.0006 kPa)	• Indicated airspeed
	Rosemount 1221-F-2A Dynamic Pressure	-2.5 to +2.5 psi (-18 to +18 kPa)	±0.1%	0.0001 psi (0.0006 kPa)	• Indicated airspeed
	Giannini 45218YE Manifold Pressure	0 to 50 in Hg	±2%	0.008 Hg (0.03 kPa)	• Used in one vertical velocity calculation
	Ball Engineering 101A Variometer	-6000 to +6000 ft/min (-30 to +30 m/s)	±200 ft/min (±1 m/s)	0.2 ft/min (0.001 m/s)	
Aircraft Location	Trimble TNL2000 GPS	(global)	30 m horizontal 100 m vertical	18 m	Trimble GPS not available in 1990. VOR and DME not recorded in 1997.
Electric Field	NMIMT Model E-100 DC Electric Field Meter	top/bot ± 650 wings ± 3200 } kV 5th ± 340 m		(coarse resolution) 0.01 $\frac{kV}{m}$	Hail pod field meter (“5th”) not installed in 1990.
NOTE: Many of these instruments do not behave as ideal instruments. The use of one measure of accuracy over the entire range of measurement is, in many cases, questionable. An accuracy representative of the most useful part of the range is given here.					

.

APPENDIX B Routinely-Computed Parameters

List of Variables Recorded or Routinely Computed
from T-28 Observations

Each different variable in the data stream is indexed with a unique tag number. Those used for either of the deployments are listed here.

Tag	Variable	Remarks
100	**Time**	The T-28 data system is always set to local time, and recorded in a 24-hour format. It is maintained daily within a second of WWV unless otherwise noted.
101	**Dynamic Pressure 1**	
102	**Dynamic Pressure 2**	Both dynamic pressures are read from the same pitot tube line (with the inlet out on the right wing) using two different but nearly identical sensors. [hPa]
103	**Static Pressure 1**	
104	**Static Pressure 2**	Both static pressures are read from the same static pressure line (inlet on the rear fuselage) using two different but nearly identical sensors. [hPa]
105	**Rate of Climb**	The instantaneous rate of change of aircraft altitude, read from a standard aircraft variometer. The recorded data are unfiltered and much noisier than the damped cockpit display. [m s^{-1}]
106	**Rosemount Temperature**	This is static temperature computed from the reading of a standard, deiced, Rosemount aircraft total air temperature probe. It commonly suffers from wetting and reads low in clouds. [°C]
107	**Reverse Flow Temperature**	This is static temperature computed from the reading of a platinum resistance element placed inside a custom-design “reverse-flow” housing. It normally does not get wet in cold clouds or in regions of high precipitation water concentration. Apparently, ice may sometimes build up to such an extent on the housing that temperature readings are affected even though the sensor is not wetted. Its response to

		changes in angle of attack is greater than that of the Rosemount probe. [°C]
108	**Manifold Pressure**	Pressure inside the engine manifold (an indicator of power being developed by the engine) is recorded from a standard aircraft engine pressure sensor. [inches of mercury]
109	**Acceleration**	Vertical acceleration is determined by a Humphrey gyro/accelerometer. [g's]
110	**Pitch**	The accelerometer also gives angle of the fuselage relative to horizontal. [deg]
111	**Roll**	Finally, the accelerometer gives angle of the wings relative to horizontal. Angle is positive for a left bank (left wing down). [deg]
112	**J-W liquid water**	The J-W probe yields concentration of water in clouds represented in droplets less than approximately 30 μm diameter. [g m^{-3}]
113	**VOR**	The VOR gives the direction to the VORTAC (a radio direction-finding beacon used by aircraft) to which it is tuned. [deg]
114	**DME1**	This is distance to the VORTAC to which the #1 DME is tuned. [n mi]
116	**Voltage Regulator**	Voltage of power source for some instruments. [volts]
117	**Heading**	Indicates direction (from magnetic north) towards which the aircraft is heading. [deg]
119	**PMS End Element 1**	Voltage readings of PMS end diodes.
120	**PMS End Element 2**	
121	**Interior Temperature**	Temperature inside the data acquisition system computer in the baggage bay. [°C]
124	**Heater Current**	Total current consumed by de-icing circuits (A).

130	**Event Bits**	Bits corresponding to various events recognized by the data system, including an indication that the system is running, that the in-cloud switch is activated by the pilot (when visually entering cloud), that the foil impactor is running, and that the cockpit voice recorder is activated.
131	**GPS Warning Codes**	Bits corresponding to various status messages from the GPS system. (Not installed in 1990.)
140	**FSSP size counts**	This tag contains information concerning the number of counts in each of the 15 available FSSP size channels. [number per channel per second] (FSSP not installed in 1997.)
141	**FSSP total counts**	The total number of droplets counted by the FSSP during a second.
142	**FSSP average diameter**	The arithmetic average diameter of all droplets recorded during a second. [μm]
143	**FSSP concentration**	The actual concentration of droplets computed from FSSP counts divided by the volume sampled in 1 s ("Standard method"). A rudimentary correction for probe activity is made. [# cm^{-3}]
144	**FSSP Water**	The liquid water concentration computed from the FSSP data for a second ("Standard method"). [g m^{-3}]
145	**FSSP Activity**	The fraction of time the FSSP is active during the current second.
147	**PMS 2DC Shadow Or Count**	The number of times the 2D-C probe was triggered out of its wait state by the passage of a new particle. (Not installed in 1997.)
150	**Hail size counts**	This tag contains information on the number of particles in each of the 14 hail spectrometer size channels. [number per channel per second]
151	**Slow Particle**	The number of particles rejected because they passed through the hail spectrometer too slowly (indicating they were probably water or ice shed from the probe structure rather than airborne hydrometeors). [number per second]

152	**Hail total counts of (150)**	Total number of particles accepted by the hail spectrometer. [number per second]
153	**Hail average diameter**	The average diameter of all particles accepted by the hail spectrometer in the last second. [cm]
154	**Hail concentration**	The computed concentration corresponding to all particles accepted by the hail spectrometer in the last second. [number per cubic meter]
155	**Hail Water**	The mass concentration computed from the observed particle spectrum assuming spherical particles and a bulk particle density of 0.9 grams per cubic centimeter. [grams per cubic meter]
160	**Top Field Mill (low res)**	The electric field indicated by the low sensitivity channel on the field mill mounted in the aircraft canopy looking up. Field mill data are recorded at 20 Hz. [kV m^{-1}] (Recorded as potential gradient and also uncalibrated in 1990, see text.)
161	**Bottom Field Mill (low res)**	The electric field indicated by the low sensitivity channel on the field mill located in the baggage bay door looking down. [kV m^{-1}] (Recorded as potential gradient and also uncalibrated in 1990, see text.)
162	**Left Field Mill (low res)**	The electric field indicated by the low sensitivity channel on the field mill mounted in the left wing tip facing outward. [kV m^{-1}] (Recorded as potential gradient and also uncalibrated in 1990, see text.)
163	**Right Field Mill (low res)**	The electric field indicated by the low sensitivity channel on the field mill mounted in the right wing tip facing outward. [kV m^{-1}] (Recorded as potential gradient and also uncalibrated in 1990, see text.)
164	**Top Field Mill (high res)**	The electric field indicated by the high sensitivity channel on the top field mill. [kV m^{-1}] (Recorded as potential gradient and also uncalibrated in 1990, see text.)
165	**Bottom Field Mill (high res)**	The electric field indicated by the high sensitivity channel on the bottom field mill. [kV m^{-1}] (Recorded as potential gradient and also uncalibrated in 1990, see text.)

166	**Left Field Mill (high res)**	The electric field indicated by the high sensitivity channel on the left field mill. [kV m^{-1}] (Recorded as potential gradient and also uncalibrated in 1990, see text.)
167	**Right Field Mill (high res)**	The electric field indicated by the high sensitivity channel on the right field mill. [kV m^{-1}] (Recorded as potential gradient and also uncalibrated in 1990, see text.)
168	**Fifth Field Mill (low res)**	The electric field indicated by the low sensitivity channel on the fifth field mill, located in one of the hail spectrometer pylons under the left wing. [kV m^{-1}] (Not installed in 1990.)
172	**Latitude**	Computed internally in the GPS receiver. [deg] (Not installed in 1990.)
173	**Longitude**	Also computed internally in the GPS receiver. [deg] (Not installed in 1990.)
174	**Groundspeed**	Computed internally in the GPS receiver (by differentiating the position data with respect to time). [m/s] (Not installed in 1990.)
175	**Ground Track Angle**	The direction towards which the aircraft is moving relative to the ground, with respect to magnetic north. [deg] (Not installed in 1990.)
176	**Magnetic Deviation**	The difference between magnetic north and true north as indicated automatically by the GPS receiver based on the current position. [deg] (Not installed in 1990.)
177	**Time Since Solution**	The time since the GPS was last able to compute an accurate position solution based on a sufficient number of satellites. The GPS updates position based on dead reckoning if it does not have a sufficient number of satellites in view. [s] (Not installed in 1990.)
200	**Date**	As indicated by the data acquisition system computer clock. [yymmdd]
201	**Month**	mm [integer number]

202	**Day**	dd [integer number]
203	**Year**	yy [integer number]
204	**Flight**	A serial number assigned to each T-28 flight beginning with the "first" research flight. (Flight #1 occurred in 1972.)
205	**Altitude**	The altitude in a standard atmosphere corresponding to the recorded static pressure. [m]
206	θ_e	The equivalent potential temperature corresponding to the recorded temperature and assuming saturation with respect to liquid water (should be valid in-cloud). [K]
207	**Saturation Mixing Ratio**	The mixing ratio of water vapor corresponding to saturation with respect to liquid water at the recorded temperature. [g kg^{-1}]
208	**Point dz/dt**	The rate of change of altitude of the aircraft computed by differentiating the pressure altitude with respect to time. This represents an independent estimate of the rate of climb to be compared to tag 105. [m s^{-1}]
209	**Indicated Air Speed**	What the airspeed would be if the aircraft were flying at sea level and indicating the observed dynamic pressure. [m s^{-1}]
210	**Updraft (uncorrected)**	The estimated upward speed of the air relative to the ground computed from changes in the aircraft altitude and other factors, but not corrected for horizontal aircraft acceleration. [m s^{-1}]
211	**Calculated TAS**	The true speed of the aircraft relative to the air computed from the observed dynamic and static pressures, and temperature. [m s^{-1}]
212	**Updraft Correction Factor**	A correction to tag 210, the simple (uncorrected) updraft calculation, that accounts for horizontal accelerations of the aircraft. [m s^{-1}]
213	**Cooper Updraft**	The sum of the uncorrected updraft and the correction factor. [m s^{-1}]

214	**Kopp Updraft**	An updraft calculated somewhat differently than the Cooper updraft [Kopp, 1985]. In most situations, it yields a less noisy and more physically plausible updraft result for the T-28 than the Cooper method. [m s^{-1}]
216	**Turbulence**	The turbulent energy dissipation rate estimated from observed fluctuations in true airspeed. [$cm^{2/3}$ s^{-1}]
217	**Air Density**	Computed from the recorded temperature and static pressure. [kg m^{-3}]
218	**J-W Mixing Ratio**	The mixing ratio of cloud water per unit mass of dry air based on the J-W reading and computed air density. [g kg^{-1}]
219	**FSSP Mixing Ratio**	The mixing ratio of cloud water per unit mass of dry air calculated from the FSSP water concentration. [g kg^{-1}] (Not installed in 1997.)
220	**Hail Mixing Ratio**	The mixing ratio of hail mass per unit mass of dry air based on the computed hail water and air density. [g kg^{-1}] (Not installed in 1997.)
260	**Ambient Vert Electric Field**	The component of the ambient electric field that is vertical in the aircraft frame of reference. Positive means a positive test charge would drift upward relative to the aircraft in the field. [kV m^{-1}] (Recorded as potential gradient and uncalibrated in 1990.)
261	**Plane Vert Electric Field**	The field due to charge on the aircraft, computed by summing the readings of the top and bottom mill and normalizing based on self-charging tests. Positive means a positive test charge would be repelled away from the aircraft due to its charge. [kV m^{-1}] (Recorded as potential gradient and uncalibrated in 1990.)
262	**Ambient Hor Electric Field**	The ambient field oriented perpendicular to the aircraft along the wings, positive meaning a positive test charge would drift to the right in the field. [kV m^{-1}] (Recorded as potential gradient and uncalibrated in 1990.)

263	**Plane Hor Electric Field**	The field due to charge on the aircraft, computed by summing the wingtip mill readings and normalizing. Positive means a positive charge would be repelled away from the aircraft due to its charge. [kV m^{-1}] (Recorded as potential gradient and uncalibrated in 1990.)
264	**Ambient Vert Field (roll cor)**	The component of the ambient field that is truly vertical with respect to earth coordinates. [kV m^{-1}] (Recorded as potential gradient and uncalibrated in 1990.)
265	**Ambient Hor Field (roll cor)**	The component of the ambient field perpendicular to the aircraft path and truly horizontal with respect to earth coordinates. [kV m^{-1}] (Recorded as potential gradient and uncalibrated in 1990.)
272	**Latitude (deg)**	GPS coordinates broken into separate degree and minute components. (GPS not available in 1990.)
273	**Latitude (min)**	GPS coordinates broken into separate degree and minute components. (GPS not available in 1990.)
274	**Longitude (deg)**	GPS coordinates broken into separate degree and minute components. (GPS not available in 1990.)
275	**Longitude (min)**	GPS coordinates broken into separate degree and minute components. (GPS not available in 1990.)
276	**Ground Track Angle (True N)**	The direction of motion relative to the ground with respect to true north, derived from the GPS ground track angle with respect to magnetic north. (GPS not available in 1990.)

APPENDIX C Details of 1990 Intercomparison Passes

The results for each of ten passes, conducted on the 24th and 25th of July, are discussed herein. Table C-1 summarizes the figures referenced by the discussion.

Table C-1 Summary of 1990 Intercomparison Plots

Fig. #				
24 Jul 90	25 Jul 90	Pass	X-axis	Y-axis
C1 a,b	C7 a,b	1	Time (hr mn sec)	y, z comp (kV/m)
C2 a,b	C8 a,b	2	"	"
C3 a,b	C9 a,b	3	"	"
C4 a,b	C10 a,b	4	"	"
	C11 a,b	5	"	"
	C12 a,b	6	"	"
C5 a-d	C13 a-f	1-4 (24 Jul 90 1-6 (25 Jul 90)	E_{yo} (kV/m)	E_y (kV/m
C6 a-d	C14 a-f	"	E_{zo} (")	E_z (")

The *Y* and *Z* components of the meter readings are in the aircraft frame of reference, in which the *Y* direction is along the wing span (positive leftward) and the *Z* direction is positive upward and orthogonal to *Y*. The *X* component was not reported for either system. On the T-28 and SPTVAR, the *Y* and *Z* components (E_y and E_z for T-28 and E_{yo} and E_{zo} for SPTVAR) are computed using (2) for the T-28 system, and (10) from Winn (1993) for the SPTVAR system.

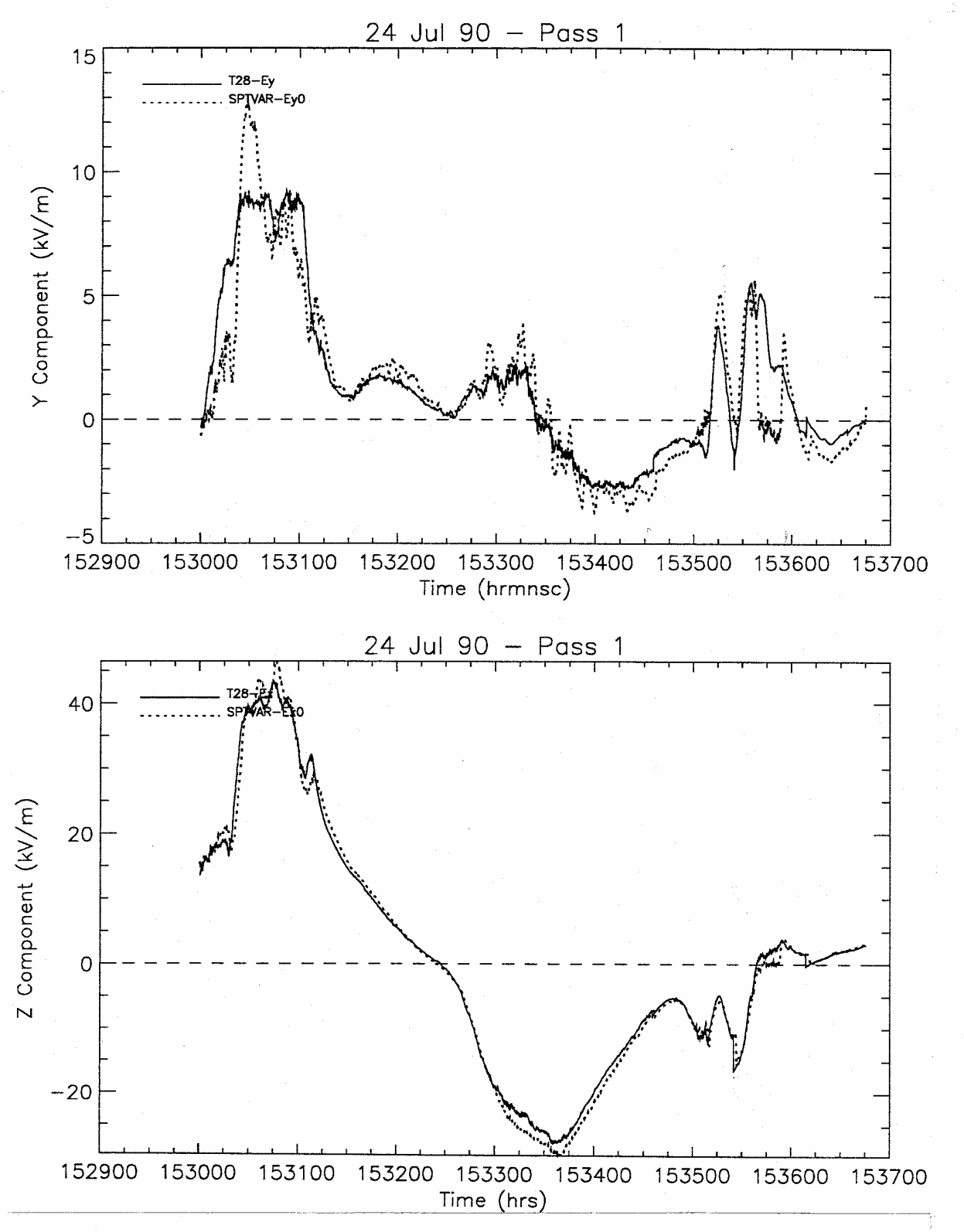

Fig. C1. Comparison of SPTVAR and T-28 E_y and E_z components on Pass 1, 24 July 1990.

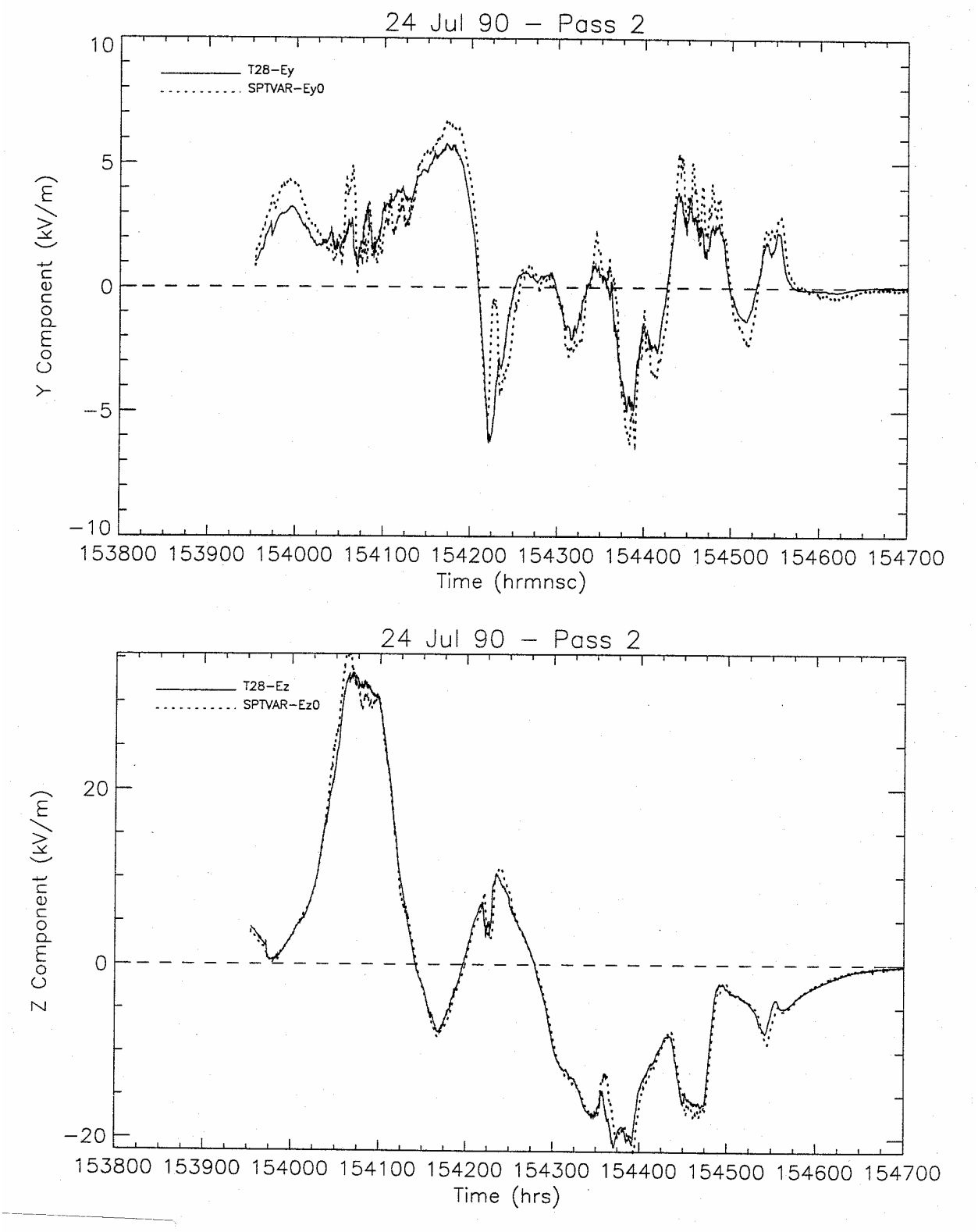

Fig. C2. Comparison of SPTVAR and T-28 E_y and E_z components on Pass 2, 24 July 1990.

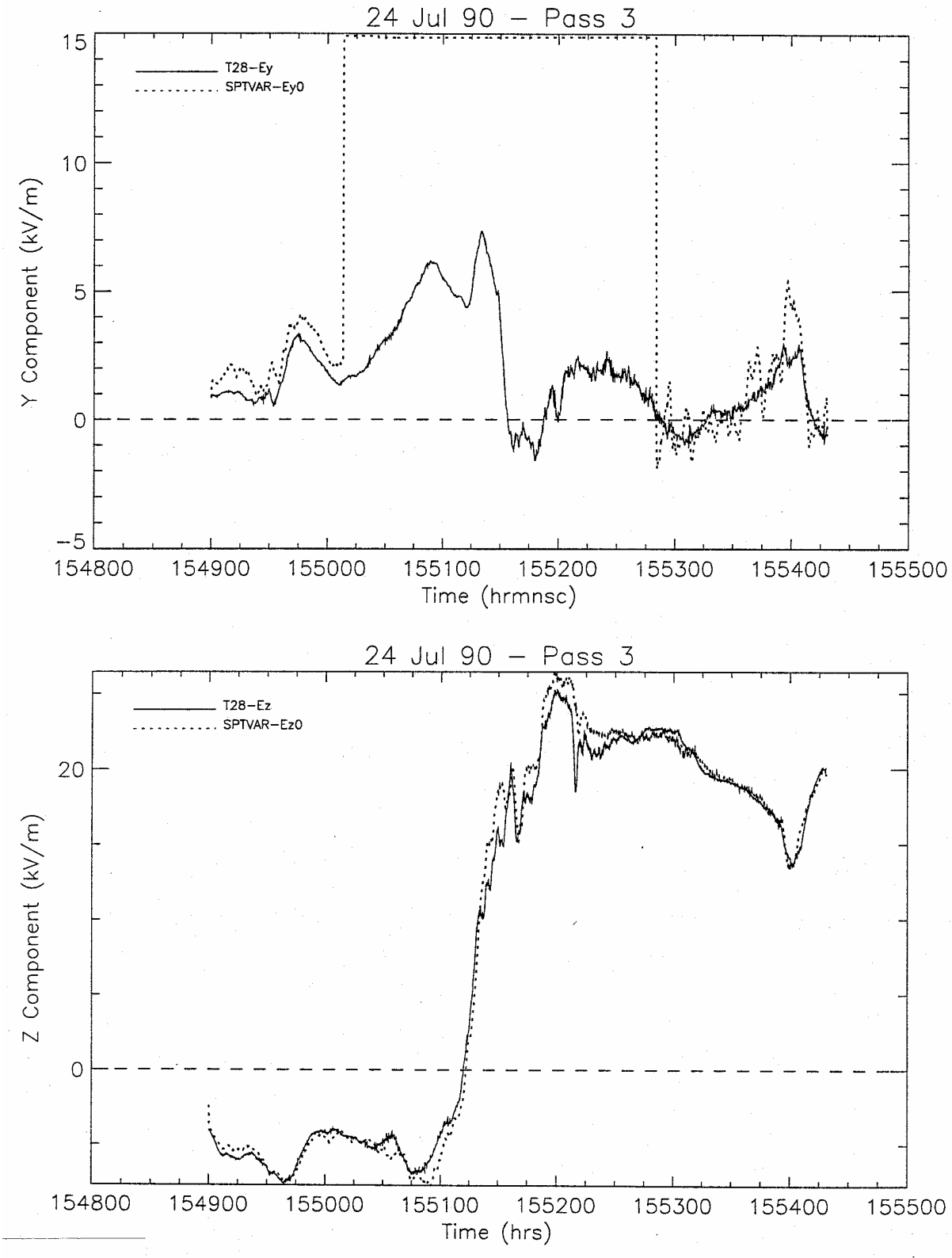

Fig. C3. Comparison of SPTVAR and T-28 E_y and E_z components on Pass 3, 24 July 1990.

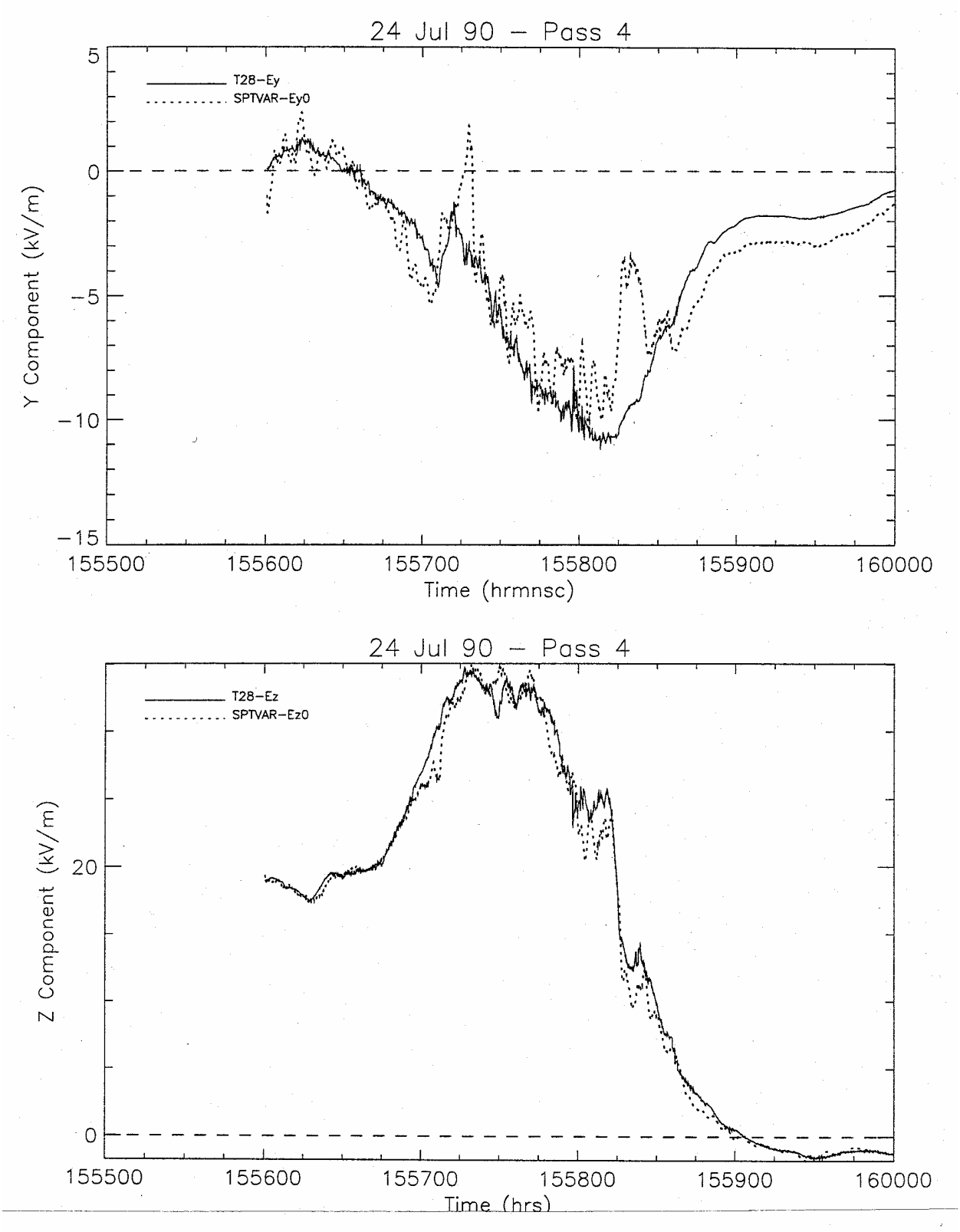

Fig. C4. Comparison of SPTVAR and T-28 E_y and E_z components on Pass 4, 24 July 1990.

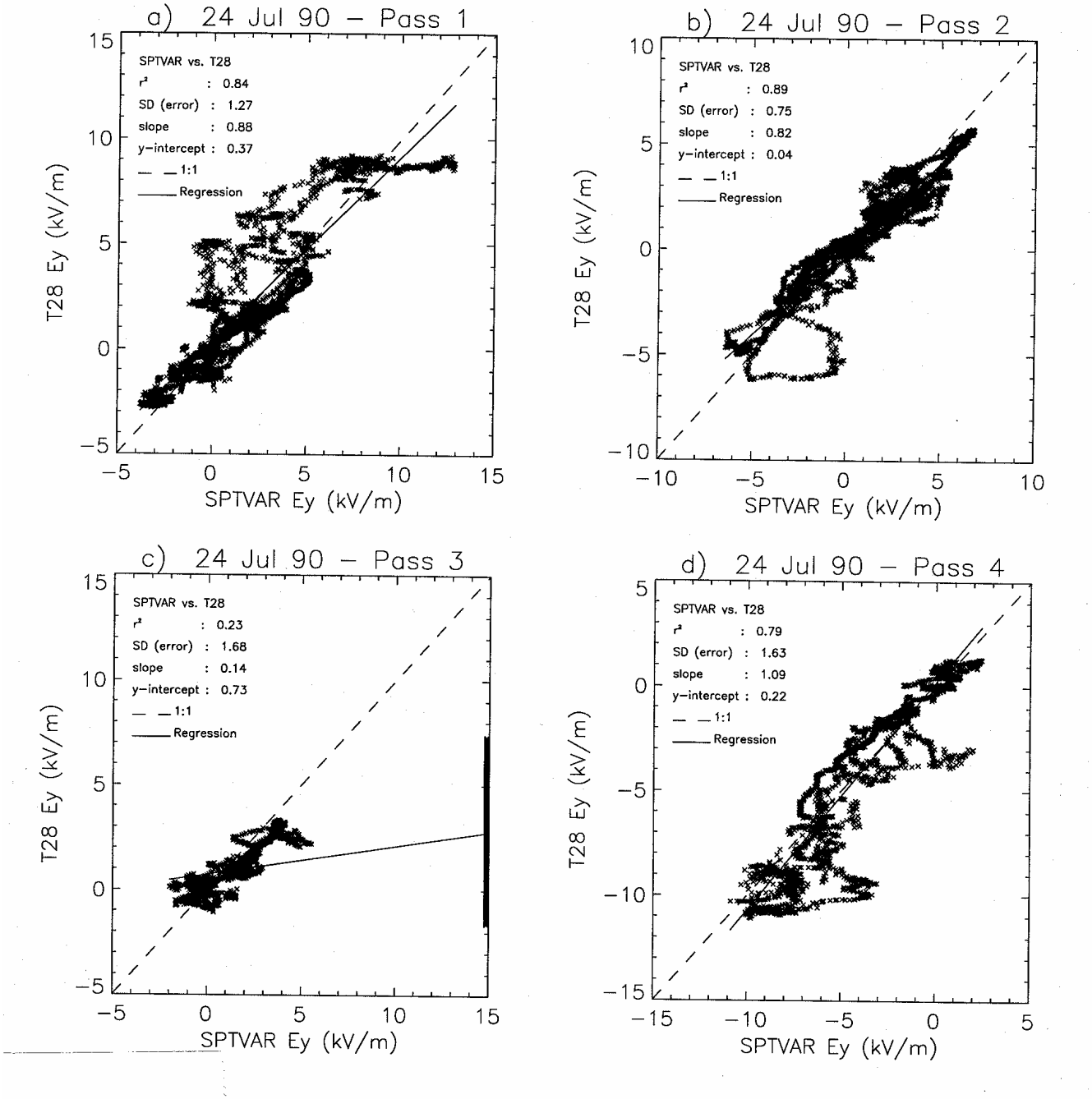

Fig. C5. Regression results comparing SPTVAR and T-28 E_y for 4 passes, 24 July 1990.

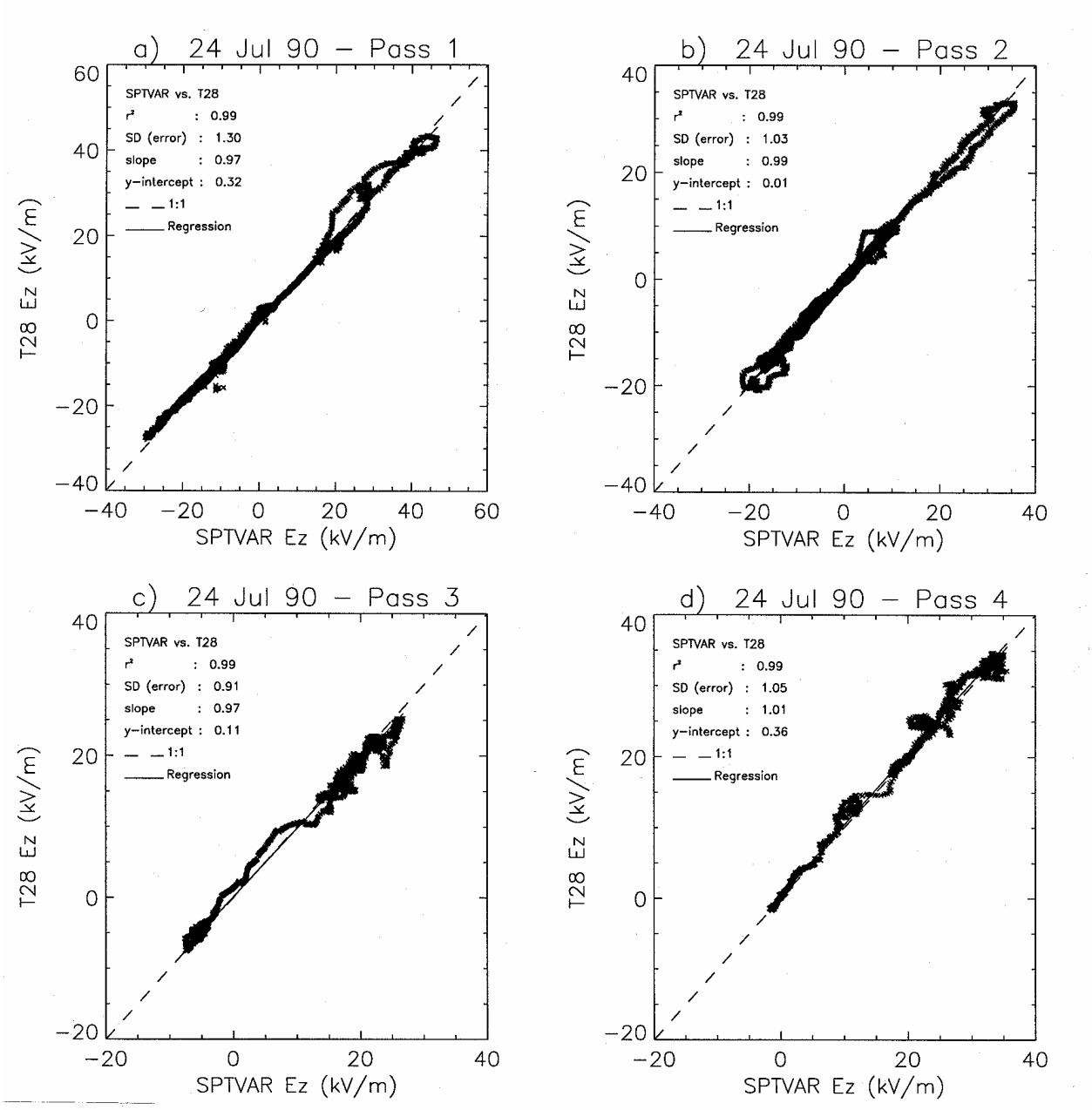

Fig. C6. Regression results comparing SPTVAR and T-28 E_z for 4 passes, 24 July 1990.

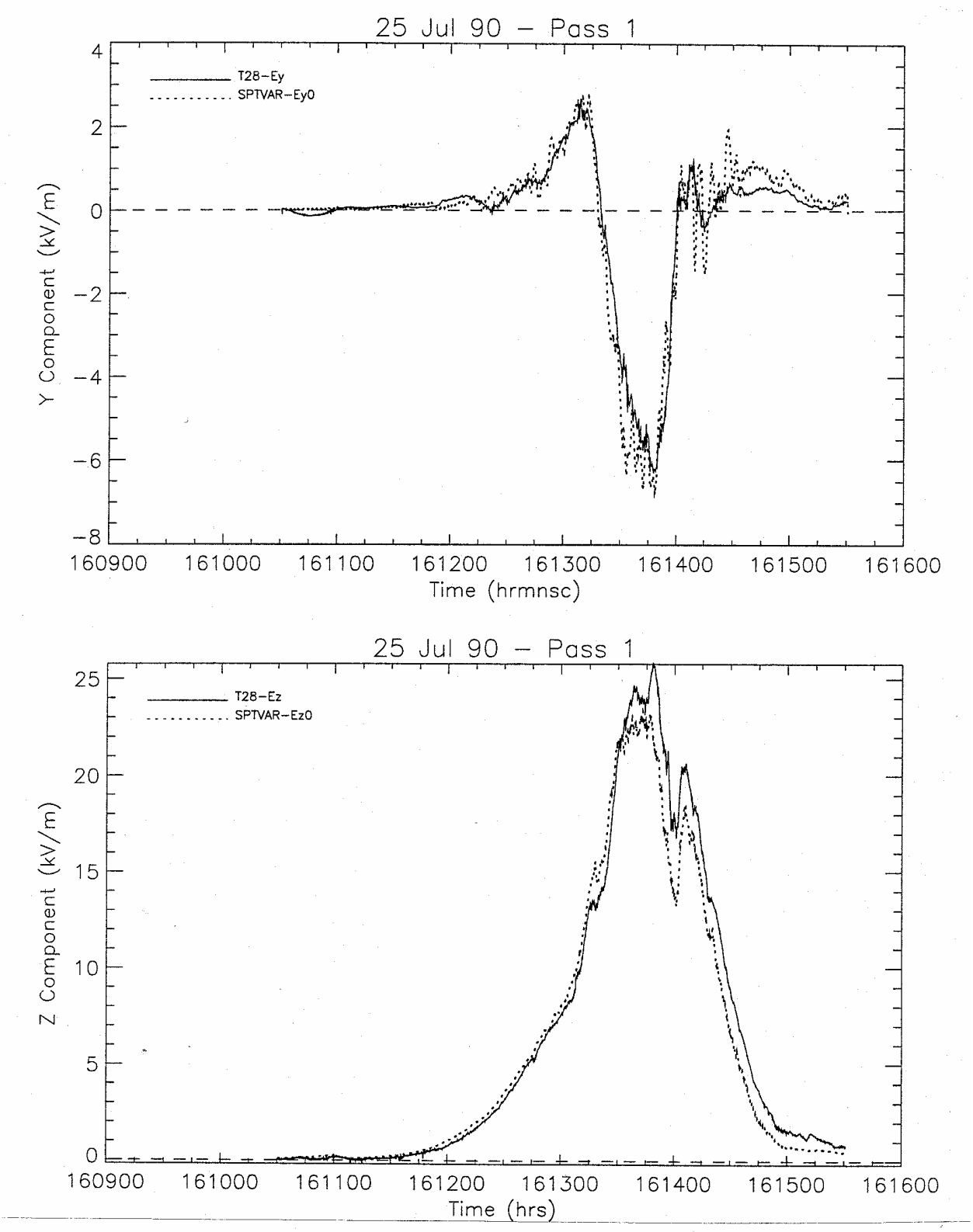

Fig. C7. Comparison of SPTVAR and T-28 E_y and E_z components on Pass 1, 25 July 1990.

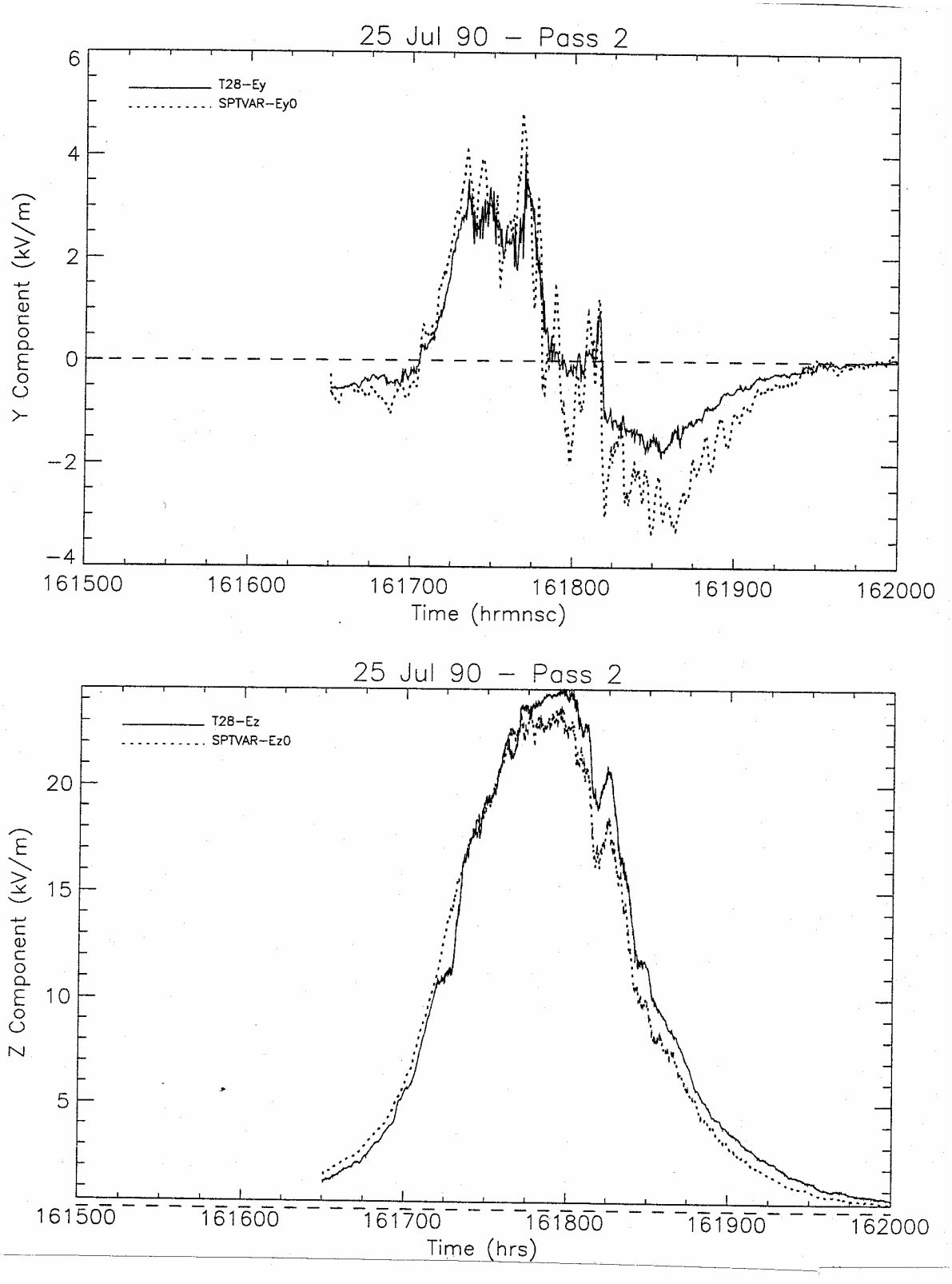

Fig. C8. Comparison of SPTVAR and T-28 E_y and E_z components on Pass 2, 25 July 1990.

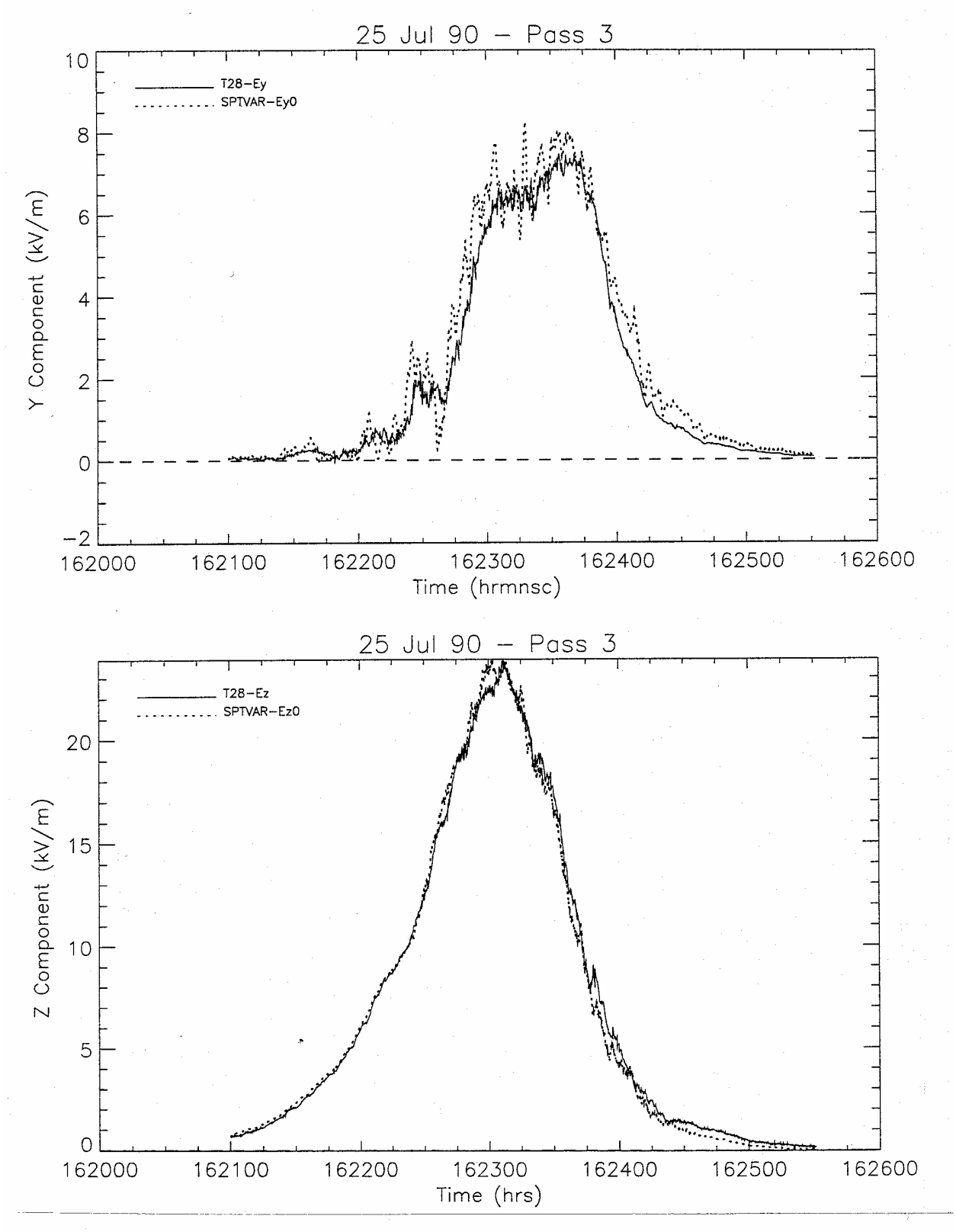

Fig. C9. Comparison of SPTVAR and T-28 E_y and E_z components on Pass 3, 25 July 1990.

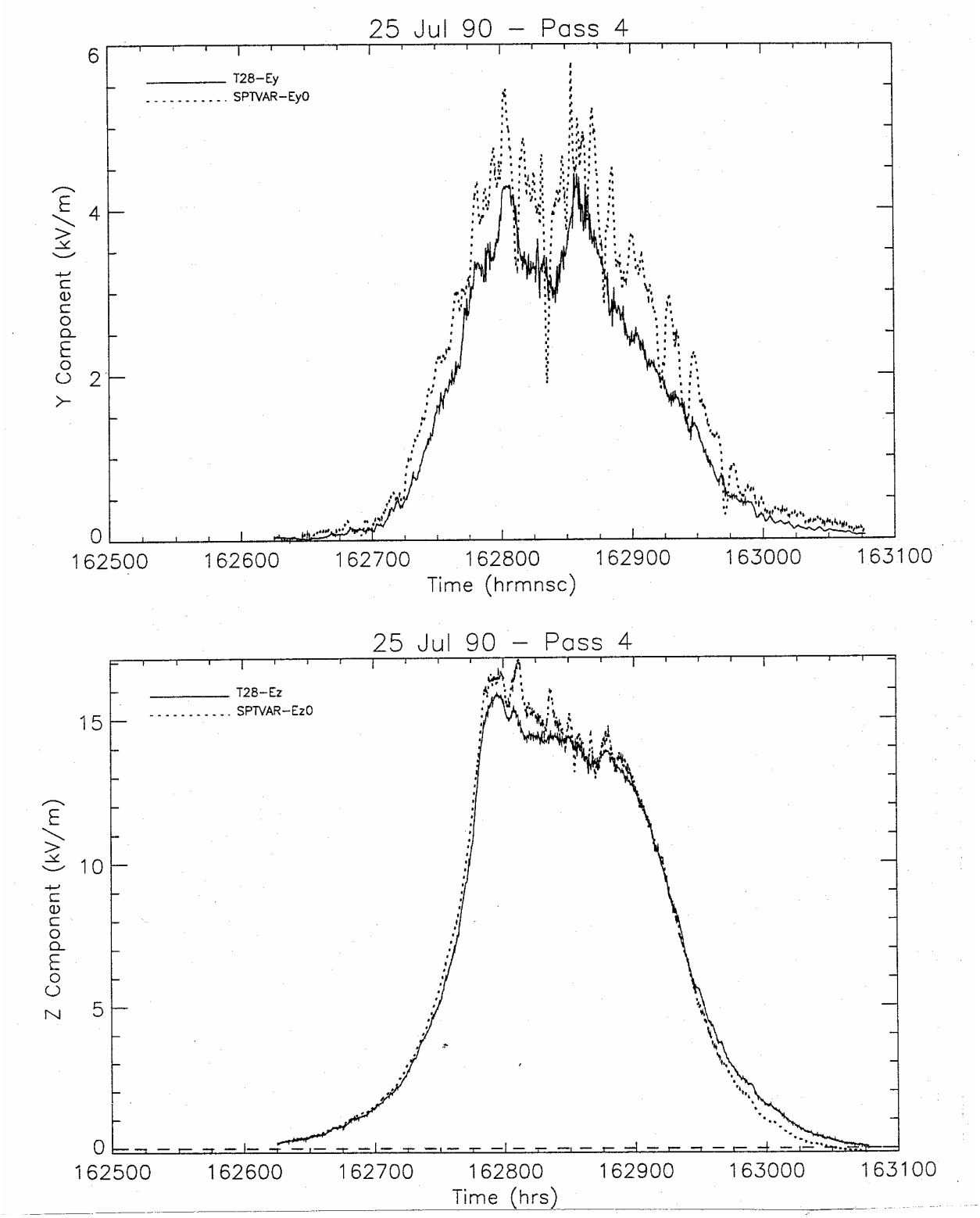

Fig. C10. Comparison of SPTVAR and T-28 E_y and E_z components on Pass 4, 25 July 1990.

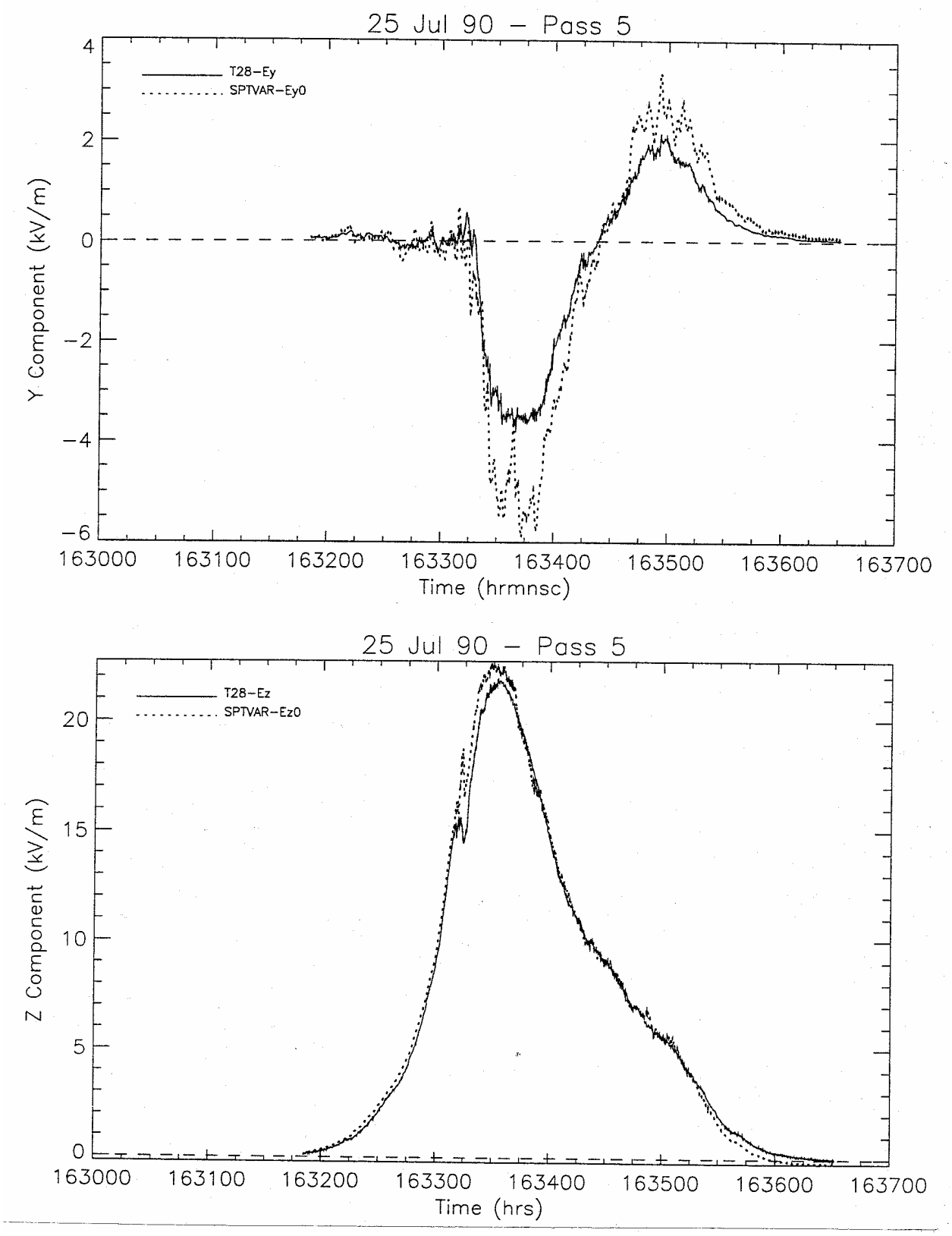

Fig. C11. Comparison of SPTVAR and T-28 E_y and E_z components on Pass 5, 25 July 1990.

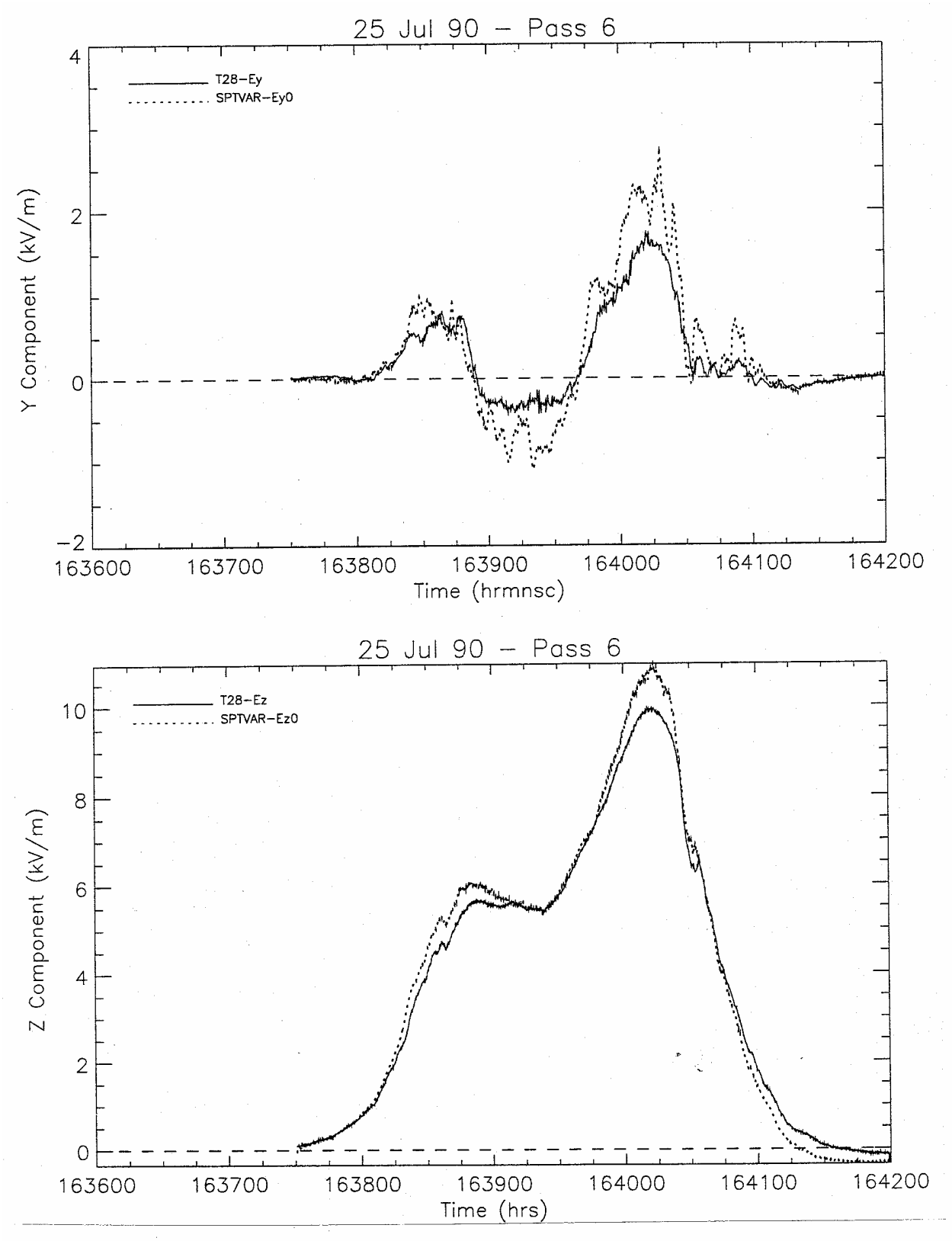

Fig. C12. Comparison of SPTVAR and T-28 E_y and E_z components on Pass 6, 25 July 1990.

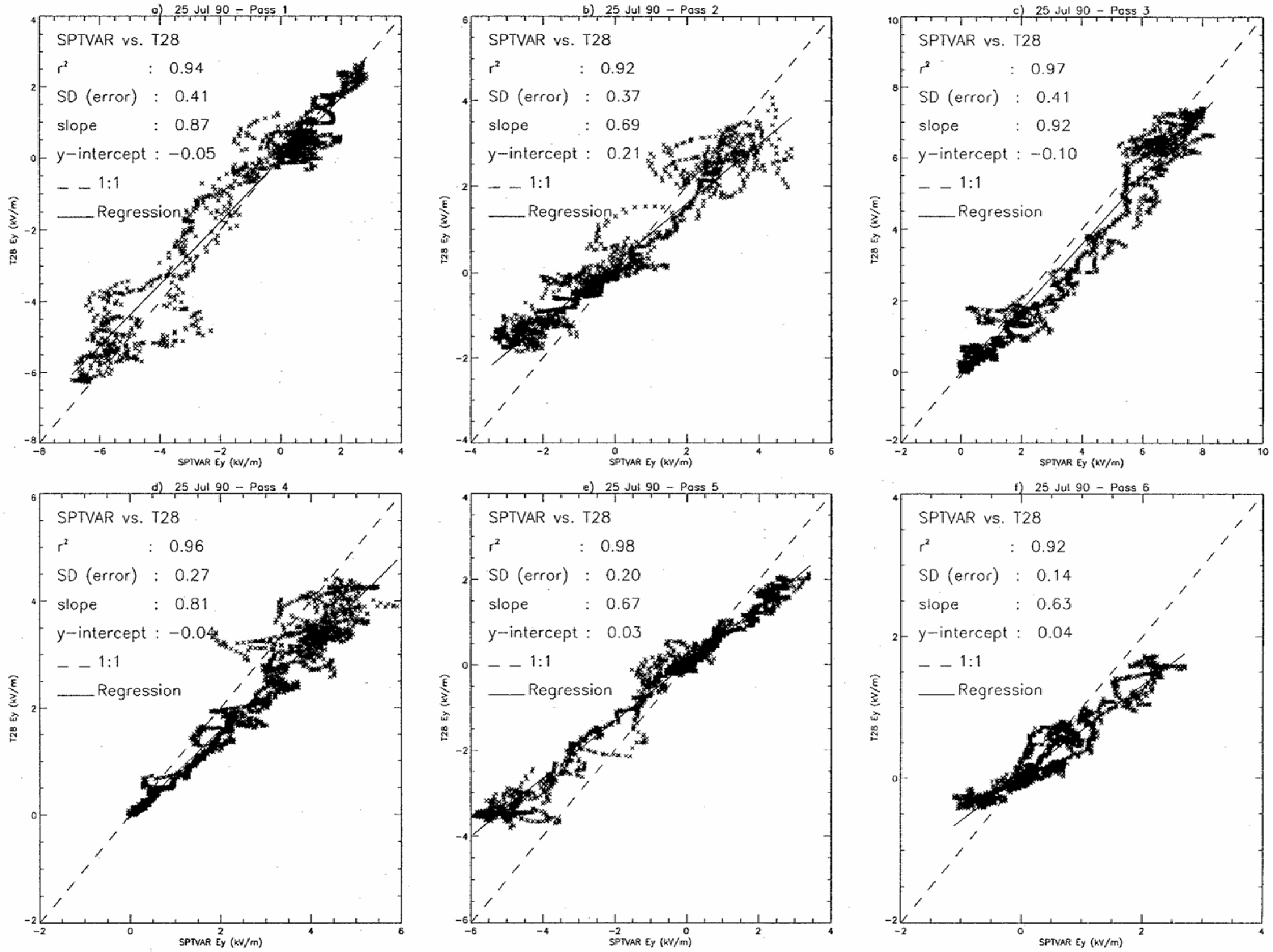

Fig. C13. Regression results comparing SPTVAR and T-28 E_y for 6 passes, 25 July 1990.

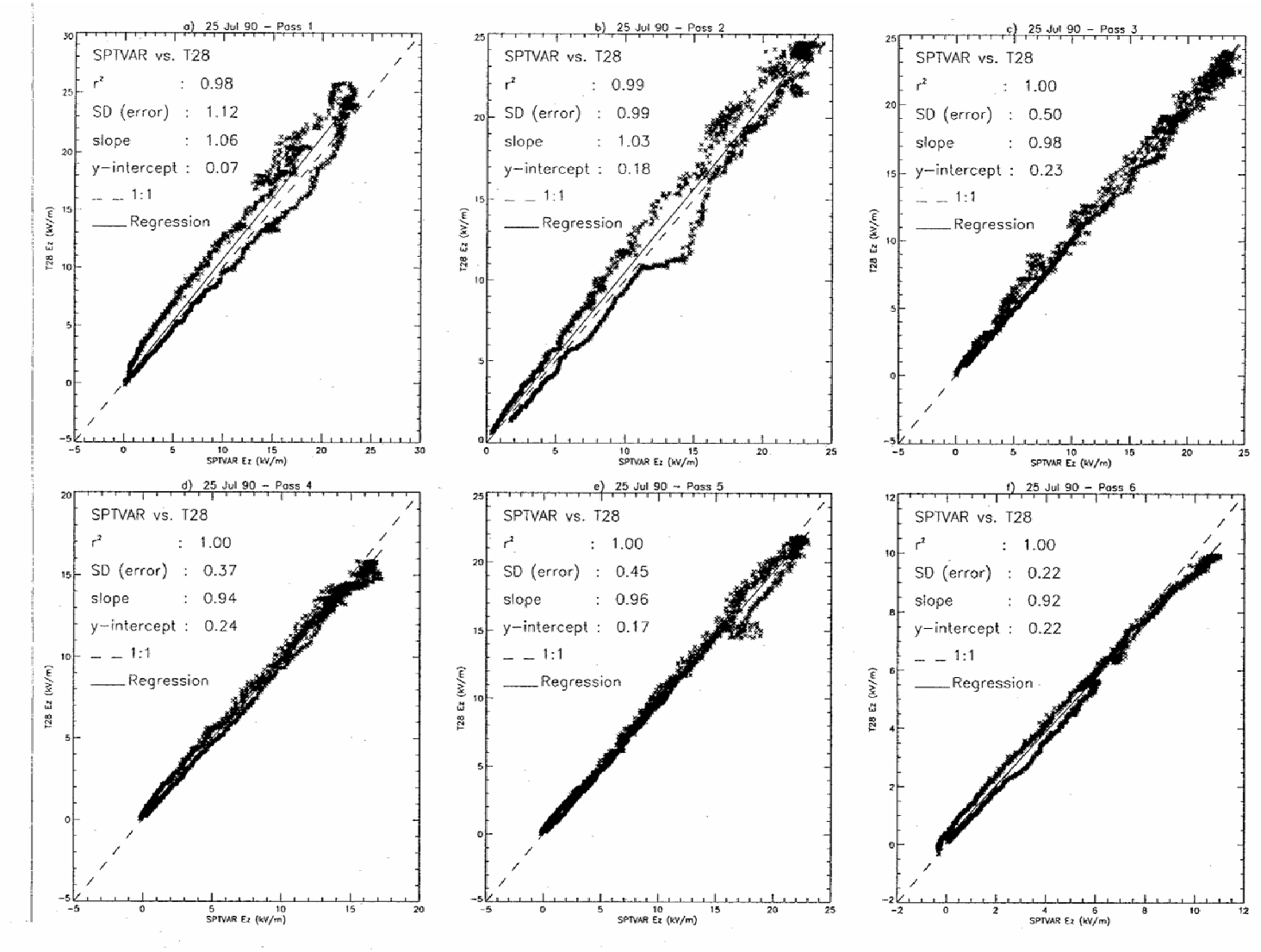

Fig. C14. Regression results comparing SPTVAR and T-28 E_z for 6 passes, 25 July 1990.

Pass 1 (24 Juy 1990)

Y Component

Time Sequence (Fig. C1a)

Significant differences in the measurements between the two systems are noted near the beginning of the pass (153000-153100) in which the T-28 system peaks at 9 kV/m and the SPTVAR system peaks at nearly 13 kV/m. The T-28 system response shows evidence of saturation or effects of ions, with its clipped appearance. After 153100, both systems indicate very similar trends until 153530, in which the T-28 indicates values somewhat less than the SPTVAR system. For about 15 seconds, just before 153600, the two systems differ significantly, and then fall into alignment again with the T-28 indicating less than the SPTVAR.

Regression (Fig. C5a)

The r^2 value is 0.84, indicating good correlation between the measurements. The slope is 0.88, indicating the T-28 system yields values lower, on the average, than the SPTVAR system.

Z Component

Time sequence (Fig. C1b)

Both systems indicate virtually the same values over the entire pass with the exception of some small differences at local maxima (e.g. 153045 and 153300-153400). This is not unexpected, as the meters from which the *z*-component is computed are on the fuselage on both aircraft, and (2), from which the T-28 E_z is computed, was derived specifically by requiring T-28 E_z to agree with SPTVAR E_{zo}.

Regression (Fig. C6a)

Very good regression results with $r^2 = 0.99$ and slope = 0.97.

Pass 2 (24 July 1990)

Y Component

Time sequence (Fig. C2a)

Both systems indicate very similar trends in a field that varies between positive and negative, the most notable difference being the T-28 measurements are consistently lower in magnitude compared to those of the SPTVAR (except near 154215).

Regression (Fig. C5b)

The regression results are much like the previous pass in which $r^2 = 0.89$ and the slope = 0.82. The slope value is consistent with Pass 1 results in that the T-28 system measures values lower, on average, than the SPTVAR system.

Z Component

Time Sequence (Fig. C2b)

Both systems indicate very good agreement with a few minor differences located at local maxima and minima.

Regression (Fig. C6b)

Again, as in the Z component of Pass 1, the regression results indicate very good agreement between the two systems ($r^2 = 0.99$ and slope = 0.99).

Pass 3 (24 July 1990)

Y Component

Time Sequence (Fig. C3a)

An apparent dropout in the SPTVAR signal occurs from 155010 to 155250. Before the dropout, the two systems show similar trends, but the T-28 is measuring about 1 kV/m lower than the SPTVAR. After the dropout, the SPTVAR shows more transients, or high frequency content, than does the T-28 system. Near 155400, the T-28 indicates values about 2 kV/m lower than the SPTVAR system.

Regression (Fig. C5c)

The dropout in the SPTVAR signal invalidates the regression statistics. The scatter about the 1:1 line, exclusive of the dropout interval, is low.

Z Component

Time Sequence (Fig. C3b)

There is generally good agreement between the two systems. The T-28 result is slightly lower than the SPTVAR result for the higher values of E_z encountered between 155115 and 155300.

Regression (Fig. C6c)

As in the previous two passes, the regression results are very good ($r^2 = 0.99$, slope = 0.97).

Pass 4 (24 July 1990)

Y Component

Time Sequence (Fig. C4a)

In the previous three passes, the T-28 consistently measured magnitudes lower than the SPTVAR. This is true here in the beginning of the pass, from 155600 to 155710 and, at the end of the pass, from 155830 to 160000; however, in the middle, from 155710 to 155830, the T-28 generally indicates magnitudes higher than the SPTVAR.

Regression (Fig. C5d)

The two systems indicate a relatively high correlation in their measurements with $r^2 = 0.79$. The intervals over which the T-28 measured values higher than the SPTVAR system apparently dominated those of the converse, resulting in a slope greater than 1.0 (1.09).

Z Component

Time Sequence (Fig. C4b)

Both systems indicate a large positive field over most of the pass that peaks near 35 kV/m. The agreement is very good with some small 2-3 kV/m differences occurring near 155700, 155800, and 155815.

Regression (Fig. C6d)

As in Passes 1-3, the regression statistics indicate very good results where $r^2 = 0.99$ and slope = 1.01.

Pass 1 (25 July 1990)

Y Component

Time Sequence (Fig. C7a)

From the beginning of the pass to about 161330, both systems show good agreement. Subsequently, both systems show similar trends, but the T-28, for the most part, indicates magnitudes less than the SPTVAR system.

Regression (Fig. C13a)

The correlation between the two systems is high with $r^2 = 0.94$. The lower magnitudes determined from the T-28 system over the last half of the pass caused the slope to be less than 1.0 (0.87).

Z Component

Time Sequence (Fig. C7b)

Similar characteristics are noted here as in the Y component. That is, there is good agreement up to 161330; however, over the remainder of the pass, the T-28 indicates magnitudes 2-3 kV/m higher than the SPTVAR system.

Regression (Fig. C14a)

The correlation value is high ($r^2 = 0.98$). The higher values measured by the T-28 system over the last half of the pass are reflected in the greater-than-one slope value of 1.06.

Pass 2 (25 July 1990)

Y Component

Time Sequence (Fig. C8a)

Except for a short 30-second interval at the beginning of the pass, the T-28 E_y magnitudes are consistently lower than those determined from the SPTVAR system, in both positive and negative fields.

Regression (Fig. C13b)

The regression statistics indicate high correlation between the two systems (r^2 = 0.92). Since the T-28 measures magnitudes consistently lower than the SPTVAR, over most of the pass, the slope is 0.69, much less than one.

Z Component

Time Sequence (Fig. C8b)

Over the first part of the pass (to about 161720), the T-28 indicates magnitudes 1-2 kV/m lower than the SPTVAR system. Subsequently, to the end of the pass, the T-28 indicates magnitudes 1-2 kV/m higher than the SPTVAR system.

Regression (Fig. C14b)

The correlation coefficient is very high (r^2 = 0.99). The interval over which the T-28 measures values higher than the SPTVAR system, dominate slightly, manifesting a slope in the regression line of 1.03.

Pass 3 (25 July 1990)

Y Component

Time Sequence (Fig. C9a)

Both systems respond in a similar manner to a positive E_y field that peaked near 8 kV/m. As in many of the previous passes, the T-28 measures consistently lower magnitudes than the SPTVAR system.

Regression (Fig. C13c)

The measurements are highly correlated (r^2 = 0.97). The slope of 0.92 bears out the observation in the time sequence that the T-28 measures consistently lower magnitudes than the SPTVAR system.

Z Component

Time Sequence (Fig. C9b)

Both systems show very good agreement with differences being less than 1 kV/m.

Regression (Fig. C14c)

The regression statistics are very good with r^2 = 1.00 and slope = 0.98.

Pass 4 (25 July 1990)

Y Component

Time Sequence (Fig. C10a)

This is much like the previous pass (Pass 3). That is, both systems indicate a positive E_y field in which the T-28 system measures magnitudes lower than the SPTVAR system.

Regression (Fig. C13d)

The correlation coefficient is very high ($r^2 = 0.96$). The low slope value of 0.81 bears out the observation in the time sequence; that is, the T-28 measures magnitudes lower than the SPTVAR system.

Z Component

Time Sequence (Fig. C10b)

Over most of the pass, the two systems show very good agreement. Around 162800, for about 30 seconds, the T-28 measures values 1-2 kV/m lower than the SPTVAR system. The clipped, noisy character of the T-28 peak suggests the effects of ions streaming over one or both of the fuselage meters on the T-28.

Regression (Fig. C14d)

The correlation coefficient is very high ($r^2 = 1.00$). The slope of the regression line is slightly less than one (0.94).

Pass 5 (25 July 1990)

Y Component

Time Sequence (Fig. C11a)

Again, the T-28 is consistently measuring values less than the SPTVAR system. The SPTVAR signal also indicates more high frequency characteristics in the field, which could be noise.

Regression (Fig. C13e)

The measurements correlate very well ($r^2 = 0.98$). However, the lower measurements of the T-28, with respect to the SPTVAR system, produce a regression line with slope much less than one (0.67).

Z Component

Time Sequence (Fig. C11b)

From 163310 to 163345, the T-28 indicates values 1-2 kV/m less than the SPTVAR system. Over the rest of the pass, the agreement between the two systems is very good, with differences much less than 1 kV/m.

Regression (Fig. C13e)

The measurements are highly correlated ($r^2 = 1.00$) and the regression line has a slope slightly less than one (0.96).

Pass 6 (25 July 1990)

Y Component

Time Sequence (Fig. C12a)

Same comments as Y component for previous pass (Pass 5).

Regression (Fig. C13f)

The measurements correlate well ($r^2 = 0.92$). However, once again, the slope of the regression line is much less than one (0.63).

Z Component

Time Sequence (Fig. C12b)

Over several intervals, the T-28 measures magnitudes 1-2 kV/m lower than the SPTVAR (163815-163900, 163950-164010, and for about 5 seconds around 164030). From 164040, till the end of the pass, the T-28 measures higher magnitudes.

Regression (Fig. C13f)

The measurements correlate very well ($r^2 = 1.00$). The intervals in which the T-28 is measuring values lower than the SPTVAR system produce a slope somewhat less than one (0.92).

APPENDIX D Details of 1997 Intercomparison Passes

The results for each pass during the 1997 intercomparisons are discussed in detail. Table D-1 summarizes the figures that support each discussion.

Table D-1 Summary of 1997 Intercomparison Plots

Figure #		Pass	X axis	Y axis
Flt. 694	Flt. 695			
D1a-c	D20 a-c[1]	1	Time (hr mn sc)	*X*, *Y*, *Z* components (kV/m)
D2 a-c	D21 a-c	2	"	"
D3 a-c	D22 a-c	3	"	"
D4 a-c	D23 a-c	4	"	"
D5 a-c	D24 a-c	5	"	"
D6 a-c	D25 a-c	6	"	"
D7 a-c	D26 a-c	7	"	"
D8 a-g[2]	D27 a-g[2]	1-7	E_{xn} (kV/m)	E_{qy}, E_{xo} (kV/m)
D9 a-g[2]	D28 a-g[2]	1-7	E_{yn} (kV/m)	E_y, E_{yo} (kV/m)
D10 a-g[2]	D29 a-g[2]	1-7	E_{zn} (kV/m)	E_z, E_{zo} (kV/m)
D11 a-g[2]	D30 a-g[2]	1-7	EW Range (km)[3]	NS Range (km)[3]
D12 a-g[2]	D31 a-g[2]	1-7	EW Range (km)[4]	Alt (m ASL)[4]
D13 a-c[5]	D32 a-c[5]	1	Time	Pitch, Roll, Heading
D14 a-c	D33 a-c	2	"	"
D15 a-c	D34 a-c	3	"	"
D16 a-c	D35 a-c	4	"	"
D17 a-c	D36 a-c	5	"	"
D18 a-c	D37 a-c	6	"	"

D19 a-c	D38 a-c	7	“	“

(1) a, b, and c correspond to X, Y, and Z components, respectively

(2) a-g correspond to Passes 1-7, respectively

(3) X and Y components of electric field are superimposed on horizontal projection of trajectory

(4) X and Z components of electric field are superimposed on vertical profile of trajectory

(5) a-c correspond to pitch, roll, and heading, respectively

The *X, Y,* and *Z* components of the electric field determined from meter readings using eq. (2) are in the aircraft frame of reference, in which the *X* direction is along the fuselage (longitudinal, positive forward), the *Y* direction is along the wing span (positive to the left) and orthogonal to *X*, and the *Z* direction is positive upward and orthogonal to both *X* and *Y*. In the T-28 system, the *X* component is labeled as a measurement of aircraft charge (E_{qy}). E_{qy} is a weighted sum of the wingtip meter readings (see eq (2)). In Section 4.4 it has been shown that the *X* component of the electric field and E_{qy} are highly correlated in clear air and when charge on the aircraft is small, as it usually is.

In the SPTVAR systems, the *X, Y,* and *Z* components of the electric field from the older system are indicated as E_{x0}, E_{y0}, and E_{z0}, respectively, and from the newer system as E_{xn}, E_{yn}, and E_{zn}, respectively. Figures D1-D7 and D20-26 indicate times in which precipitation was present by a “P” along the upper edge of the plot. These symbols indicate times when the meter readings are possibly less accurate as the hydrometeors exchange charge with the plane during impact.

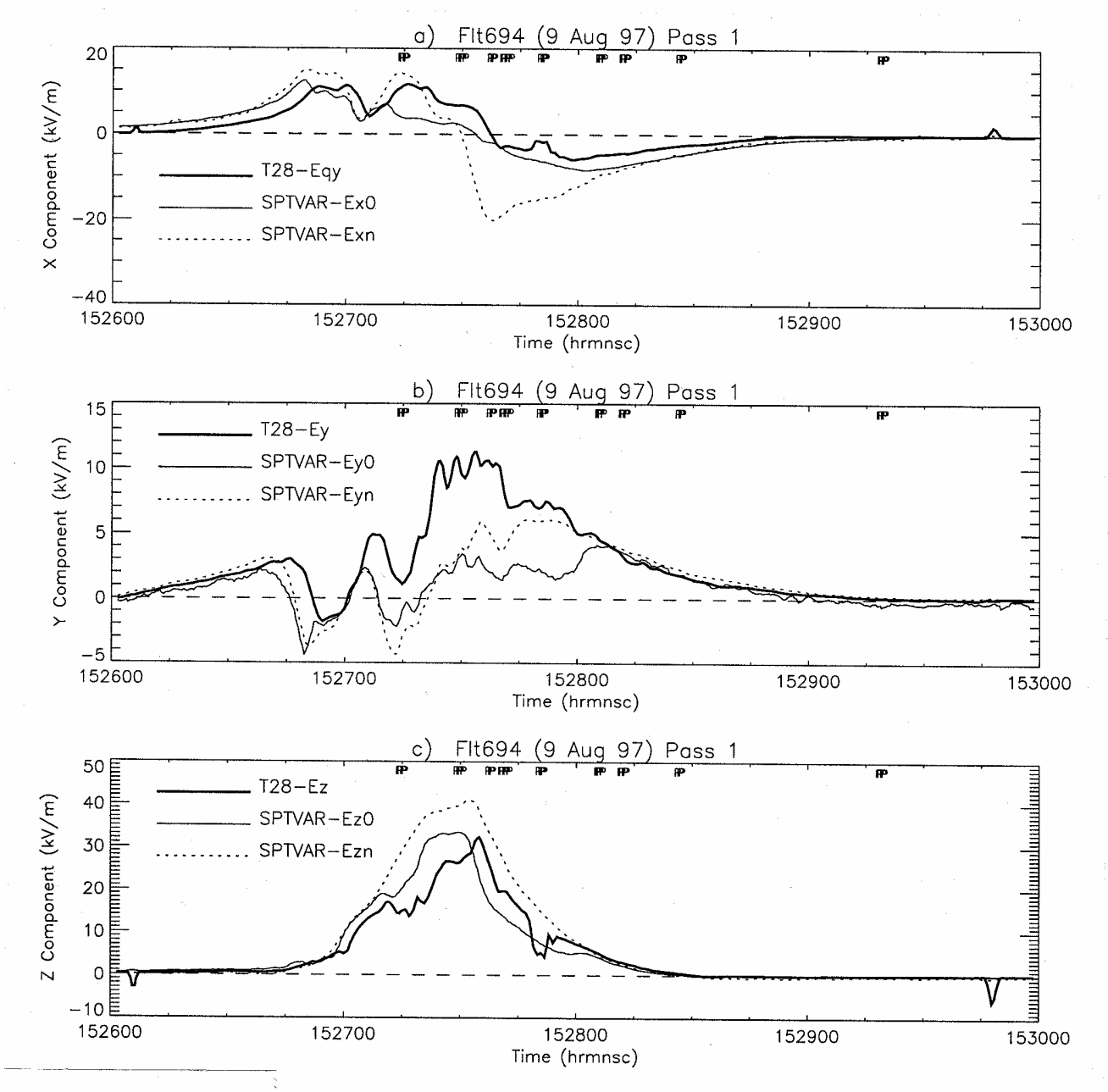

Fig. D1. Electric field components during the 1st intercomparison leg on 9 Aug 1997, as deduced using standard processing algorithms. Components E_{qy}, E_y, and E_z are from the T-28. Components E_{x0}, E_{y0}, and E_{z0} are from the old fuselage-mounted SPTVAR field meter system. Components E_{xn}, E_{yn}, and E_{zn} are from the new SPTVAR pod meter system.

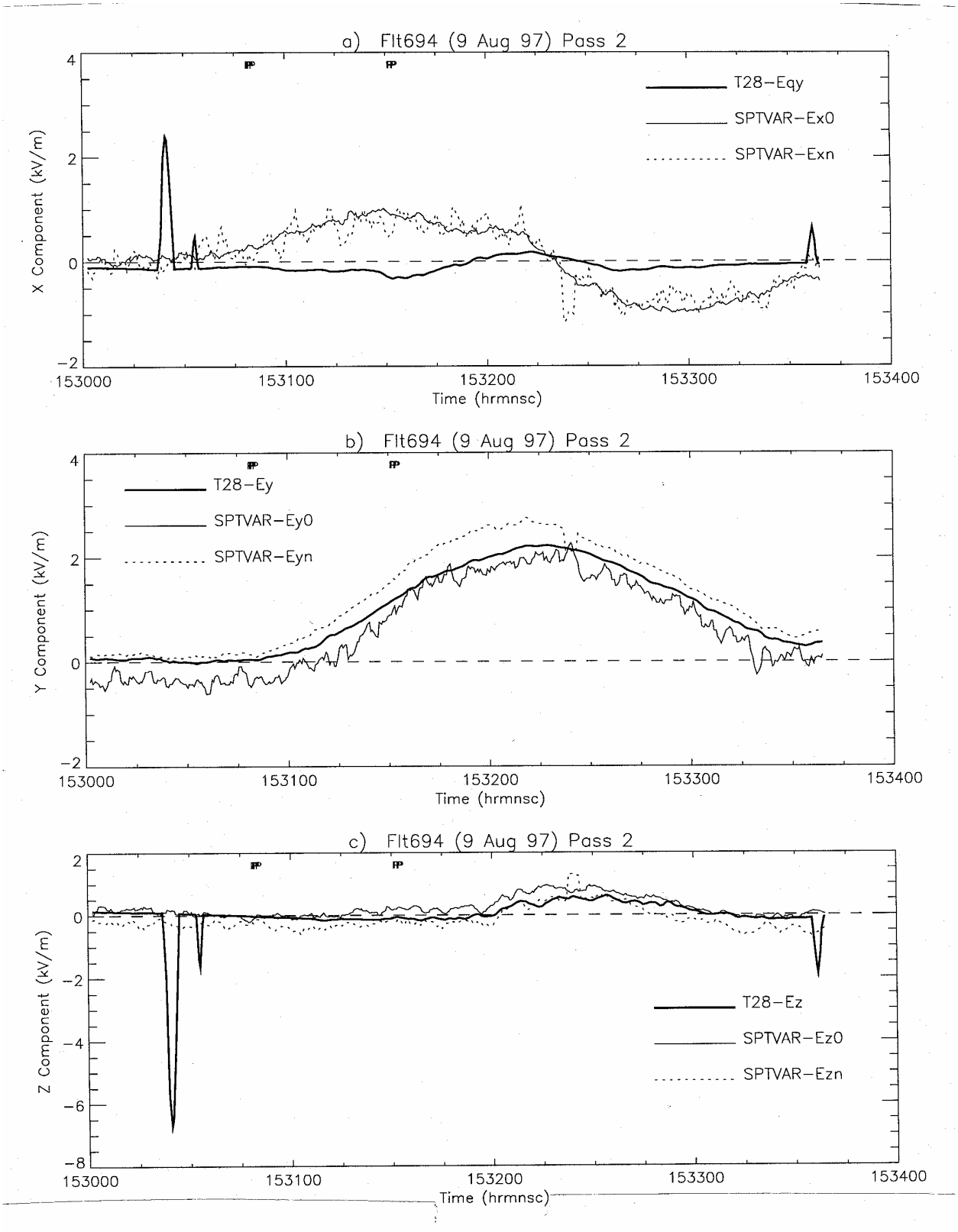

Fig. D2. As in Figure D1, but for the 2nd intercomparison leg on 9 Aug 1997.

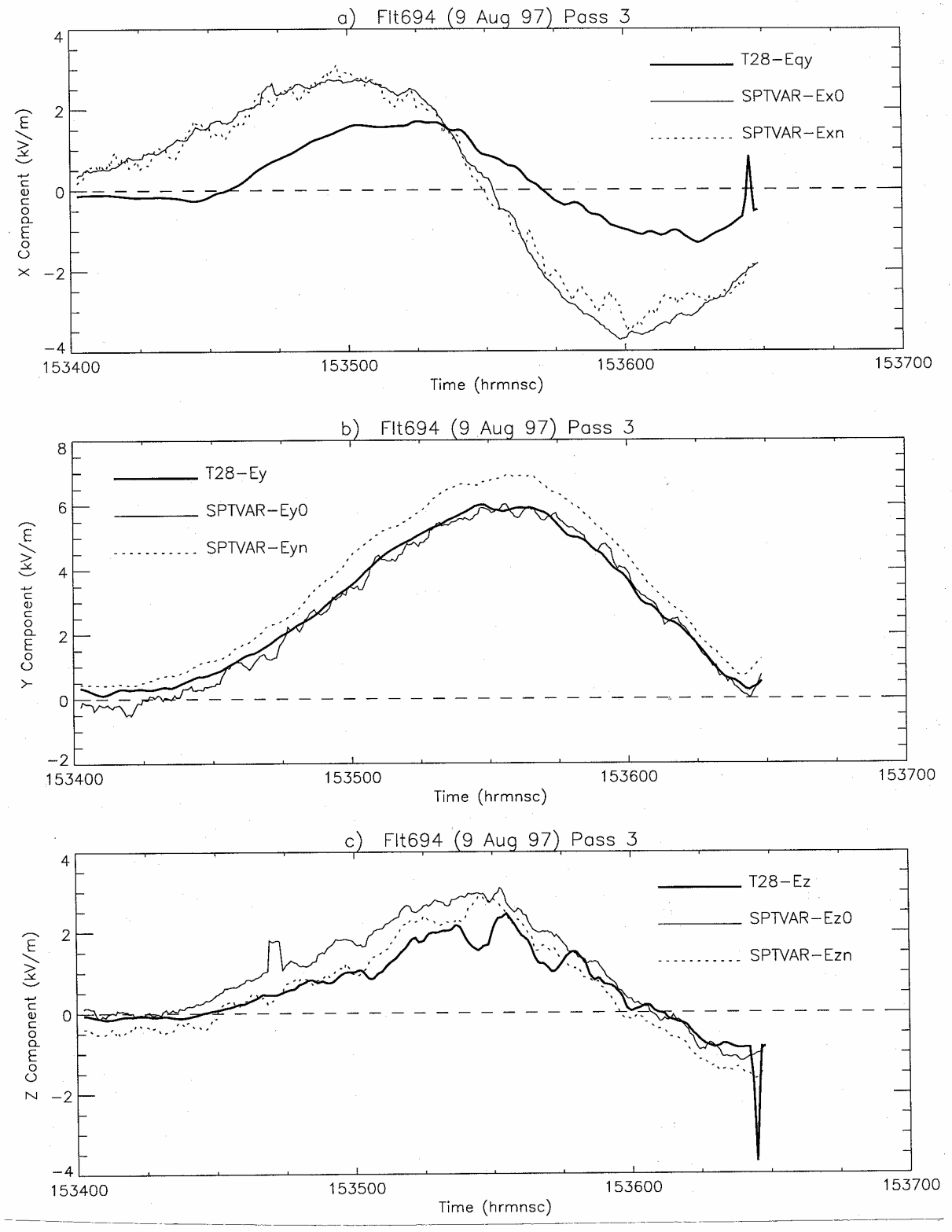

Fig. D3. As in Figure D1, but for the 3rd intercomparison leg on 9 Aug 1997.

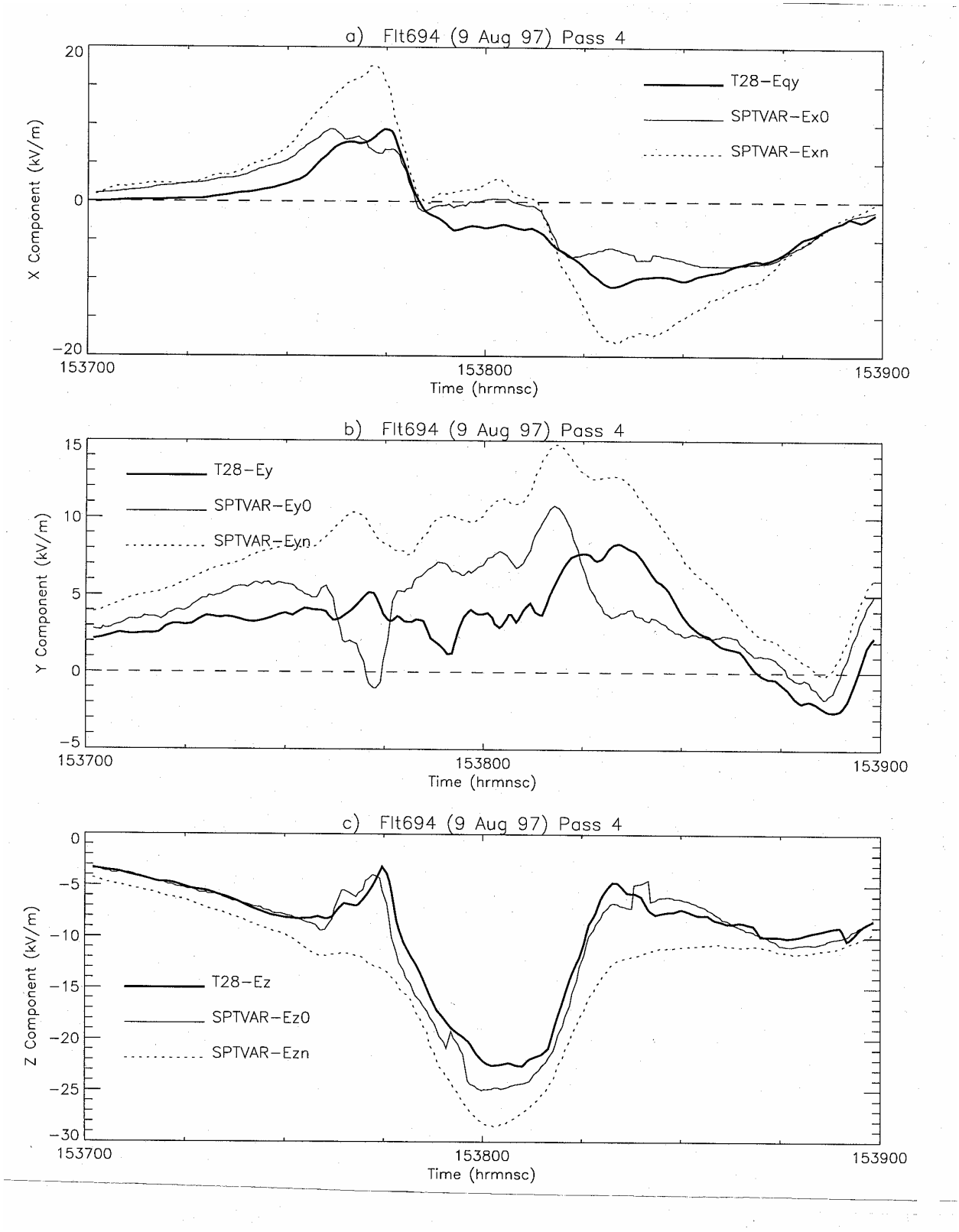

Fig. D4. As in Figure D1, but for the 4th intercomparison leg on 9 Aug 1997.

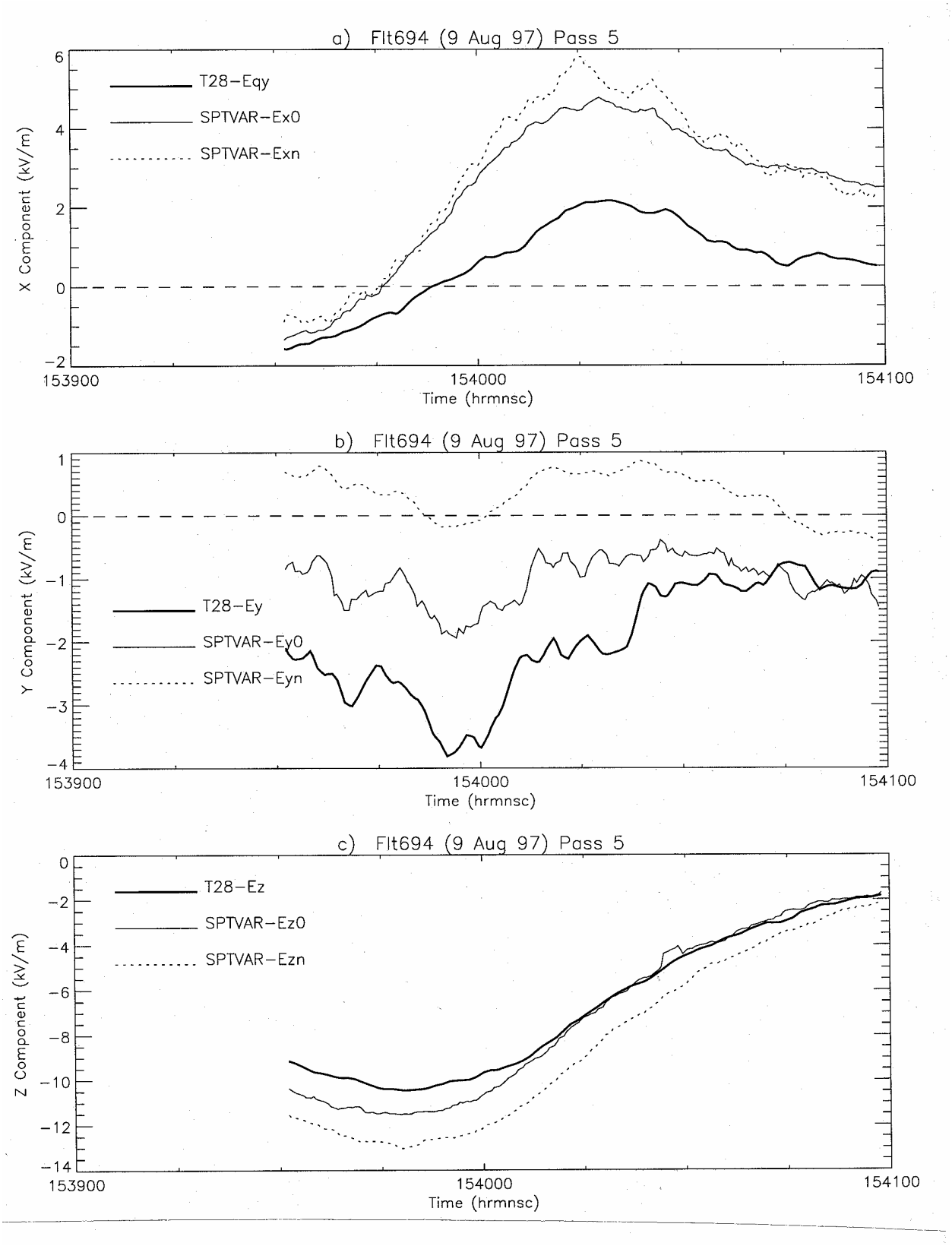

Fig. D5. As in Figure D1, but for the 5th intercomparison leg on 9 Aug 1997.

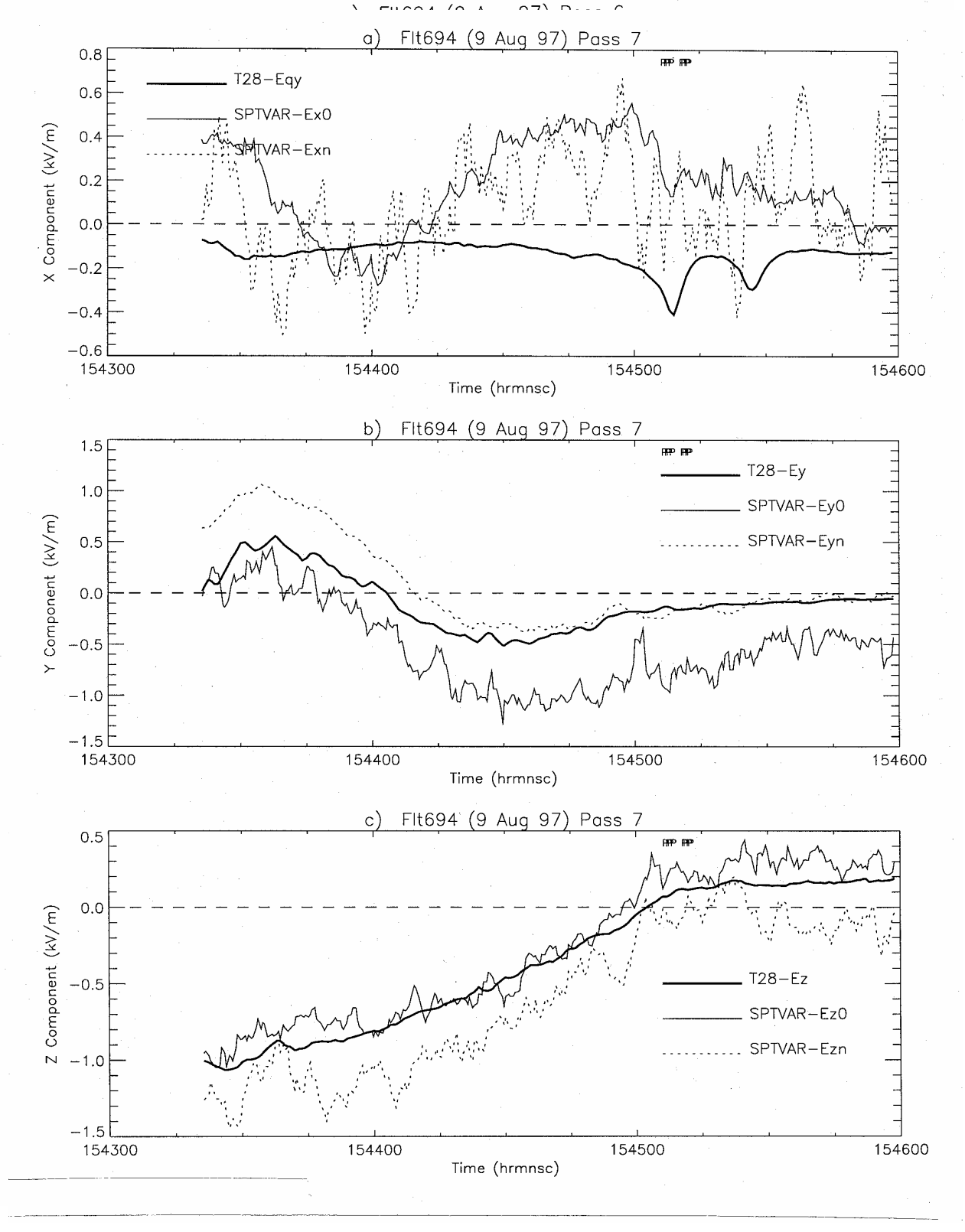

Fig. D6. As in Figure D1, but for the 6th intercomparison leg on 9 Aug 1997.

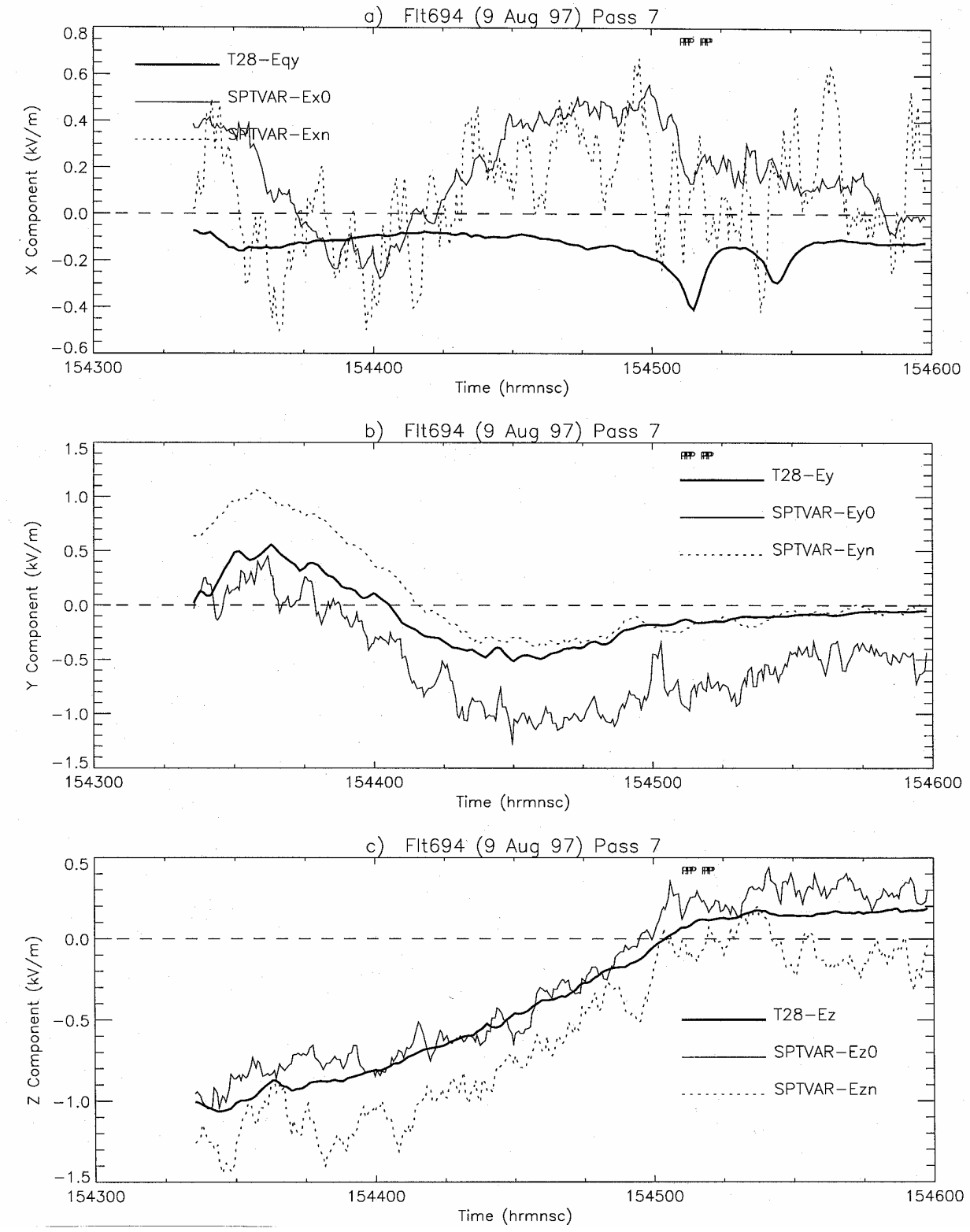

Fig. D7. As in Figure D1, but for the 7th intercomparison leg on 9 Aug 1997.

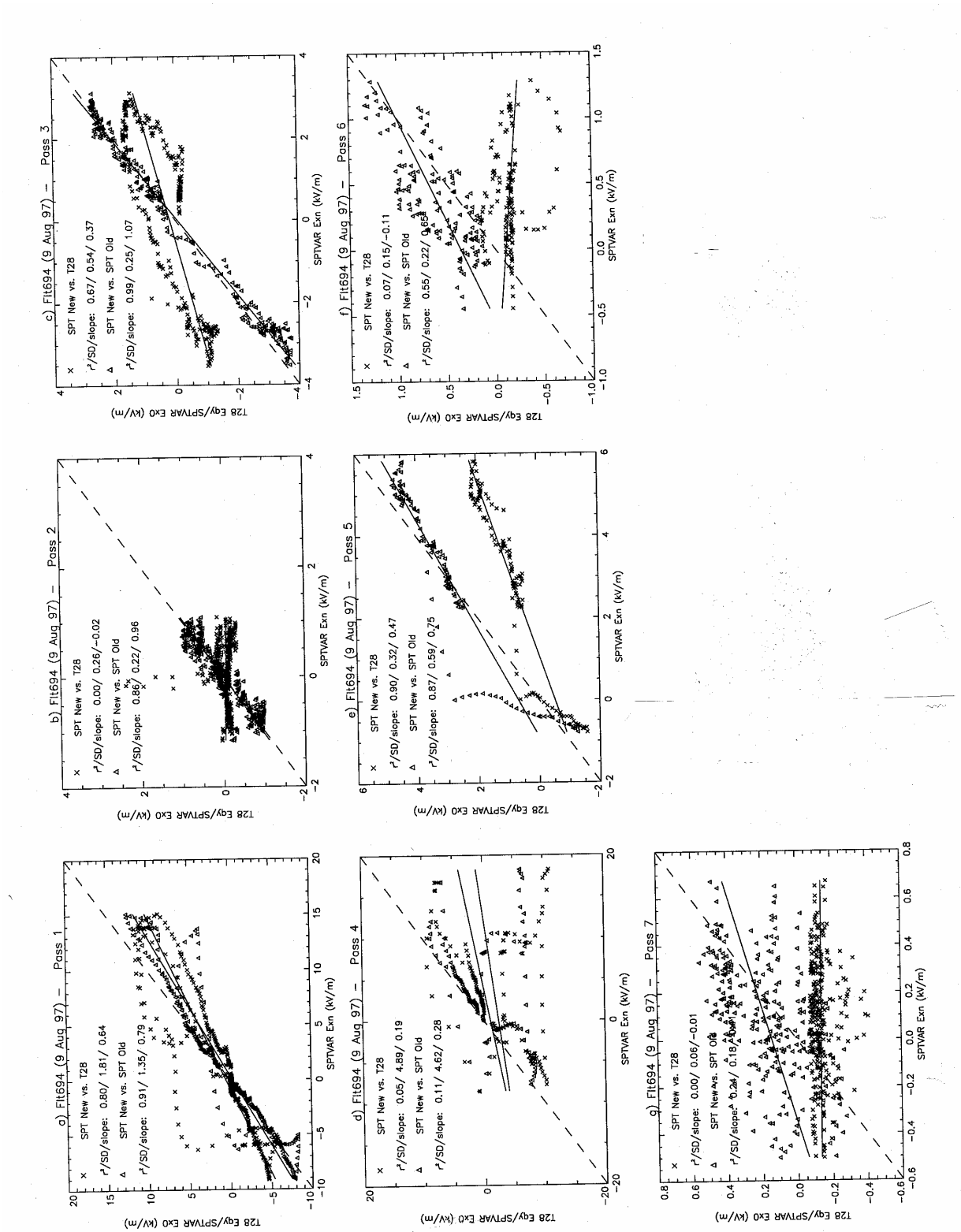

Fig. D8. Regression results comparing E_x from SPTVAR old and new systems, and T-28 E_{qy} on 9 August 1997.

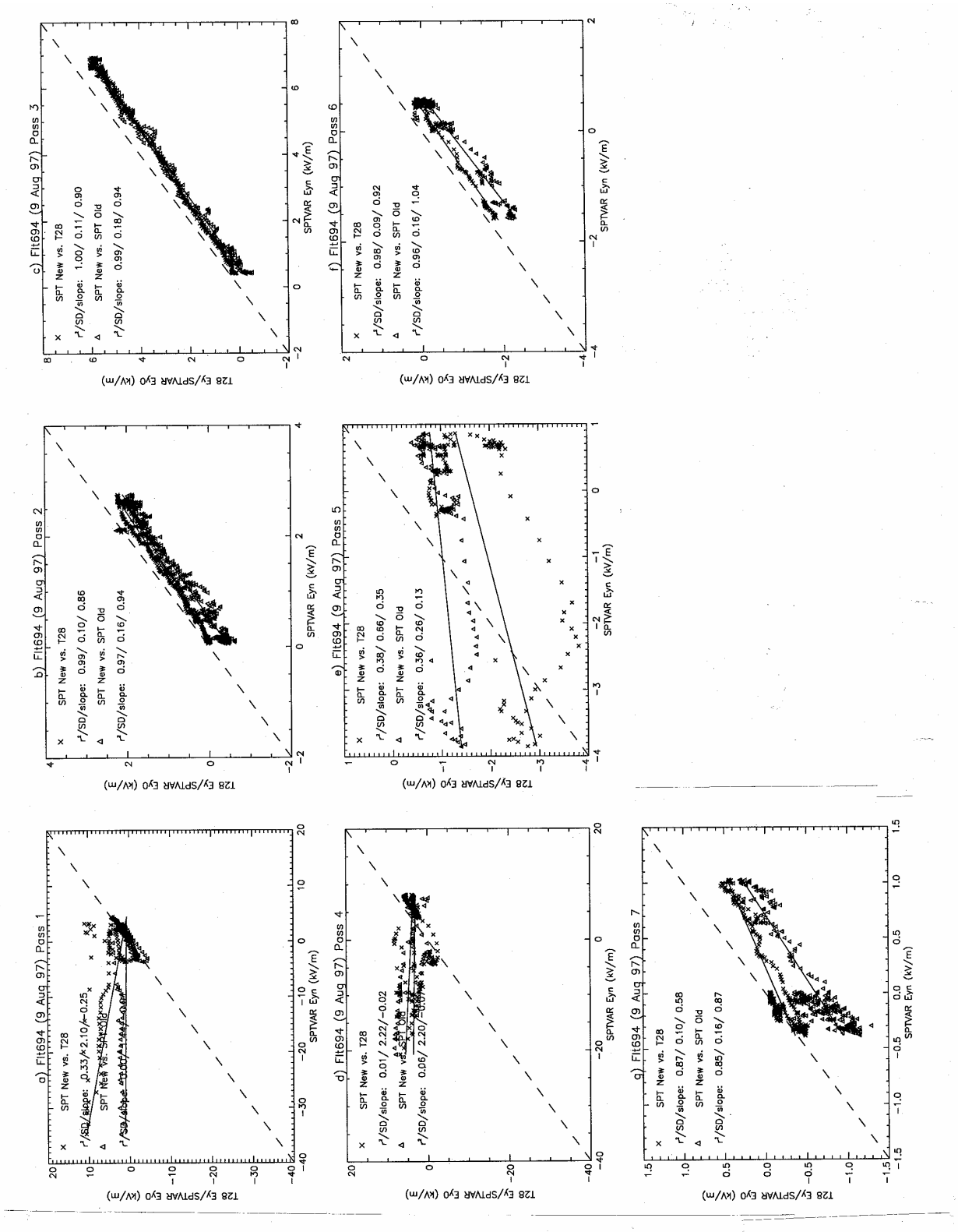

Fig. D9. Regression results comparing Ey from SPTVAR old and new systems and the T-28 on 9 August 1997.

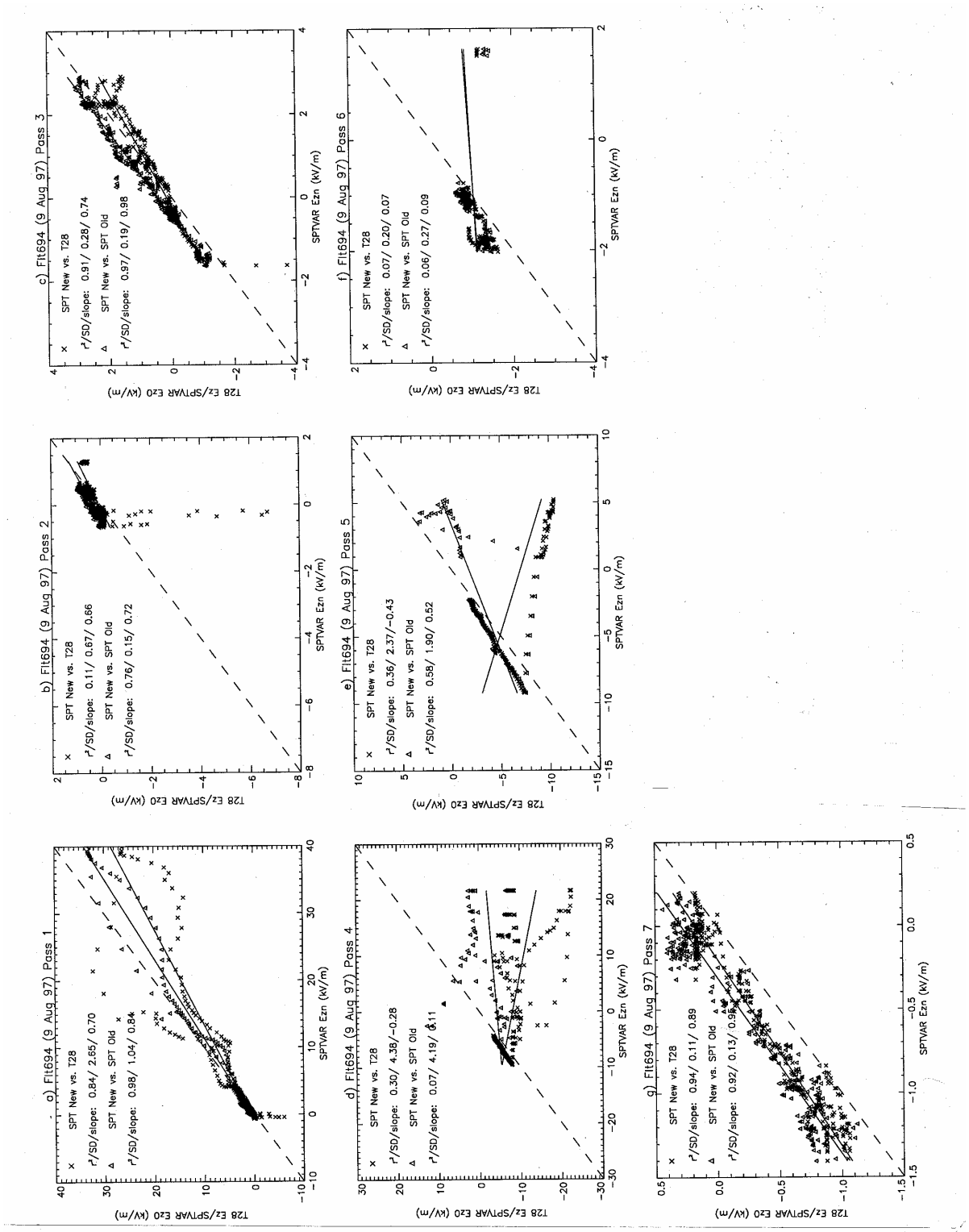

Fig. D10. Regression results comparing Ez from SPTVAR old and new systems and the T-28 on 9 August 1997.

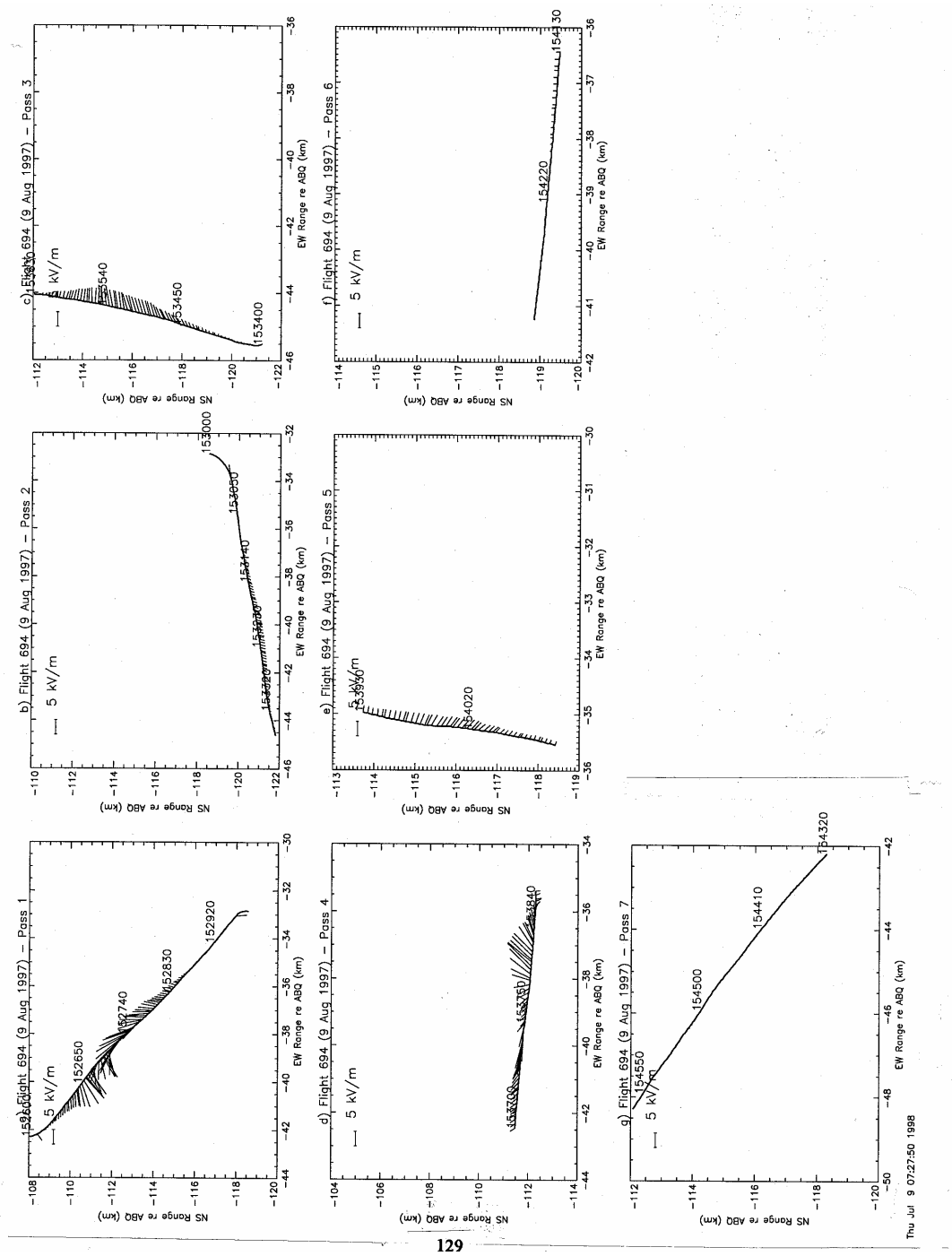

Fig. D11. Projection of the electric field vector on a horizontal plane at the T-28 altitude, based on T-28 measurements during intercomparison legs on 9 August 1997. Eqy has been used to represent the x-component of the field vector.

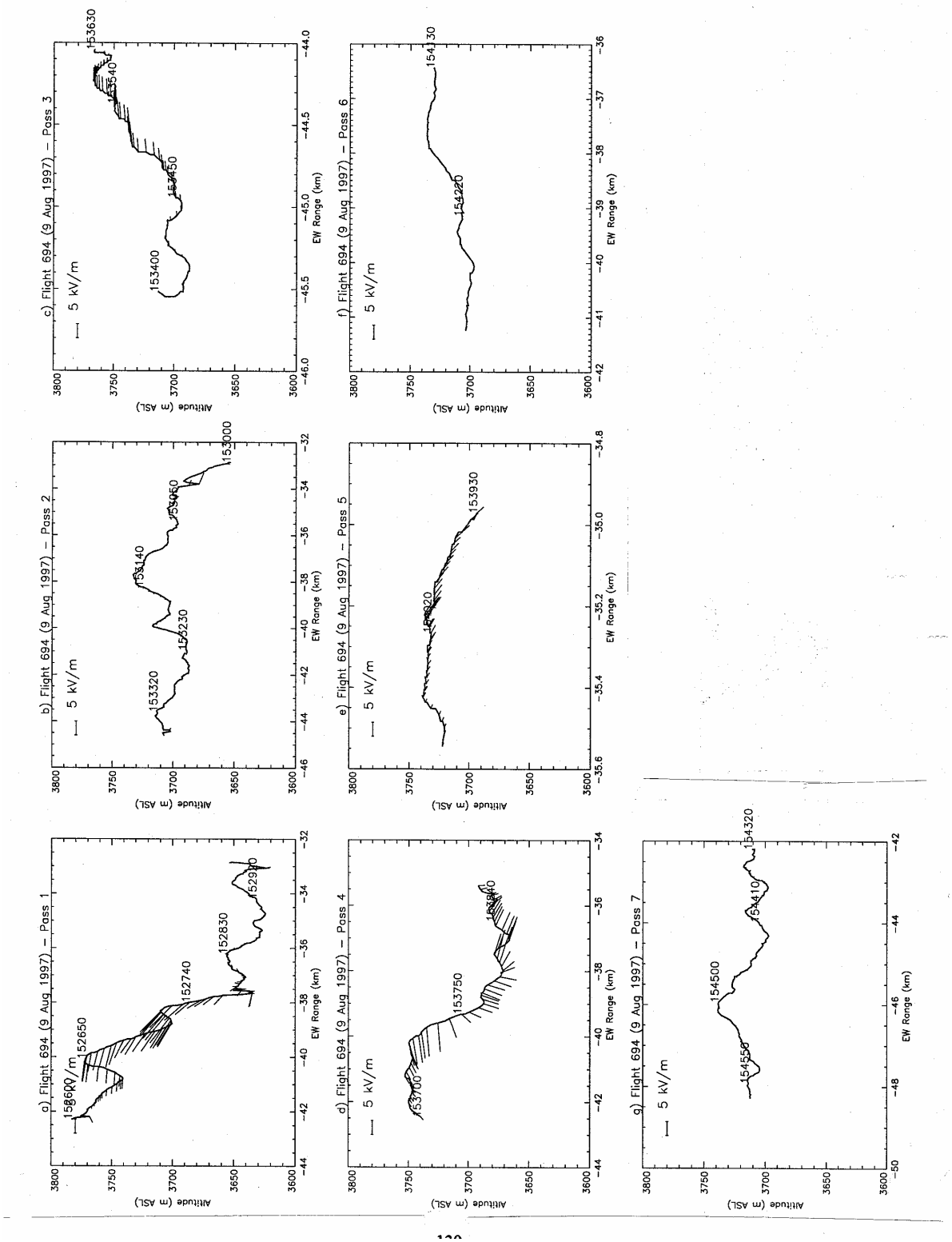

Fig. D12. Projection of the electric field vector on an east-west vertical plane along the T-28 track, based on T-28 measurements during intercomparison legs on 9 August 1997. E_{qy} has been used to represent the x-component of the field vector.

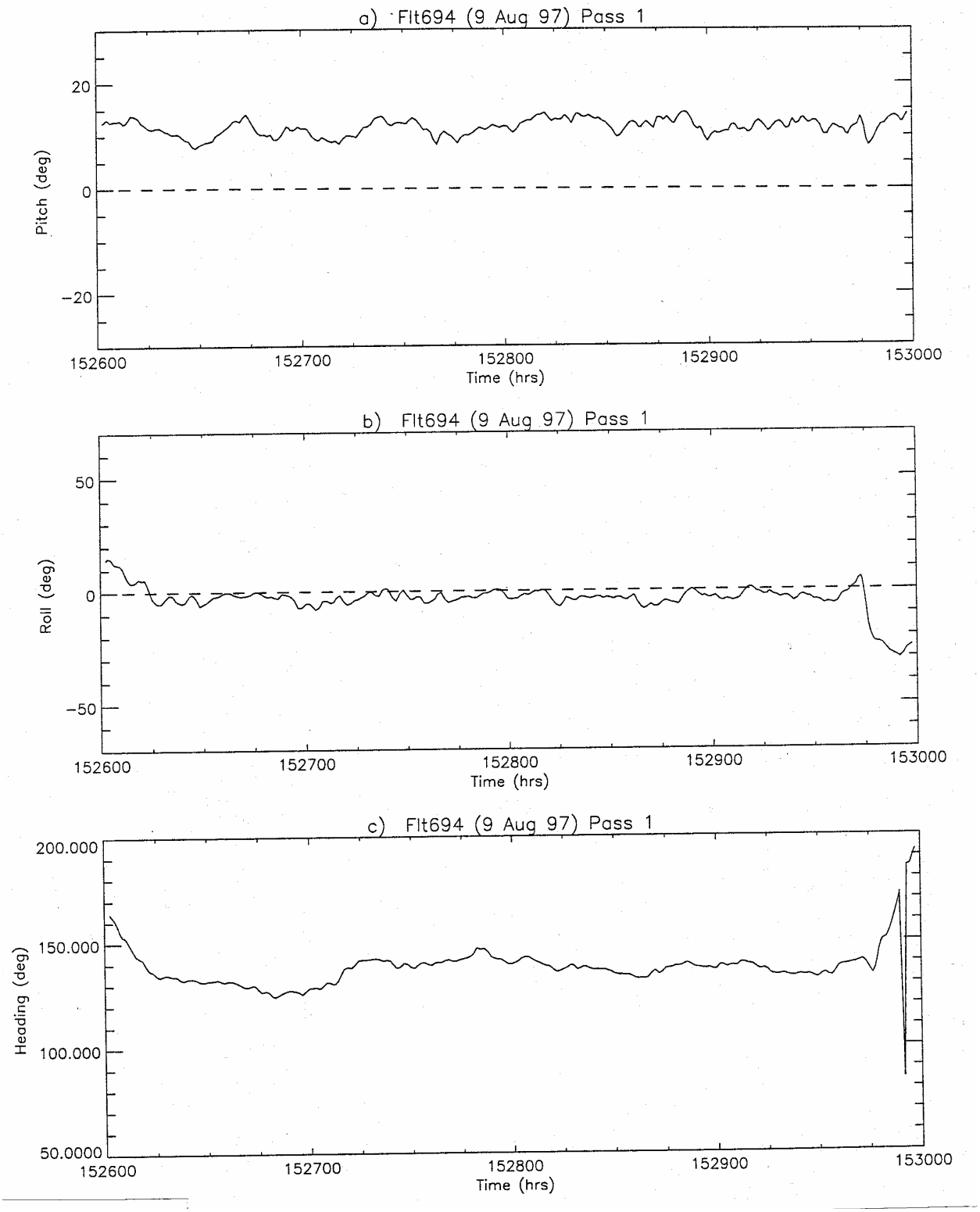

Fig. D13. Pitch, roll, and heading for the T-28 during the 1st intercomparison leg on 9 August 1997.

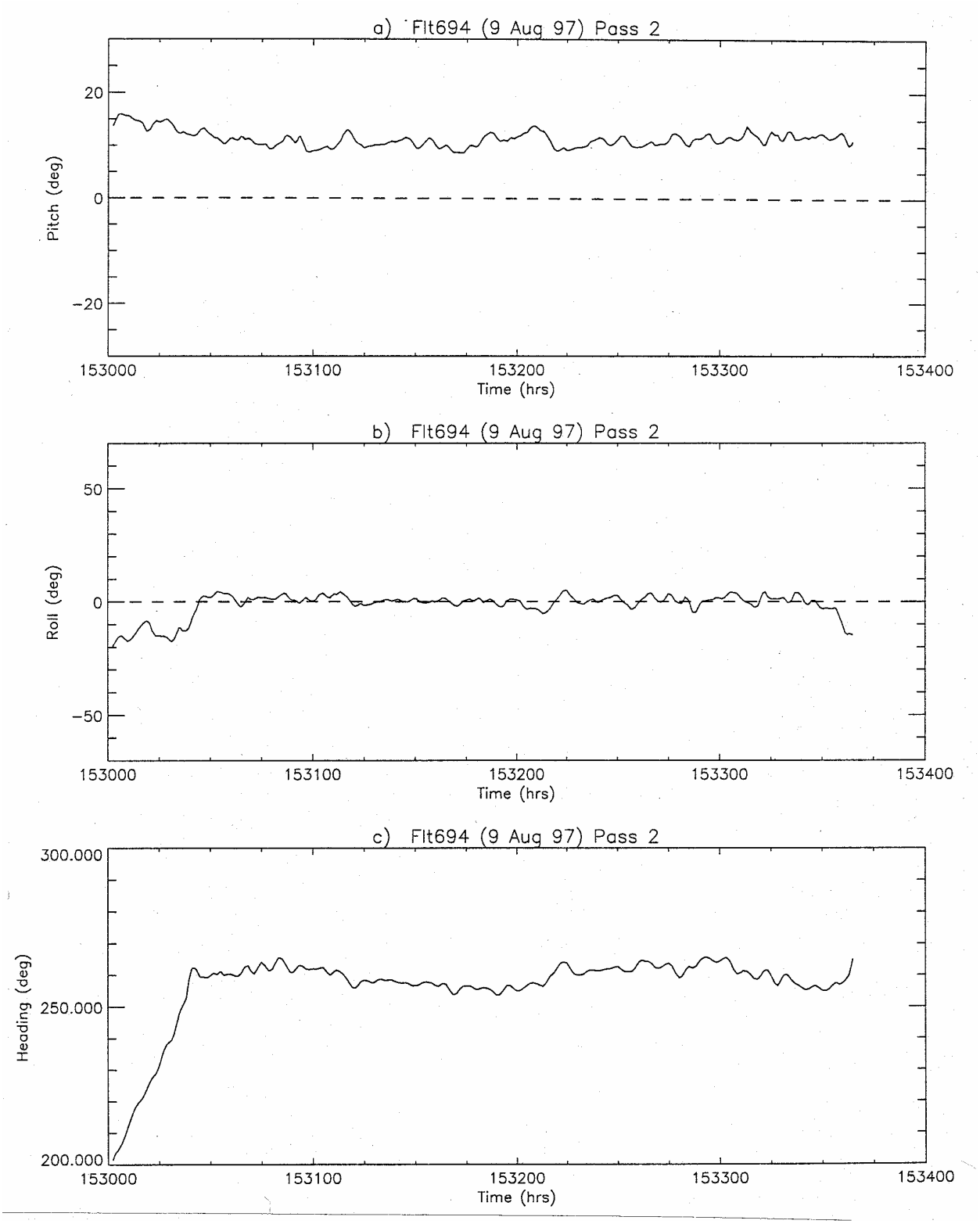

Fig. D14. Pitch, roll, and heading for the T-28 during the 2nd intercomparison leg on 9 August 1997.

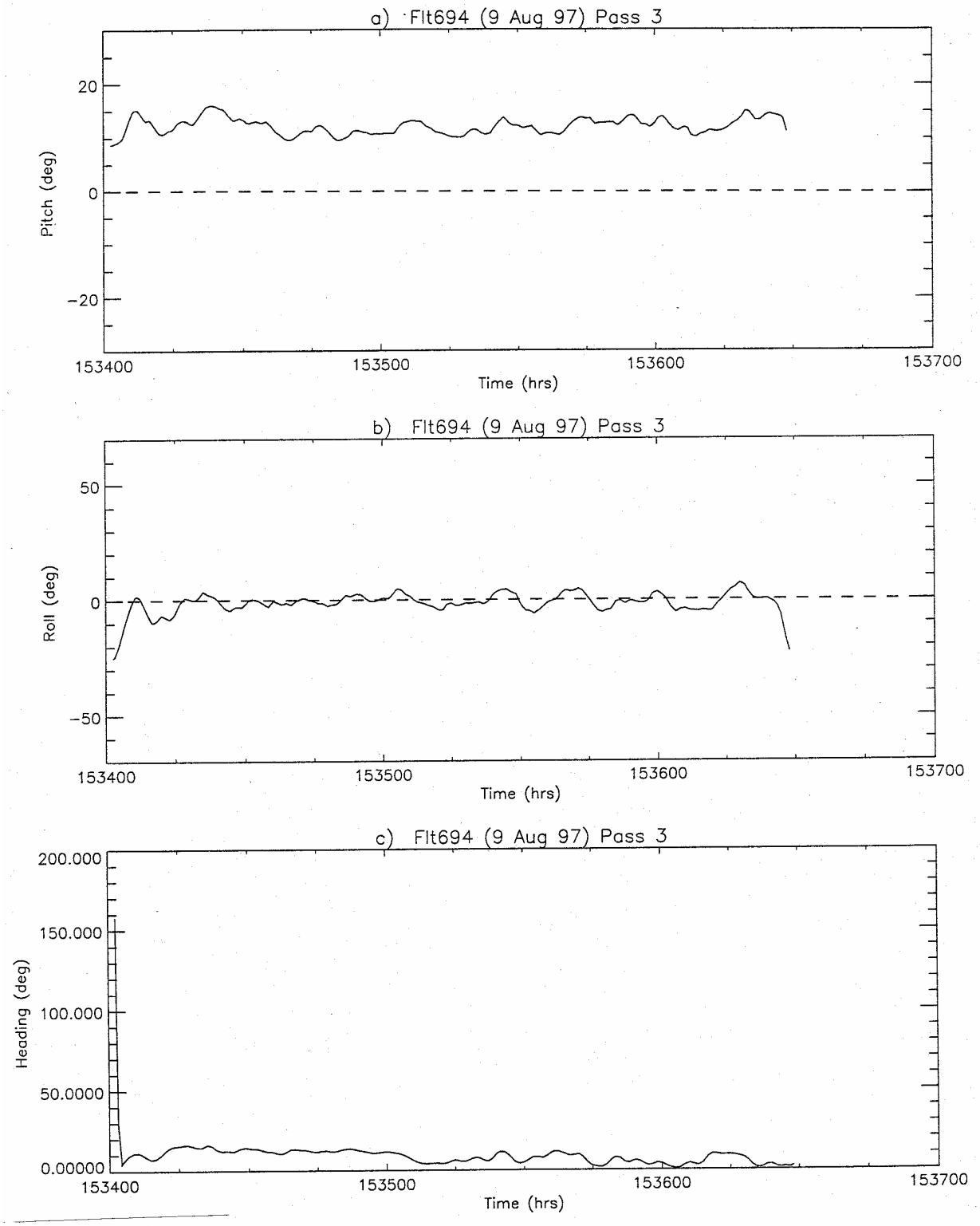

Fig. D15. Pitch, roll, and heading for the T-28 during the 3rd intercomparison leg on 9 August 1997.

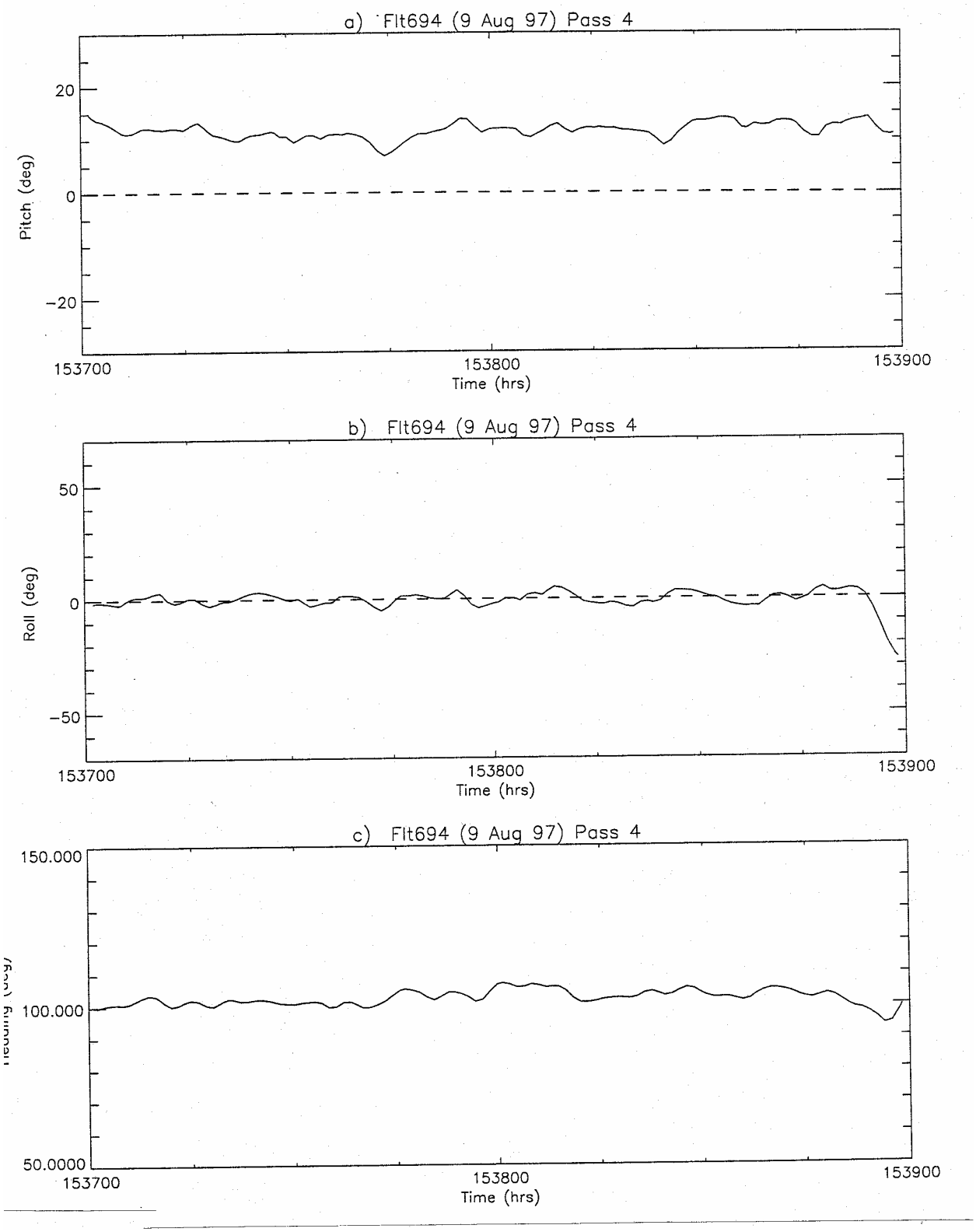

Fig. D16. Pitch, roll, and heading for the T-28 during the 4th intercomparison leg on 9 August 1997.

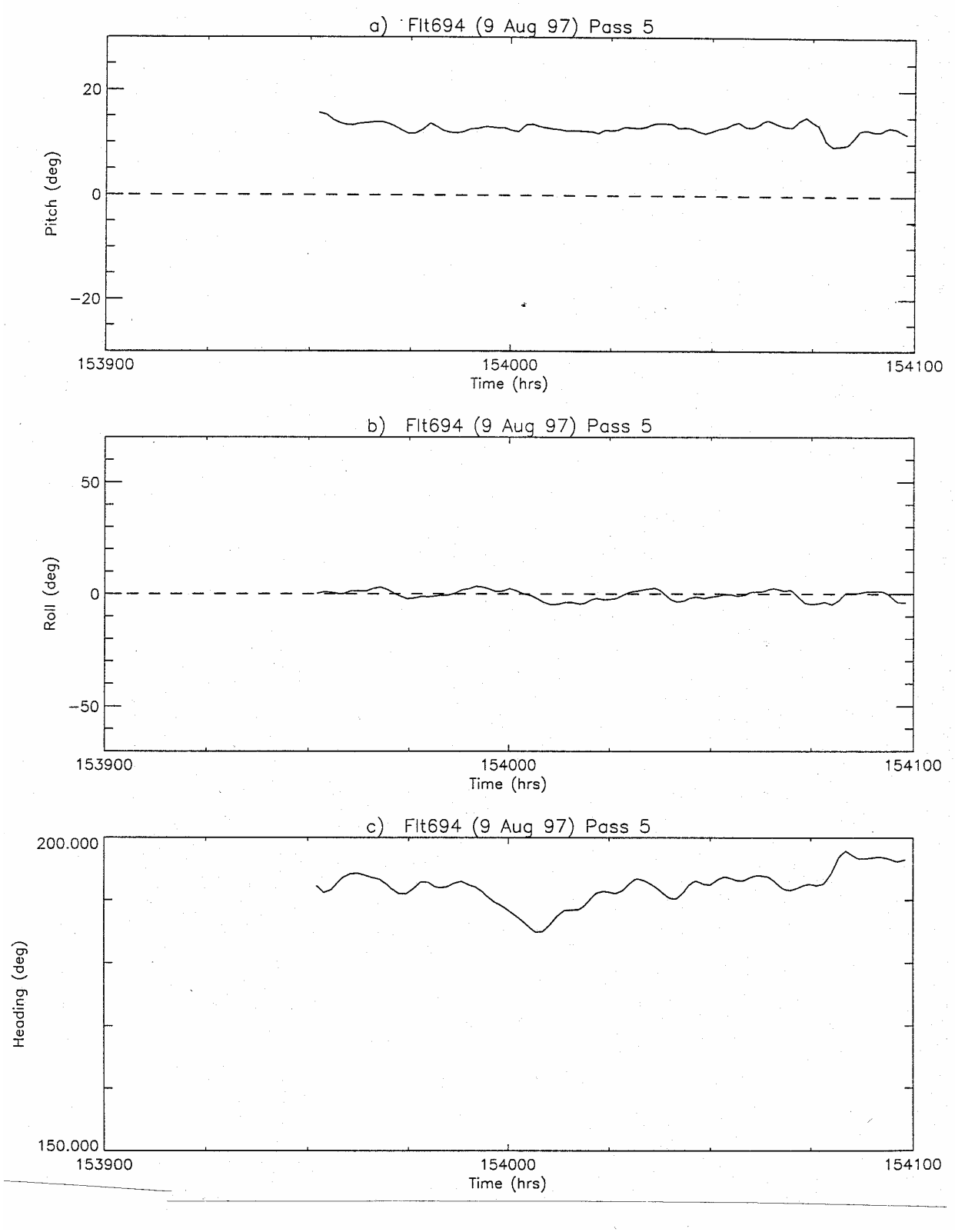

Fig. D17. Pitch, roll, and heading for the T-28 during the 5th intercomparison leg on 9 August 1997.

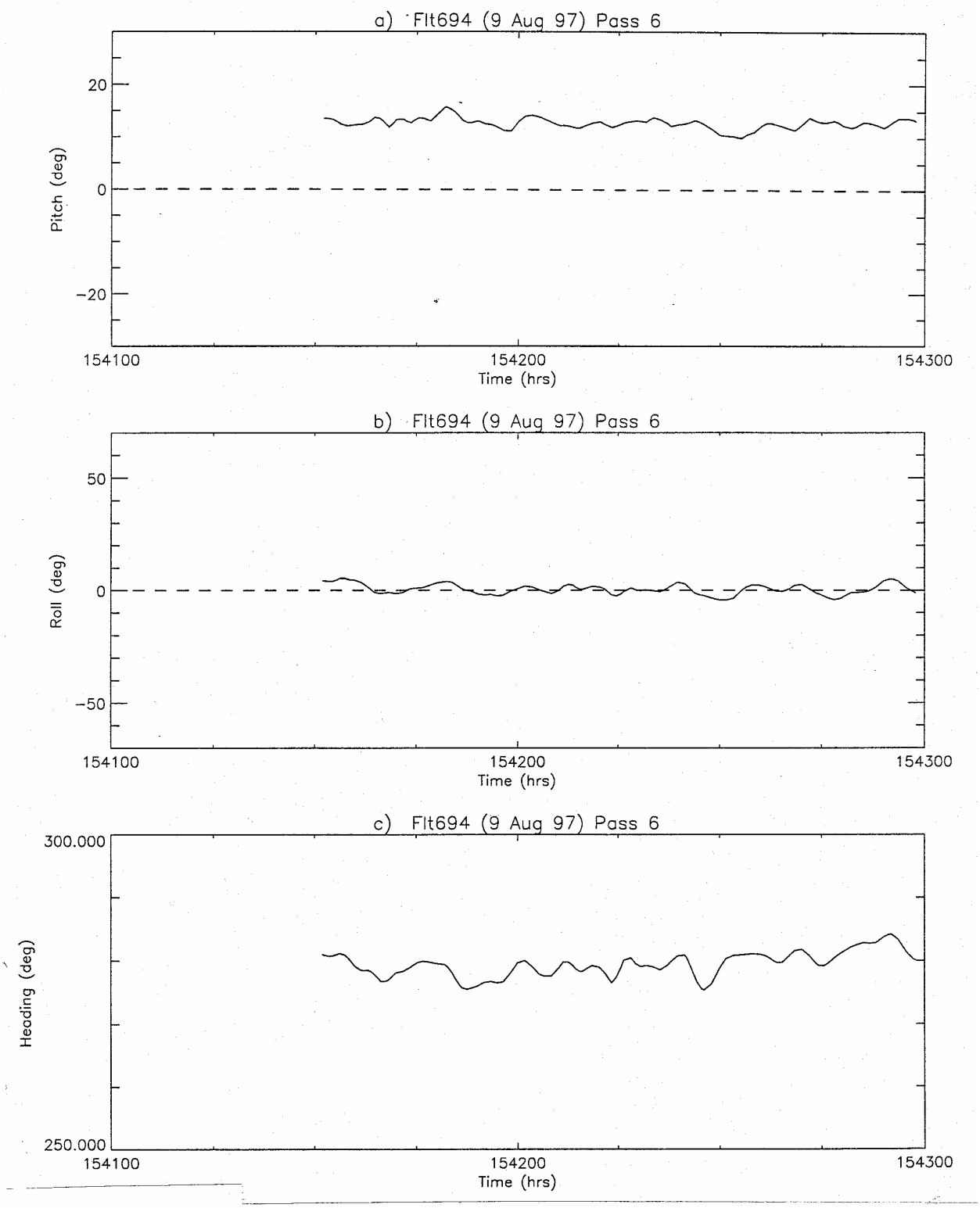

Fig. D18. Pitch, roll, and heading for the T-28 during the 6th intercomparison leg on 9 August 1997.

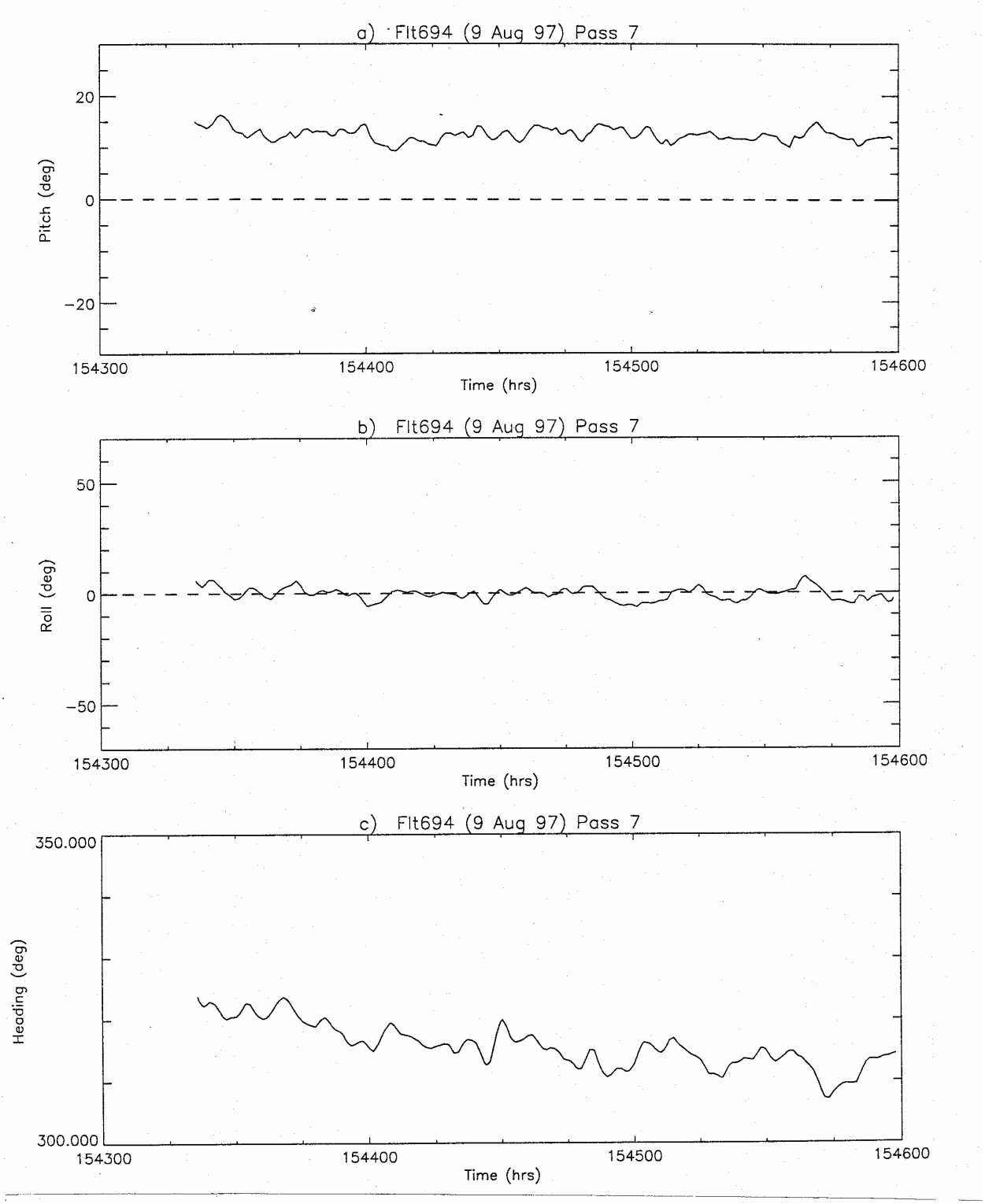

Fig. D19. Pitch, roll, and heading for the T-28 during the 7th intercomparison leg on 9 August 1997.

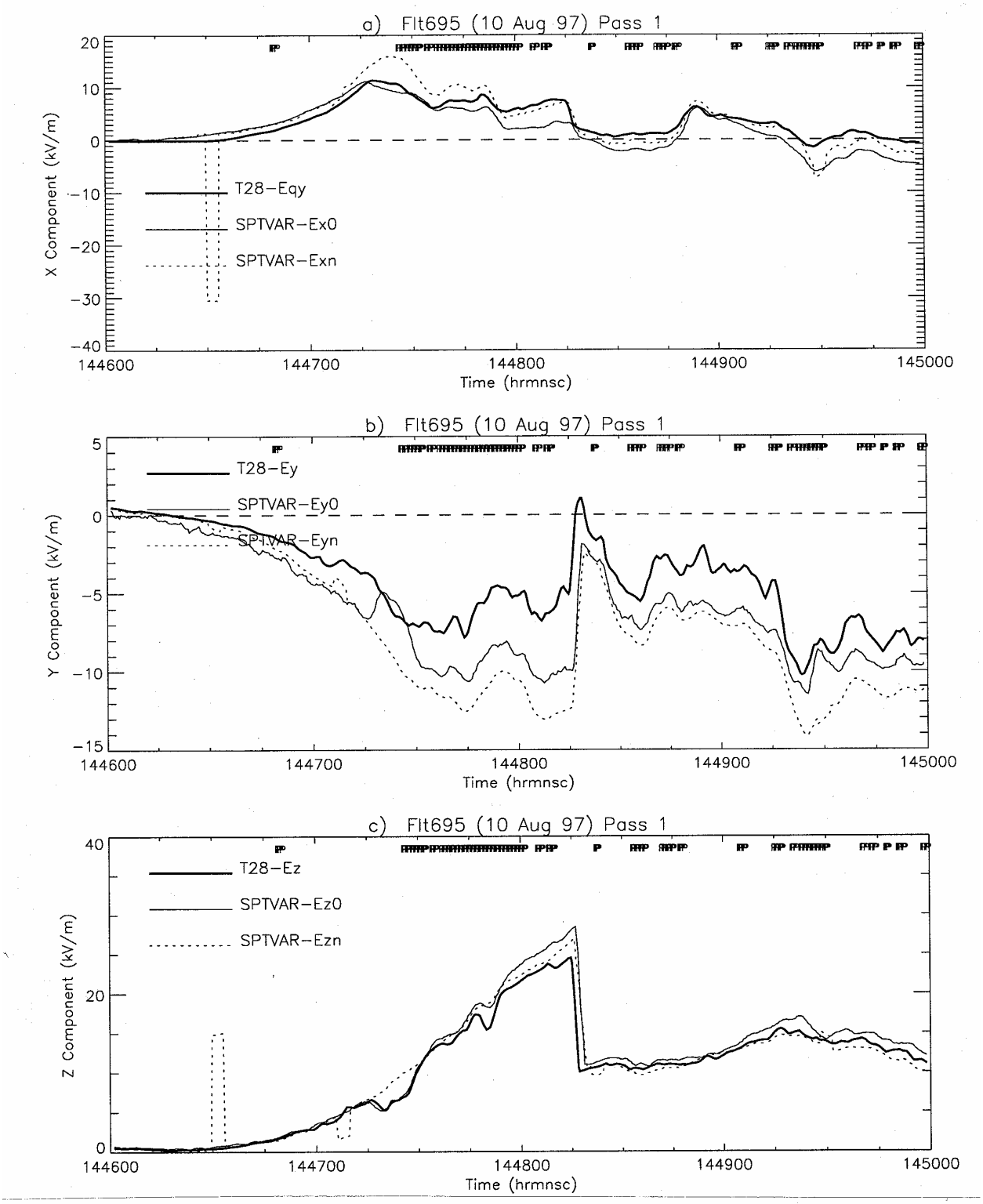

Fig. D20. As in Figure D1, but for the 1st intercomparison leg on 10 Aug 1997.

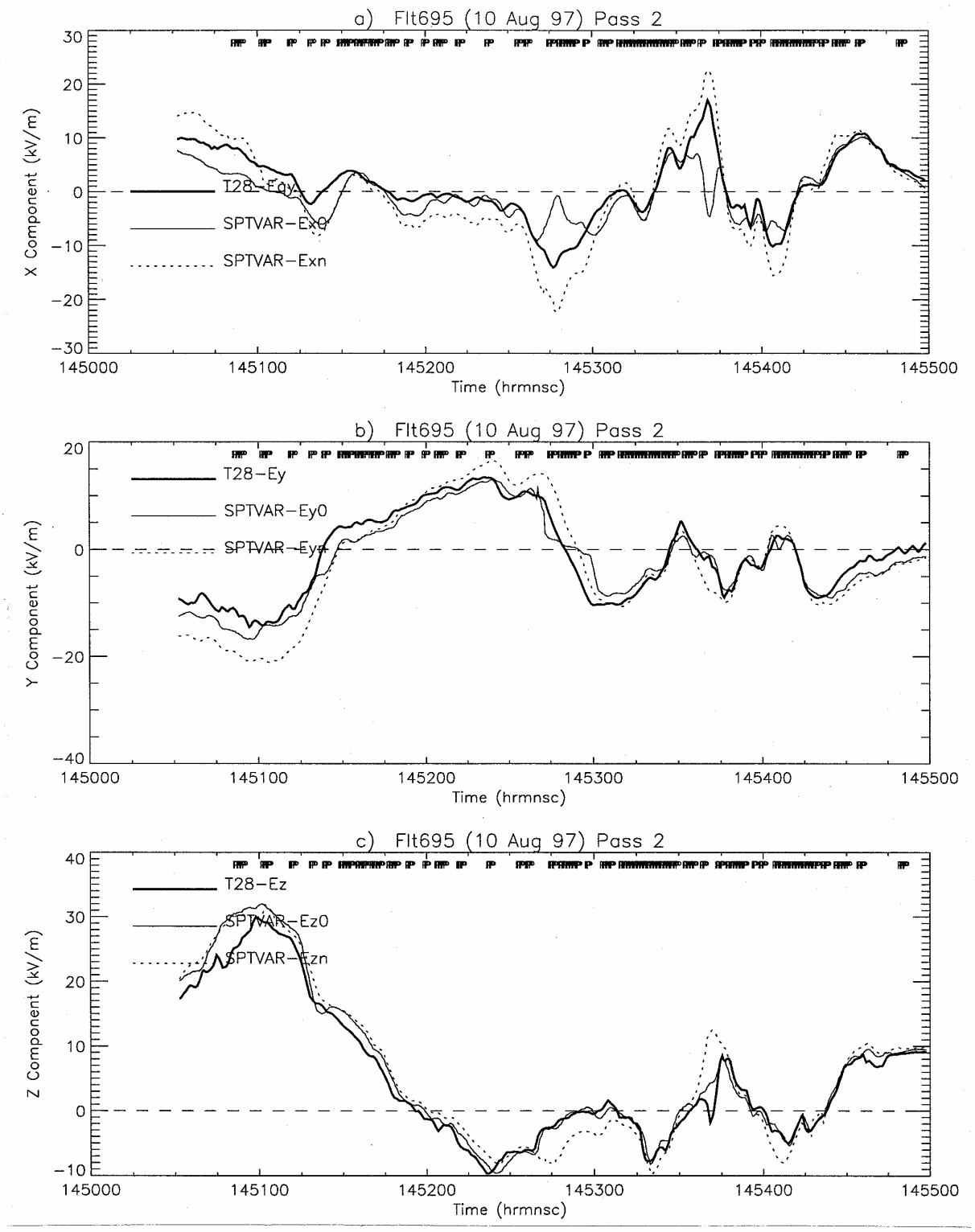

Fig. D21. As in Figure D1, but for the 2nd intercomparison leg on 10 Aug 1997.

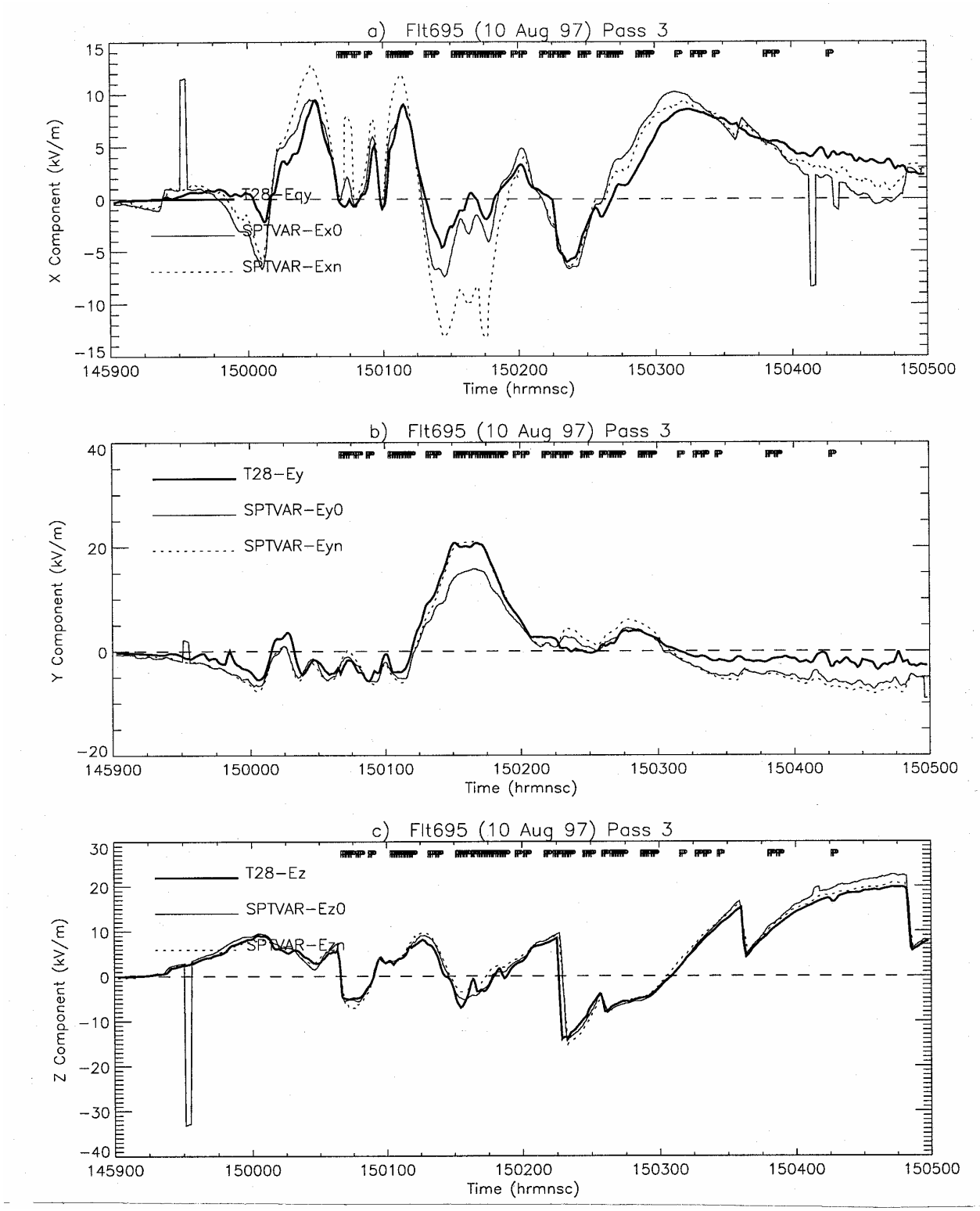

Fig. D22. As in Figure D1, but for the 3rd intercomparison leg on 10 Aug 1997.

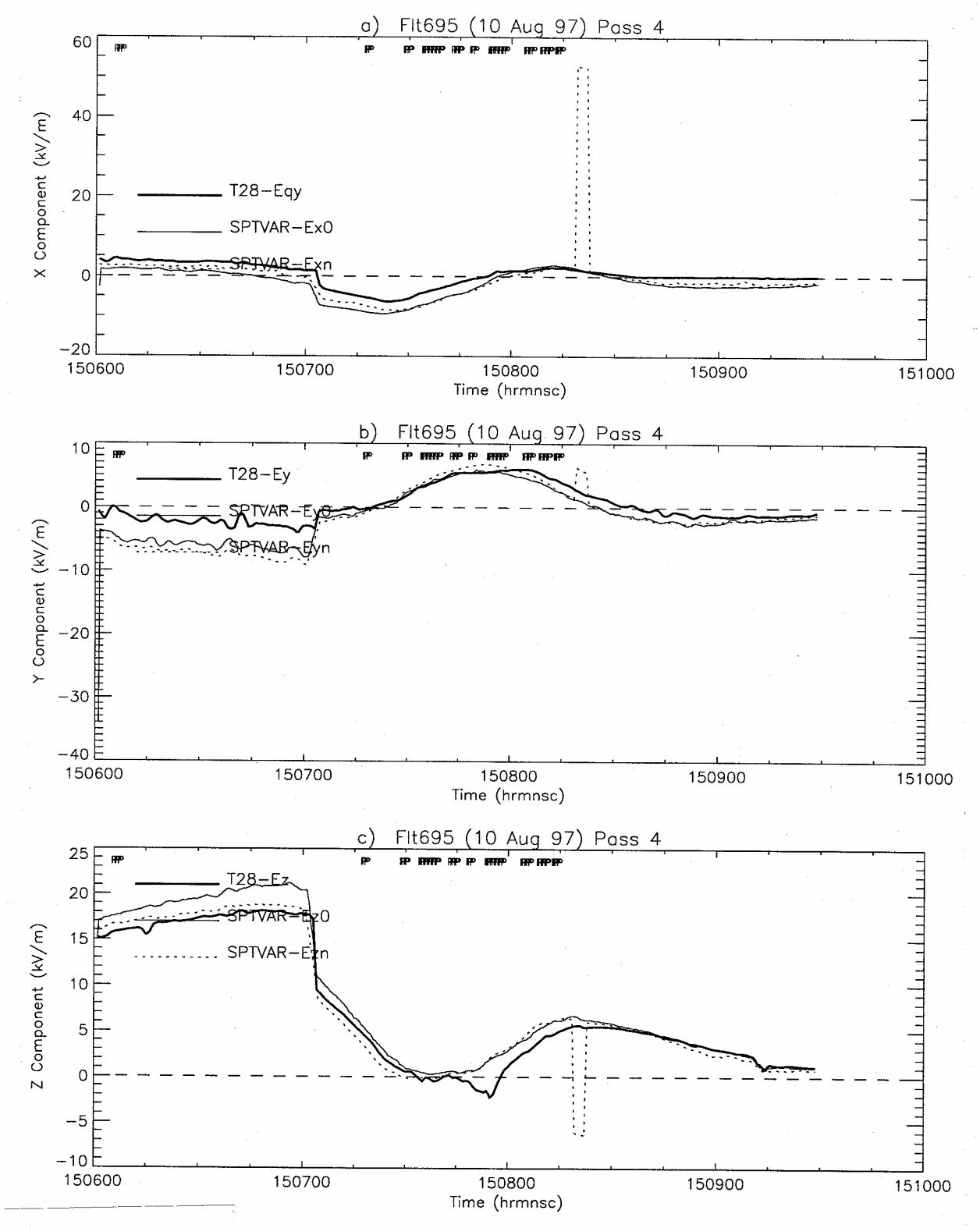

Fig. D23. As in Figure D1, but for the 4th intercomparison leg on 10 Aug 1997.

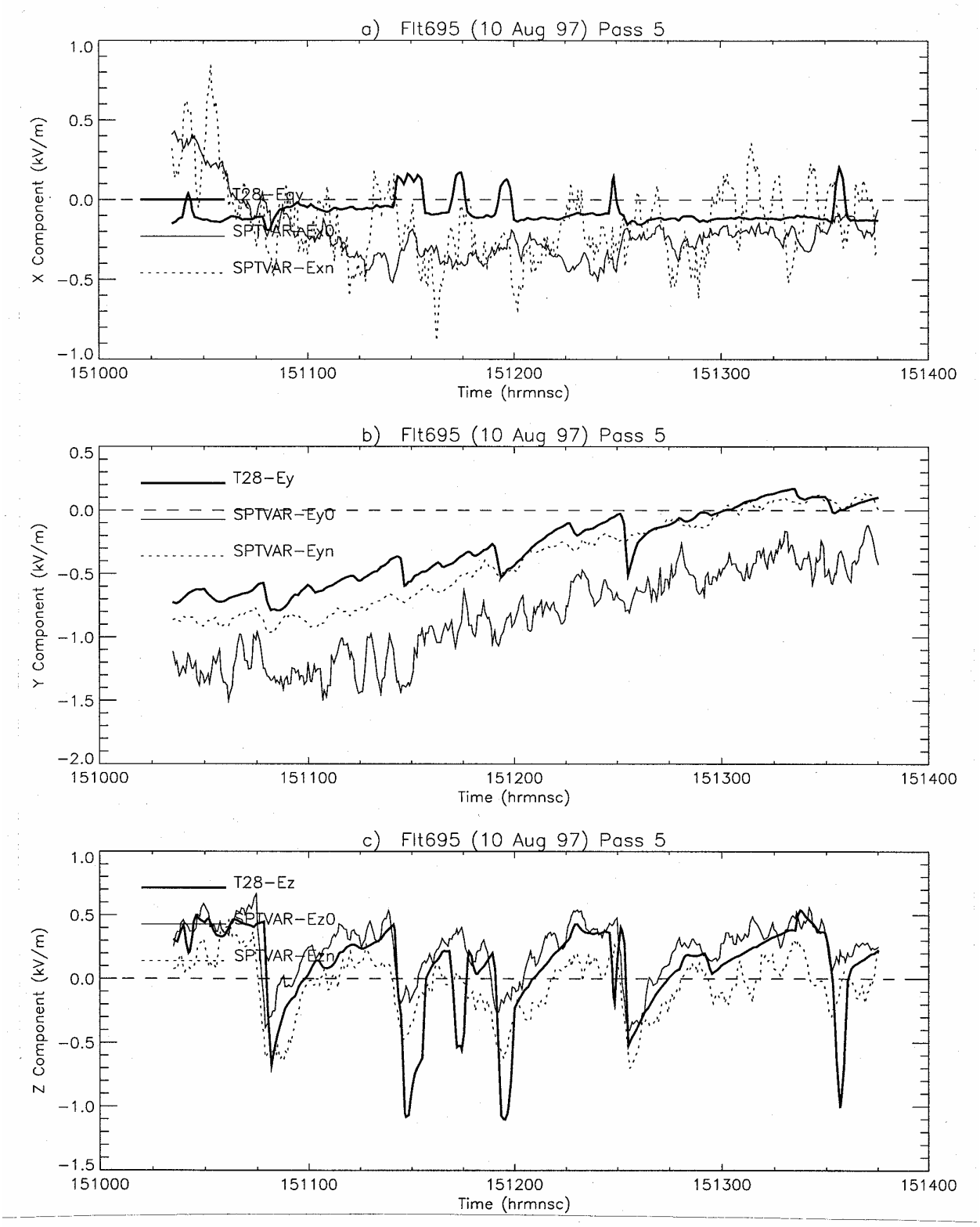

Fig. D24. As in Figure D1, but for the 5th intercomparison leg on 10 Aug 1997.

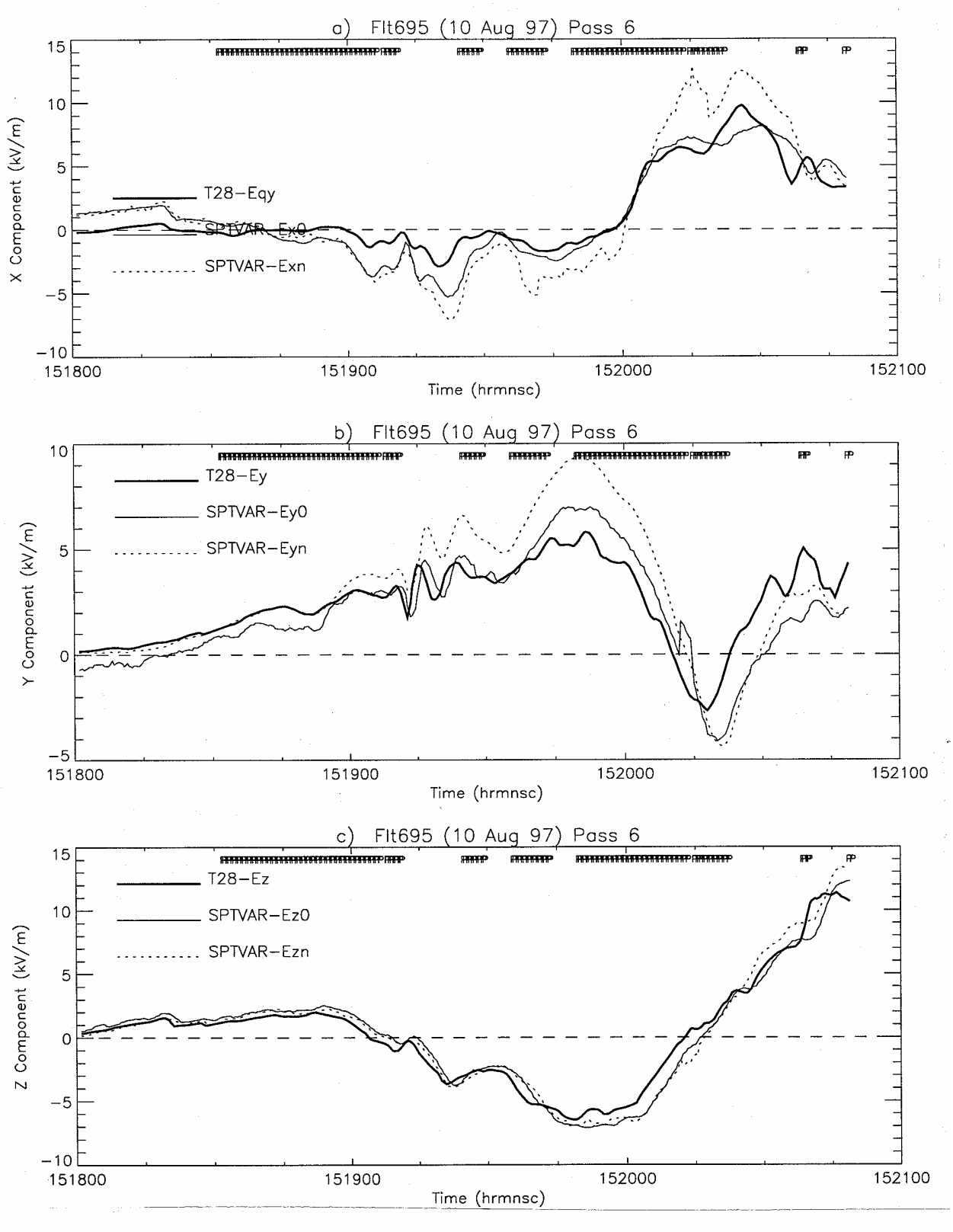

Fig. D25. As in Figure D1, but for the 6th intercomparison leg on 10 Aug 1997.

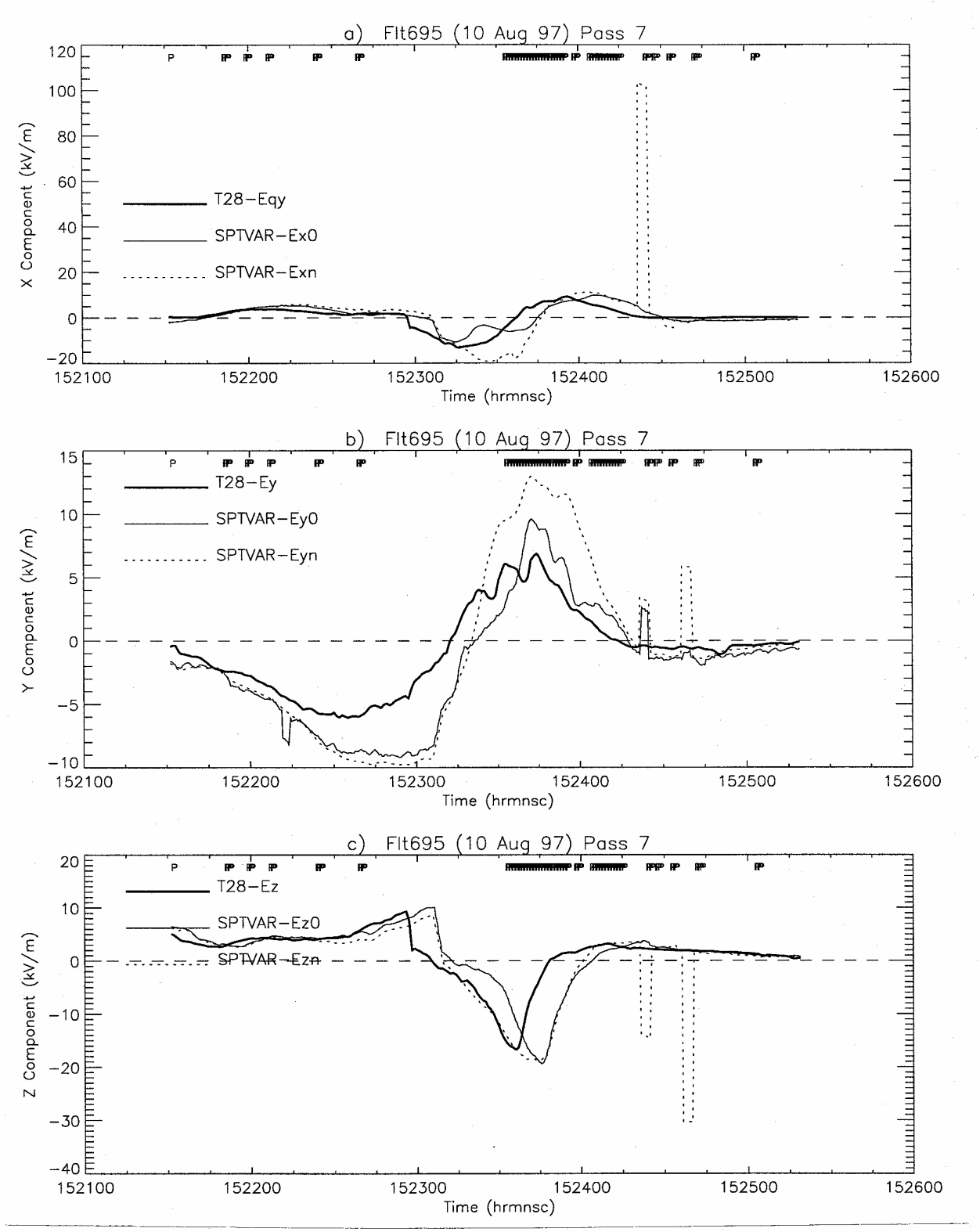

Fig. D26. As in Figure D1, but for the 7th intercomparison leg on 10 Aug 1997.

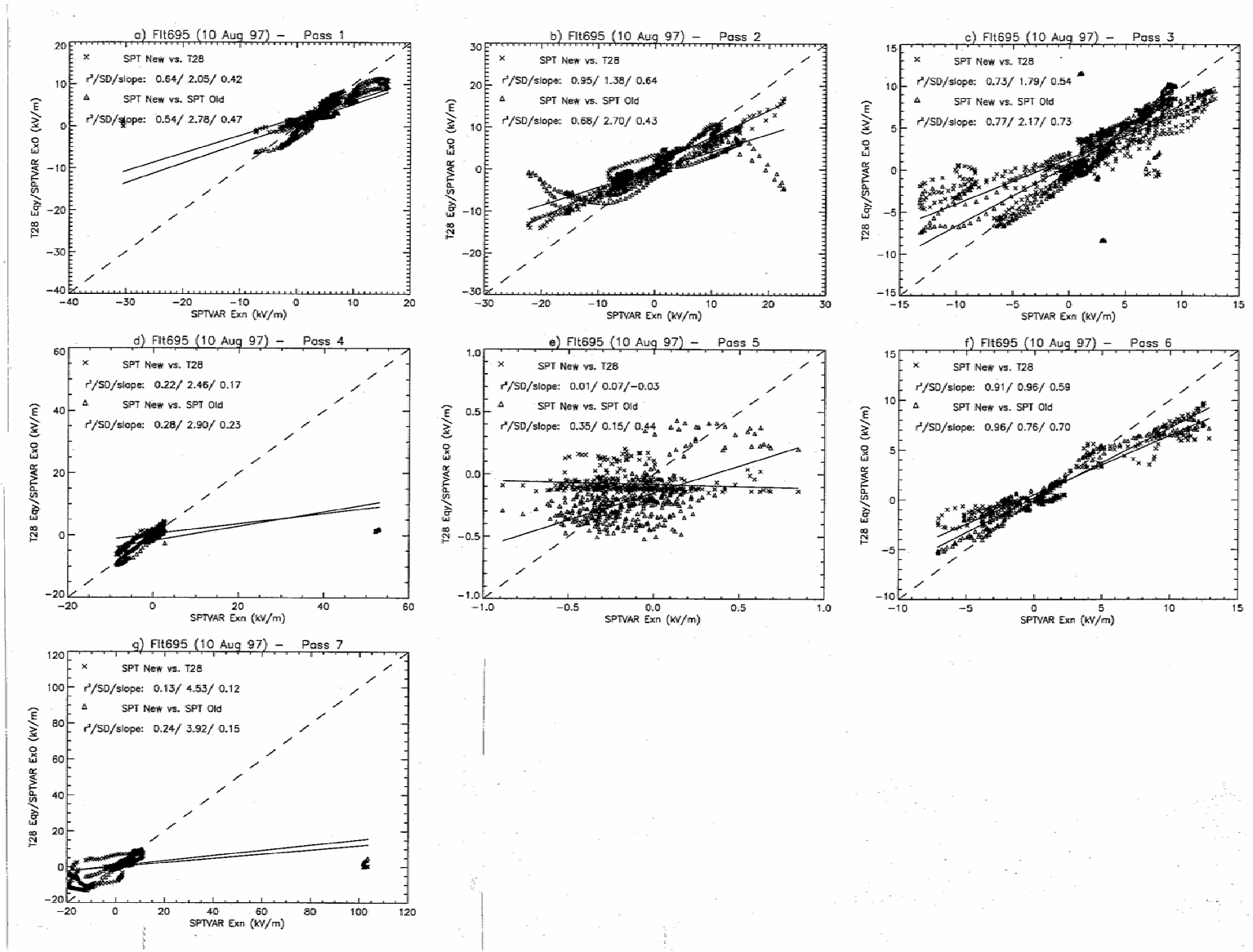

Fig. D27. Regression results comparing E_x from SPTVAR old and new systems, and T-28 E_{qy} on 10 August 1997.

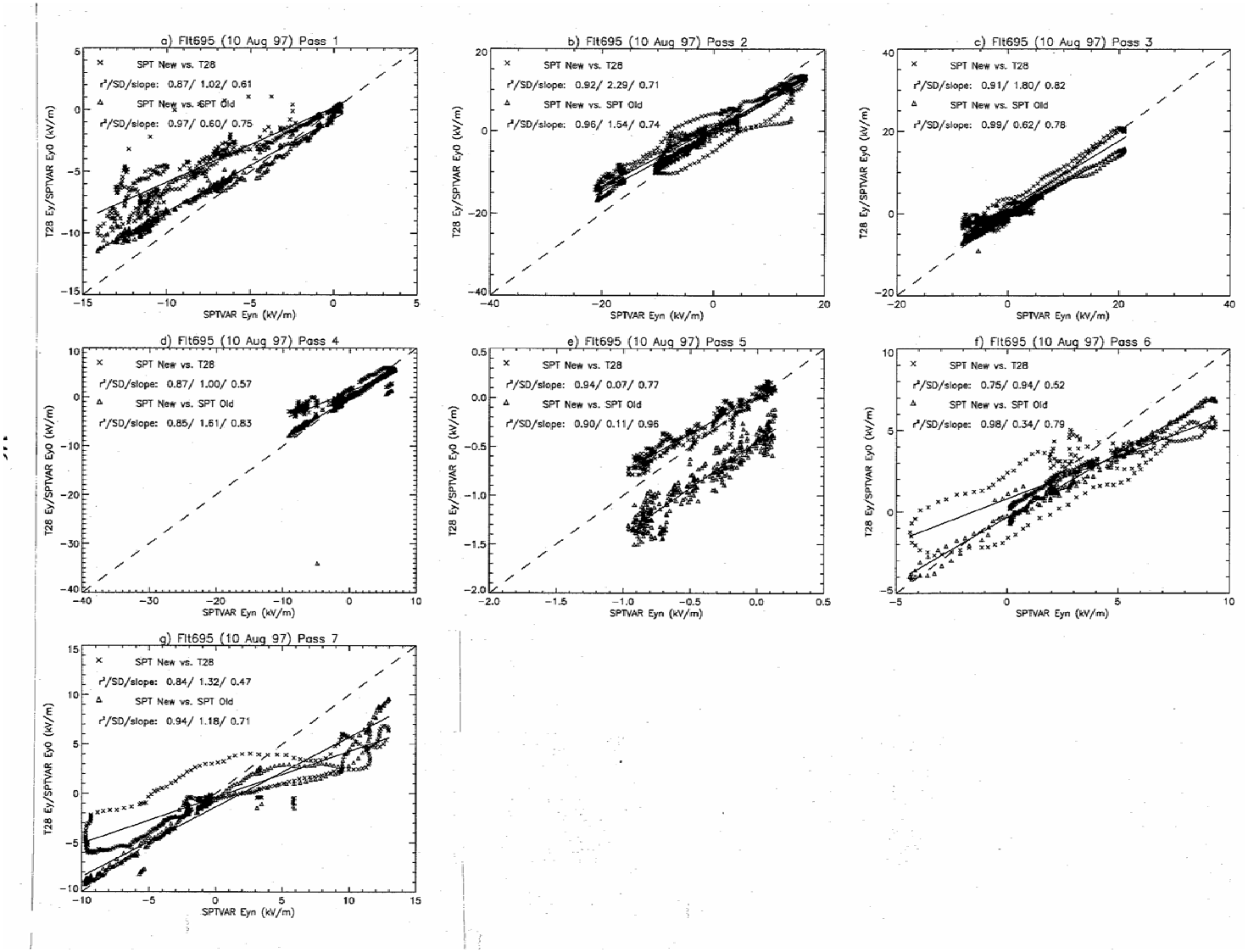

Fig. D28. Regression results comparing E_y from SPTVAR old and new systems and the T-28 on 10 August 1997.

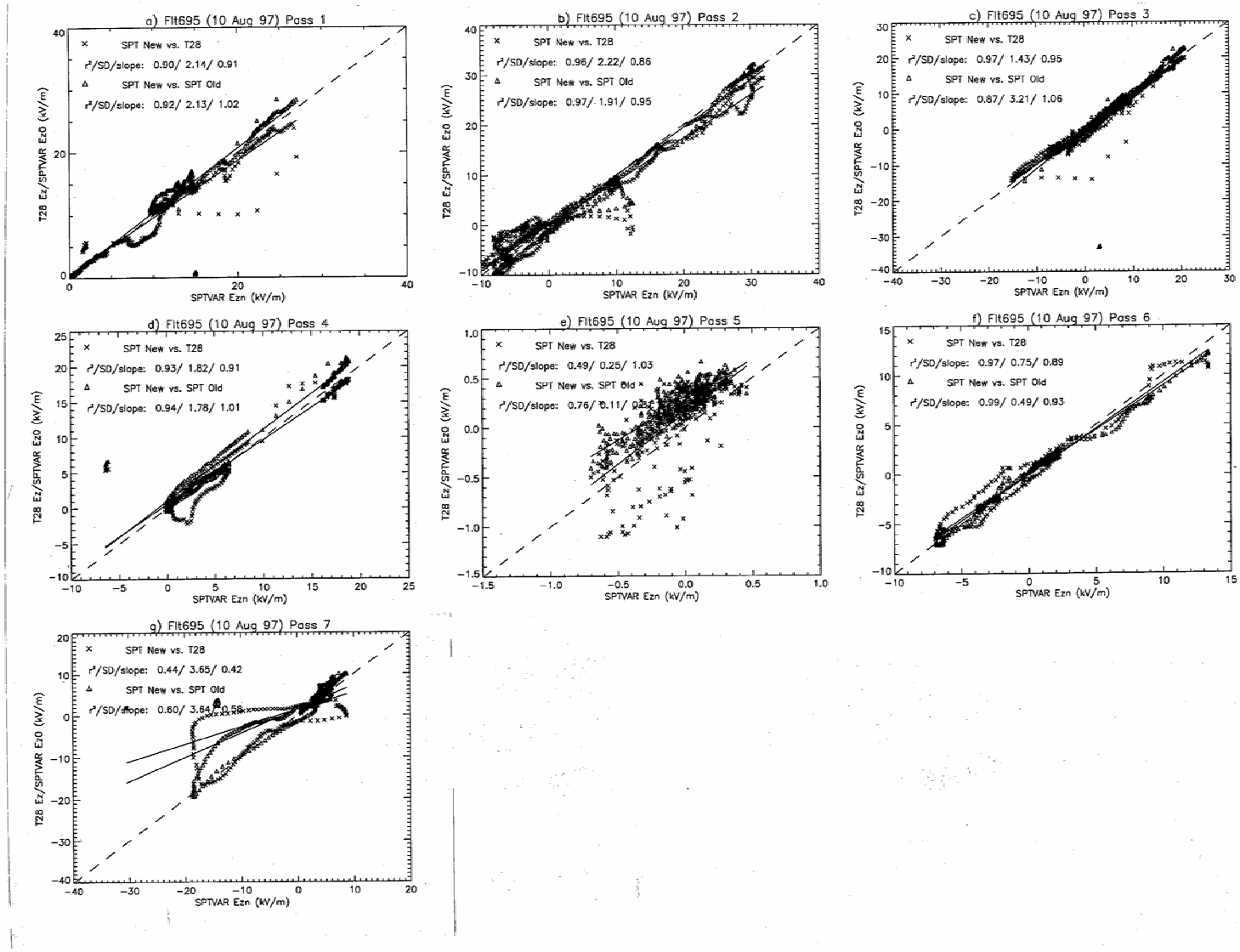

Fig. D29. Regression results comparing E_z from SPTVAR old and new systems and the T-28 on 10 August 1997.

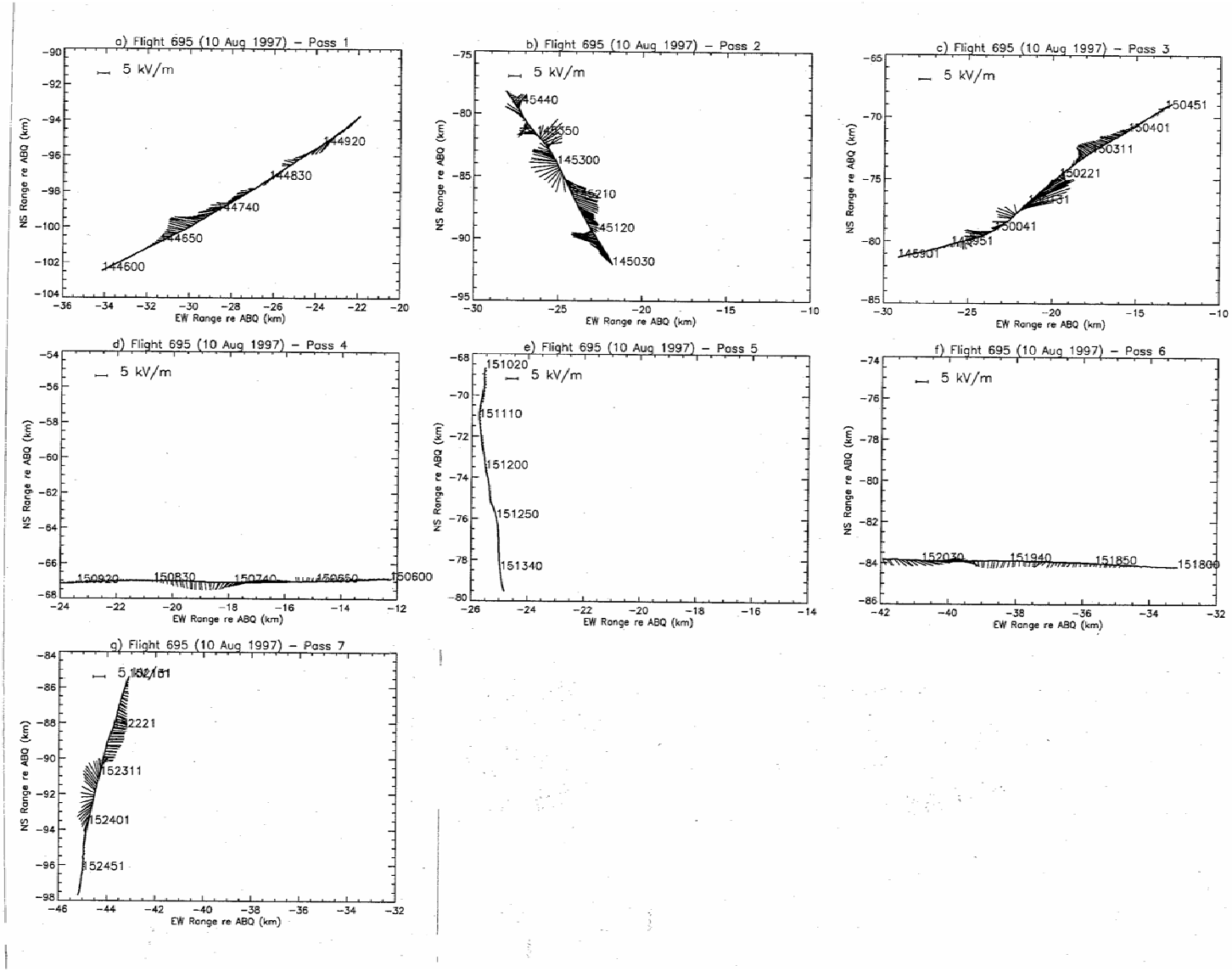

Fig. D30. Projection of the electric field vector on a horizontal plane at the T-28 altitude, based on T-28 measurements during intercomparison legs on 10 August 1997. E_{qy} has been used to represent the x-component of the field vector.

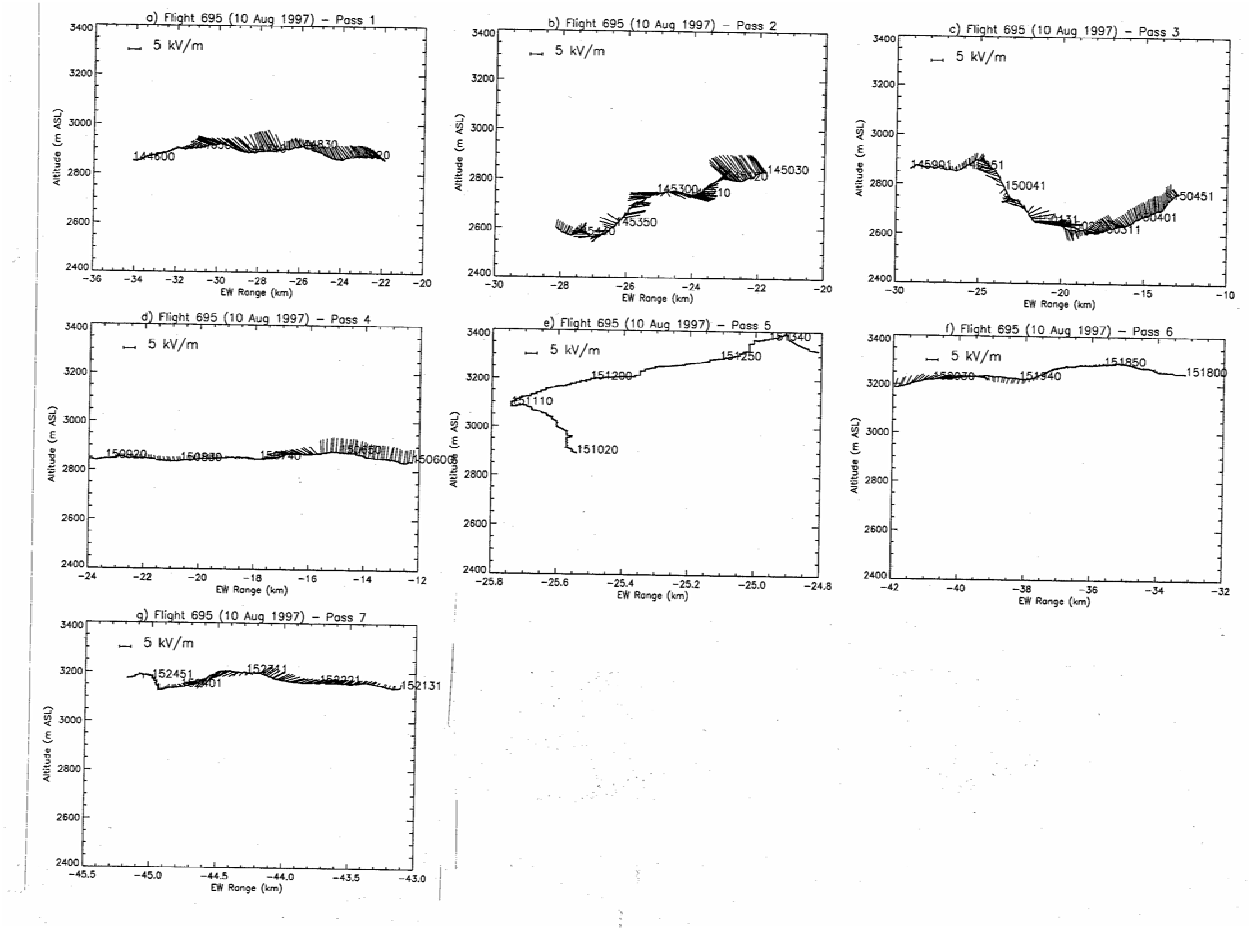

Fig. D31. Projection of the electric field vector on a vertical plane along the T-28 track, based on T-28 measurements during intercomparison legs on 10 August 1997. E_{qy} has been used to represent the x-component of the field vector.

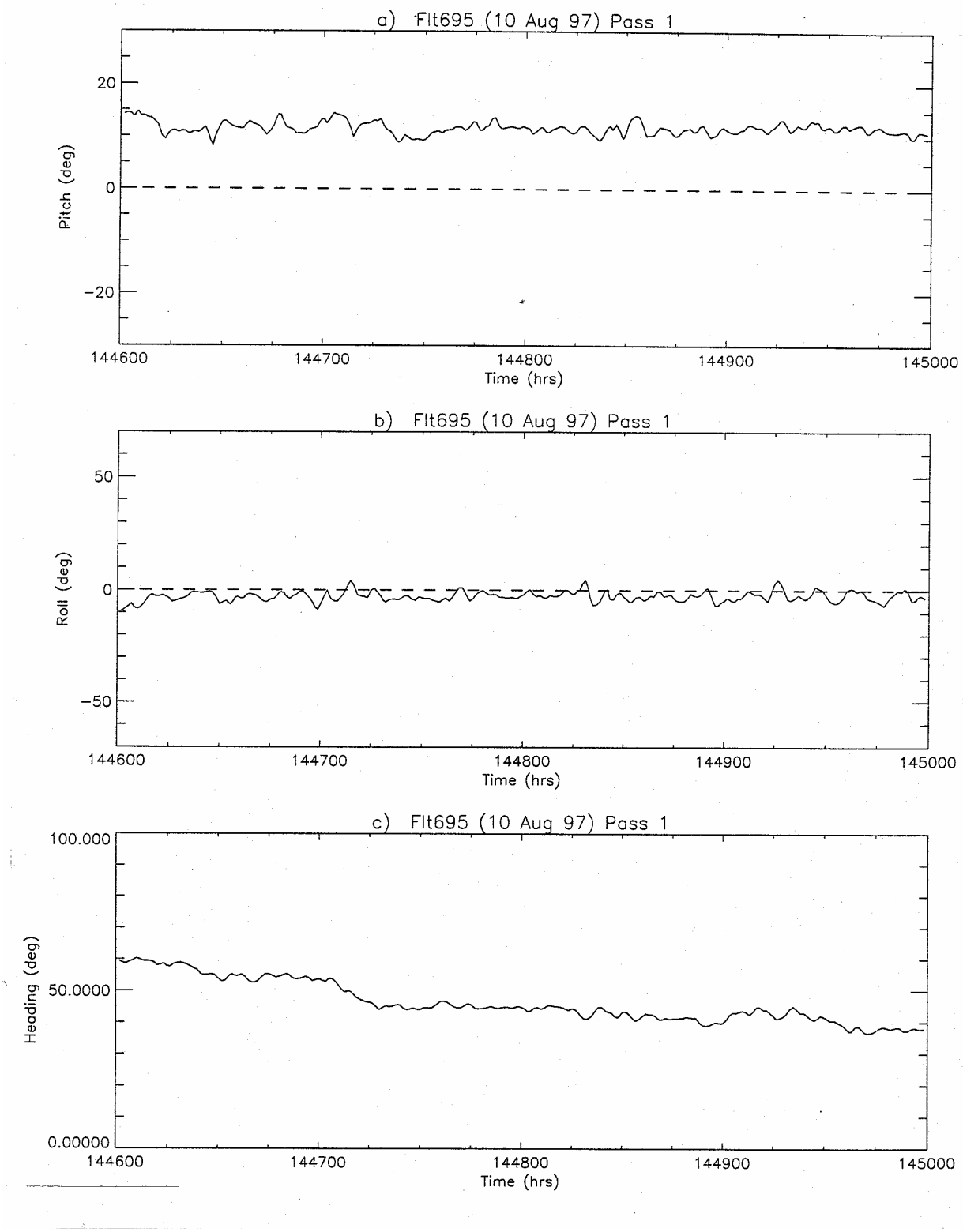

Fig. D32. Pitch, roll, and heading for the T-28 during the 1st intercomparison leg on 10 August 1997.

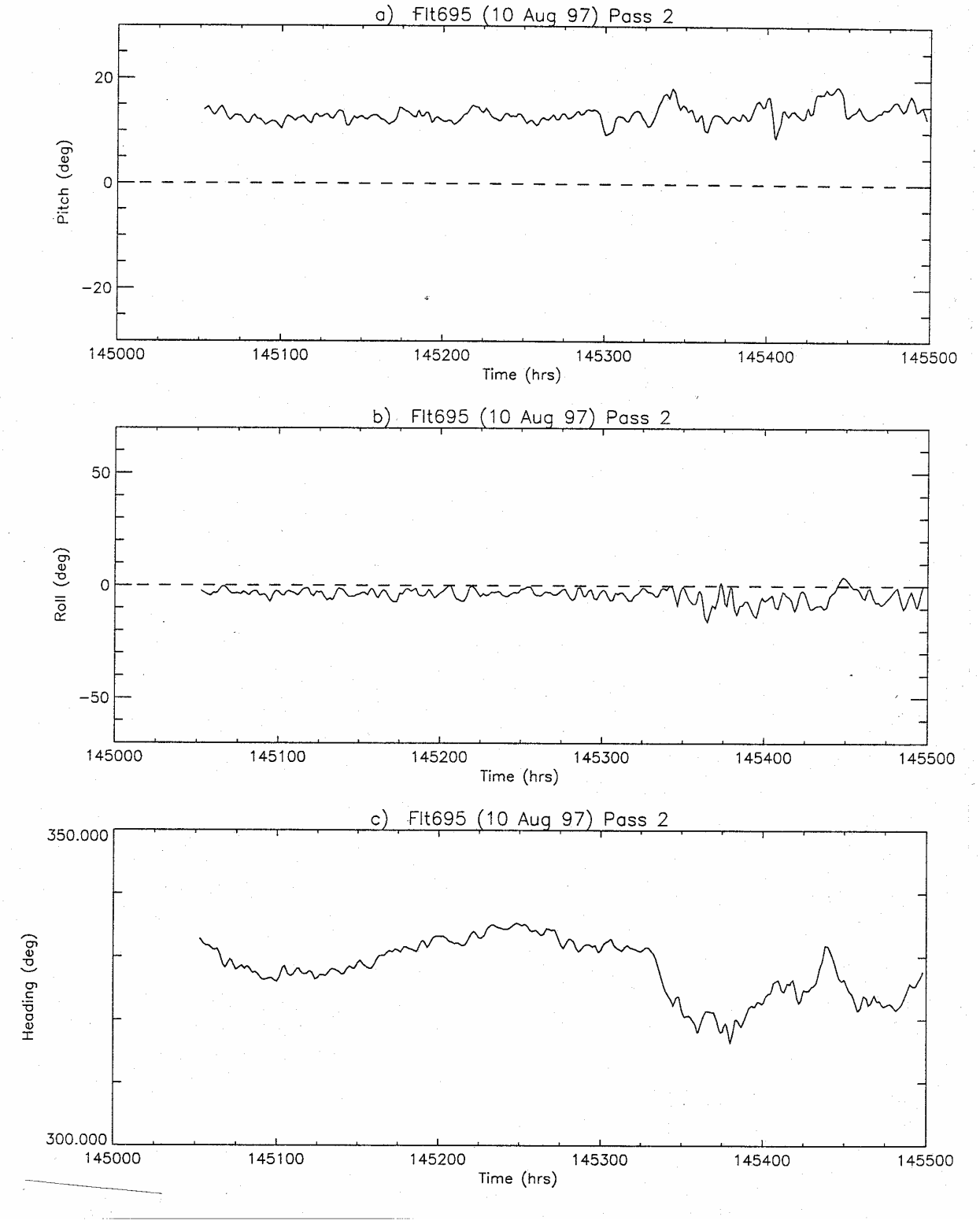

Fig. D33. Pitch, roll, and heading for the T-28 during the 2nd intercomparison leg on 10 August 1997.

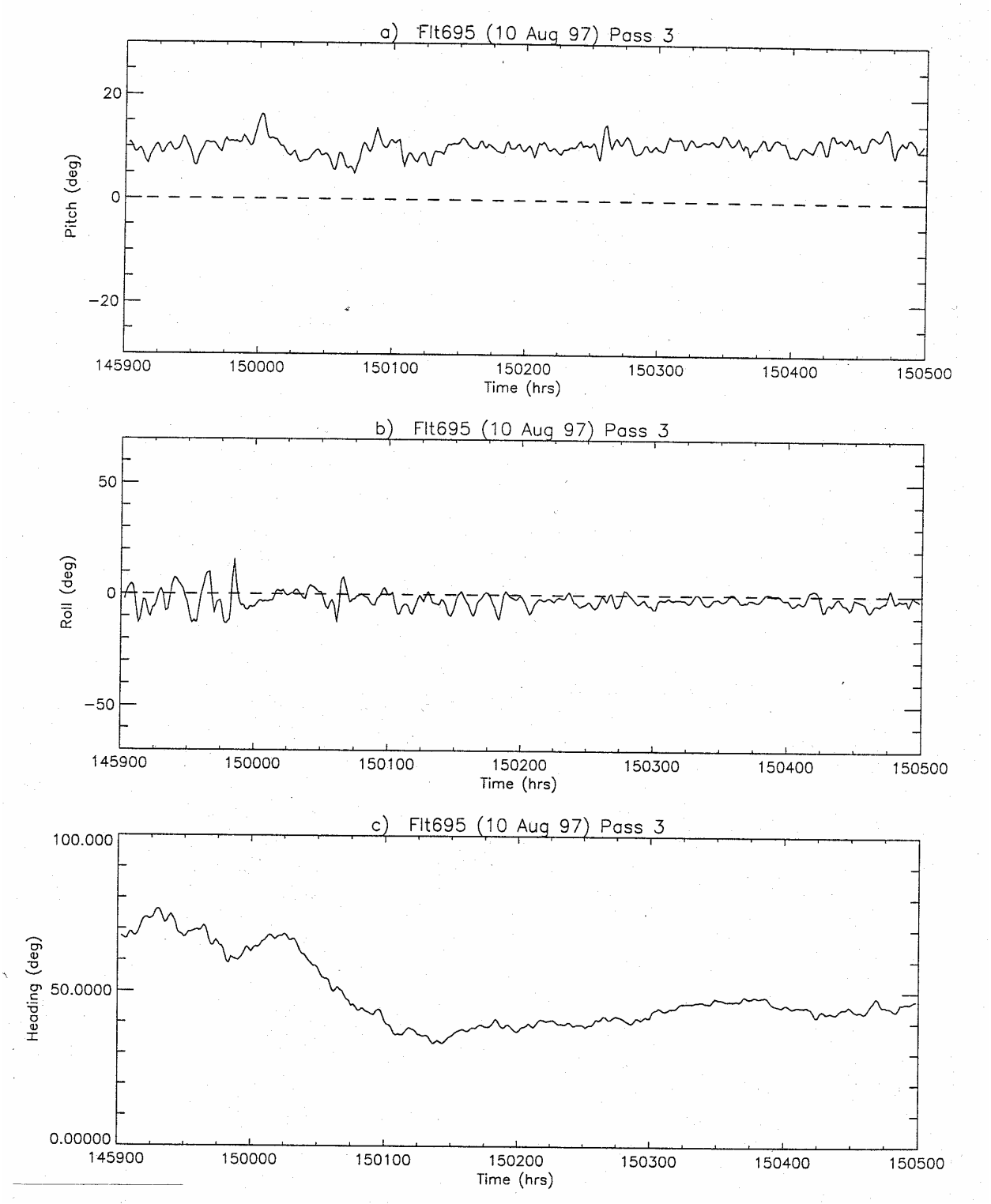

Fig. D34. Pitch, roll, and heading for the T-28 during the 3rd intercomparison leg on 10 August 1997.

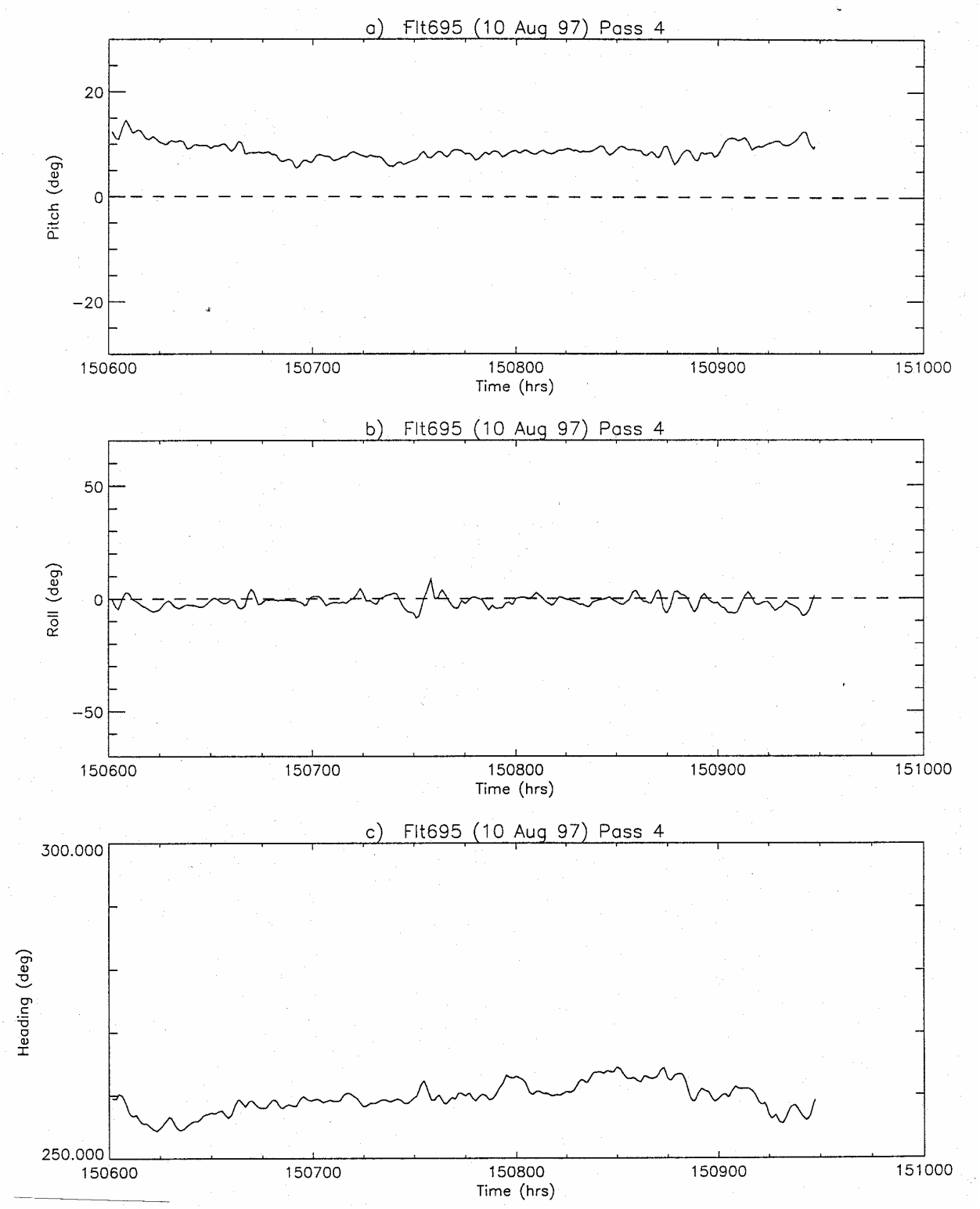

Fig. D35. Pitch, roll, and heading for the T-28 during the 4th intercomparison leg on 10 August 1997.

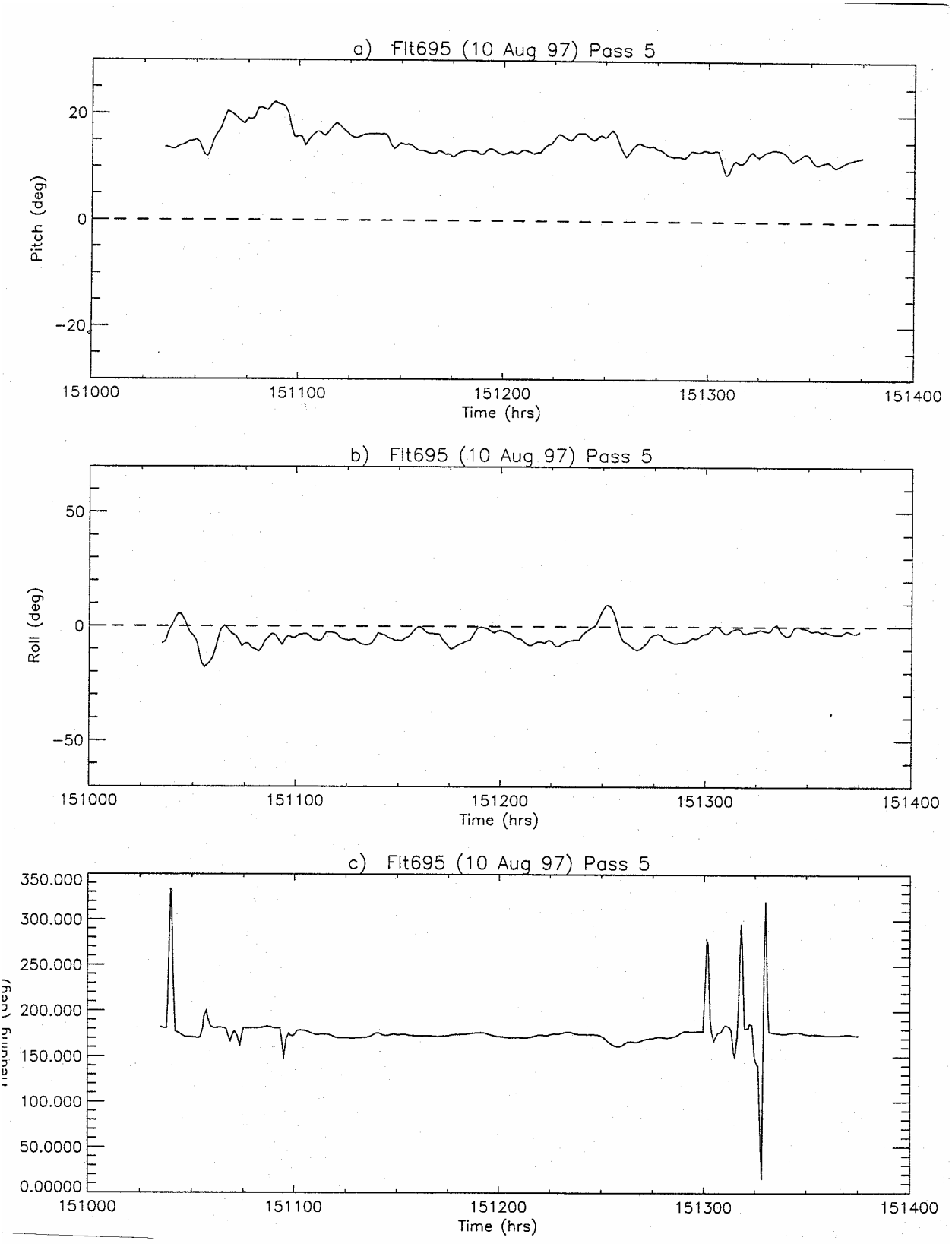

Fig. D36. Pitch, roll, and heading for the T-28 during the 5th intercomparison leg on 10 August 1997.

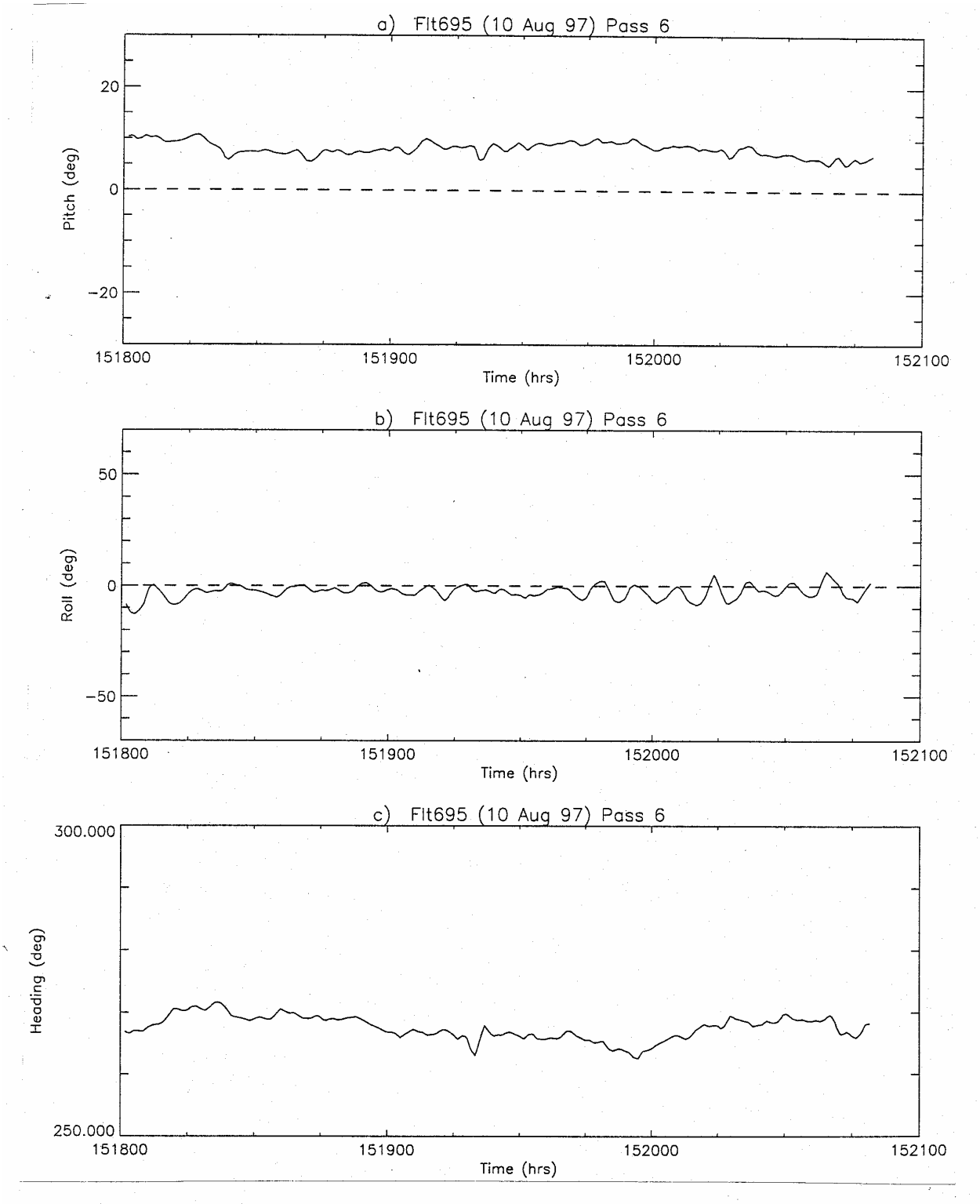

Fig. D37. Pitch, roll, and heading for the T-28 during the 6th intercomparison leg on 10 August 1997.

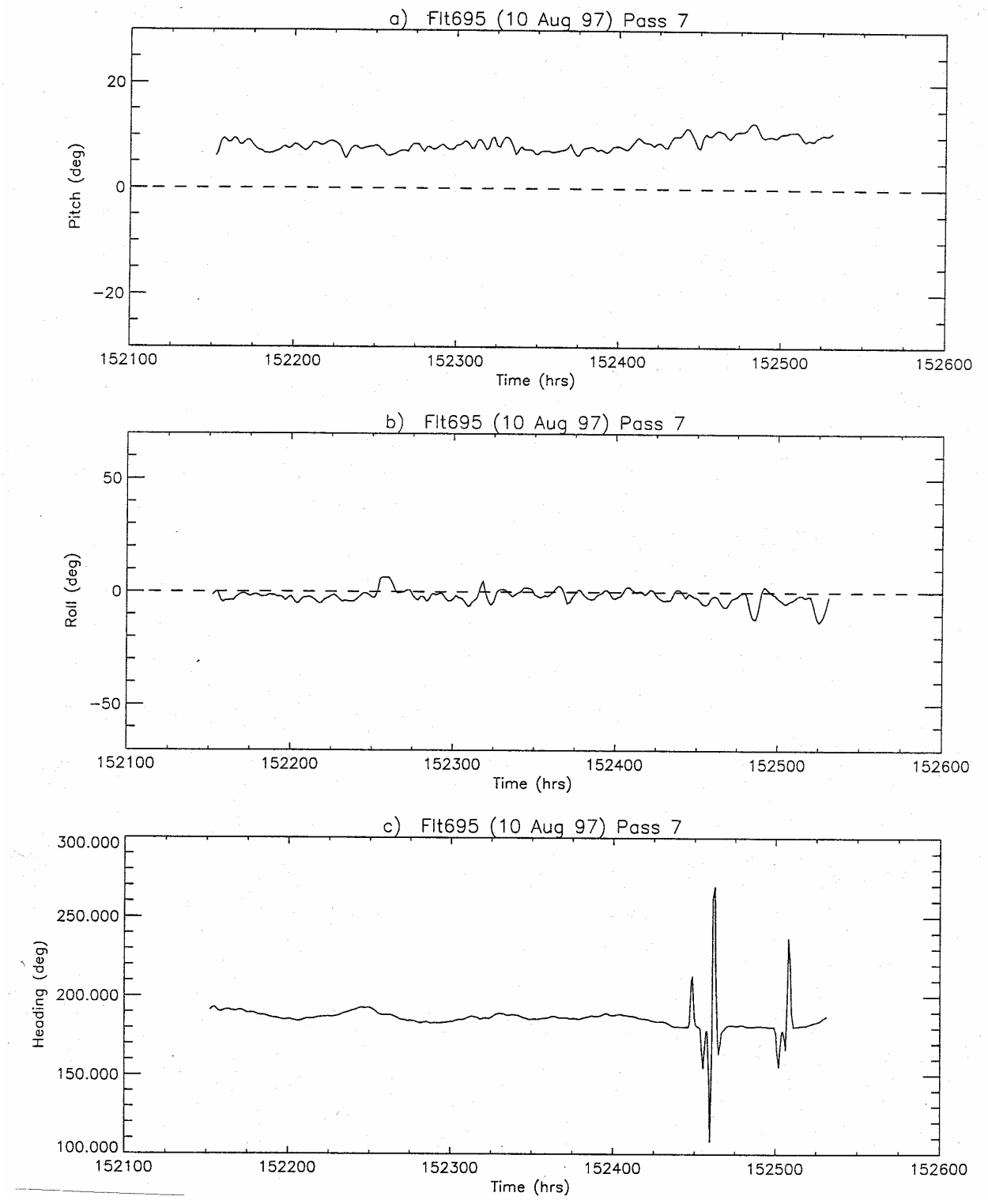

Fig. D38. Pitch, roll, and heading for the T-28 during the 7th intercomparison leg on 10 August 1997.

Pass 1 (9 August 1997)

X Component

Time Sequence (Fig. D1a)

All three systems indicate a positive field from the beginning of the pass (152600) to about 152730. This is followed by a negative excursion for the remainder of the pass. The two positive spikes at the beginning and ending of the pass in the T-28 data are caused by radio transmissions.

Regression (Fig. D-8a)

New SPTVAR vs. T-28 system: The slope is 0.64, indicating that E_{qy} needs to be re-scaled to match E_x in magnitude. The enhancement matrix (8) indeed is consistent with this. Compare the E_l and E_r elements in the 1st (x) and 4th(Q) columns. Their ratios match the slope in this regression. The r^2 value is 0.8, indicating a good correlation in the trends.

New vs. old SPTVAR system: The slope of 0.79 indicates the old SPTVAR system is measuring smaller fields than the new one. The correlation is high at 0.91.

Y Component

Time Sequence (Fig. D-1b)

All three systems show a very similar field up to 152705, with a small 2-3 kV/m positive peak, followed by a small negative field with a 2-4 kV/m peak. Over the next 15 seconds, all the systems show a similar trend, except the T-28 meters indicate a positive field while the two SPTVAR systems indicate a negative field. Over the remainder of the pass, the agreement among all three systems is very good.

Regression (Fig. D-9a)

New SPTVAR vs. T-28 system: The regression results are poor during this pass due to the large negative excursion in the new SPTVAR measurements. Examination of the scatter in the points indicates that the regression would be fair if that interval were excluded.

New vs. old SPTVAR system: As above, the large negative excursion in the new SPTVAR system measurements results in a poor regression. The scatter of the points exclusive of this interval indicates good correlation between the measurements.

Z Component

Time Sequence (Fig. D-1c)

All three systems indicate a positive field over the entire pass, which peaks near 152730. The T-28 system appears to lag the SPTVAR systems by a few seconds, probably due to the spatial displacement of the planes. The two transients near the

beginning and ending of the pass in the T-28 data are caused by radio transmissions.

Regression (Fig. D-10a)

New SPTVAR vs. T-28 system: The slope is 0.70 and indicates that the retrieval based on the new SPTVAR system is yielding larger fields than retrieval based on the T-28 system. The scatter is relatively large, as evidenced by the standard deviation about the regression of 2.64. The correlation is good with an r^2 value of 0.84.

New vs. old SPTVAR system: The new SPTVAR system was measuring larger values than the old system, as indicated by the slope of 0.72. The r^2 value is close to one. Most of the scatter is caused by the interval between 152710 and 152730.

Horizontal and Vertical Fields (Figs. D-11a, D-12a)

During the first part of the pass the fields are pointing slightly upward and toward the west. During the later half of the pass, they switch to the north and more upward.

Pass 2 (9 August 1997)

X Component

Time Sequence (Fig. D-2a)

Magnitudes are very small. The new and old SPTVAR systems show very good agreement in tracking a small positive field that peaks about 153130, near 1 kV/m, followed by a negative one that peaks at 153300, near 1 kV/m. The measurements from the T-28 indicate negligible fields during this pass with little resemblance to the SPTVAR system measurements.

Regression (Fig. D-8b)

New SPTVAR vs. T-28 system: As expected, from examination of Fig. D-8a, there is little correlation in measurements with a slope and regression coefficient of nearly zero.

New vs. old SPTVAR system: The slope is nearly one and the regression coefficient is 0.86, indicating good agreement between the two systems.

Y Component

Time Sequence (Fig. D-2b)

All three systems indicate very good agreement in a small positive field that peaks about 153215, in the vicinity of 2-2.5 kV/m.

Regression (Fig. D-9b)

New SPTVAR vs. T-28 system: The slope of 0.86 indicates the T-28 is retrieving smaller fields. The correlation is very good with $r^2 = 0.99$.

New vs. old SPTVAR system: The regression is very good with a slope of 0.94 and r^2 of 0.97. A small bias of about 0.5 kV/m is present between the two systems during this pass.

Z Component

Time Sequence (Fig. D-2c)

All three systems indicate negligible to small positive fields that peak near 153230, at less than 1.0 kV/m. The transients in the T-28 data near the beginning and ending of the pass are caused by radio transmissions.

Regression (Fig. D-10b)

New SPTVAR vs. T-28 system: The regression results are deceivingly poor here as the radio transmission transients in the T-28 data skew the slope and introduce relatively large deviations from the best fit.

New vs. old SPTVAR system: The regression results are not as good as other passes due to the small fields. There appears to be a 0.5 kV/m bias between the two systems during this pass.

Horizontal and Vertical Fields (Figs. D-11b, D-12b)

Small fields are oriented mostly to the south and horizontally.

Pass 3 (9 August 1997)

X Component

Time Sequence (Fig. D-3a)

The two SPTVAR systems indicate very good agreement in a positive field from the beginning of the pass to 153530, peaking near 153500, at about 3 kV/m, followed by a negative-going field, to the end of the pass. The T-28 system indicates a similar pattern but appears to lag the SPTVAR system measurements by about 15 seconds, with an amplitude about 60 percent of the SPTVAR systems.

Regression (Fig. D-8c)

New SPTVAR vs. T-28: The slope indicates the T-28 is retrieving an E_{qy} magnitude less than half of E_x of the new SPTVAR system due partly to the lag mentioned above and partly to the smaller measured values. The curve in the alignment of the points also is indicative of the lag.

New vs. old SPTVAR system: The regression results are very good with a slope of 1.09 and r^2 of 0.99.

Y Component

Time Sequence (Fig. D-3b)

All three systems show good agreement in the measurement of a positive field that peaks near 153530 at about 6-7 kV/m.

Regression (Fig. D-9c)

New SPTVAR vs. T-28 system: The regression results are very good with a slope of 0.9 and correlation factor of 1.0. The T-28 system is retrieving values about 90 percent of those of the new SPTVAR system.

New vs. old SPTVAR system: Very good results with a slope of 0.94 and correlation factor of 0.99. There is a small 0.5 to 1.0 kV/m bias between the two systems.

Z Component

Time Sequence (Fig. D-3c)

All three systems show fair agreement in the measurement of a positive field that peaks near 153530, at 2-3 kV/m.

Regression (Fig. D-10c)

New SPTVAR vs. T-28 system: The slope indicates the T-28 is measuring fields 74 percent smaller than those of the new SPTVAR system. The correlation factor is high at 0.91.

New vs. old SPTVAR system: The regression between these two systems is very good, with a slope and r^2 of 0.98.

Horizontal and Vertical Fields (Figs. D-11c, D-12c)

The field vectors indicate a charge center is located horizontally toward the east.

Pass 4 (9 August 1997)

X Component

Time Sequence (Fig. D-4a)

The two SPTVAR systems indicate good agreement during the first 30 seconds of the pass, but disagree over the remainder of the pass. The T-28 system appears to lag the SPTVAR measurements by several seconds. Given the relatively large magnitudes of the measured components, the disagreement is puzzling.

Regression (Fig. D-8d)

New SPTVAR vs. T-28 system: The regression results are poor. It appears that the scatter is low about the points over the first half of the pass but is very large subsequently.

New vs. old SPTVAR system: As in the previous regression, results also are poor. Again, the scatter is low over the first half of the pass, but is large subsequently.

Y Component

Time Sequence (Fig. D-4b)

As in the X component, there is fair agreement in a positive field among the three systems in the first half of the pass, but a large divergence, not only between the new SPTVAR and T-28 system, but also between the new and old SPTVAR systems, over the last half of the pass.

Regression (Fig. D-9d)

New SPTVAR vs. T-28 system: As expected from examination of the above time sequence plots, the scatter in the points over the first half of the pass is low, but is very high subsequently.

New vs. old SPTVAR system: Same comments as above.

Z Component

Time Sequence (Fig. D-4c)

Given the relatively large magnitude of E_z, the disagreement between E_z retrieved from the 3 systems is puzzling.

Regression (Fig. D-10d)

New SPTVAR vs. T-28 system: Same comments as for the Y component.

New vs. old SPTVAR system: Same comments as for the Y component.

Horizontal and Vertical Fields (Figs. D-11d, D-12d)

During the first half of the pass, the fields are oriented toward the northwest and downward. Over the last half of the pass, the fields are oriented toward the northeast and still downward.

Pass 5 (9 August 1997)

X Component

Time Sequence (Fig. D-5a)

All three systems follow a similar trend from a negative field at the beginning of the pass and transitioning to a positive field over the remainder of the pass. Magnitude is relatively small. The only good agreement in magnitude of the measurements is between the new and old SPTVAR systems, over the last 45 seconds of the pass.

Regression (Fig. D-8e)

New SPTVAR vs. T-28 system: The scatter of the points appears to fall along two lines – one for the beginning and negative field interval of the pass, and another for the later and positive field interval of the pass. Over the latter part of the pass, the T-28 is measuring fields about half those of the new SPTVAR system. If the first part of the pass were excluded, the r^2 value would be greater than 0.9.

New vs. old SPTVAR system: The same scatter characteristics are observed here as in the above regression. Over the later part of the pass, the r^2 value is greater than 0.87.

Y Component

Time Sequence (Fig. D-5b)

The trends in the measurements among the three systems show little similarity. For example, from about 154000 to 154045, the new SPTVAR system is measuring 1 kV/m positive fields while the old SPTVAR and T-28 systems are measuring negative fields of differing magnitudes.

Regression (Fig. D-9e)

New SPTVAR vs. T-28 system: The scatter of the points and the statistics indicate little correlation between the measurements.

New vs. old SPTVAR system: Agreement is poor.

Z Component

Time Sequence (Fig. D-5c)

Over the first half of the pass, there is little similarity in the trend and magnitude of the measurements among the three systems; however, over the last half of the pass, after 154015, the agreement is good.

Regression (Fig. D-10e)

New SPTVAR vs. T-28 system: The scatter of the points over the last half of the pass is small; however, the large scatter over the first half of the pass yields poor regression statistics.

New vs. old SPTVAR system: The old SPTVAR system behaves more like the T-28 system than the new STPVAR system.

Horizontal and Vertical Fields (Figs. D-11e, D-12e)

The vectors indicate the field is oriented toward the east and southeast and downward.

Pass 6 (9 August 1997)

X Component

Time Sequence (Fig. D-6a)

The measurements from the new and old SPTVAR systems bear some resemblance, especially during the first 30 seconds of the pass. However, there is no similarity between the T-28 system measurements and the two SPTVAR systems. Note the fields are small here (less than 1.5 kV/m).

Regression (Fig. D-8f)

New SPTVAR vs. T-28 system: The scatter and statistics indicate no correlation between the two sets of measurements.

New vs. old SPTVAR system: The slope indicates the old SPTVAR system is measuring about 66 percent of the new one. The scatter is relatively large since the field strength is small. The r^2 value is only 0.57.

Y Component

Time Sequence (Fig. D-6b)

All three systems indicate very similar trends, starting with an approximate 2 kV/m negative field, and transitioning to a nearly-zero or slightly positive field.

Regression (Fig. D-9f)

New SPTVAR vs. T-28 system: Both the scatter and statistics indicate a relatively good regression, given the small fields. The slope is 0.92 and r^2 is 0.99.

New vs. old SPTVAR system: Same comments as previous regression, except slope is 1.03 and r^2 is 0.96.

Z Component

Time Sequence (Fig. D-6c)

All three systems indicate a fairly constant negative field of 1-2 kV/m. A large transient of unknown cause (~5 seconds duration) appears in the new SPTVAR system measurements just after 154145.

Regression (Fig. D-10f)

New SPTVAR vs. T-28 system: Both scatter and statistics indicate a good regression, given the small 1-2 kV/m fields. The slope is 0.89 and r^2 is 0.94.

New vs. old SPTVAR system: Same comments as previous regression except slope is 0.95 and r^2 is 0.92.

Horizontal and Vertical Fields (Figs. D-11f, D-12f)

Small horizontal fields are apparent over the first half of the pass (154130-154220) pointing toward the north.

Pass 7 (9 August 1997)

X Component

Time Sequence (Fig. D-7b)

The field strength is very low during this pass (less than 0.5 kV/m). The T-28 system indicates fields over most of the pass of less than 0.2 kV/m. There appears to be little similarity among the three systems, probably due to the small fields.

Regression (Fig. D-8g)

New SPTVAR vs. T-28 system: The scatter and statistics indicate no correlation between the measurements.

New vs. old SPTVAR system: Same comments as above regression.

Y Component

Time Sequence (Fig. D-7b)

All three systems indicate similar trends starting with a positive field that peaks about 154330 and transitions to a negative field over the last two-thirds of the pass. The new SPTVAR and T-28 system show good agreement in the magnitude of the field over the last half of the pass, but the T-28 system measures about half of the new SPTVAR system over the first half of the pass. There is a bias of about 0.5 kV/m between the new and old SPTVAR systems, which has been observed in many of the previous passes.

Regression (Fig. D-9g)

New SPTVAR vs. T-28 system: The scatter shows that the data fit two regression lines. In the first half of the pass, the slope is much less than one and in the last half, the slope is close to one. The scatter is small and r^2 would be greater than 0.86, if the data were partitioned.

New vs. old SPTVAR system: Given the small fields present, the scatter is surprisingly low about the regression line in which r^2 is 0.85. The slope is 0.87.

Z Component

Time Sequence (Fig. D-7c)

All three systems show very similar trends and magnitudes, starting with a 1-1.5 kV/m negative field and transitioning to a nearly zero or small positive field after 154500.

Regression (Fig. D-10c)

New SPTVAR vs. T-28 system: The scatter and statistics indicate a good regression with a slope of 0.89 and r^2 of 0.94.

New vs. old SPTVAR system: Same comment as above regression, except slope is 0.95 and r^2 is 0.92. A small bias of 0.3 kV/m is evident between these two sets of measurements.

Horizontal and Vertical Fields (Figs. D-11g, D-12g)

Negligible fields are observed by the T-28 system during this pass.

FLIGHT 695 (10 August 1997)

Pass 1

X Component

Time Sequence (Fig. D-20a)

All three systems indicate similar trends and positive fields over most of the pass. The new SPTVAR system shows a large negative transient of unknown cause near the beginning of the pass. Significant precipitation is indicated over this pass but does not seem to degrade E_{qy}.

Regression (Fig. D-27a)

New SPTVAR vs. T-28 system: The scatter of the points indicates good correlation between the measurements in which the T-28 indicates lower values than the new SPTVAR system. However, the regression line and statistics are affected by this transient and yields slope and r^2 values that are artificially low.

New vs. old SPTVAR system: Same comments as for the new SPTVAR vs. T-28 regression.

Y Component

Time Sequence (Fig. D-20b)

All three systems indicate relatively large negative fields. The old SPTVAR system measured the field to be smaller in magnitude than the new SPTVAR system, while the T-28 indicated half the magnitude over much of the pass. The rapid change at 144815 is probably due to lightning.

Regression (Fig. D-28a)

New SPTVAR vs. T-28 system: The slope of the regression line (0.61) reflects what is observed in the time sequence; that is, the T-28 system E_y is significantly less than E_{yn} from the new SPTVAR system. The scatter about the regression line is low ($r^2 = 0.87$).

New vs. old SPTVAR system: The old SPTVAR system indicates values about 76 percent of those from the new SPTVAR system. The scatter about the regression line is very low and the correlation is high ($r^2 = 0.96$).

Z Component

Time Sequence (Fig. D-20c)

All three systems indicate very good agreement in both trend and magnitude. The new SPTVAR system indicates the same transient, as it did in the *X* component, near the beginning of the pass. Two other smaller transients occur between 144700 and 144715, and at 144930. The rapid change at 144815 is probably due to lightning.

Regression (Fig. D-29c)

New SPTVAR vs. T-28 system: The scatter and regression results are very good with a slope of 0.91 and r^2 factor of 0.90.

New vs. old SPTVAR system: Same comment as above, except with a slope of 1.06 and r^2 of 0.84.

Horizontal and Vertical Fields (Figs. D-30a, D-31a)

Throughout most of this pass the electric fields are oriented west northwest and upward.

Pass 2 (10 August 1997)

X Component

Time Sequence (Fig. D-21a)

All three systems indicate similar trends, but of differing magnitudes. The field oscillates from positive to negative fields for about three cycles. Significant precipitation persists throughout this pass.

Regression (Fig. D-27c)

New SPTVAR vs. T-28 system: The regression indicates the T-28 E_{qy} values are about 65 percent of E_x from the new SPTVAR system. The scatter about the regression is low and the correlation is high (r^2 = 0.95).

New vs. old SPTVAR system: The regression line indicates that the old SPTVAR system E_{xo} is even lower than the T-28 E_{qy} - only 43% of the new SPTVAR E_{xn} measurements. There is some significant scatter near the extremes and is reflected in both the low value of slope (0.43) and the relatively low value of r^2 (0.68).

Y Component

Time Sequence (Fig. D-21b)

There is good agreement among the three systems in the measurements of a relatively large field that oscillates between negative and positive.

Regression (Fig. D-28b)

New SPTVAR vs. T-28 system: The regression line indicates the T-28 E_y is only 71 percent of the new SPTVAR E_{yn}. The scatter about the regression is relatively low (r^2 = 0.92).

New vs. old SPTVAR system: The regression is very similar to the above with a slope of 0.74 and r^2 of 0.96.

Z Component

Time Sequence (Fig. D-21c)

There is good agreement in trend and magnitude among all three systems as the relatively large field oscillates between positive and negative.

Regression (Fig. D-29c)

New SPTVAR vs. T-28 system: The regression results bear out the observations of the time sequence that the agreement is very good. The slope is 0.86 and r^2 is 0.96.

New vs. old SPTVAR system: Same comment as above except slope is 0.95 and r^2 *i*s 0.97.

Horizontal and Vertical Fields (Figs. D-30b, D-31b)

The field vectors estimated from the T-28 system switch from westward to eastward pointing at least three times. At the beginning and ending of the pass, they are oriented upward. Over the middle part of the run, they are oriented downward. The indication is that the charge distribution near the aircraft track is composed of several discrete charge centers.

Pass 3 (10 August 1997)

X Component

Time Sequence (Fig. D-22a)

All three systems indicate similar trends but significantly different magnitudes are observed over about half of the pass. There is a transient in the old SPTVAR data near the start of the pass.

Regression (Fig. D-27c)

New SPTVAR vs. T-28 system: The regression indicates the T-28 E_{qy} is about 54 percent of E_{xn} from the new SPTVAR system. The scatter is relatively large (r^2 is only 0.73).

New vs. old SPTVAR system: Most of the points appear to cluster about the 1:1 line, but some of the scatter causes the slope to be artificially low at 0.73. The scatter also causes the r^2 value to have a low value of 0.77.

Y Component

Time Sequence (Fig. D-22b)

All three systems show similar trends. The new SPTVAR E_{yn} and T-28 E_y appear to agree better in the magnitude of the positive fields but the new and old SPTVAR E_{yn} and E_{yo} appear to agree better in the magnitude of the negative fields.

Regression (Fig. D-28c)

New SPTVAR vs. T-28 system: The values during the positive field appear to lie on the 1:1 line. The large scatter from the values during the negative field cause the slope (0.82) to be less than one. The scatter is relatively low overall and correlation is high (r^2 = 0.91).

New vs. old SPTVAR system: Most of the points, during the period of negative field, lie on the 1:1 line. During the positive field period the old SPTVAR system is measuring values lower than the new one. The scatter is very low and the correlation is very high (r^2 - 0.99).

Z Component

Time Sequence (Fig. D-22c)

All three systems indicate very good agreement in both trend and magnitude. The same transient observed in the old SPTVAR system, in the X component, near the beginning of the pass, is seen here. Several rapid field changes due to lightning are evident.

Regression (Fig. D-29c)

New SPTVAR vs. T-28 system: The regression results are very good with a slope of 0.95 and r^2 of 0.97.

New vs. old SPTVAR system: Same as for the comparison between SPTVAR E_{zo} and T-28 E_z, except slope is 1.06 and r^2 is 0.87.

Horizontal and Vertical Fields (Figs. D-30c, D-31c)

As in the previous pass, the fields appear to be very dynamic and switch from south (145951), to west (150041), to northeast (150131), and finally to northwest (150311). Except for a short period near the beginning of the pass (145951), in which the fields point downward, the fields are oriented upward during most of the pass. The changes in the field orientation are somewhat correlated with changes in altitude. Evidence in the E_z record of lightning suggest that lightning may be at least partially responsible for the complicated distribution of charge near the aircraft track.

Pass 4 (10 August 1997)

X Component

Time Sequence (Fig. D-23a)

All three systems indicate relatively good agreement in trend with small and somewhat different magnitudes over some parts of the pass. There is a large transient in the new SPTVAR system just after 150815. Precipitation was present during the middle of the pass. Lightning is probably responsible for the rapid change indicated just after 150700.

Regression (Fig. D-27d)

New SPTVAR vs. T-28 system: The regression results are unrepresentative due to the transient in the new SPTVAR data. Otherwise, the scatter appears to be low and lie on the 1:1 line.

New vs. old SPTVAR system: Same comments as for the above regression.

Y Component

Time Sequence (Fig. D-23b)

All three systems indicate a similar trend and all agree in magnitude over the last two-thirds of the pass; however, during the first third of the pass, before the lightning event when a negative field is present, the T-28 indicated less than half the magnitude of the new and old SPTVAR systems.

Regression (Fig. D-28c)

New SPTVAR vs. T-28 system: As indicated above, the scatter of the points, during the positive field (after the lightning), is along the 1:1 line, and is low; however, the scatter before the lightning during the negative field period, is high and shows a 4-6 kV/m bias with respect to the new SPTVAR system.

New vs. old SPTVAR system: The old SPTVAR system is indicating values somewhat lower than the new SPTVAR system as the slope is 0.85. The scatter appears to be very low but the low r^2 value (0.69) is caused by the transient in the new SPTVAR system data.

Z Component

Time Sequence (Fig. D-23c)

All three systems indicate similar trends; however, over the first half of the pass, the old SPTVAR system indicates values higher than those from the other two systems. The transient, apparent in the *X* and *Y* component of the new SPTVAR system, is also observed here.

Regression (Fig. D-29d)

New SPTVAR vs. T-28 system: The regression results are very good with a slope of 0.91 and r^2 of 0.93.

New vs. old SPTVAR system: Same as above except slope is 1.01 and r^2 is 0.94.

Horizontal and Vertical Fields (Figs. D-30d, D-31d)

The vectors indicate a north pointing field over the first third of the pass (before the lightning), south pointing over the next third of the pass, and north pointing again over the last third of the pass. The field is oriented upward over most of the pass.

Pass 5 (10 August 1997)

X Component

Time Sequence (Fig. D-24a)

The field is very small here. The new and old SPTVAR indicate negative E_x less than 0.5 kV/m over most of the pass. The T-28 system indicates negligible E_{qy} less than 0.2 kV/m.

Regression (Fig. D-27e)

New SPTVAR vs. T-28 system: The regression results indicate little correlation between the two systems for these small fields.

New vs. old SPTVAR system: Same comments as above regression.

Y Component

Time Sequence (Fig. D-24b)

All three systems indicate small magnitudes and a similar trend in which a small negative field decreases from 0.5-1.5 kV/m to nearly zero or slightly negative at the end of the pass. The old SPTVAR system indicates the fields are about 0.5 kV/m larger than either of the other two systems. Rapid field changes in the plots indicate several lightning events.

Regression (Fig. D-28e)

New SPTVAR vs. T-28 system: The regression indicates the T-28 is measuring values about 77 percent of those of the new SPTVAR system. The scatter was low and correlation is high ($r^2 = 0.94$).

New vs. old SPTVAR system: The slope is good at 0.96, the scatter is low, and the correlation is high ($r^2 = 0.90$). There is an approximate 0.5 kV/m bias between the two systems.

Z Component

Time Sequence (Fig. D-24c)

The three systems indicate some similar trends in a small field that is generally less than 0.5 kV/m. The new and old SPTVAR systems indicate better agreement, except for a 0.2 kV/m bias between them. Several lightning-induced field changes are clearly indicated, in agreement with the changes in E_y.

Regression (Fig. D-29e)

New SPTVAR vs. T-28 system: The slope is close to one (1.03) but the scatter is large relative to the size of the fields ($r^2 = 0.49$).

New vs. old SPTVAR system: There is relatively large scatter about the regression line ($r^2 = 0.76$) but the alignment along the 1:1 line is fairly good. The ~0.2 kV/m bias between the two systems is manifested as a displacement of the points above the 1:1 line.

Horizontal and Vertical Fields (Figs. D-30e, D-31e)

The fields are negligible during this pass.

Pass 6 (10 August 1997)

X Component

Time Sequence (Fig. D-25a)

Once again, the three systems indicate similar trends. In general, the old SPTVAR E_{xo} and T-28 E_{qy} have magnitudes lower than the new SPTVAR system E_{xn}.

Regression (Fig. D-27f)

New SPTVAR vs. T-28 system: The T-28 E_{qy} is about 59 percent of E_{xn} of the new SPTVAR system. The scatter is relatively low and correlation is high (r^2 = 0.91).

New vs. old SPTVAR system: The old SPTVAR system E_{xo} is about 70 percent of the new SPTVAR system. The scatter is low and correlation is high (r^2 = 0.96).

Y Component

Time Sequence (Fig. D-25b)

The three systems show similar trends with the T-28 indicating magnitudes lower than the new SPTVAR system, over most of the pass, but higher near the end. The T-28 appears to lead the other two systems in some of the significant features (local minimum and maximum). It is unknown whether the T-28 was spatially ahead of the SPTVAR during this pass.

Regression (Fig. D-28f)

New SPTVAR vs. T-28 system: The regression indicates that the T-28 E_y is about half of E_{yn} of the new SPTVAR system (slope = 0.52); however, the scatter indicates that over much of the pass the slope was much higher (i.e., the correlation was better).

New vs. old SPTVAR system: The regression is relatively good with a slope of 0.79 and r^2 of 0.98.

Z Component

Time Sequence (Fig. D-25c)

The agreement in trend and magnitude among the three systems is very good.

Regression (Fig. D-29f)

New SPTVAR vs. T-28 system: The regression results are very good with a slope of 0.89 and r^2 of 0.97.

New vs. old SPTVAR system: Same as above, except slope is 0.93 and r^2 is 0.99.

Horizontal and Vertical Fields (Figs. D-30f, D-31f)

The fields are generally south or southeast pointing. Over the first and last third of the pass, the fields are upward pointing. During the middle part of the pass they are downward pointing.

Pass 7 (10 August 1997)

X Component

Time Sequence (Fig. D-26a)

This is much like the previous six passes on this day - the trends are similar but the magnitudes are significantly different over some intervals of the pass. Again, the T-28 system indicates values lower than the new SPTVAR system as does the old SPTVAR system. There is a large 100 kV/m transient in the new SPTVAR system data between 152415 and 152430.

Regression (Fig. D-27g)

New SPTVAR vs. T-28 system: The correlation is better between the two systems than the statistics indicate, due to the large transient in the new SPTVAR system data. However, even without the transient, the scatter appears to be relatively large.

New vs. old SPTVAR system: Same comments apply as for the above regression, except the scatter about the 1:1 line is much lower than that for the new SPTVAR vs. T-28 comparison.

Y Component

Time Sequence (Fig. D-26b)

All three systems show a large negative field, followed by a large positive field, followed by a small negative field. The T-28 system indicates values much lower than the new SPTVAR system. The old SPTVAR system agrees well with the new SPTVAR system in the first half of the pass, but agrees better in magnitude with the T-28 system in the last half of the pass. Two significant transients in the new SPTVAR system data occur between 152415 and 152445.

Regression (Fig. D-28g)

New SPTVAR vs. T-28 system: The regression indicates the T-28 is measuring values about half of those of the new SPTVAR system (slope = 0.47). The scatter and correlation are moderate (r^2 = 0.84).

New vs. old SPTVAR system: During the negative field, the points fall on the 1:1 line and the scatter is low. However, during the positive field, the scatter is large and not along the 1:1 line.

Z Component

Time Sequence (Fig. D-26c)

The three systems indicate similar trends and magnitudes; however, the T-28 system appears to lead the SPTVAR systems by 10 seconds. It is unknown whether the planes were displaced sufficiently in space during this pass to cause this. Two transients in the new SPTVAR system are apparent, coincident with transients in the *Y* component.

Regression (Fig. D-29g)

New SPTVAR vs. T-28 system: The regression results appear poor due to the displacement of the T-28 signal from the new SPTVAR system signal. However, shifting the T-28 data in time would show good correlation.

New vs. old SPTVAR system: The scatter of the points, for most of this pass, falls nearly along the 1:1 line. The large scatter that occurs as a result of the time displacement, from 152310 to 152345, causes the statistics to indicate poor results.

Horizontal and Vertical Fields (Figs. D-30g, D-31g)

During the first half of the pass, the fields are aligned to the east and pointing upward. They abruptly switch to the northwest and downward near the middle of the pass. They then rotate from northwest to southwest. The field switches back to the upward direction near the end of the pass.

APPENDIX E - Explanation of Sign Disparity Between E_{QY} and E_{qz}

Explanation of an interesting phenomenon of T-28 electric field measurements

Knowing airplane charge is of value in electric field measurement using airplanes. Before a full matrix equation like equation (8) is obtained, we used two independent estimates of the charge acquired by the T-28:

$$E_{qy} = 0.0308 \, (E_l + E_r) \qquad \text{(E1)}$$

$$E_{qz} = 0.09 \, (E_t + 2 \, E_b) \qquad \text{(E2)}$$

E_{qy} and E_{qz} are thought to be mainly proportional to the airplane charge. The coefficients 0.0308 and 0.09 are chosen to make the two quantities equal to each other when there is no ambient field and to make them comparable to coefficients used to deduce the ambient electric field.

The top frame of Figure E1a shows an interesting phenomenon often observed from the T-28 measurement of E_{qy} and E_{qz}. The example shows that when the T-28 is flying toward a negative charge (E_x positive), E_{qy} will go positive and E_{qz} starts positive, but then E_{qz} flips negative as the magnitudes of both increase. After this flip occurs, E_{qz} remains an almost perfect mirror of E_{qy}. This phenomenon has puzzled us since we began acquiring electric field measurements.

However, after deriving the matrix A and developing a hypothesis to explain the corona emission process, the phenomenon can be explained explicitly. First consider the E_{qy} and $E_{qz.}$ According to matrix equation (8), substituting E_i ($i = t, b, l, r$) in terms of ($E_x \, E_y \, E_z$ and Q) into equation (E1) and (E2), we have:

$$E_{qy} = 0.52 \, E_x - 0.06 \, E_y + 0.15 \, E_z + 0.35 \, Q \; \ldots\ldots\ldots\ldots \qquad \text{(E3)}$$

$$E_{qz} = 0.16 \, E_x - 0.05 \, E_y + 0.09 \, E_z + 0.37 \, Q \; \ldots\ldots\ldots\ldots \qquad \text{(E4)}$$

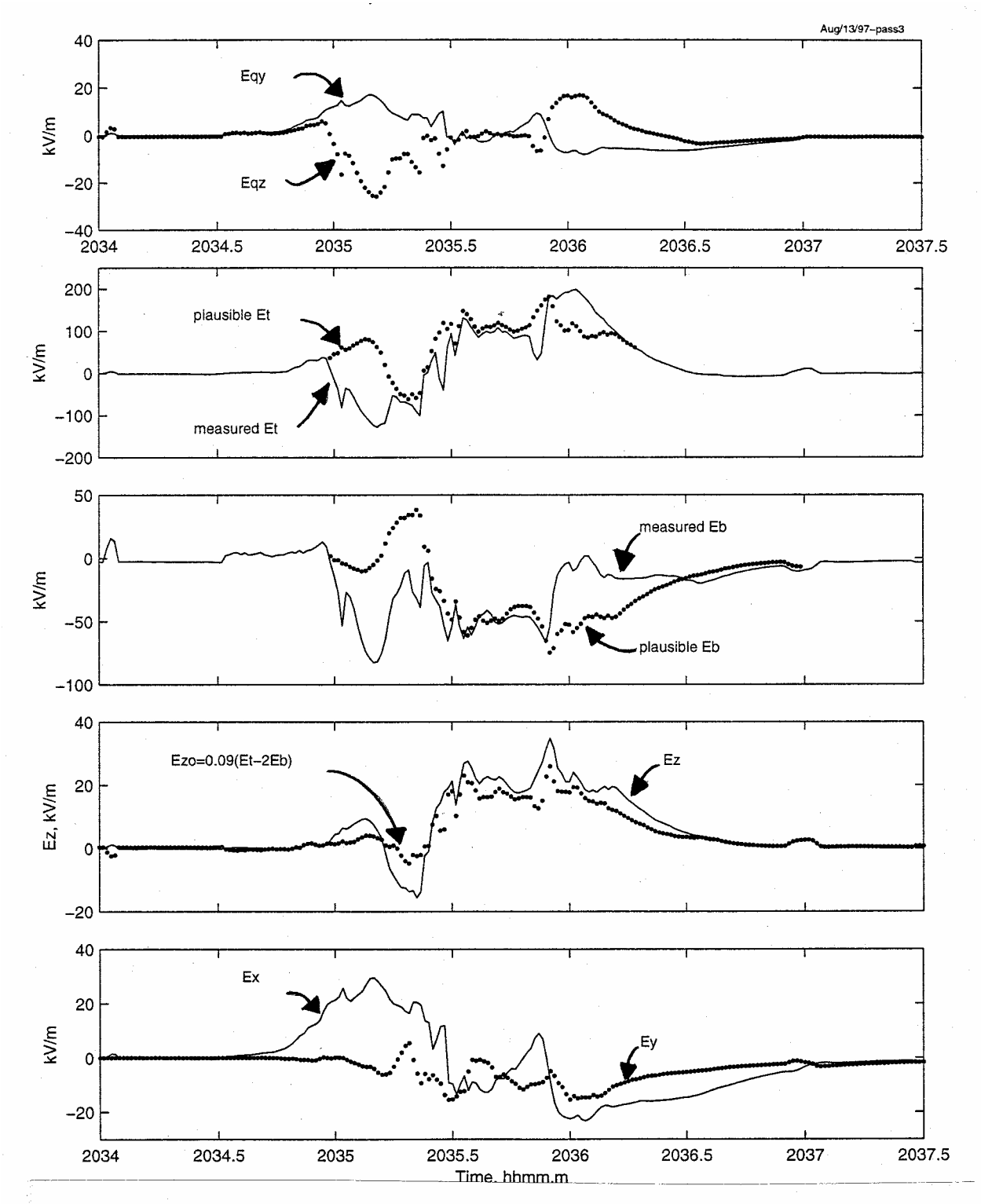

Fig. E1a. Corona ions cause E_{qz} to flip in sign and mirror E_{qy}. Plausible E_t is (1.025E_x -0.796E_y +5.37E_z), and plausible E_b is (0.36E_x +0.1E_y -2.04E_z); whereas (E_x E_y E_z) is calculated from the signals E_l, E_r and E_f. Data are from the third penetration through a severe thunderstorm in New Mexico, from time 20:34 to 20:37:30 UTC on Aug. 13, 1997.

The coefficients of equations (E3) and (E4) show that E_{qy} and E_{qz} are mainly proportional to E_x and Q. If the signals are correct (not affected by corona ions), E_{qy} and E_{qz} should both go positive or both go negative when E_x or Q are dominant. That explains the behavior of E_{qy} and E_{qz} before E_{qz} flips in sign. But, as the airplane is flying toward a negative charge, strong polarization of the airframe by the E_x field component causes positive corona ions to be emitted from the front of the T-28. These ions pass over the fuselage meters. The effects of positive corona ions dominate the measurement of E_{qz} , making E_{qz} flip in sign. In Figure E1a, measured E_t suddenly changes its trend to look similar to $-E_x$ after E_x becomes stronger than about 18kV/m. At this threshold it is expected the propeller tips will start to produce corona ions, corresponding to the time around 20:35 in E1a.

Meter reading E_b also looks similar to $-E_x$ at the same time as E_t does. Since E_{qy} is not affected by the corona ions, E_{qy} keeps varying similarly to E_x as E_x increases. Therefore E_{qy} and E_{qz} mirror each other while corona is affecting the fuselage meters.

It should be mentioned again that when corona ions are emitted due to the strong polarization of the airframe, the airplane charge may remain almost the same as it was before emission began. That is because the airframe has as many sharp edges or points at extremities of the possible ambient field polarization axis. When corona of one sign are emitted at some location on the airplane, corona of an opposite sign will be emitted on other locations so that the total charge on the airplane will not change if the airplane has acquired the maximum equilibrium charge it can hold.

Evidence of this point is shown in Figure E1d. In the figure (second and third frame), the top fuselage meter is affected by the corona ions from time 20:40:45 to 20:41:25 while the bottom meter was not significantly affected by the corona ions. Because the plausible E_b, which is equal to $A_{bx}E_x + A_{by}E_y + A_{bz}E_z$, and measured E_b, which should be $(Q + A_{bx}E_x + A_{by}E_y + A_{bz}E_z)$, are almost identical, we infer that Q is almost negligible for the whole period from 20:39:00 to 20:42:25 UTC. That is, though a strong ambient field has caused corona ions to be emitted and to severely affect the top fuselage meter, the emission of these corona ions neither increases nor decreases the airplane charge conspicuously. The airplane charge remains as negligible as it was before or after the corona ions are emitted.

Figures E1b and Figure E1c are additional examples where E_{qy} and E_{qz} mirror each other when corona ions are emitted. All Figures E1a, E1b, E1c and E1d , are from the same date when the T-28 was penetrating a severe thunderstorm in New Mexico in 1997. The quantity E_{qz} flips sign when ambient field components E_x or E_z become larger than about 15 kV/m, the threshold for the airplane to be sufficiently polarized to emit corona ions.

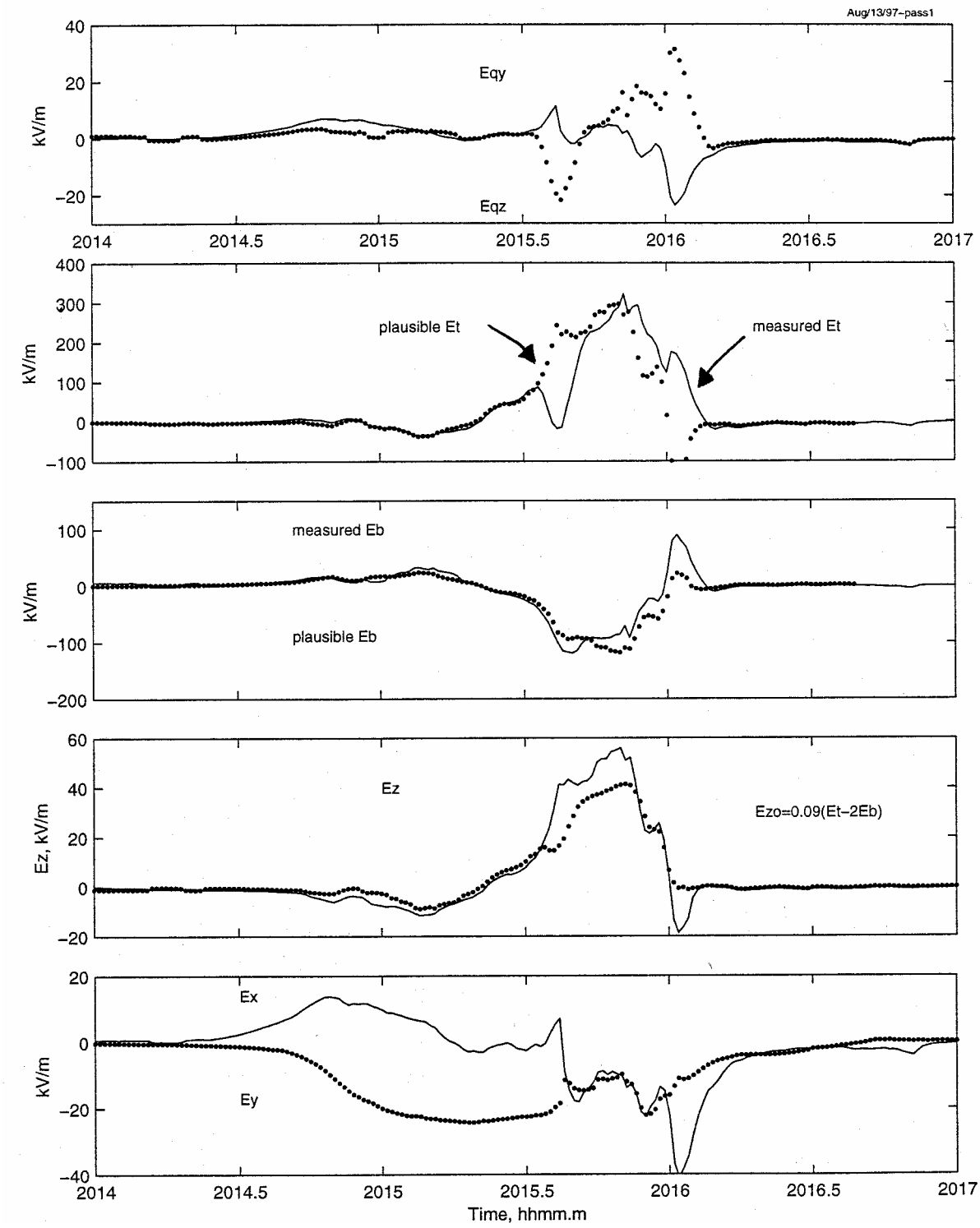

Fig. E1b. Same as Figure E1a, but the time was from 20:14 to 20:17 UTC, First penetration of the same storm on Aug. 13, 1997.

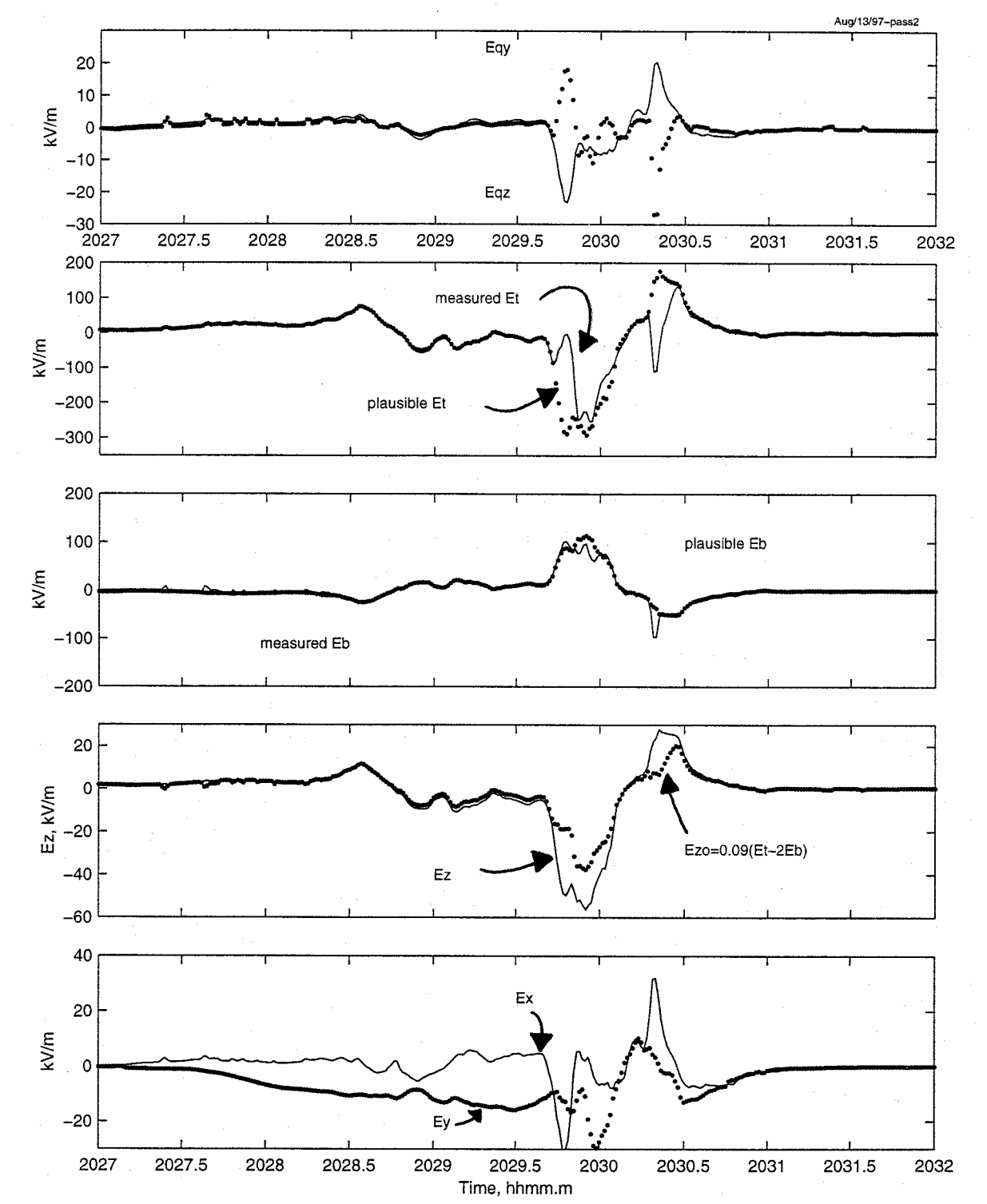

Fig. E1c. Same as Figure E1a, but the time was from 20:27 to 20:32 UTC, second penetration of the same storm on Aug. 13, 1997.

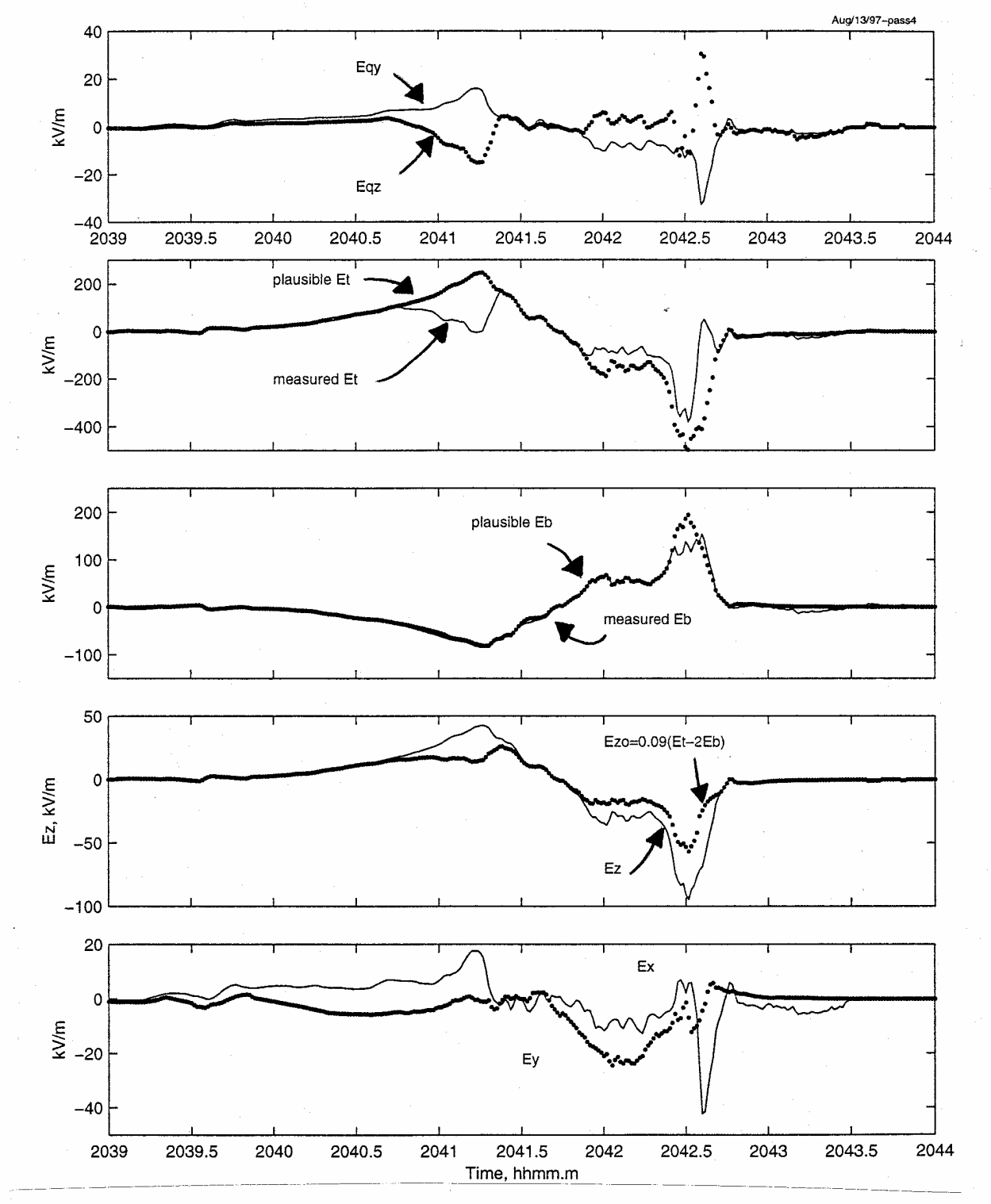

Fig. E1d. Same as Figure E1a, but the time was from 20:39 to 20:44 UTC, Fourth penetration of the same storm on Aug. 13, 1997.